INFORMATION TO USERS

This manuscript has been reproduced from the microfilm master. UMI films the text directly from the original or copy submitted. Thus, some thesis and dissertation copies are in typewriter face, while others may be from any type of computer printer.

The quality of this reproduction is dependent upon the quality of the copy submitted. Broken or indistinct print, colored or poor quality illustrations and photographs, print bleedthrough, substandard margins, and improper alignment can adversely affect reproduction.

In the unlikely event that the author did not send UMI a complete manuscript and there are missing pages, these will be noted. Also, if unauthorized copyright material had to be removed, a note will indicate the deletion.

Oversize materials (e.g., maps, drawings, charts) are reproduced by sectioning the original, beginning at the upper left-hand corner and continuing from left to right in equal sections with small overlaps.

ProQuest Information and Learning
300 North Zeeb Road, Ann Arbor, MI 48106-1346 USA
800-521-0600

GAS FLOWS AND MIXING IN MODELS OF THE INCO FLASH SMELTING FURNACE

By

LORIS MOLINO, B.Sc., M.Eng.

A Thesis

Submitted to the School of Graduate Studies

in Partial Fulfillment of the Requirements

for the Degree of

Doctor of Philosophy

in

Chemical Engineering

McMaster University

GAS FLOWS AND MIXING IN MODELS OF THE INCO FLASH SMELTING FURNACE

DOCTOR OF PHILOSOPHY IN ENGINEERING (2001) McMASTER UNIVERSITY

(Chemical Engineering) Hamilton, Ontario

TITLE: GAS FLOWS AND MIXING IN MODELS OF THE INCO FLASH SMELTING FURNACE

AUTHOR: Loris Molino, B.Sc. (Queen's University) M.Eng. (McMaster University)

SUPERVISORS: Professor M.H.I.Baird

Dr.C.M.Diaz

Professor G.A.Irons

NUMDER OF PAGES: xxvi, 182, A61, B77, C17

ABSTRACT

The flow of gases in the Inco flash smelting furnace has been studied, with the primary objective of improving the mixing of gases in the uptake. Experimental trials were performed in physical models of the furnace gas space in which the flow patterns were examined by means of flow visualization, tracer mixing studies and velocity distribution measurements. Two different models of the flash furnace and uptake have been built and operated: a 1/20 linear scale water model and a 1/5 linear scale air model. Similarity of the flow patterns in the uptake was expected between the models and the plant, given the close agreement of the scaling criteria.

These experiments indicated that the most significant factor affecting the mixing in the uptake is the afterburner configuration. In the range applicable to the plant operation, Reynolds number and jet momentum were found to have little effect on the mixing in the uptake. The afterburner configuration which provided the best mixing conditions, had staggered opposite pairs of jets flowing at 90° to the longitudinal axis of the furnace. The staggered jet arrangement allowed for maximum coverage of the uptake cross-section while keeping the opposing jets close enough that they still interact. This configuration was implemented in the plant at Copper Cliff in 1996.

A mathematical model has been developed using the computational code FLUENT v 4.5 to simulate the flow of gases in the air model. The principal objective was to determine whether the mathematical model could successfully simulate the flow patterns observed in the air model without the addition of afterburner flow in the uptake. The mathematical model predictions suggest that the furnace flow is very prone to become asymmetric. The results of the numerical simulations indicated that very small inequalities in the jet angles or jet flows can lead to asymmetric flow.

The predicted asymmetric flow conditions and measured dimensionless fields were qualitatively similar. The steady state numerical model cannot account for the temporal flow instability at the transition between the furnace and uptake, as was observed in the physical models. The flow instability at this transition produced a pulsating-type flow pattern, which was driven by cyclic imbalances of pressure in the system.

In the furnace space, the turbulent jets from adjacent nozzles flowed directly toward the model floor where they combined to form a single jet stream. The strong jet flows make it inevitable that extensive separation from the side walls and roof occurs. This effect is amplified by the abrupt junction to the uptake. Projecting the air model findings to the plant, the amount of recirculation was estimated to be about three times the flow through the burner jets.

TABLE OF CONTENTS

LIST OF TABLES

LIST OF FIGURES

LIST OF SYMBOLS

Symbol

A	Cell size, m^2
a	Burner scale ratio
C	Dimensionless concentration
c	Tracer concentration, ppm
$\bar{c}$	Well mixed tracer concentration, ppm
c_p	Heat capacity, J/kg/°C
c_ϕ	Dimensionless tracer concentration
D	Hydraulic diameter, m
D'_p	Turbulent diffusivity of particles, m^2/s
DC	Dimensionless concentration
DT	Dimensionless temperature
DV	Dimensionless velocity
d	Diameter, m
E	Turbulent dispersion coefficient, m^2/s or cm^2/s
f	Frequency, s^{-1}
Fr	Froude number
g	Gravitational acceleration, 9.8 m/s^2
H	Sensible heat, W
k	Turbulent kinetic energy, m^2/s^2
L	Linear scale ratio
l	Furnace length, m
ℓ	Characteristic dimension, m
ℓ_m	Jet momentum penetration distance, m

M	Second moment of tracer concentration
M_r	Momentum ratio
m	number of jets
$\dot{m}$	Mass flow through burner jets, kg/s
n	number of measurements
N_d	Dispersion number ratio
P	Pressure, Pa
Q	Total flow, L/min
Q_r	Recirculation Flow, L/min
q	Jet flow, L/min
R	Recirculation Ratio
Re	Reynolds number
Sc'_p	Turbulent Schmidt number of particles
St	Strouhal number
T	Temperature, °C
$\bar{T}$	Average temperature, °C
TI	Local rms turbulent intensity
t	Time, seconds
t_t	Time scale of turbulence, s
U_r	Velocity ratio
u	Velocity, m/s
$\bar{u}$	Mean velocity component of velocity at a point, m/s
u'	Fluctuating velocity component of velocity at a point, m/s
V	Volume, m^3
v	velocity, m/s
$\bar{v}$	mean velocity, m/s
x	axial distance, cm

Greek Symbol

α	Conductivity temperature correction factor, $^{o}C^{-1}$
ε	Kinetic energy dissipation, m^2/s^3
κ	Specific conductivity, mS/cm
ρ	Fluid density, kg/m^3
σ	Statistical variance of tracer concentration curve, s^2
μ	Fluid viscosity, kg/m/s
μ_t	Turbulent viscosity, kg/m/s
θ	Dimensionless time
θ_{PF}	Plug flow volume fraction
τ	Nominal residence time, s
τ_p	Relaxation time of particles, s
$\bar{\tau}$	Actual mean residence time, s

Subscripts

ad	Adiabatic
c	Concentration
eff	Effective
f	Flame/Furnace
g	Gas
i,j	Node coordinate
j	Jet
m	Model
o	Initial
PF	Plug flow
p	Plant
r	Recirculation flow

t	Thermal
U	Uptake
v	Volume
vp	Velocity profile
WM	Well Mixed

Superscript

t	Turbulent

ACKNOWLEDGEMENTS

I would like to express my sincere gratitude to my advisors Dr. M. H. I. Baird, Dr. C. M. Diaz and Dr. G. A. Irons for their continuous guidance, patience, and encouragement through the course of this research. I consider myself extremely fortunate to have had them as advisors, mentors and friends. They allowed me considerable freedom to direct the course of this study, and maintained an enthusiastic interest in this research.

Dr. Baird's profound knowledge of fluid mechanics, and his constructive criticism and innumerable discussions have been instrumental in the completion of this work. For this I am extremely grateful.

Dr. Diaz's insight to industrial research in process metallurgy has been instrumental in defining the scope of this study and promoting its value within the Inco organization. It was a tremendous honor to have worked for him at Inco's research facility in Mississauga, and I look forward to our continued working relationship.

Dr. Irons' vast knowledge and experience in applying computational fluid mechanic techniques to process metallurgical operations have been essential to this research. I am sincerely thankful for his mentoring in this area.

I am also particularly grateful to Dr. S. W. Marcuson for his support and interest in this research project. His willingness to assist me has been truly exemplary and inspirational.

I would like to extend my appreciation to Mr. R. Slayer (Inco), Mr. S. Cort (Nels Consulting) and Mr. D. King (Nels Consulting) for their cooperation and unending assistance in the construction and operation of the flash furnace models. The efforts of Mr. R. Slayer in the design,

construction and operation of the gas and solids sampling equipment are gratefully acknowledged. Mr. J. Hrepic also assisted in the gas and solids sampling in the flash furnace uptake.
I am very appreciative of Dr.L.Gu for his support and many useful discussions during the development of the computational fluid dynamic model in the FLUENT code.

Special mention must me made of my wife, Kirsti, for her support and endless patience, without which the work would not have been fulfilled. I am truly indebted to her. I would also like to thank my parents and sisters for their encouragement.

The financial support by Inco Limited is sincerely acknowledged.

Chapter 1

INTRODUCTION

The process known as flash smelting was pioneered by Inco Limited (Canada) and Outokumpu Oy (Finland) in the 1940's. In the process, a finely divided sulfide ore concentrate is flash smelted by burning some of its sulfur and iron content while the concentrate is suspended in an oxidizing medium, similar to pulverized coal combustion. The products of the flash smelting process are a sulfide matte, an iron-silicate slag and an off-gas containing sulfur dioxide.

Since its introduction in the 1950's, the flash smelting technology has become the dominant industrial method for processing copper concentrate (Pannel, 1988) and, to a significant extent, has been employed for treating nickel concentrates. In the Inco technology, concentrate and commercial-grade (95%) oxygen are injected horizontally through four burners, comprising two at each end of a rectangular reverberatory-type furnace. The Outokumpu flash furnace, essentially an upright U shape, injects concentrate and oxygen-enriched air through a burner(s) downward into a cylindrical reaction shaft. The texts by Boldt and Queneau (1967) and Davenport and Partelpoeg (1987) provide a description of the fundamental design and operational differences between the Inco and Outokumpu flash smelting furnaces.

The flash smelting technology offers notable advantages over other smelting processes:

- Flash smelting technology combines into one process step, the roasting, smelting and partial conversion of a sulfide concentrate. The heat generated by the controlled oxidation of the iron and sulfur in the concentrate is entirely utilized in the smelting of

the charge. Depending upon the oxygen concentration in the input gas, and factors such as the desired matte grade and concentrate composition, the process can be operated autogenously, with no additional heat input from fossil fuels.

- Elevated levels of SO_2 permit economical treatment of the off-gas to recover a substantial part of the sulfur content of the concentrate. In addition, the sulfur dioxide generating reactions take place in a confined space, thus minimizing fugitive emissions. This is of particular importance with regard to the current environmental regulations.

Despite these undoubted advantages, the flash smelting process has some inherent shortcomings. For example, the flash smelting process has a relatively low specific smelting rate, expressed in Nm^3 O_2 used per hr per m^3 of furnace volume. As a result, bath smelting processes, such as the Noranda reactor, the El Teniente converter and the Mitsubishi process, have become flash smelting's major competitor for new and replacement copper smelting capacity (Kellogg and Diaz, 1992). In nickel smelting applications, flash smelting's only major competitor for new and replacement capacity is electric furnace smelting. The advantages of the electric smelting process are its ability to smelt all types of material, including scrap, and lower metal losses to the slag (Davenport and Partelpoeg, 1987). However, the electric furnace has two main disadvantage: i) large requirements for electrical energy, and ii) a stream, albeit small, of weak SO_2 gas unsuitable for fixation.

Furthermore, it has been reported that the flash smelting of copper concentrates in the Outokumpu furnace generates a considerable amount of dust, which requires re-processing and causes operational problems in the off-gas system (Partelpoeg, 1988). In the Inco furnace, despite lower dust generation, problems have also been experienced with dust accumulations in the uptake through which the hot process gas travels between the furnace and the off-gas system.

The treatment of flash furnace matte also causes additional difficulties in the downstream Peirce-Smith converting operation in which the remaining iron and some additional sulfur are removed by oxidation with air. The off-gas produced in this converting process is difficult and expensive

to treat (large volumes of weak SO_2 gas produced intermittently), thus negating one of the major benefits of flash smelting. To circumvent this intrinsic problem of the Peirce-Smith converter, Outokumpu and Kennecott (U.S.A.) developed the flash converting process for the treatment of copper mattes. In this process, matte produced in the flash furnace is cooled, granulated, ground, dried and then oxidized to blister copper with tonnage oxygen in a furnace (Hanniala, 1993; George et al., 1995). Worldwide however, the Peirce-Smith converter remains the most common means of converting copper mattes (Biswas and Davenport, 1996).

1.1 Flash Smelting at Inco

Inco Limited piloted the autogenous flash smelting with both copper and nickel concentrates in the late 1940's (US Patent #2,668,107, issued 1954). In 1952, the first commercial flash furnace, designed to treat copper concentrate at a nominal rate of 450 tonnes per day, was commissioned at Inco's Copper Cliff Smelter (The Staff, The International Nickel Company of Canada, 1955). A second flash furnace, commissioned in December 1953, was designed to treat 900 tonnes of copper concentrate per day. This furnace was later expanded in 1968 to process at rates of 1400 tonnes per day.

Much later, in 1976, the flash smelting of nickel concentrate was evaluated on a commercial scale at the Copper Cliff Smelter (Solar, 1979). This industrial experience reported that the nickel partition coefficient (% Ni_{MATTE}/ % Ni_{SLAG}) of 69±10 was independent of matte grade and was higher than the corresponding value of about 50 for the reverberatory furnace.

In 1978, Inco established the feasibility of cleaning copper converter slags by recycling them to the flash furnace (Antonioni et al., 1979). The ability to recycle 100% of converter slag was an important feature of the Inco flash smelting technology and was adopted at Asarco's Hurley smelter in 1983, and at Phelps Dodge's Chino Smelter in 1984. The extensive industrial experience gained at the Hurley and Chino smelters has substantiated the evidence that full converter slag recycle does not

affect the favourable copper partition coefficient of about 70 which is characteristic of the Inco flash furnace.

The results of the 1976 and 1978 commercial tests led Inco to carry out a commercial test of nickel flash smelting with 100% converter slag recycle in 1984. This experimental campaign confirmed the effectiveness of the Inco flash furnace for cleaning converter slag with full recycle. Under full recycle, the partition coefficient of nickel remained close to 70 (Diaz and Landolt, 1986).

Inco carried out industrial scale tests on oxygen flash smelting of a nickel-copper concentrate in 1985 and 1987 as part of the developmental stages of the Sulfur Dioxide Abatement Program. The results fulfilled the expectations raised by the experience with copper flash smelting. Today, Inco processes about 3600 tonnes of concentrate per day, containing about 20% copper-nickel, through two newly constructed larger flash furnaces that were commissioned in October 1991 and August 1993, respectively. The design of the new furnaces follows the concepts developed by Inco in more than forty years of operation of its copper flash furnace. In December 1993, the copper flash furnace, dating from 1953, was decommissioned as part of Inco's Sulfur Dioxide Abatement Program.

1.2 The Inco Flash Smelting Process (1991 to Present)

The flash smelting furnace is a rectangular, symmetrical refractory-lined box with two burners at each end (inclined downward 12°), and a central gas uptake (figure 1.2.1). The furnace has external dimensions of 30.5 m by 8.2 m with an overall height (from bottom plate to the top of the roof) of 6.9 m. The inside brick hearth dimensions at the slag line are 28.6 m by 6.4 m.

Dry finely-divided concentrate, recycled dust and siliceous flux are mixed with a stream of commercial-grade (95%) oxygen in the burners (figure 1.2.2) prior to the formation of a flame in the furnace freeboard. The burners have an internal diameter of 24.8 cm and an overall length of 1.8 m. Although the burners are integral to the furnace operation, there is little available information about the basis for burner design and the flash smelting flame.

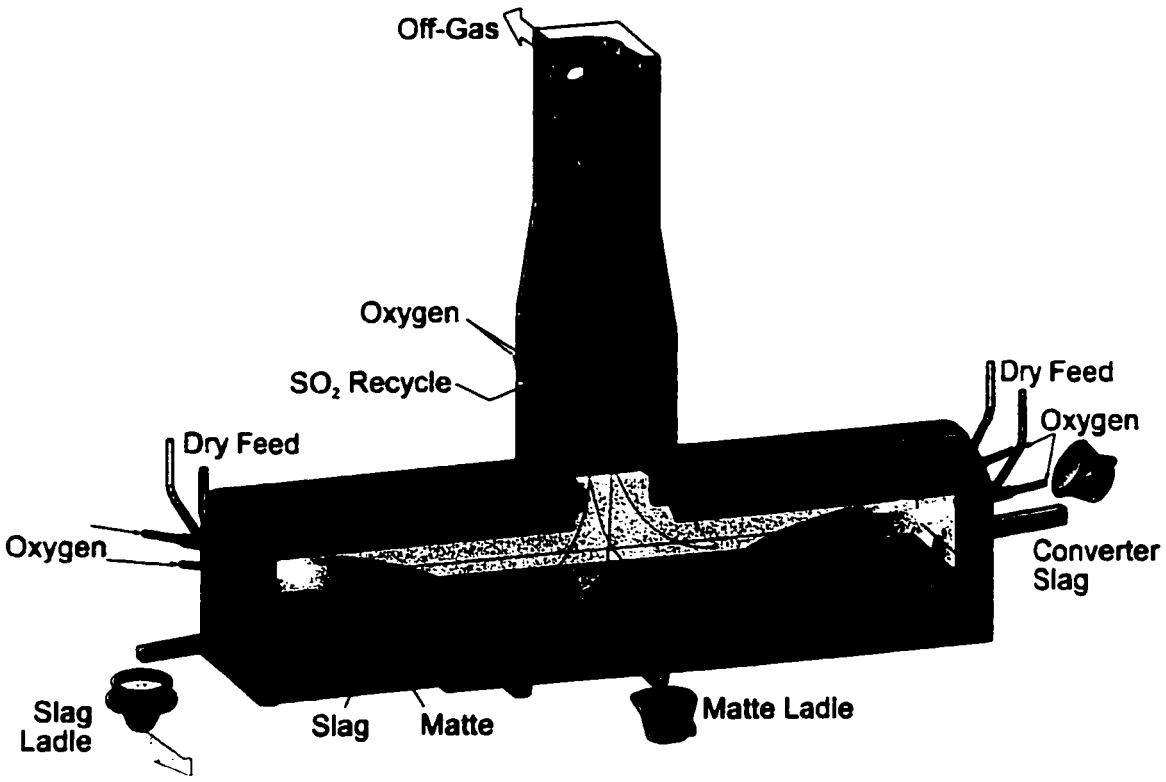

Figure 1.2.1 Schematic of the Inco Flash Furnace at Copper Cliff, Ontario

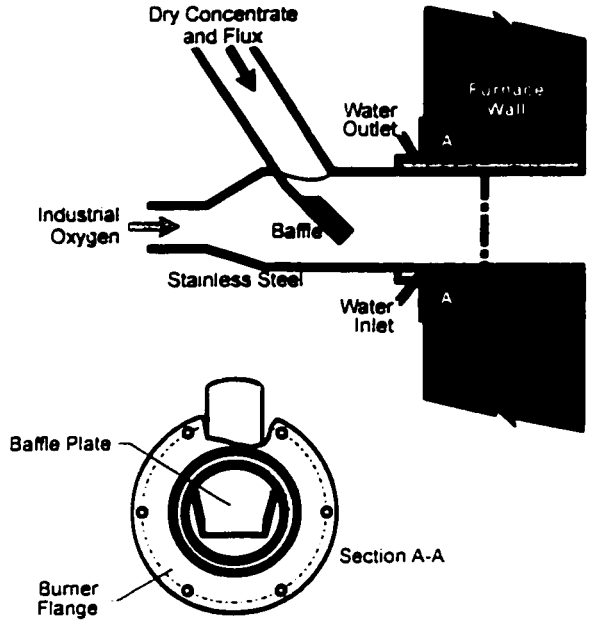

Figure 1.2.2 Schematic of the Concentrate Burner

The "flash" combustion of some of the iron and sulfur occurs while the concentrate is suspende in an oxidizing medium. Regulating the ratio of gaseous oxygen to feed controls the extent of th iron and sulfur oxidation reactions. Typical reactions occurring within the flash smelting furnac and the corresponding heat of reaction at 25°C are (Robie et al., 1978; and Shridar and Dalv 1975):

	ΔH°_{298} (kJ/mol)
Mineral Decomposition	
$CuFeS_2 + 0.5O_2 = 0.5Cu_2S + FeS + 0.5SO_2$	- 99.2
$NiFe_{0.89}S_{1.68} + 0.123O_2 = 0.333Ni_3S_2 + 0.89FeS + 0.123SO_2$	- 9.6
$FeS_{1.14} + 0.14O_2 = FeS + 0.14SO_2$	- 22.6
Slag Formation	
$FeS + 1.5O_2 = FeO + SO_2$	-467.8'
$FeO + SiO_2 = 0.5Fe_2SiO_4$	- 13.8
$FeO + 0.167O_2 = 0.333Fe_3O_4$	- 99.6

The inherent attractiveness of flash smelting is that full advantage of the very high surface-to volume ratio of the concentrate is taken, and a fast specific reaction rate is achieved. Ignition o the concentrate particles (80% < 75μm) occurs upon entrance in the furnace freeboard, and th oxidation reactions are completed in the order of a tenth of a second (Inco Staff, 1977; Jorgense et al., 1977, 1978, 1982, 1983, 1988). In the Jorgensen's experiments, it was determined that th particle-gas reactions are oxygen mass transfer controlled once the particles reach their ignitio temperature and that the principal mechanism for heating the particles to their ignitio temperature is conduction/convection heat transfer between the particles and the surrounding ga By comparison, radiation from the walls and between particles and the surroundings is th dominant mode of heat transfer in the commercial operation (Hahn and Sohn, 1990; Munro an Themelis, 1991). Smelting temperature is maintained at about 1260°C by the heat released fro the oxidation reactions and the combustion of fossil fuel (coke). A typical material balance for th

In the mid 1980's, Inco carried out residence time distribution studies in the copper flash furnace to examine mixing in the slag layer of the commercial flash furnace under 100% converter slag recycle (Marcuson, 1985). Further to this study, Inco in collaboration with McMaster University established an experimental program to simulate the flow characteristics of the furnace slag under different concentrate burner configurations and with slag return (Baird et al., 1991 and 1996; Molino, 1994).

2.1.1 Concentrate Burner Modeling

A study by ASARCO closely examined the flow characteristics of the concentrate burners. The flame pattern issuing from the concentrate burners was deemed responsible for excessive deterioration of the wall and roof refractory brick in the center of the furnace (ASARCO staff, 1987). The ASARCO team felt that improved heat dissipation in the furnace could be achieved through changes in burner design. By moving the flame front towards the furnace end walls, the amount of heat dissipated in the center of the furnace would be reduced. In this effort ASARCO involved researchers from Combustion Engineering Company (CE) and Thames Polytechnic Engineering School, UK.

The studies, performed on half- and full-scale plexiglas models of the burners with a continuous flow of air and solids, compared several burner designs. Although the specifics of the experiments were not available, a brief summary was given in the ASARCO report. In this study, flow visualization tests were conducted using smoke as a tracer. The gas velocities were measured at the burner discharge plane, and the particle velocities at the burner discharge were measured using a Laser Doppler Anemometer. The model studies concluded that:

- the original Inco burner design with the segmented baffle plate was unevenly distributing the solid feed material because the velocity profile was skewed toward the bottom of the burner.

- the best distribution of the feed material was given by a burner with the solid feed

introduced into the center of the oxygen flow, a cylindrical mixing section and a conical diffuser or an eductor that uses a high velocity jet to induce particles into a flow stream.

In 1989, Inco commissioned a burner modeling study by Acres Davy McKee (ADM). The objective of the model study was to assist Inco in the development of an improved burner design. Localized erosion limited the operating life of the burners in the copper flash furnace to about 100 hours, equivalent to 1600 tonnes of dry solid charge.

A full-scale air model of several burner designs was tested at the ADM laboratory (ADM staff, 1989). Similarity calculations were based on gas flow, and the Reynolds number in the model (50000) was about 50% of the estimated Reynolds number in the burner. The testing involved static pressure and velocity profile measurements at several planes in the burner model with gas flow only. Testing with solids was performed only to qualitatively assess the erosion in the burner. The authors compared the results from the different models and concluded that a conical diverging burner produced the best flow conditions. Commercial tests at Copper Cliff were undertaken using the conical burner design developed by ADM. Although the burner was not susceptible to serious erosion, it significantly increased the dust generation rate in the furnace (Humphris, 1990).

A shortcoming of the ADM experimental program was the lack of a continuous feed of solids. The entrainment of solids into a gas stream is known to be accompanied by considerable energy losses, i.e. results in the dissipation of more mechanical energy (Bohnet and Wagenknecht, 1978).

In 1995, plant trials were conducted in an effort to extend the life of burners used in the flash furnaces at Copper Cliff. The plant trials evaluated the impact of aerodynamic shaping of the baffle plate and using ceramic liners in the barrel of the burner. The aerofoil, based on a recommendation made by Baird (1995), was added to the backside of the baffle plate so as to streamline the flow of oxygen entering the barrel of the burner. The effect of the aerofoil and ceramic liners resulted in reduced wall erosion, thus extending burner life from about 3000 tonnes

(120 hours) of dry solid charge to about 20000 tonnes (800 hours). However, these modification to the burner design did not achieve good gas/solid mixing.

In 1995 and 1996, Baird and Rama Rao carried out modeling experiments concentrating mainly on the achievement of a uniform solids flux distribution at the burner model exit. The burner flow behaviour was observed in a 1:6 scale cold model, fed continuously with air and glass beads (Baird, 1995 and 1996). This experimental work examined the effect of the baffle mixing plate designs. Wall erosion in the model was evaluated by using thin latex paint coatings inside the model. The gas-solids behaviour in the region beyond the burner face, at which the flame would form, was not investigated.

The tests revealed that more uniform mixing of the concentrate and oxygen streams could be achieved with a perforated-type baffle plate. However, in plant trials, the test burner had a very limited life compared with the conventional Inco baffle plate-type burner.

2.1.2 Slag Flow Modeling

A modeling study of the slag flow in the furnace was carried out by Baird et al. (1996). Flow patterns and tracer response measurements were evaluated for several different burner jet configurations in a 1:10 scale model. Baird et al. reported that the principal mechanism for lateral circulation of the slag bath was the momentum transferred from the burner jets to the bath. Under normal operation of the model (four jets) the observed flow pattern corresponded to four circulation loops upon which random fluctuations were imposed. The convergence angle of the jets significantly affected the circulation velocities. In general, a steeper convergence angle improved the rate of slag circulation - the circulation velocities were slow at a jet convergence angle of 4° and significantly increased at 12°. This information led Inco to increase the burner convergence angles on the flash furnace at Copper Cliff.

A two-dimensional mathematical model was developed to simulate the spread and dilution of the tracer after it was added at one end of the cold model. The tracer conservation equation was

solved using the finite elements method and a stream function allowed the calculation of the fluid velocities. The dispersion coefficient in the conservation equation was estimated by comparing the calculated mixing time with experimentally determined values. The model was successful in simulating tracer mixing in the cold model.

An alternative approach to modeling the furnace slag flow was presented by Molino (1994) based on tracer measurements in one of the current flash furnaces at Copper Cliff. The model assumed the slag to flow through two unequal-size ideal stirred tanks in series. The assumption was rationalized as follows: a larger initial tank corresponded to mixing due to the momentum transfer from the burner jets as well as the addition of converter slag, and a second smaller mixed tank resulted from the semi-continuous rapid removal of slag. The tanks-in-series model was used to analyze the tracer response studies carried out in the commercial furnaces. When fitted to the response curves, the model predicted a 9:1 volume ratio of the larger to the smaller tank.

2.2 Outokumpu Flash Furnace - Physical and Mathematical Modeling

Several researchers have developed mathematical models of the Outokumpu flash furnace focusing on burner design and furnace gas-particle flow patterns. Some of the research papers in the literature are briefly described in table 2.2.1. These models differ in terms of their complexity with respect to the assumptions made regarding the fluid flow within the furnace and the chemical reaction kinetics. All these models are based on steady state conditions.

2.2.1 Modeling of the Outokumpu Furnace Reaction Shaft

Seppo Ruottu (1979) was the first to develop a two-dimensional model of the Outokumpu flash furnace reaction shaft for copper concentrate. This work was carried out to investigate the possibility of using technical oxygen as the oxidizer in the flash smelting reactor. It was felt that, by using the conservation equations to describe the flash smelting phenomena, the results would provide a numerical solution to the physical process. The model utilized the complete time-

averaged turbulent Navier-Stokes equations, written in cylindrical coordinates. In total the mathematical model consisted of eighteen differential equations, describing the conservation of mass, heat and momentum.

The complexity of the equations precluded an exact mathematical description. Therefore, a number of simplifying assumptions were incorporated into the model, including:

- the assumption of constant mixing length in the one equation model describing the transport of turbulence through convection and diffusion, thus contradicting the convention that the mixing length depends strongly on local conditions.

- the assumption of thermal equilibrium between the particles and gas - this may be valid in the downstream region far from the burner where the heat exchange between the particles and the gas is not significant.

- the omission of the influence of particles on the physical properties of the fluid as well as the assumption of incompressible gas, neglecting the large temperature gradients in the reactor.

These assumptions introduced a considerable degree of approximation into the calculations and empirical parameters were introduced to fit the model to the experimental data. The fitted parameters were derived for experiments carried out in a water cooled chamber with a diameter of 1.2 m and height of 2 m. The use of empirically fitted parameters "tune" the predicted values to experimental measurements greatly restricts the applicability of the model to elucidate the transport phenomena occurring in larger scale furnace.

Table 2.2.1 Models of Outokumpu Flash Smelting Burners and Reaction Shafts

Author	Basis of Paper	Mathematical Model Type
Kim and Themelis (1986) Munro and Themelis (1991)	Reaction shaft with simple single burner entry	1-D, non-isothermal
Funkunaka et al. (1976)	Reaction shaft with simple single burner entry	2-D, turbulent free jet, non-isothermal
Kimura et al. (1986)	Reaction shaft with simple single burner entry	2-D, turbulent free jet, non-isothermal
Ruottu (1979)	Reaction shaft with simple single burner entry	2-D, turbulent one-equation model, constant mixing length, non-isothermal
Hahn and Sohn (1986, 1988, 1990)	Reaction shaft with simple single and double entry burners	2-D, turbulent K-ε model, isothermal and non-isothermal
Koh and Taylor (1992)	Complex burner geometry (KNS venturi type burner)	2-D, turbulent K-ε model, non-isothermal
Nguyen et al. (1992)	Reaction shaft with simple single entry burners - 1 to 4 burners in a 1:14 scale water model	3-D, single phase turbulent K-ε model, isothermal and non-isothermal
Jorgensen and Elliot (1992)	Reaction shaft with complex burner geometry (KNS venturi type burner) - 4 burners in a 1:14 scale water model and 1:4 scale burner model (air)	3-D, two phase turbulent K-ε model, non-isothermal
Sutalo et al. (1994)	Reaction shaft with detailed burner geometry - 1 burner in a 1:14 scale water model	3-D, single phase turbulent K-ε model, isothermal
Smith (1991)	Reaction shaft with single entry burner - 1 to 4 burners in a 1:20 scale water model	

The most complex model of the Outokumpu flash furnace was developed by Hahn and Sohn (1986, 1988, 1990), based on two-dimensional particle and gas flow (axisymmetric, no swirl). In their initial work, the distribution and trajectories of particles in a turbulent gas jet injected into a flash furnace shaft were examined under isothermal conditions. The complete time-averaged Navier-Stokes equations described the flow of gas, and the particle phase was treated in the Lagrangian framework. The Boussinesq approximation together with the k-ε model for turbulent viscosity were used to describe the transport of turbulence in the gas phase. The correlation equations proposed by Melville and Bray (1979) were implemented to account for the effect of the presence of particles on the fluid flow field. The model neglected the contribution to the gas-phase momentum caused by gas expansion and assumed the pressure gradient, virtual mass, and Basset forces acting on the particles to be negligible compared with the aerodynamic drag force.

The TEACH code, developed by Gosman and Pun (1969), was used to solve the gas-phase equations of a recirculating flow in a confined system. The SIMPLER algorithm (Patankar, 1980) was incorporated to calculate the pressure field. The Lagrangian particle equations of motion were solved by the particle-source-in-cell (PSI-CELL) technique, developed by Crowe (1977). For this work, a grid of 32 x 32 was used. For the purpose of validation, the model predictions were compared with experimental data taken from the literature. In general, there was good agreement with the experimentally measured data. This study supported previous findings (Dunn and Smith, 1984) that radially directed gas jets disperse the concentrate more uniformly.

Hahn and Sohn (1990) later extended this model to incorporate the chemical reactions associated with the flash smelting of a chalcopyrite concentrate as well as heat/mass transport phenomena. The overall objective of this research was to develop a comprehensive mathematical model for the processes taking place in the flash furnace reaction shaft. The modeling of heat transfer processes assumed that radiation was the principal mode of heat transfer in the flash furnace. Only radiant heat transfer between the particles, the gas and the walls was considered - particle-particle heat transfer by radiation was neglected. Radiation was modelled using the four flux model for radiative heat transfer combining the absorbing, emitting and anisotropic scattering phenomena. Particle reaction kinetics were treated based on the studies of Chaubal and Sohn (1986).

Predictions of the mathematical model successfully fitted experimental measurements. A major conclusion of this model was that most of the combustion is completed in the upper zone of the reaction shaft within 1 m from the burner tip, and hence the reaction shaft could be made shorter.

The mathematical model of Hahn and Sohn did not consider such phenomena as particle fragmentation, dust generation and particle agglomeration, despite experimental evidence supporting the importance of these phenomena in chalcopyrite smelting (Kimura et al., 1986; Kemori et al., 1988). If the Sumitomo group is correct, the particle-particle agglomeration occurring in the lower section of the reaction shaft is an important mechanism for reducing dust generation. For this reason, the reaction shaft perhaps should not be made any shorter.

The formation of dust during the flash smelting of chalcopyrite concentrates has been reported to be affected by two competing factors: particle fragmentation and particle agglomeration. Kim and Themelis (1986) developed a uni-dimensional model, which incorporated a mechanism for particle fragmentation, to predict the composition and temperature of particles and gas as a function of distance from the burner. The objective of the study was to develop a sound understanding of the reaction mechanism and rate phenomena involved in a chalcopyrite reaction system. The principal limitation of the uni-dimensional model is that it assumes uniform velocity, temperature and particle density at a given distance from the entry point. The model does not consider the radial dispersion of fluid properties, the contribution of turbulent diffusion to the gas phase momentum and the flow field, the effect of particles on turbulence and the dispersion of particles due to turbulent fluctuations. It therefore introduces a degree of approximation which may be unacceptable, especially in the entry region of the reactor. Nonetheless, despite the simplifying assumptions made, the model predictions were similar to those made by Hahn and Sohn (1990). The mass, heat and momentum balances were solved numerically by a "backward" difference technique which produces an implicit formulation for the particular variables. The control volume element was a disc of the total gas-particle envelope, and the axial thickness was determined based on the rate of temperature change in the preceding control volume. A maximum temperature change of 10°C was allowed within a control volume. Details on the determination of the chemical reaction rate, mass transfer and heat transfer constants were not discussed.

Munro and Themelis (1991) adapted this model for an experimental flash reactor (0.13 m ID x 2 m), operating so as to simulate the particle-gas stream in the reaction shaft of an Outokumpu copper flash smelter. The experimental conditions were in the range of industrial operations. Despite the simplicity of this approach, the projections of the uni-dimensional model were in good agreement with the experimental findings.

Themelis, Wu and Jiao (1988) were the first to predict the increase in particle size occurring in an Outokumpu furnace as reported by the Sumitomo group. The model utilized the isothermal jet theory with an equation originally developed for describing the collision and agglomeration phenomena of rain droplets, (Saffman and Turner, 1956). The analysis of the collision and agglomeration phenomena takes account of the fact that collisions between liquid droplets are due to both gravity effects and to turbulent eddies which move one particle against another. The application of this approach is valid in the flash smelting furnace because the melting of the concentrate particles begins upon entry of the charge into the furnace. It has been suggested that a burner design which promotes the agglomeration of particles may be effective in reducing dust formation.

2.2.2 Modeling of the Outokumpu Concentrate Burner

The previous modeling studies paid little attention to the burners and made gross simplifications as to the manner in which the charge was introduced to the furnace. The concentrate burner is the entry point for the reactants into the furnace reaction shaft, and it has considerable effect on the rapid reaction processes occurring in the furnace. Recognizing the importance of burner design, several researchers have investigated the extent of mixing and the formation of the jet issuing from various burner designs (Kemori et al., 1991; Jorgensen and Elliot, 1992; Koh and Taylor, 1992; Elliot et al., 1994). Although Kemori (1991) did not focus on the development of a mathematical model, his investigation demonstrated the influence of burner design on the dust generation rate and the oxygen efficiency in a pilot scale Outokumpu flash furnace.

Jorgensen and Elliot (1992), Koh and Taylor (1992) and Elliot et al. (1994) used the PHOENICS fluid dynamics code to model the burner and reaction shaft of the Kalgoorlie Nickel Smelter (KNS). The mathematical model was used as a tool to examine the effect of burner design on the flow patterns of gases and the dispersion and reaction rate of the concentrate particles in the shaft. To facilitate the mathematical modeling procedure for two phase flow, Jorgensen and Elliot created two models: one to simulate a single burner and the other to model the reaction shaft with four burners. The two models were run in series with the output from the burner model defining the inlet condition to the shaft for each of the four burners. The approach taken in this study was a combination of mathematical modeling and supportive experimentation. The experimentation involved collecting data from the actual furnace itself, a $^1/_4$ scale air model of the burner and a $^1/_{14}$ scale water model of the furnace. In contrast, the models developed by Koh and Taylor and Elliot et al. were validated with results obtained in pilot scale hot models. Irrespective of the validation procedures adopted, the predicted values derived with simulation models were in good agreement with the measured values. The researchers, therefore, concluded that the simulation models can be used with confidence both to predict the flash furnace performance as a function of design changes and variations in process inputs.

Sutalo et al. (1994) studied the flow patterns of reaction gas beneath a distributor burner in a flash furnace reaction shaft. The flow patterns were simulated in a 1/14 scale water model with a detailed burner geometry. However, the dynamic scaling criteria for the water model were not discussed. Still and video photography techniques as well as the digital particle image velocimetry (DPIV) technique were used to measure the velocity fields in two-dimensions. The average velocity vector field in the physical model showed that the main jet center was skewed away from the burner inlet. A large recirculation zone was established, making the flow far from axisymmetric. In addition, this experimental study found a temporal instability in the jet exiting from the burner, driven by cyclic imbalances of pressure fields within the system. The temporal instability resulted in a high turbulence intensity.

In this study, the flow through the burner and the reaction shaft model was simulated with an isothermal single phase three-dimensional mathematical model using the FLUENT computational

fluid dynamic code. The three-dimensional mathematical model was used to simulate the flow because the water inlet was at an angle to the shaft and the flow was not axisymmetric. The FLUENT model incorporated a boundary fitted coordinated system as the burner geometry could not be approximated by a Cartesian grid. Only half the burner and shaft was simulated as the model was symmetric in the vertical plane. The grid consisted of 65 x 50 x 21 computational cells with the grid denser in the burner and at the burner-shaft transition. FLUENT solved the governing partial differential equations for the conservation of mass and momentum. The k-ε turbulence model was used to compute the turbulent eddy viscosity. The computation was carried out for a uniform inlet velocity of 1.44 m/s and an inlet turbulence intensity of 10%. For the same inlet flow rate, the mathematical model predicted velocity magnitudes approximately three times the measured average velocity. This discrepancy in the mean velocity of the main jet region is likely due to the observed temporal instability of the jet in the water model which cannot be accounted for in a steady state mathematical model. Other potential explanations for the differences include: the experimental average velocity field was calculated for only a 19 second time period which may not be a true representation of the flow field, and the measured velocities are volume averages over a 10 mm illuminated region as compared to the predicted velocities on the plane of symmetry.

2.3 Summary

Many researchers have investigated the fluid and chemical dynamics of the Outokumpu flash smelting technology. The mathematical models developed by the various researchers to explain the physical phenomena differ in terms of the assumptions made regarding the fluid flow within the furnace and the chemical reaction kinetics. Despite the difference in both design and operation, the modeling studies of the Outokumpu furnace provide guidance for the development of a mathematical model describing the flow dynamics of the Inco furnace.

The complex mathematical model, developed by Hahn and Sohn, has effectively described the flash combustion of chalcopyrite concentrates in the Outokumpu reaction shaft from first

principles. This modeling represented a considerable achievement which has clarified the analysis of the problem by deriving all of the equations governing the complex sub-processes associated with flash smelting. The simpler approach presented by Themelis and co-workers has also successfully predicted the transport phenomena and reaction kinetics in the Outokumpu flash smelting furnace reaction shaft. But in general, these modeling studies paid little attention to the burners and made gross simplifications concerning the manner in which the charge was introduced to the furnace.

The concentrate burner is the entry point for the reactants into the furnace reaction shaft and has considerable effect on the rapid reaction processes occurring in the furnace and the formation of the jet issuing from various burner designs. This research has demonstrated the influence of burner design on the dust generation rate and the oxygen efficiency in a pilot scale Outokumpu flash furnace.

In contrast to the quite extensive literature on the Outokumpu furnace, there is limited information available about the fluid dynamic behaviour of the Inco flash furnace. The principal development work of the Inco flash smelting technology has been exclusively performed by Inco on pilot and commercial scale flash furnace. The fluid dynamic studies of the Inco technology have only been undertaken recently investigating the mixing of oxygen and concentrate in the burners and the flow patterns in the furnace slag layer. The fluid dynamics of the hot gas in the furnace and the uptake has not been examined in any great detail. This warrants the collection of more Inco data and modeling to further our understanding and improve the design and operation of the Inco flash furnace.

Chapter 3

RESEARCH OBJECTIVE AND SCOPE

The Inco oxygen flash smelting process was used for nearly a half century to treat copper concentrate and was essentially a trouble free and well-controlled operation. Routinely, matte of constant grade was produced, and the sulfur dioxide in the off-gas was fixed as liquid. The main difficulty encountered with this operation was the accumulation of build-up in the uptake, which required regular removal. Therefore, there was little incentive to pursue an extensive study of the flash smelting flame and furnace dynamics.

It was not until the implementation of bulk concentrate flash smelting that the need for fundamental data on the furnace dynamics became apparent. The complex interactions of heat, mass and momentum transfer along with the chemical reactions that occur simultaneously in the gas space of the Inco flash furnace are not very well understood. Moreover, mathematical models have not been formulated to describe the fluid dynamic behaviour of gases in the freeboard and uptake, and there is little data in this area. To realize further productivity gains and higher furnace availability, a firm understanding of the transport phenomena specific to the Inco flash smelting process is required. In the current flash smelting operation at Copper Cliff, the aspects which warrant a detailed investigation are:

- the influence of the concentrate burner design on the behaviour of the combustion flame and the mechanisms of dust generation.

- the influence of flow patterns in the furnace gas space on the reaction dynamics (secondary combustion), heat dissipation and accretion formation in the furnace uptake.

Owing to the production problems associated with the flash furnace uptake, the focus of this research project has been on the second of the above items. The two primary objectives were:

- to determine the critical phenomena affecting the flow patterns and mixing behaviour in the furnace and uptake gas space.

- to evaluate the effect of alternative injection arrangements on the mixing of gases in the uptake and utilize this information in order to recommend improvements to the original furnace uptake design.

To accomplish these objectives, a number of experimental investigations have been performed both in scaled cold models and in the commercial furnace at Copper Cliff. This experimental data has provided the data necessary to understand the fundamental aspects of the furnace gas flow patterns. The development of a mathematical model provided a tool for the simulation of the flow patterns observed in the models. The outcome of the experimental and modeling efforts has been used to make recommendations to improve industrial practice.

3.1 Experimental Objectives

The objectives of the experimental work were as follows:

- to determine the factors which are important to the mixing of gases in the furnace uptake, and the predominant features of the furnace flow patterns. The experimental data were used to support the development of a computational fluid dynamic model.

- to relate the findings of the physical modeling to the operation of the flash furnace uptake.

3.2 Mathematical Modeling Objectives

The objectives of the mathematical model were as follows:

- to predict, within a reasonable degree of error, the experimental data generated by the scaled models of the furnace under the flow conditions examined in the experiments.

- to analyze the parameters that influenced the flow patterns observed in the scaled cold models.

- to evaluate the merits of numerical modeling as a design tool for recommending plant improvements.

In order to realize these objectives, the computational fluid dynamics code FLUENT was used to simulate the flow through the physical models and therefore, the furnace. This code solved the governing partial differential equations for the conservation of mass, momentum and turbulent quantities in 3-dimensional boundary fitted coordinates (BFC).

Chapter 4

EXPERIMENTAL METHODOLOGY

To accomplish the experimental objective, described in Chapter 3, a series of experimental studies were carried out involving primarily physical modeling techniques. The physical modeling experiments examined the effect of flow variables on the mixing of gases in the furnace uptake and the predominant features of the furnace flow. The physical models are discussed below, together with a description of the experimental procedures. The analysis of the experimental data is presented in Chapter 5.

In the design and operation of furnaces, the aerodynamic factors are often of major importance and a detailed study of the flow behaviour using cold models is advantageous. The principal reason for using models is to determine the effect of modifications in design without incurring the expense or risk of making these changes on the commercial scale. This technique is useful in this project because the flash furnace environment makes it extremely difficult to obtain accurate information on the flow patterns.

4.1 Physical Modeling - Scaling Criteria

The physical modeling study focused on seeking an afterburner configuration which would improve gas mixing in the uptake. Towards this purpose, physical modeling techniques were used to investigate the flow patterns and mixing in two different models of the flash furnace and uptake. The first model was a 1/20 linear scale model using water as the fluid. The second model

used air at a 1/5 linear scale.

4.1.1 Geometric Scaling Criteria

Geometric scaling requires that the dimensions of a model are scaled linearly from those of the plant by a linear scale ratio, L, defined as the ratio of the plant dimensions to the model dimensions. The water and air models incorporated the essential geometrical details of the commercial flash furnace freeboard and uptake, including the transition passage between the uptake and the gas-quenching chamber.[1] The floor of the model represented the surface of the molten slag in the hearth of the furnace. The physical dimensions of the commercial furnace and the models are given in table 4.1.1.

As indicated in table 4.1.1, the linear scale ratios, L, of the water and air models were 20 and 5, respectively. In the case of the water model, the linear scale ratio was selected, on the basis of volumetric flow requirements to maintain dynamic similarity, also taking into account the laboratory's supply and consumption of water. The air model's linear scale ratio was limited to 5 due to space constraints in the laboratory.

The burners in the furnace and the uptake were not scaled linearly but were instead scaled according to an equivalent burner diameter as defined by Thring and Newby (1952). In their paper, the equivalent burner diameter was defined as the aperture through which the same mass flow rate emerges with the same jet momentum as the full-scale furnace but with the density, ρ_f, of the combustion products at flame temperature instead of the density ρ_o of the burner fluid. That is, in a full-scale cold model, the burner jet velocity is maintained similar. To achieve this in a full-scale model, the burner jet diameter was scaled according to the square root of the density ratio, ρ_f/ρ_o. In scaling the concentrate burners, the density of the burner fluid (ρ_o = 6.6 kg/m^3) and combustion products (ρ_f = 2.0 kg/m^3) is based of the presence of gas and solids. The flame temperature was assumed to be 1300 °C.

---

[1] For convenience, the commercial flash furnace and uptake will be referred to as the plant.

Table 4.1.1 Plant and Model Dimensions, in metres

	Plant	Water Model	Air Model
Linear Scale Ratio, L:	1	20	5
Furnace:			
Length	29.3	1.47	5.86
Width	7.1	0.36	1.42
Height (freeboard)	4.4	0.22	0.86
Uptake:			
Height Total	15.1	0.76	3.02
Bottom Section	4.7	0.23	0.94
Middle Section	4.2	0.22	0.86
Top Section	6.2	0.31	1.22
Bottom Section Width	4.4	0.22	0.89
Bottom Section Length	4.0	0.20	0.81
Top Section Length	4.4	0.22	0.89
Top Section Width	2.8	0.14	0.56
Burners:			
Separation Distance	3.4	0.17	0.68
Angle (Down/Horizontal)	12°/12°	12°/12°	12°/12°
Afterburners/SO_2 Recycle			
Distance from top of furnace roof	2.7	0.13	0.53

The Thring-Newby similarity criterion makes allowance for the temperature difference, which exists in the plant between the main furnace chamber fluid, and the burner fluid prior to entering the furnace. To ascertain the conditions for approximate similarity, Thring and Newby assumed that (1) chemical reaction only affects mixing through its effects on temperature and density, (2) the temperature and density are nearly uniform throughout the jet, and (3) momentum is conserved in the free jet. Thring and Newby used an isothermal model with burners scaled to the equivalent diameter, to predict the flame pattern of an atomized oil fired burner.

The problem was similar in modeling the flash furnace, in that an isothermal constant density mixing model was employed to approximate the jet contour of a hot flame burning solid fuel. In this case, the two systems differed because (1) the density in the flame varied from point to point due to temperature and molecular weight differences as well as the distribution of the solid fuel, (2) chemical reaction was occurring, and (3) the solid fuel considerably increased the density of the jet issuing the burner. According to Thring and Newby, the diameter for the burners in the model furnace and uptake was determined using the burner diameter scale ratio as defined by equation 4.1.1,

$$a = L\sqrt{\frac{\rho_f}{\rho_o}} \qquad (4.1.1)$$

Table 4.1.2 gives the burner diameter scale ratio and size used for the furnace and the uptake model.

Table 4.1.2 Plant and Model Furnace And Uptake Burners, in cm

	Plant	Water Model	Air Model
Furnace Burner Inside Diameter:			
Scale Ratio, a	1	11.0	2.7
Calculated		2.3	9.0
Actual	24.8	2.1	9.7
Afterburner O_2 Inside Diameter:			
Scale Ratio, a	1	12.6	3.1
Calculated		0.42	1.67
Actual	4.9	0.32	1.59
SO_2 Recycle Inside Diameter:			
Scale Ratio, a	1	8.9	2.2
Calculated		1.64	6.57
Actual	14.6	0.95	6.27

It is worth noting, however, that the actual diameter of the model burners differed from the calculated diameter using the Thring-Newby equation. The actual burner diameter was based on

commercially available sizes, which were close to the calculated diameter. The exception was the SO_2 recycle jet size in the water which was reduced in size to accommodate the flow capacity of the available rotameter.

Both the air and the water models were designed with a stationary bottom which was not representative of the situation in the plant. In the commercial furnace, the slag flows through the furnace with a plug flow velocity of about 0.3 cm/s, while the process gas has a plug flow velocity of about 40 cm/s, two orders of magnitude greater. Although the interfacial velocity between the process gas and the slag are equal based on the no slip boundary condition, the velocity of the slag is sufficiently low and the viscosity is high, so that it was perceived to have little bearing on the flow pattern of process gas.

4.1.2 Dynamic Scaling Criteria

Dynamic similarity is concerned with the forces which accelerate or retard moving masses in dynamic systems. It requires that the relative importance of various forces acting be the same in both the model and the plant. Geometrically similar systems are dynamically similar when the ratios of all corresponding forces are equal.

To consider the similarity between a flash furnace and a single fluid model, it was necessary to determine to what extent a single fluid model can simulate a two-phase system in which combustion takes place. In the furnace, combustion occurs once the dried concentrate issuing from the burner reaches its ignition temperature. In the flash smelting process, the concentrate particles reach their ignition temperature within 0.1 second and the reaction is completed in less than 0.1 second (Jorgensen, 1986). It is suggested that the large temperature gradients generated are confined to a small region of the furnace freeboard and that the resulting distortion of the flow patterns is not great. It is worth noting, however, that the effect of jet expansion associated with the entrainment of hot furnace gases by the jet issuing from the burner was accounted for in the Thring-Newby assumption.

Flow similarity in the models was based on a flash furnace throughput of 110 tonnes per hour of dry solid charge, which was typical of the operation. The corresponding flash furnace and uptake gas flows were calculated from a mass and heat balance (table 4.1.3). To calculate the flow rates in the model, the flame and its surroundings were assumed to have the properties of furnace gas at a smelting temperature of 1300°C. In modeling studies of an open hearth furnace, Leys and Leigh (1952) found that this gave a false picture of the flow pattern very near the burner, but a better picture as the mixing progressed. The scaling criteria used in comparing the flow conditions in the plant and the models are summarized in table 4.1.4, and discussed below.

Table 4.1.3 Flash Furnace Operating Conditions

Dry Solid Charge (tph)	110
Oxygen Consumption (Nm^3/hr)[1]	15400
Furnace Off-Gas (Nm^3/hr)	16000
Afterburner Oxygen Consumption (Nm^3/hr)	900
Cold Furnace Gas Recycle Flow (Nm^3/hr)	1800

Note 1: Nm^3 ≡ volume at normal conditions (0°C, 1 atm)

4.1.2.1 Reynolds Number

One criterion for ensuring similarity in the models is to maintain equality of Reynolds number. The dimensionless Reynolds number defines the ratio of inertial to viscous forces acting on the fluid. The superficial Reynolds number, which is based on the superficial velocity, is an indication of the level of turbulence in the furnace and uptake. In the models, the flow was in the turbulent regime. However, owing to water supply considerations, it was necessary to run the water model at reduced Reynolds number.

4.1.2.2 Dispersion Number

Although superficial Reynolds number similarity is important in fluid flow modeling, the superficial velocity has little application in a chamber with large recirculating flows. The

superficial Reynolds number tends to underestimate the level of turbulence as well as the amount of mixing. It assumes a well distributed flow situation which does not exist unless the aspect ratio (L/D) for the chamber is very large. In the furnace freeboard, the turbulence intensity is very non-uniform and there is considerable circulation. In low aspect ratio chambers such as the furnace freeboard, the entering jets create swirling and turbulence. A useful measure of the amount of turbulence and circulation in these chambers is the rate of kinetic energy dissipation averaged over the volume of the chamber, ε_v, expressed in W/m^3 (Uhl and Gray, 1966). The kinetic energy dissipation is defined as the kinetic energy flow through the burner jets dissipated through the furnace volume (equation 4.1.2). In calculating the plant conditions, the kinetic energy was based on the solids and gas issuing the tip of the concentrate burner with the same velocity. Also, implied in this calculation was a uniform solids distribution in the gas.

$$\varepsilon_v = \frac{\frac{1}{2}\dot{m}\,u^2}{V} \; ; \text{ where } u = \text{jet velocity} \qquad (4.1.2)$$

A widely used criterion for the turbulent bulk mixing effect of the kinetic energy dissipation for a flow through system is the dispersion number (equation 4.1.3). Baird and Rice (1975) illustrated by dimensional analysis that the turbulent dispersion coefficient, E, is proportional to $^1/_3$ power of the kinetic energy dissipation, assuming isotropic turbulence (equation 4.1.4). Although the turbulence in the furnace freeboard is anisotropic, this approach provides a useful technique for scaling purposes.

$$N_d = \frac{E}{\bar{v}\,l} \; ; \text{ where } \bar{v} = \text{superficial furnace velocity}, \; l = \text{furnace length} \qquad (4.1.3)$$

$$E \propto \left(\frac{\varepsilon_v}{\rho}\right)^{\frac{1}{3}} \ell^{\frac{4}{3}} \; ; \text{ where } \ell = \text{characteristic dimension} \qquad (4.1.4)$$

The exact value of the turbulent dispersion coefficient was not calculated for the plant and the models, as the proportionality constant was not known for the flash furnace geometry. In

comparing the turbulent bulk mixing effect, the ratio of the dispersion numbers between the plant and the model was used (equation 4.1.5). For scaling of mixing (recirculating flow) conditions, the similarity between the plant and the models was achieved when the ratio of dispersion numbers was unity.

$$N_{d,r} = \frac{N_{d,m}}{N_{d,p}} = \frac{E_m}{E_p}\frac{\bar{v}_p}{\bar{v}_m} L = \left(\frac{(\varepsilon_v/\rho)_m}{(\varepsilon_v/\rho)_p}\right)^{1/3} \frac{\bar{v}_p}{\bar{v}_m} L^{-1/3} ; \qquad (4.1.5)$$

where m ≡ model ; p ≡ plant

4.1.2.3 Cross Flow Jet Mixing

The mixing of jets in cross flow with a main stream is a function of the jet momentum, jet Reynolds number and the main stream Reynolds number (Rajaratnam, 1976; O'Leary and Forney, 1985; Sroka and Forney, 1989). In this published work, the main stream flow was fully developed and turbulent, and a single jet was introduced at a right angle to the main stream. The jet momentum flow determined the penetration of the jet fluid into the main stream and the mixing behaviour of the jet. In Forney's work, satisfactory mixing was achieved within 5-10 pipe diameters.

In the uptake, the afterburner jets located near the base are directed into the main stream of furnace off-gas. Although fully turbulent, the flow of furnace off-gas in the uptake is not fully developed. In addition, the afterburner jets were oriented such that opposing jets impinged on each other. Although Forney did not consider these factors in his analysis, the uptake flows in the air and water models were scaled according to the jet momentum flow ratio, the jet velocity ratio and the jet and main stream Reynolds numbers. The jet momentum flow ratio, M_r, and the velocity ratio, U_r, were determined using equations 4.1.6 and 4.1.7, respectively. In calculating these ratios for the plant, the uptake was assumed to contain no accretions on the walls. The afterburner jet and the main stream furnace flow were maintained in the turbulent flow regime.

$$M_r = \frac{\left(\dot{m}\, u\right)_{jet}}{\left(\dot{m}\, u\right)_{uptake}} \qquad (4.1.6)$$

$$U_r = \frac{u_{jet}}{u_{uptake}} \qquad (4.1.7)$$

Table 4.1.4 Dynamic Scaling Parameters for the Water and Air Models

	Plant	Water Model	Air Model
Linear Scale Ratio, L:	1	20	5
Burners:			
Jet velocity, m/s	27.6	4.6	19.4
Reynolds number	2040×10^3	92.6×10^3	126.4×10^3
Furnace:			
Velocity, cm/s	48.5	4.0	27.6
Reynolds number	18800	10900	19100
Dispersion number ratio, $N_{d,r}$	1.0	1.0	0.8
Uptake:			
Entrance velocity, cm/s	142.8	12.9	81.3
Entrance Reynolds number	45000	27500	45900
Oxygen Afterburner Jets			
Number of jets	4	4	4
Jet velocity, m/s	38.6	4.2	22.3
Reynolds number	97000	13400	23600
Momentum flow ratio, M_r	0.21	0.18	0.21
Velocity ratio, U_r	27.0	32.4	27.4
Cold Furnace Gas (SO_2) Recycle Jets			
Number of jets	2	2	2
Jet velocity, m/s	15.4	2.3	8.8
Reynolds number	199100	22300	37100
Momentum flow ratio, M_r	0.52	0.51	0.51
Velocity ratio, U_r	10.8	18.0	10.8

From table 4.1.4 it is apparent that reasonably good dynamic similarity has been obtained for the two models, except in regards the burner Reynolds number. But as pointed out earlier, this is not believed to be a factor of major importance to the fluid behaviour in the furnace.

4.2 Linear Scale Water Model (1:20)

The isothermal water model was constructed from 1.27 cm (½ in.) perspex sheet to $^{1}/_{20}{}^{th}$ linear scale of the plant furnace (figure 4.1.1). As previously mentioned, the model incorporates the essential geometric features of the plant furnace. The working fluid was water and the water flows were scaled accordingly to maintain dynamic similarity (table 4.1.5).

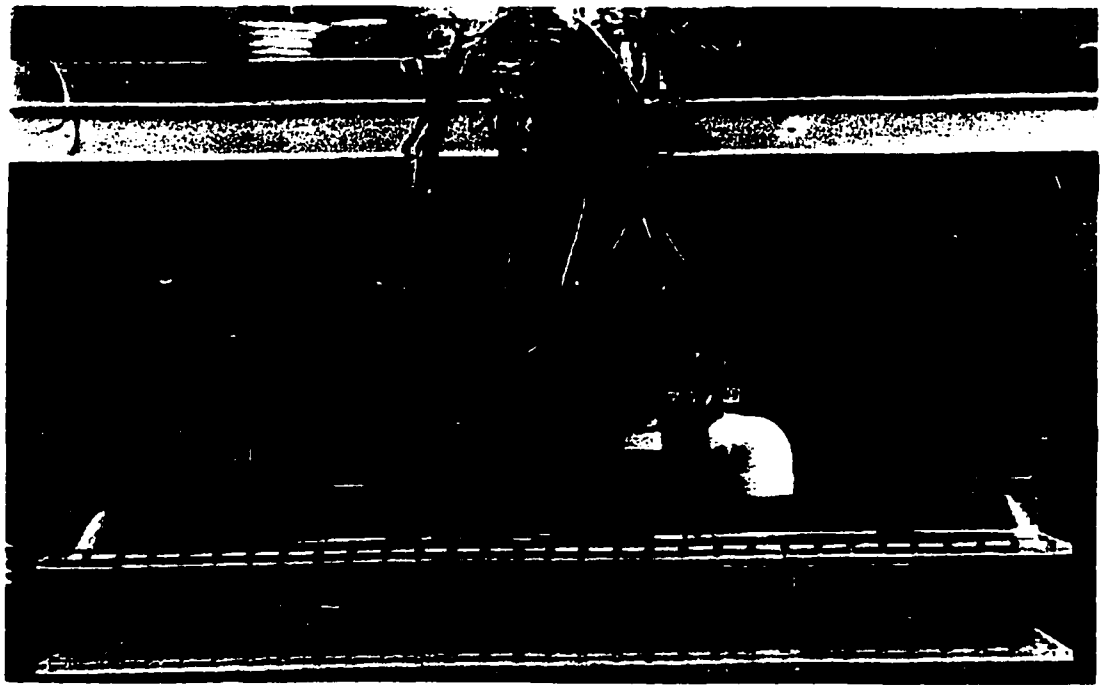

Figure 4.2.1 General Arrangement View of the Water Model

Table 4.2.1 Water Model Flows, L/min, Used in the Scaling Calculations

	Per Burner Jet	Total
Main Burner Jet	87.5	350
Uptake Afterburner Jet	2	8
Uptake Recycle Jet	10	20

4.2.1 Water Model - General Arrangement

The model was initially set up to simulate four main burner jets, four afterburner jets and two SO_2 recycle jets and was arranged as a continuous-flow, open circuit system. The model was designed to permit the testing of several alternative jet configurations in the uptake. A schematic of the model water distribution is given in figure 4.2.2. Due to the large flow through the main burners, the laboratory's internal water distribution system was unable to supply a constant flow of water. The main burners were, therefore, fed directly from the laboratory's main water supply header through a 5.08 cm (2 in.), 690 kpa (100 psi) water line. The pressure in the distribution manifold was controlled by a pressure regulating valve. The flow to each main burner jet was controlled using a globe valve and measured with a Brooks Instruments rotameter (flow meter model R10M-25-3F, float model 10 LJ-238).

The afterburner and SO_2 recycle jets were piped from the laboratory's internal water distribution system through a 2.54 cm (1 in.) water line. A pressure regulating valve controlled the pressure in the distribution manifold. The flow to the afterburner jets was adjusted by a high flow needle valve, while a globe valve was used to regulate the flow to the SO_2 recycle jets. A Brooks Instrument rotameter measured the flow of water to the afterburner jets (flow meter model R615B with tantalum float) and to the SO_2 recycle jets (flow meter model R9M-25-3F, float model 9LJ-160). The calibrated accuracy of the flow meters used to measure the water flow to the jets was 1% of the full-scale.

was started, a blue plume appeared in the region of injection. The plume spread rapidly delineating the mixing region with a small green transition band separating the base solution from the acid solution.

Each experiment was observed using both video and still photography techniques to permit careful observation of the mixing after the experiment. The video and still photographs were taken about 2 minutes after the flow of base was established. This allowed sufficient time for the model to reach steady state conditions. The still photographs were taken with a 35 mm camera set for a shutter speed of $^{1}/_{30}$ second and f-stop of 4, and captured on 400 series Kodak film. To simultaneously view both the front and side planes of the uptake, a mirror was positioned adjacent to the uptake at an angle of 45° (figure 4.1.3). The acid-base reaction method permitted the simultaneous observation of the whole flow field in the uptake as well as local details without obstruction.

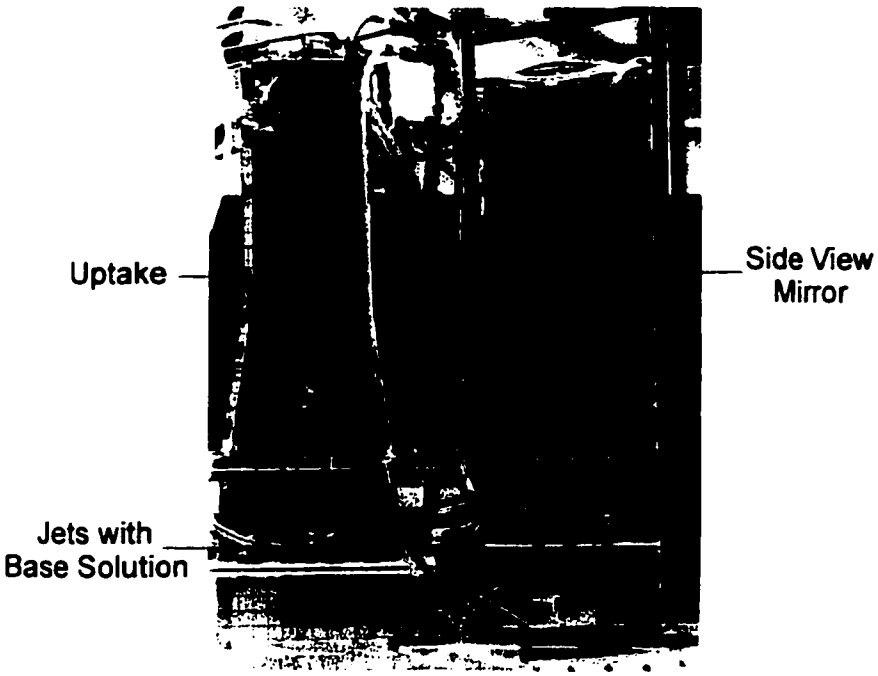

Figure 4.2.3 Typical Photograph of Acid-Base Experiment

(dark gray ≡ unreacted base; light gray ≡ reacted base)

The acid-base reaction experiments provided an excellent method for screening potential afterburner configurations. A total of 6 afterburner configurations were screened using this method; a table giving the test conditions and figures showing typical mixing patterns can be found in Appendix A.

4.2.2.2 Flow Visualization - Particle Tracking

A complementary method for visually observing the flow patterns is to introduce neutrally buoyant particles into a model. In the water model, these experiments focused on the bulk flow patterns in the furnace and the uptake. The experiments were carried out without the introduction of flow through the afterburner jets. Although these experiments can provide quantitative data, it was difficult to determine the exact position and trajectory of the particles in the flow field without the use of elaborate lighting arrangements or laser techniques to illuminate a plane within the model. These techniques are expensive, and a decision was therefore made not to use them. Instead, only qualitative data was collected.

For these experiments, black polystyrene spheres, having a specific gravity of 0.98-1.02 and a sphericity close to 1, were used as the tracer particles. The slight deviation from a specific gravity of unity was considered to be sufficiently small for the tracer particles to significantly deviate from the flow paths of the water, i.e. no gravitational errors were introduced in tracing the flow patterns. The polystyrene particles were in the size range of 1-3 mm in diameter. In this range the Stokes velocity of the particles was 0.001-0.01 cm/s which was significantly less than the superficial uptake velocity of 4-19 cm/s. This particle size range was sufficiently small that the particles followed the flow of water closely, yet was large enough for satisfactory observation.

The polystyrene particles were introduced into the model through one of the main burner jets. About 50 particles in water were injected with a 500 mL plunger-type injector over a period of approximately 30 seconds. In this way, the injection of the particles in water did not significantly disrupt the flow to the main burner jet. The trajectory of the black polystyrene particles was observed on a white background, thus facilitating the observation of the flow pattern. Each

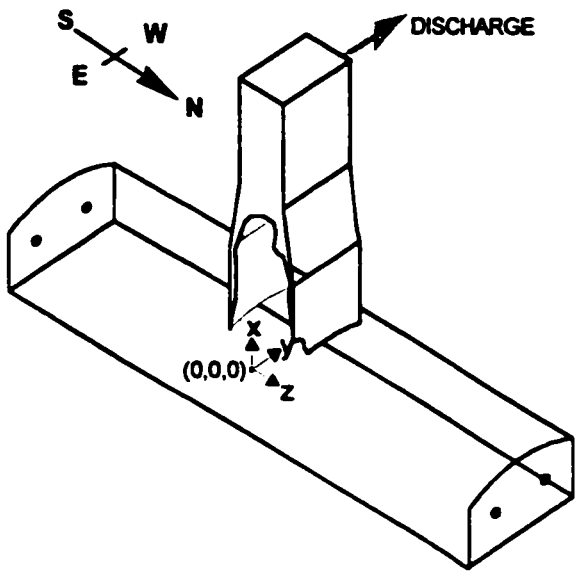

Figure 4.2.4 Particle Tracking Experiments - Coordinate System

4.2.2.3 Salt Tracer Mixing - Uniformity of Mixing in the Uptake

In order to predict the quality of mixing within the uptake downstream of the afterburners jets, it was hypothesized that the mixing of the tracer was controlled by the turbulent characteristics of the jets and the main stream flow. An experiment for measuring the uniformity of mixing within a pipeline tee mixer was proposed by Sroka and Forney (1989). This procedure was adapted for the mixing experiments carried out in the water model to provide a quantitative measure of the mixing in the uptake. In the model, an inert tracer was introduced through the afterburner jets and the steady state tracer concentration was measured at various points both upstream and downstream of the afterburner jets.

The tracer selected for these experiments was potassium chloride, KCl. The refined chemical grade potassium chloride pellets were dissolved in water to a strength of about 5% by weight KCl. Each 20 L batch was analyzed to determine its true concentration by atomic absorption spectroscopy.

The tracer solution was fed continuously to each afterburner jet using a metering pump

(MasterFlex model 7520-10) with four peristaltic heads (MasterFlex model 7016-20). The total flow of tracer solution delivered to the model was 1250 g/min (1214 mL/min) and was distributed equally to each afterburner jet. The pulsating nature of the peristaltic pump heads was not observed to introduce significant fluctuations in the tracer concentrations. At the addition rates of tracer used in these experiments, the rotational speed of the pumps was sufficiently high (maximum pump speed) that the flow was close to continuous. Therefore, feed line mixers were not installed to dampen the fluctuations caused by the pumps.

To measure the mixing from the afterburner jets, samples were extracted at 4 different elevations in the uptake (figure 4.2.5). Each sampling plane was sub-divided into 15 cells (5 x 3) of equal area to form a sampling grid, and samples were extracted from the centre of each cell. With the grid system described, the error in the sampled average uptake concentration, c_{avg}, (equation 4.2.1) was found to be on average within 5% of the well mixed concentration (equation 4.2.2) and had a maximum deviation of 25%. This was an acceptable degree of error given the non-uniform flow distribution across the uptake and the limited number of sampling points.

$$c_{avg} = \frac{1}{A}\sum_{i=1}^{5}\sum_{j=1}^{3} c_{i,j}\,\Delta A \qquad (4.2.1)$$

$$\bar{c} = c_{well\ mixed} = c_o\left(\frac{q_{jets}}{Q_{total}}\right) \qquad (4.2.2)$$

The samples were collected after the model reached steady state conditions; these samples included feed and discharge waters to determine the baseline and well mixed concentrations of tracer respectively. A metering pump with five peristaltic heads was used to draw a separate sample from five probes inserted into the model from the top of the uptake roof. Each head was sized to pump at a rate of 1.0 mL/s. Prior to collecting the sample for analysis, the probes were purged for a period of about one minute. A 60 mL sample was collected for analysis. The one minute sampling time was substantially longer than the residence time in the uptake of between 4 and 11 seconds. The concentration of tracer in the sample was therefore considered to represent the time averaged local concentration, $c_{i,j}$.

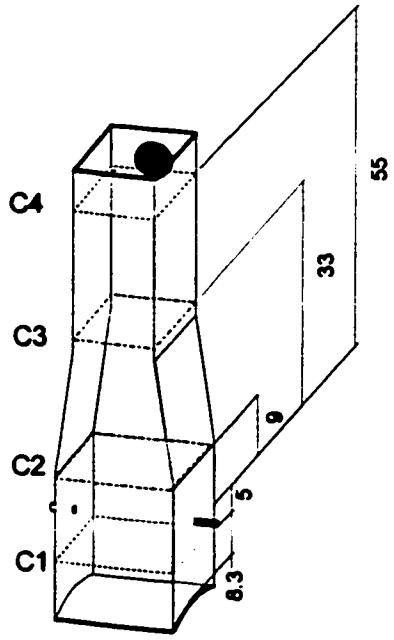

Figure 4.2.5 Uniformity of Mixing Study in Water Model - Location of Sampling Planes

(dimensions in cm, measured relative to afterburner elevation)

The sampling probes were designed so as not to disrupt the flow pattern in the vicinity of the probe tip. To maintain isokinetic sampling rates, the probes were made from 3.175 mm ($^1/_8$ in) diameter stainless steel tubing, and the tip velocity of the fluid flowing through the probe was 12.6 cm/s which was comparable to the superficial entrance velocity of between 6 and 13 cm/s. In addition, the tip of the probe was beveled to minimize the effect on the flow pattern of the passing fluid.

The samples were analyzed for the potassium ion (K^+) concentration by atomic absorption spectroscopy. The local dimensionless concentration, $C_{i,j}$, was corrected for the background level of potassium in the water and then normalized to the well-mixed tracer concentration (equation 4.2.3).

$$DC_{i,j} = C_{i,j} = \frac{c_{i,j}}{\bar{c}} \tag{4.2.3}$$

One useful method of characterizing the uniformity of the mixture within the uptake was to calculate the second moment of the tracer concentration across the uptake (Gray, 1986). Thus

the second moment, M, was defined in the form:

$$M = \frac{1}{A}\sum_{i=1}^{5}\sum_{j=1}^{3}\left(C_{i,j}-1\right)^2 \Delta A \qquad (4.2.4)$$

In an earlier paper by Forney (1985), dimensional analysis of the pipeline tee mixer problem suggested that the mixing conditions were related to the M_r, U_r, Re_j, Re_U, Fr_j and x/D_U. In the present experiments, the jet buoyancy effect was not significant provided that the modified Froude number, Fr_j, was maintained in the range of 10^2 - 10^3. Thus, the second moment of the tracer concentration was written as:

$$M = f\left(M_r, U_r, \mathrm{Re}_j, \mathrm{Re}_U, \frac{x}{D_U}\right) \qquad (4.2.5)$$

The experimental conditions and raw data are found in Appendix A for the afterburner configurations studied. The experiments carried out in the water model investigated the effect of dimensionless parameters, M_r, U_r, Re_j, Re_U, Fr_j and x/D_U. Each parameter, except for Fr_j, was varied within the range applicable to the operation of the plant uptake. In the plant, this range is limited by the chemistry of the furnace off-gas, as it determines the afterburner oxygen requirement for the oxidation of combustible sulfur species and the recycle gas flow for controlling the operating temperature. Therefore, the range over which the parameters were varied in the water model was based on the upper and lower operating flows of afterburner oxygen and SO_2 recycle gas in the plant.

Although an over-simplification of the problem, a simple 1-dimensional transport model in the axial direction was developed to estimate the amount of backmixing in the model. This model provided an estimate of the axial dispersion coefficient, E_c, which is a measure of the amount of backmixing. In this model, the tracer concentration profile was assumed to be laterally uniform upstream and downstream of the afterburner jets, and the velocity at the entrance of the uptake was assumed to be uniform. Upstream of the jets, the net flux of tracer was zero and was given by equation 4.2.6.

$$u\,c - E_c \frac{dc}{dx} = 0; \qquad \text{b.c. } x = 0 \text{ cm}, \; c = \bar{c} \tag{4.2.6}$$

$$\text{Hence: } c = \bar{c} \exp\left(u x / E_c\right) \text{ for } x < 0$$

The value of E_c was obtained by fitting data to equation 4.2.6, and the axial dispersion number was calculated using equation 4.1.3.

4.2.2.4 Salt Tracer Mixing - Residence Time Distribution in the Furnace Model

To investigate the bulk flow patterns in the water model, two exploratory experiments were carried using the residence time distribution technique. The bulk flow patterns in the model were examined without the introduction of flow to the afterburners. In these experiments, a pulse injection of an inert tracer was introduced through a main burner jet in the furnace and the tracer concentration response was measured at the discharge of the uptake. The actual residence time and the dispersion number were determined using the method described in the textbook by Levenspiel (1972). The experimental conditions and raw data are given in Appendix A.

The tracer selected for these experiments was sodium chloride, NaCl. The chemical grade sodium chloride powder were dissolved in water to a strength of about 20% by weight NaCl.. A 1 L batch was analyzed to determine the sodium (Na^+) concentration by atomic absorption spectroscopy.

The tracer solution was introduced into the furnace model with a syringe after the flows to burner jets were set at the desired flow. It is worth noting that there was no flow through the uptake jets. The syringe containing about 100 g (94 mL) of solution was injected through one burner jet in about one second. If uniformly mixed in the model, the tracer concentration would have been approximately 150 ppm NaCl. During injection, the instantaneous burner flow was increased by about 5.5 L/min.

The tracer concentration was indirectly determined by measuring the conductivity of the water. In these studies, a Yokagawa (Model SC82) conductivity meter equipped with a titanium electrode was used to measure the change in the solution conductivity at the discharge of the uptake. The cell constant for the titanium electrode, 4.5 cm^{-1}, was verified in a 0.1 N NaCl solution of known specific conductivity. The net specific conductivity due to the electrolyte was given by:

$$\kappa_t = \kappa_{observed} - \kappa_{background} \quad ; \kappa_{background} = 0.294 \text{ mS cm}^{-1} \tag{4.2.7}$$

It is typical of a strong electrolyte solution that its net specific conductivity is proportional to its concentration, to a first approximation, up to about 0.1 M. The specific conductivity is also proportional to the cell temperature. The temperature corrected specific conductivity was calculated using the following equations, as described in the Yokagawa manual:

$$\kappa_{15^\circ C} = \frac{\kappa_T}{1 + \alpha(T - 15)} \tag{4.2.8}$$

$$\alpha = \frac{\kappa_{T_2} - \kappa_{T_1}}{\kappa_{T_1}(T_2 - 15) - \kappa_{T_2}(T_1 - 15)} = 0.0251 \pm 0.0013 \tag{4.2.9}$$

Figure 4.2.6 illustrates the relationship between the temperature corrected specific conductivity and concentration of dilute NaCl solutions. During the residence time distribution experiments, the readings on the display screen of the Yogagawa conductivity meter were recorded with a video camera. The method of data acquisition, unfortunately, limited the precision with which data could be recorded, especially when recording the concentration decay. The conductivity was displayed with a $\pm$ 0.001 mS cm^{-1} accuracy, which was equivalent to $\pm$ 0.7 ppm NaCl.

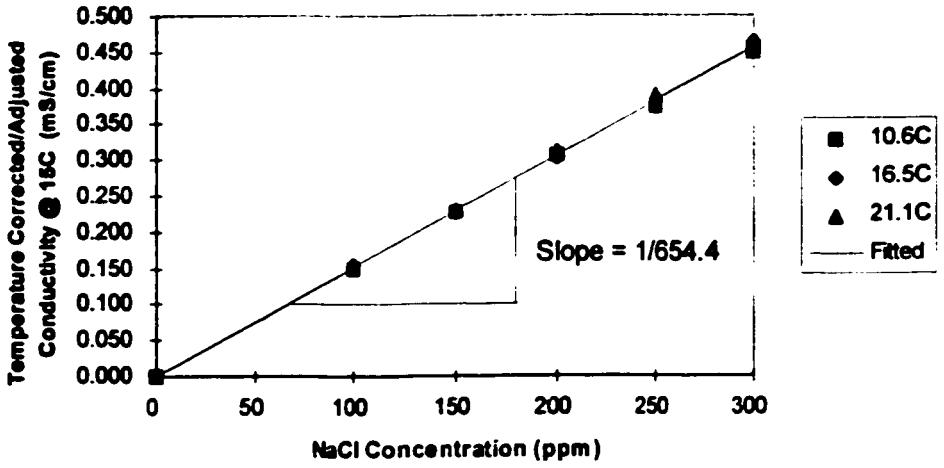

Figure 4.2.6 NaCl Concentration - Temperature Corrected Specific Conductivity Relationship

The nominal residence time or space time was equivalent to the plug flow residence time as defined by $\tau = V/Q$. The actual mean residence time was calculated from the first moment of the tracer concentration curve measured at the discharge of the model (equation 4.2.10). The statistical variance of the concentration curve, taken about the actual mean residence time, is an indication of the spread of the distribution of concentration with time (equation 4.2.11). The degree of back mixing is quantified in terms of the dispersion number (equation 4.1.3) which measures the relative importance of back mixing to bulk convection. Levenspiel showed that the dispersion number for a closed vessel can be calculated from an analytical expression for the variance of the concentration curve (equation 4.2.12).

$$\bar{\tau} = \frac{\sum t_i c_i \Delta t_i}{\sum c_i \Delta t_i} \qquad (4.2.10)$$

$$\sigma^2 = \frac{\sum t_i^2 c_i \Delta t_i}{\sum c_i \Delta t_i} - \bar{\tau}^2 \qquad (4.2.11)$$

$$\sigma_\theta^2 = \frac{\sigma^2}{\bar{\tau}^2} = 2\frac{E}{u\ell} - 2\left(\frac{E}{u\ell}\right)\left(1 - e^{-\frac{E}{u\ell}}\right) \qquad (4.2.12)$$

where u = superficial velocity

ℓ = distance travelled by tracer

In analyzing the concentration response curve, it was advantageous to express the tracer concentration and time in dimensionless units, thus allowing the direct comparison of the tracer response curves. The dimensionless concentration is defined as the measured tracer concentration divided by the calculated well mixed tracer concentration (equation 4.2.13). The dimensionless time was interpreted as the fraction of the time required for one complete volume change of the water content of the model (equation 4.2.14).

$$c_\theta = \frac{\bar{\tau}}{\sum c_i \Delta t_i} c_i \qquad (4.2.13)$$

$$\theta = \frac{t_i}{\bar{\tau}} \qquad (4.2.14)$$

4.3 Linear Scale Air Model (1/5)

The isothermal air model was fabricated of 1.27 cm (½ in.) plywood and 0.635 (¼ in.) perspex to $^1/_5{}^{th}$ linear scale of the plant (figure 4.3.1); plywood was used to construct the furnace floor and sidewalls, and perspex formed the furnace roof and uptake. The flows of air to the model were set to maintain dynamic similarity (table 4.3.1).

Figure 4.3.1 General Arrangement View of the Air Model

Table 4.3.1 Air Model Flows, L/min, Used in the Scaling Calculations

	Per Burner	Total
Main Burner Jet	8750	35000
Uptake Afterburner Jet	265	1060
Uptake Recycle Jet	1665	3330

4.3.1 Air Model - General Arrangement

The initial set-up of the model incorporated four main burner jets, four afterburner jets and two SO_2 recycle jets. The model was designed to allow the testing of alternative jet configurations in the uptake. The model was designed as a continuous flow, open circuit, push-pull system. A schematic of the model air distribution is found in figure 4.3.2.

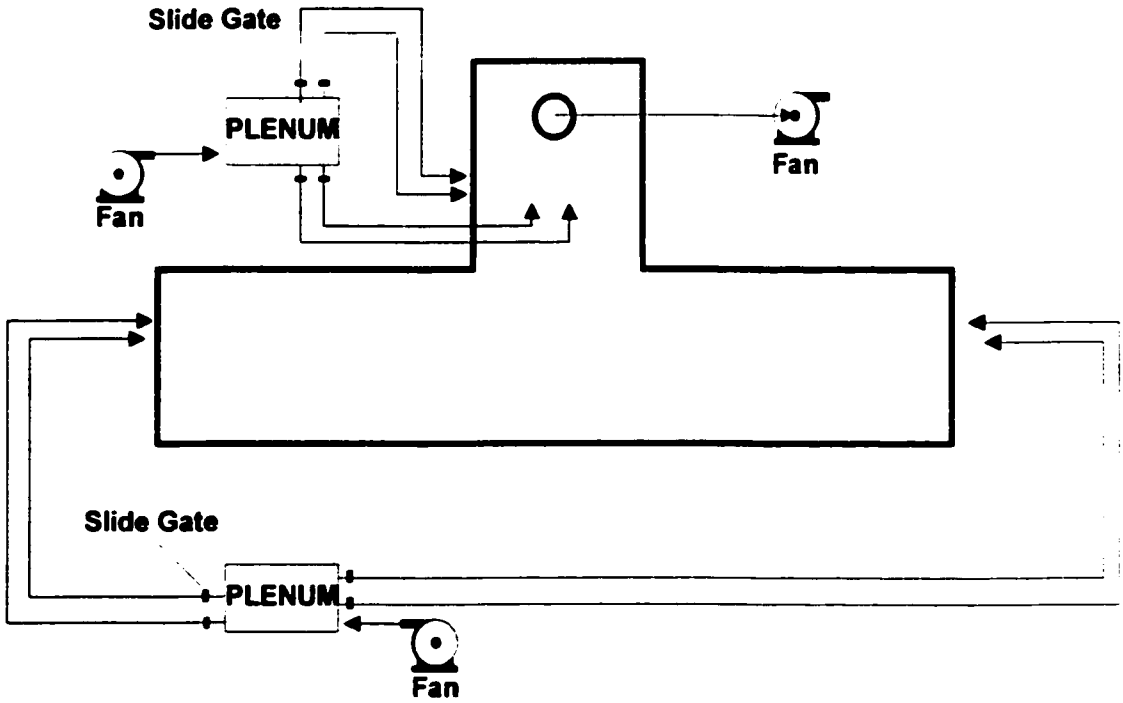

Figure 4.3.2 Schematic of Model Air Distribution

The air flows to the main burner and SO_2 recycle jets were supplied with centrifugal fan (Buffalo Forge Blower) capable of delivering upto 83450 L/min (3000 cfm). The fan delivered air at about 5 kPa (20"wc) to a plywood distribution plenum equipped with six outlets. Slide gates on each outlet were used to adjust the flow of air to the jets in the model. The air flow to the main burner jets was ducted with 10.2 cm (4 in.) nominal diameter ABS pipe, whereas the SO_2 recycle jets were supplied through 5.1 cm (2 in.) diameter corrugated flexible vinyl reinforced hose.

A second centrifugal fan supplied upto 8345 L/min (300 cfm) of air to the afterburner jets. The fan outlet was ducted to a plywood plenum equipped with four off-takes to distribute the air flow to each jet, and guillotine dampers on each off-take controlled the air flow to the jets. A 5.1 cm (2 in.) diameter corrugated reinforced vinyl hose was used to duct the flow from the plenum. The flexible hose permitted the evaluation of alternative afterburner configurations. The jet nozzle size was adjusted to the desired size with ABS inserts.

The flow rate of air to each main burner jet was determined indirectly from a flow-pressure calibration curve. The calibration curve was developed by measuring the flow in the duct supplying the main burners with a standard pitot tube. A 24-point traverse was performed on each duct, 21 diameters downstream of the distribution box and about 8 diameters upstream of the first elbow. Three flow settings were used to develop the calibration curve. Pressure taps were installed on the duct to measure the pressure drop across the elbow.

The flow to the uptake jets was measured with a standard pitot tube at a single point. The duct size was sufficiently small that detailed traversing was not warranted. The accuracy of this method was within 10% of an 8-point traverse measurement. A flow-pressure calibration curve was developed for the after burner jets.

The pressure inside the furnace section of model was maintained close to neutral with a third fan located on the discharge. It was necessary to operate the model in this manner to avoid undesirable leaks into the laboratory when conducting flow visualization tests with smoke or SO_2-NH_3. The discharge air flow from the top of the uptake was ducted with 50.8 cm (20 in.) diameter cardboard tubing to the centrifugal exhaust fan.

4.3.2 Experimental Methodology

The primary objectives of the air modeling work were to define the flow fields and mixing characteristics in the furnace and uptake and to relate the findings to the operation of the plant and the water model. The flow patterns of the air model are expected to closely approximate those of the plant, given the agreement of the similarity criterion. The experiments carried out in the air model focused primarily on obtaining quantitative data about the flow and mixing behaviour. The experimental techniques involved flow visualization using smoke tests, velocity distributions and thermal mixing.

4.3.2.1 Velocity Distribution in Air Model

The air model provided a direct means of obtaining the distribution, magnitude and direction of the flow at any cross-sectional plane. At each sampling point, a hot wire anemometer measured the magnitude of the velocity, and a yarn streamer, attached to the tip of anemometer shield, indicated the predominant direction of the flow. The hot wire anemometer was selected over the pitot tube because the hot wire is sensitive to low velocities and possesses a fast response time to allow the measurement of fluctuations of the turbulence at a given point.

The magnitude of the velocities was measured with a Thermo-System Incorporated (TSI) anemometer, model 1051, with a platinum fine wire sensor mounted on the tip of the probe. The basic variable measured by the hot wire is the rate of heat transfer from the wire. Since this is not the variable of interest in these experiments, a calibration was made between the bridge voltage and the velocity. The calibration was performed by measuring the velocity of air in a duct (30.5 cm ϕ x 10 m L). The flow through the duct was adjusted to the desire flow setting by adjusting the dampers on the outlet of a centrifugal fan, connected to one end of the pipe. The velocities were measured a distance of 26 diameters downstream of the fan. A 48-point pitot traverse showed that the flow in the pipe had a uniform (plug flow) velocity profile over $\pm$ 0.95 R, with a measured root mean square (rms) turbulence intensity of about 1-2%. To facilitate the interpretation of the bridge voltage signal, the 0-30 V bridge voltage signal was linearized to a 0-5 V analog signal, and a relationship with velocity was developed (figure 4.3.3).

The axial component of the mean velocity and the rms turbulence intensity were measured on a grid of points lying in three vertical planes through the furnace and three horizontal planes in the uptake (figure 4.3.4). The grid density of the planes (P1, P2, P3) in the furnace was 9x5 while the densities in the lower and upper planes in the uptake were 6x6 (P4, P5) and 6x5 (P6), respectively. With the grid system selected, the furnace cross-section was sub-divided into 43 cells (figure 4.3.5). In the uptake, the cross-sectional area of the sampling planes was sub-divided in cells of equal area. To explore the sensitivity to grid density, a set of measurements was made on a 9x9 grid in planes P2 and P3 and on a 6x10 grid in plane P5.

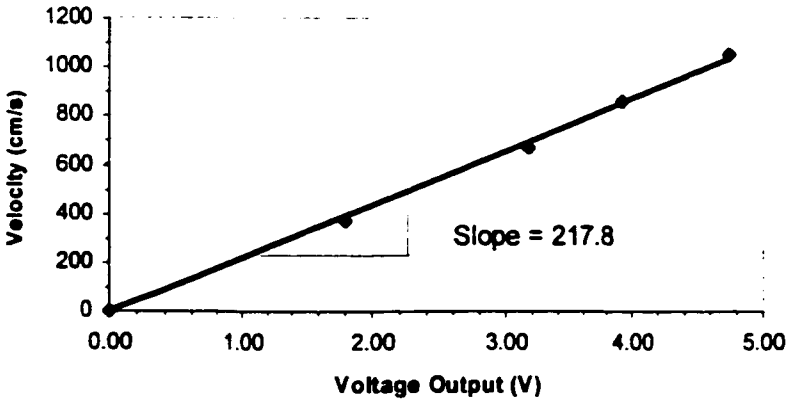

Figure 4.3.3 TSI 1051 Anemometer- Linearized Bridge Voltage vs. Velocity

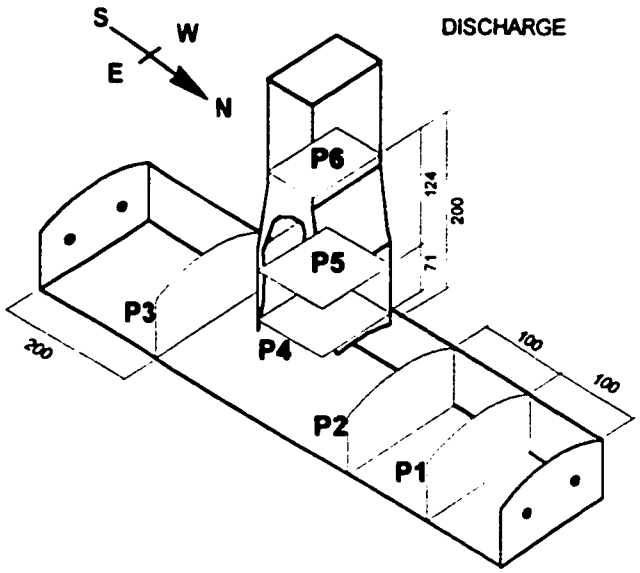

Figure 4.3.4 Velocity Distribution in Air Model - Grid Sampling Plane Location

(dimensions in cm)

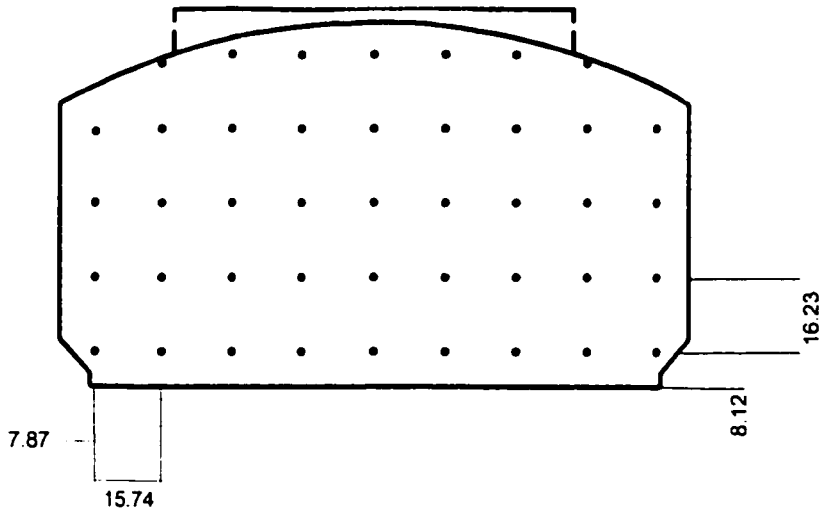

Figure 4.3.5 Velocity Distribution in Air Model - Grid Spacing in Planes P1, P2, P3

(dimensions in cm)

In these experiments, only the axial component of the velocity was measured. To achieve this, the hot wire was shielded on two sides (figure 4.3.6). When compared with the lateral velocity component, the axial velocity was more than an order of magnitude greater. A support structure was fabricated to guide the anemometer probe to the desired position in the model (figure 4.3.7).

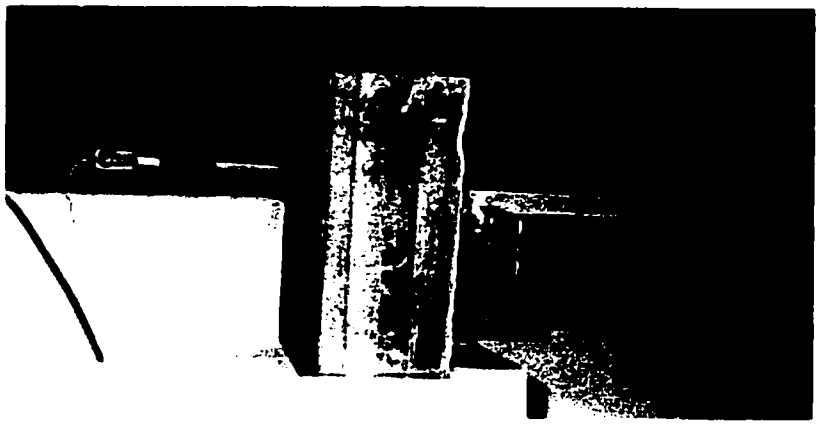

Figure 4.3.6 Anemometer Probe with Shielded Hot Wire Sensor

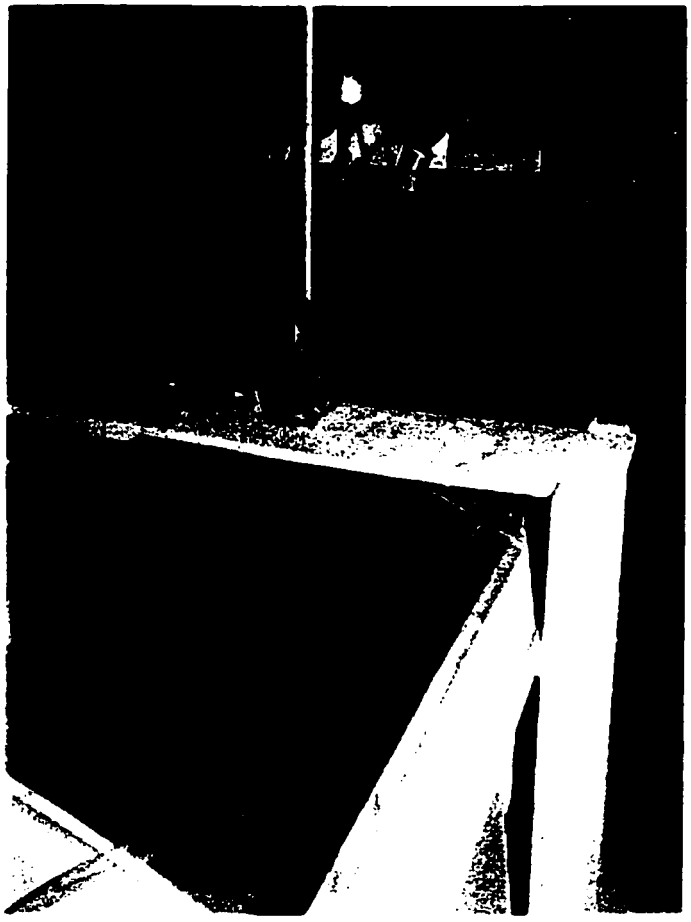

Figure 4.3.7 Velocity Distribution in Air Model - Typical Experimental Set-Up

The axial component of the velocity was sampled at each grid node for about 1 minute once steady state was reached at the desired flow conditions. The average local axial velocities and the root mean square (rms) turbulence intensities were determined from sample sizes of approximately 180 data points. The average local axial velocity was calculated using equation 4.3.1 and made dimensionless (equation 4.3.2) with respect to the superficial velocity, $\bar{v}_{\text{measured flows to jets}}$, based on the measured flows to the jets (equation 4.3.3). The superficial velocity, $\bar{v}_{\text{velocity profile}}$, based on the average local axial velocities (equation 4.3.4), was found to be on average within 10% of the superficial velocity calculated from the measured flows to the jets.

$$\bar{v}_{i,j} = \frac{1}{n}\sum_{n=1}^{n} v_{i,j} \quad ; \text{where n = number of measurements} \tag{4.3.1}$$

$$DV_{i,j} = \bar{V}_{i,j} = \frac{\bar{v}_{i,j}}{\bar{v}} \tag{4.3.2}$$

$$\bar{v}_{\text{measured flows to jets}} = \frac{\sum_{m=1}^{m} q_m}{A} \quad ; \text{ where m = number of jets} \tag{4.3.3}$$

$$\bar{v}_{\text{velocity profile}} = \frac{1}{A}\sum_{i=1}^{I}\sum_{j=1}^{J} \bar{v}_{i,j}\,\Delta A_{i,j} \tag{4.3.4}$$

The local rms turbulence intensity in the axial direction was computed from the variance of the data points (equation 4.3.5). For this work, the data acquisition system (DAS) recorded data from the anemometer module at a conversion rate of about 3 Hz. It is worth noting that the conversion rate was significantly slower than the turbulent time scale, which was on the order of 10^{-3} seconds. Therefore, the local rms turbulence intensity computed from this data was only approximate.

$$TI_{rms} = \frac{\sqrt{\dfrac{\sum_{n=1}^{n}\left(v_{i,j} - \bar{v}_{i,j}\right)^2}{n}}}{\bar{v}_{i,j}} \tag{4.3.5}$$

The experimental conditions and the velocity distributions measured are summarized in Appendix B. These experiments primarily focused on examining the nature of the bulk flow patterns in the furnace and uptake without the introduction of flow through the afterburner jets. Additional testing was performed to evaluate the impact of the direction of the exhaust on the bulk flow patterns by rotating the uptake 180^0 and to investigate the effect of the afterburners on the bulk flow patterns.

4.3.2.2 Thermal Mixing - Uniformity of Mixing in the Uptake

The experimental methodology of the thermal mixing experiments simulated the uniformity of mixing studies carried out in the water model using potassium chloride. The method of measuring the mixing uniformity, proposed by Sroka and Forney (1989), was used. In the air model, heated air was introduced through the afterburner jets as a step change, and the steady state temperature rise was measured at horizontal planes downstream of the jets.

For these experiments, the air supplied to the afterburners was continuously heated with a propane torch 36.6 kW (125,000 Btu/hr) firing into the suction side of the fan. Limited by the vinyl hoses connecting the plenum to the jets, the temperature in the plenum was controlled to about 105°C (220°F) by manually regulating the flow of propane. The temperature of the air flowing to each jet was measured with T-type thermocouples.

The temperature distribution on a given plane was measured with an array of T-type thermocouples. A typical experimental set-up is given in figure 4.3.8. The thermocouple wires were supported on a 0.32 cm ($^1/_8$ in.) diameter rod which spanned the width of the uptake (7 thermocouples per rod). The temperature distribution was measured at 3 different elevations in the uptake (figure 4.3.9). Sampling planes T1 and T2 were sub-divided into 42 cells (7 x 6) of equal area to form a sampling grid, whereas plane T3 was sub-divided into 35 cells (7 x 5) of equal area. The temperatures were sampled at the centre of each cell.

In these experiments, two sets of temperature distributions were collected per sampling plane for each set of flow conditions. The initial temperature profile was obtained after the air flows to the main burner were stabilized. The final temperature profile was taken after introducing the hot afterburner jets. At steady state, the root mean square, rms, of the temperature fluctuations was 0.5-1.0%. Steady state temperature measurements were based on 2 minutes of data collection, giving about 60 temperatures per sampling node. The average local background and steady state temperatures were given by equation 4.3.6. and the average local temperature rise was defined as the difference between the local final and initial temperatures (equation 4.3.7).

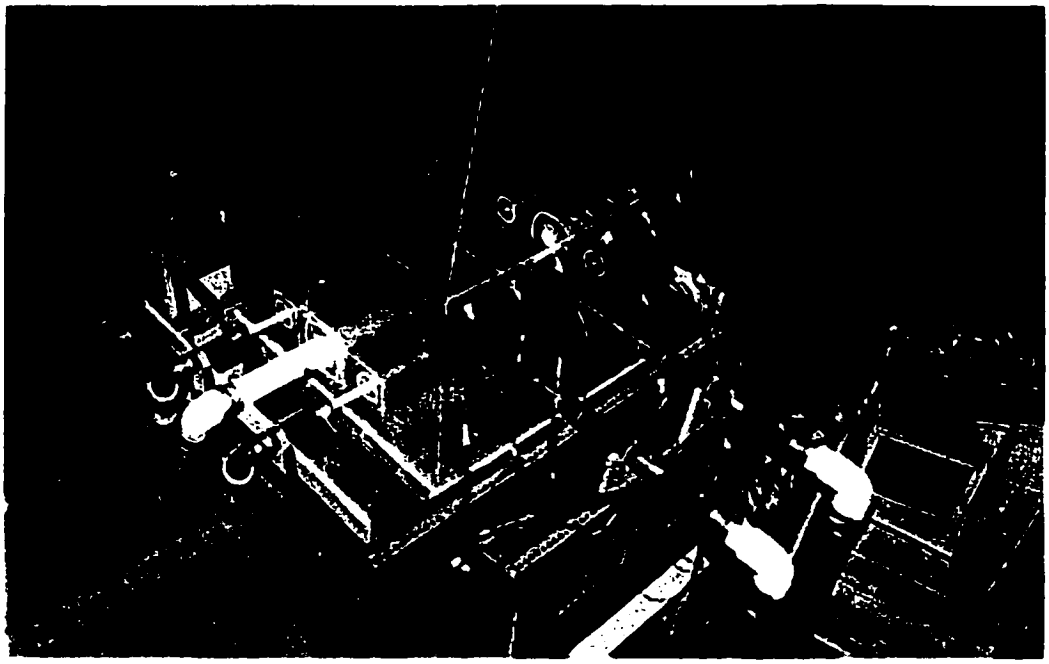

Figure 4.3.8 Thermal Mixing in Air Model - Experimental Set-up

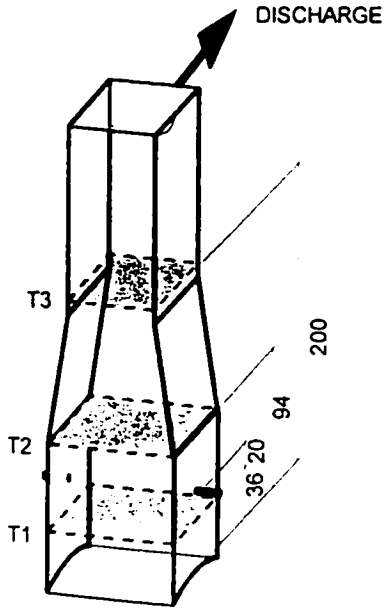

Figure 4.3.9 Thermal Mixing in Air Model - Location of Sampling Planes

(dimensions in cm, measured relative to top of roof arch)

$$\overline{T}_{i,j} = \frac{1}{n}\sum_{n=1}^{n} T_{i,j} \quad ; \text{ where n = number of measurements} \tag{4.3.6}$$

$$\Delta\overline{T}_{i,j} = \overline{T}_{final_{i,j}} - \overline{T}_{initial_{i,j}} \tag{4.3.7}$$

The temperature rise data, $\Delta\overline{T}_{i,j}$, was made dimensionless with respect to the adiabatic temperature rise, as calculated from the heat balance (equation 4.3.8). In this way, the results obtained for each set of experimental conditions could be compared directly. It was worth noting that the average temperature rise on sampling planes T2 and T3 (equation 4.3.9) was in good agreement with the adiabatic temperature rise, differing by no more than 0.2°C. Equation 4.3.10 describes the dimensionless temperature rise for a given sampling point.

$$\Delta T_{ad} = \left(\frac{\Delta H_{jets_{fce}} + \Delta H_{jets_{uptake}}}{\rho\left(Q_{jets_{fce}} + Q_{jets_{uptake}}\right) c_p} \right) ; \text{ where } \Delta H_{jet} = \rho Q_{jet} c_p \Delta T_{jet} \tag{4.3.8}$$

$$\Delta T_{jet} = (T_{final} - T_{initial})_{jet}$$

$$\Delta\overline{T} = \frac{1}{A}\sum_{i=1}^{7}\sum_{j=1}^{5or6}\Delta\overline{T}_{i,j}\,\Delta A \tag{4.3.9}$$

$$DT_{i,j} = \Delta\overline{T}^{d}_{i,j} = \frac{\Delta\overline{T}_{i,j}}{\Delta T_{ad}} \tag{4.3.10}$$

In characterizing the lateral uniformity of the mixture within the uptake, the second moment of the dimensionless temperature rise across the uptake was used. Thus the second moment, M, was defined in a form analogous to the equation used to evaluate the uniformity of mixing in the water model:

$$M=\frac{1}{A}\sum_{i=1}^{7}\sum_{j=1}^{5or6}\left(\Delta\overline{T}^{d}_{i,j}-1\right)^2\Delta A \tag{4.3.12}$$

As previously discussed in section 4.1.3, the experiments carried out in the air model investigated the effect of the dimensionless parameters, M_r, U_r, Re_j, Re_U, Fr_j and x/D_U. In these experiments, the jet buoyancy effects was deemed insignificant as the modified Froude number, Fr_j, was maintained on the order of 10^4. Each parameter, except for Fr_j, was varied within the range applicable to the operation of the plant uptake. In the plant, this range is limited by the chemistry of the furnace off-gas, as it determines the afterburner oxygen requirement for the oxidation of combustible sulfur species and the recycle gas flow for controlling the operating temperature. Therefore, the range in which the parameters were varied in the model were based on the upper and lower operating flows of afterburner oxygen and recycle gas in the plant. The experimental conditions and raw data are given in Appendix B for afterburner configurations studied.

A 1-dimensional transport model, similar to the one used for the water model experiments, was developed to estimate the amount of backmixing in the model. This model provided an estimate of the axial dispersion coefficient, E_t, which is a measure of the amount of backmixing. In this model, the lateral temperature rise profile was assumed to be uniform upstream and downstream of the afterburner jets, and the velocity profile at the entrance of the uptake was also assumed to be uniform. Upstream of the jets, the net flux of heat was zero and was given by equation 4.3.13.

$$u(T-T_o) - E_t \frac{d(T-T_o)}{dx} = 0; \quad \text{b.c. } x=0 \text{ cm}, \quad T-T_o = \Delta T_{ad}$$

$$\text{Hence: } (T-T_o) = \Delta T_{ad} \exp\left(\frac{u\,x}{E_t}\right) \text{ for } x < 0 \tag{4.3.13}$$

The value of E_t was calculated using equation 4.3.13 and hence the dispersion number was obtained using equation 4.1.3.

4.3.2.3 Data Acquisition System (DAS)

Virtually all data acquisition in the air model was carried out automatically by a data acquisition

system (DAS). The data collected during the air model experiments was the linearized bridge voltage, temperature and pressure data. The linearized bridge voltage, a measure of velocity, was measured with a TSI hot wire anemometer (Model 1051). The temperature data was collected using OMEGA T-type thermocouples, and the pressure data, an indirect measure of air flows to the jets, was converted to a 0-5 V analog signal with low pressure transducers (OMEGA PX164-010D5V). The pressure transducer converted the pressure signal (0-2.5 kPa) to a voltage signal (0-5 V).

The analog signals from each input were routed through 4 x 16-channel multiplexer board (OMEGA EXP-16). All inputs to the multiplexer board were converted to 0-5 V signal. The multiplexer board had provisions for 48 thermocouple inputs, 1 velocity input and 15 pressure inputs. The analog output from the multiplexer board was wired to an 8-channel 12 bit high speed successive approximation analog-to-digital (A/D) converter (OMEGA DAS-8). The A/D converter had a maximum conversion rate of 40 kHz. The full-scale input of each A/D channel is 5 volts with a resolution of 2.44 millivolts.

The digital output from the converter was interpreted with a BASIC program operating in a 286 SX IBM compatible personal computer. Two BASIC programs were written, one for temperature and pressure data acquisition and the other for velocity data acquisition. The temperature and pressure voltage reading were converted by the program to degrees Fahrenheit using a series third order curve-fit equation and to kilo Pascal using a linear curve fit. The program downloaded directly the linearized bridge voltage data with no curve fit. The program stored the data in text files.

Although the A/D conversion time was 40 kHz, the actual conversion rate was limited by the settling time of the board, the channel select multiplexer and the BASIC program (table 4.3.2). The low frequency data collection of temperatures and pressures was sufficient for the thermal mixing studies that were carried out at steady state. However, the conversion rate of the velocity data, although sufficient for determining the average local velocity, was slow compared with the turbulent time scale, which was on the order of 1000 Hz. Therefore, in defining the turbulence

intensity, the data was only approximate.

Table 4.3.2 Analog-to-Digital Signal Conversion Rates

	Conversion Rates (Hz)
Temperature	0.5
Pressure	0.5
Velocity	3

The accuracy and integrity of the data acquired by the data acquisition system were verified either by comparison with data collected by other means (e.g. inclined manometers to check the pressure data) or by comparison with direct voltage measurements taken by a hand-held multimeter (e.g. velocities). After the end of an experimental trial, a second computer was used to convert the raw data text files into a format which was usable by the MS-Office Excel package. The program also converted all the linearized bridge voltage readings to velocities.

Chapter 5

EXPERIMENTAL RESULTS

In Chapter 4, the experimental techniques used in physical modeling were discussed in detail. The physical modeling study provided a simple means of obtaining data about the flow conditions in the furnace and uptake of the commercial operation. The modeling was carried out in two scaled models of the flash furnace and uptake, a 1:20 linear scale water model and a 1:5 linear scale air model. Similarity of the flow patterns was expected between the model and the prototype given the close agreement of the scaling criteria. The experimental techniques involved flow visualization, velocity distributions and mixing studies.

The modeling effort was focused on defining two aspects of the flow conditions:

1. the bulk flow patterns in the furnace gas space.

2. the factors which affect the mixing of afterburner and furnace gases in the uptake.

5.1 Bulk Flow Patterns in the Furnace Gas Space

The bulk flow patterns in the furnace gas space were investigated in, first, the water model and, then, the air model using three different experimental techniques. In the water model, the techniques involved residence time distribution studies and flow visualization with neutrally buoyant particles, while in the air model velocity profiles were measured. In these experiments,

the bulk flow patterns in the models were examined mainly without the introduction of flow to the afterburners.

5.1.1 Residence Time Distribution

Two exploratory experiments were carried in the water model using the residence time distribution technique. In these experiments, a pulse injection of an inert tracer was introduced through a main burner jet in the furnace and the tracer concentration was measured at the discharge of the uptake. The actual residence time and the dispersion number were determined using the method described by Levenspiel (1972). The experimental conditions are summarized in table 5.1.1.

Table 5.1.1 Residence Time Distribution - Experimental Conditions in Water Model

	Total Flow, Q (L/min)	Reynolds Number		Nominal Residence Time, V/Q (sec)
		Furnace	Uptake	
RTD-1	124	3900	9900	64.0
RTD-2	348	10900	27400	23.2

The experimental tracer response curves are plotted in figure 5.1.1 in terms of dimensionless concentration and time. The residence time distribution plots were quite similar, suggesting that the flow pattern was independent of the retention time. The response curves exhibited a short induction time, a rapid rise in tracer concentration followed by an exponential decay. Several important features of the dimensionless plots were noted:

- the dimensionless induction time, θ_{PF}, was 0.13-0.14, indicative of plug flow.
- the peak dimensionless concentration, C_{θ}, occurred between the dimensionless times of 0.20 and 0.25.

- the peak dimensionless concentration, C_θ, was 1.2-1.3 which suggested that the system comprised a plug flow and a well mixed region..
- after the peak, the dimensionless tracer concentration, C_θ, decayed exponentially with time, as would be expected for ideal backmix flow.
- the very long tail was indicative of a well mixed region.

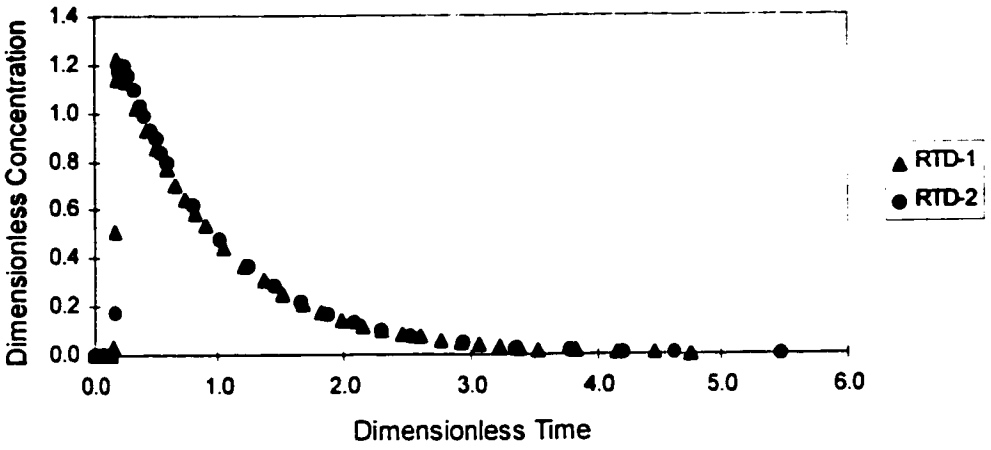

Figure 5.1.1 Tracer Response Curves in Water Model

The mixing parameters derived from the response curve are summarized in table 5.1.2. The actual and nominal residence times were in good agreement, suggesting that no dead volumes existed in the furnace gas space.

Table 5.1.2 Comparison of Mixing Parameters in Water Model RTD Experiments

	Residence Time (sec)		Dimensionless	Dispersion	Tracer
	Apparent	Actual	Variance	Number	Recovery (%)
RTD-1	64.0	64.7	0.59	0.55	87.5
RTD-2	23.2	23.6	0.60	0.56	92.4

In comparing the two experiments, it was apparent that the dimensionless variance and dispersion numbers were comparable, suggesting that the flow patterns were independent of residence time. The calculated dispersion number was low due, principally, to the long induction time. The induction time suggested that a section of the model exhibited plug flow behaviour, which has little or no dispersion. The initial flow region of the jet and the upper section of the uptake could represent the plug flow regime in the model. The volume of the plug flow regime was estimated with equation 5.1.1 to be about 13.5% of the total volume of the model. By comparison the volume of the uptake was 20.9% of the total volume. The initial flow region of the jet was calculated to occupy a very small volume of the model, less than 0.2% of the total volume of the model.

$$\frac{V_{PF}}{V_{TOT}} = \theta_{PF} = 0.135 \qquad (5.1.1)$$

Figure 5.1.2 plots the tracer response curve excluding the induction time as well as the response curve for an ideal mixer. The first order decay suggested that the mixing was approaching ideal conditions. Although "perfect" mixing would yield a dispersion number of infinity, the calculated values for the well-mixed space implied "good mixing"; the calculated dispersion numbers, excluding the induction time, were 1.40 and 1.31 for RTD-1 and RTD-2, respectively. The well-mixed behaviour was indicative of a flow regime with a large amount of recirculation. It was the turbulent mixing action of the main burner jets that produced the large recirculating flow in the furnace and lower uptake regions of the model. The volume of the model exhibiting well-mixed conditions was calculated using equation 5.1.2 to be about 86.5% of the total volume.

$$\frac{V_{WM}}{V_{TOT}} = 1 - \theta_{PF} = 0.865 \qquad (5.1.2)$$

From the experimental data, the percent recovery of the tracer was estimated by calculating the area under the response curve and the volumetric flow of water through the model. In all tests,

the tracer recovery was less than 100%. Full measured recovery was not anticipated considering the long tail of the tracer response curve and the accuracy of the conductivity measurements.

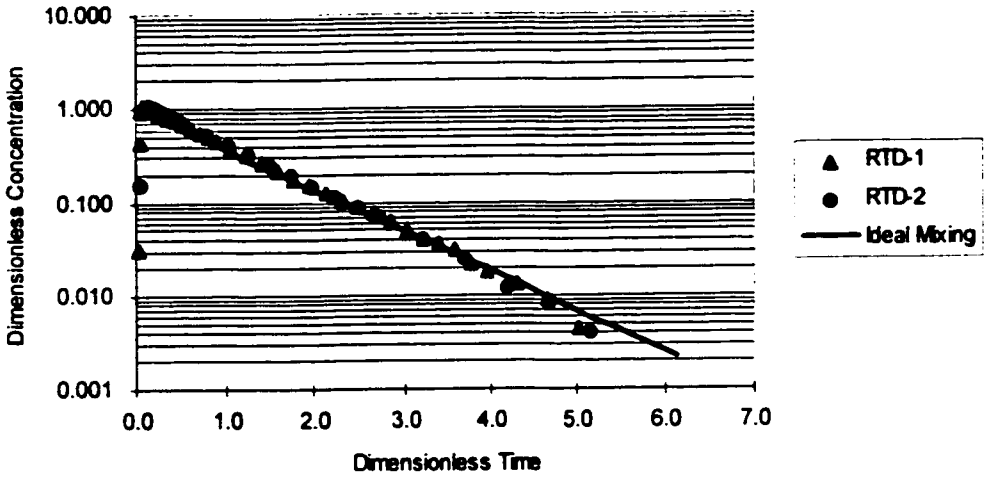

Figure 5.1.2 Tracer Response Curve in Water Model (Induction Time Excluded)

5.1.2 Flow Visualization with Neutrally Buoyant Particles

These experiments were effective in demonstrating qualitatively the significant features of the flow patterns in the water model. Although it was difficult to obtain precise velocity measurements, estimates of the particle velocity were made by streak photography. No effort was made to obtain more accurate data by using elaborate lighting arrangements or laser techniques to illuminate the model.

The experimental conditions for which the particle tracking experiments were conducted are tabulated in table 5.1.3. The tracer particles were injected through one of the main burner jets. The tracer particles issuing from the jet were seen to flow directly towards the floor of the model with a dilation of about $26^{\circ} \pm 2^{\circ}$, determined visually from still photographs (figure 5.1.3). The angle of the jet was larger than classical case of a confined jet which has diverging angle of about

18-20^0 (Thring, 1962). The jet impingement on the model floor created a small separation zone adjacent to the end wall of the furnace.

Table 5.1.3 Particle Tracking Experiment - Test Conditions in Water Model

Burner:	Flow	87 L/min
	Tip Velocity	467 cm/s
Furnace:	Total Flow, Q	348 L/min
	superficial velocity	4.0 cm/s
Uptake:	superficial entrance velocity	12.9 cm/s
	discharge velocity	183 cm/s

At the point of jet impingement, adjacent jets merged forming a single stream flowing toward the uptake. The converged stream did not conform to the profile of the furnace roof but flowed at high velocity over the bottom of the model. Particle velocities measured in this main stream by streak photography ranged between 9 and 32 cm/s. The high velocity jet produced an extensive zone of separation that enveloped the main stream. In the separated zone, a large volume of water flowed back toward the end wall of the model, which was referred to as recirculation.

In the furnace, the flow was highly turbulent and three-dimensional thus it was not possible to observe at any one instant a flow pattern, which represented the time-averaged flow. The time-averaged flow pattern was developed from video observations of the particle flow patterns over extended periods. Figure 5.1.4 illustrates schematically the furnace flow patterns.

Little expansion of the main stream could be observed as it moved toward the uptake. The velocity remained high to the point where the stream turned vertically to the uptake. At this junction, opposing main streams impinged prior to the flow turning sharply 90° into the uptake. The collision produced a stagnation plane and a zone of separation under the uptake. The stagnation plane was not stationary, and its location was observed to fluctuate in a quasi-random fashion which was indicative of temporal instabilities in the jets.

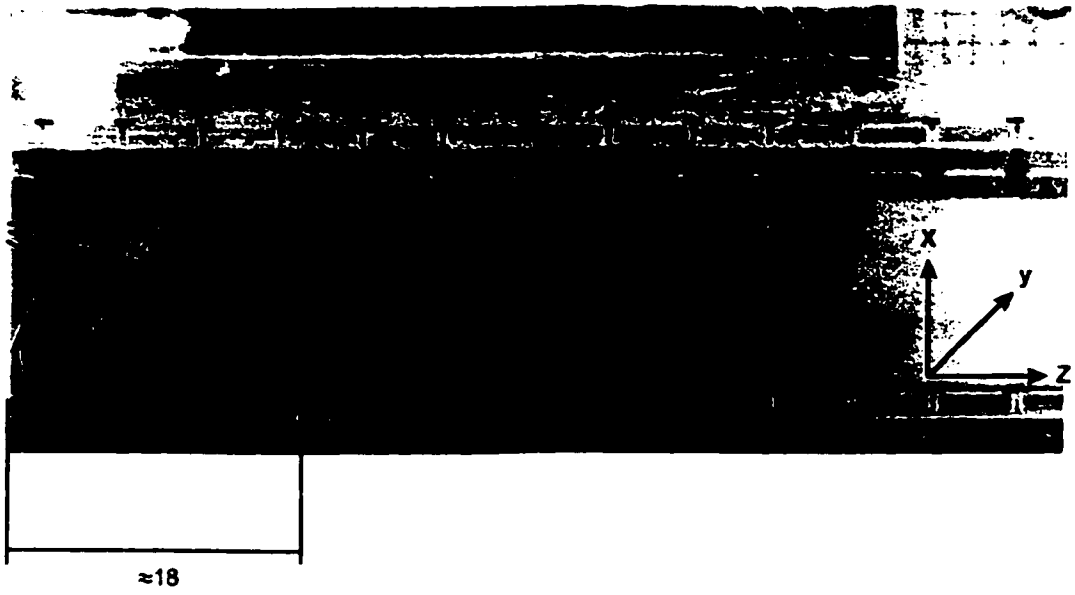

Figure 5.1.3 Particle Tracking Experiment - Furnace Flow

(dimension in cm)

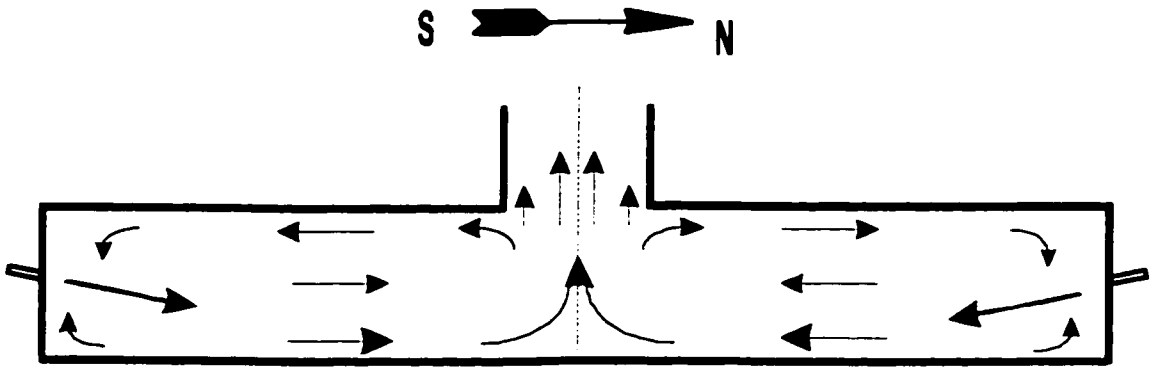

Figure 5.1.4 Schematic Illustration of Flow Pattern through the Furnace

Although difficult to quantify, the particles in the main stream entering the uptake were observed to flow with a higher velocity in the centre. A zone of separation was produced along the uptake walls, perpendicular to the longitudinal axis of the furnace and especially in the west corner. Particles in this zone were seen to flow back into the furnace. The flow at the furnace-uptake transition was very unstable and appeared to be related to the instability of the impinging streams in the furnace.

In the uptake, the particle flow was predominantly uni-directional in the axial direction but the particles did not travel with uniform velocity. The non-uniformity was especially pronounced along the lateral (E-W) axis, perpendicular to the longitudinal (N-S) axis of the furnace. Particle velocities, measured in the upper section of the uptake, illustrated this trend (table 5.1.4.) The difference in velocity was influenced by the discharge, which was located on the west side of the uptake. Figure 5.1.5 illustrates schematically the flow patterns in the upper section of the uptake.

Table 5.1.4 Particle Velocities in the Uptake of the Water Model, cm/s

East	West	Distance from Uptake Entry, cm
9-18	19-26	46 ± 2
9-17	19-24	56 ± 2

Note: The superficial velocity in the upper section of the uptake was 18.7 cm/s.

Small zones of separation were noted in the bottom corners of the tapered section and in the corners at the top of the uptake. Tracer particles remained entrained in these low flow pockets for extended periods.

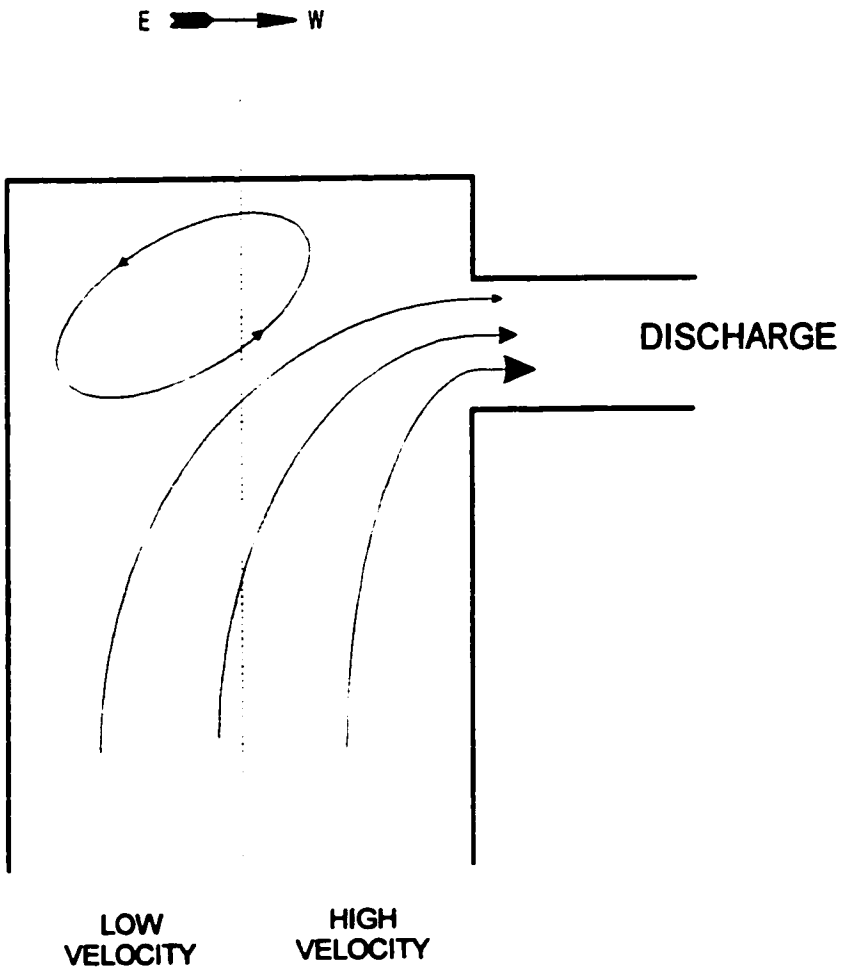

Figure 5.1.5 Schematic Illustration of Flow Pattern in the Uptake of the Water Model

5.1.3 Velocity Profiles Measured in the Air Model

The air model provided a direct means of obtaining the distribution, magnitude and direction of the flow at a cross-sectional plane. A hot wire anemometer was used to measure the magnitude of the velocity, and a yarn streamer, attached to the tip of anemometer shield, indicated the predominant direction of the flow. A total of nine (9) experiments were carried out to examine the flows in the air model. The experimental conditions, based on average jet flows, are summarized in table 5.1.5. The flows to each burner jet were no more than ±5 % different than the average jet flow.

Table 5.1.5 Velocity Distribution - Experimental Conditions in Air Model

Test		V1A	V1B	V1C	V2A	V2B	V2C	V2D	V3A	V4A
Afterburner Configuration		----	----	----	----	----	F	A	----	
Burner	Ø (cm)	9.80	9.80	9.80	9.80	9.80	9.80	9.80	4.98	7.40
	Reynolds # (x 10^3)	194.7	194.6	195.2	127.8	125.2	124.8	125.1	243.7	144.6
	Velocity (m/s)	29.8	29.8	29.9	19.6	19.2	19.1	19.2	73.4	29.3
Furnace	Grid Density	5 x 9	9 x 9	5 x 9	5 x 9	5 x 9	5 x 9	5 x 9	5 x 9	5 x 9
	Reynolds # (x 10^3)	29.4	29.4	29.5	19.3	18.9	18.9	18.9	18.7	16.5
	Superficial Velocity (cm/s)	42.5	42.5	42.6	27.9	27.3	27.3	27.3	27.0	23.9
Uptake	Grid Density – Lower	6 x 6	10 x 6	6 x 6	6 x 6	6 x 6	6 x 6	6 x 6	6 x 6	6 x 6
	- Upper	6 x 5		6 x 5	6 x 5		6 x 5	6 x 5		
	Entrance Reynolds # (x 10^3)	70.7	70.6	70.8	46.4	45.4	45.3	45.4	44.9	33.5
	Superficial Entrance Velocity (cm/s)	125.3	125.2	125.6	82.3	80.6	80.3	80.5	79.6	59.5
Afterburner O_2 Jet	Reynolds # (x 10^3)							25.4		
	Velocity (m/s)							24.0		
SO_2 Recycle Jet	Reynolds # (x 10^3)							37.2		
	Velocity (m/s)							8.9		
SO_2 Recycle+O_2 Jet	Ø (cm)						3.81			
	Reynolds # (x 10^3)						57.3			
	Velocity (m/s)						22.6			

Note 1: In test V1C, the uptake was rotated 180° around its longitudinal axis, so that the discharge was on the east side.
Note 2: Superficial velocity calculated based on measured flow to the jets

5.1.3.1 Flow Patterns

The velocity profiles measured in the air model were in agreement with the more qualitative observations made in the water model. In the air model, the measured velocity profiles obtained using the experimental technique described in section 4.3.2, were reproducible. This section describes the flow patterns observed with the 9.8 cm diameter jets and the afterburner jets turned off. The 9.8 cm jets were used for most of the experiments carried out in the air model.

In the furnace, the combined flow from adjacent jets was skewed to the east side of the model while a large back flow enveloped the jet flow along the west side and the roof line. Typical dimensionless velocity (DV) profiles measured on different cross-sectional planes in the furnace model are illustrated in figure 5.1.6. The dimensionless velocities were several times greater than the superficial velocity in the furnace due to the strong jet flows issuing from the end wall. In plane P1, the highest measured velocities were located in the center of the combined jet stream. As the flow progressed (planes P2 and P3), the high velocity region shifted lower along the model floor as was expected with jets angled at 12° down. The recirculating flow traveled in more or less plug flow with a dimensionless velocity of 4-5, i.e. the flow was reasonably uniform.

At the entrance to the uptake, the air velocities were highest through the centre and a back flow into the furnace was observed on the west side along the north and south walls. Downstream of the entrance, a region of higher velocity was established along the west wall of the uptake, i.e. the side of the discharge. The most significant factor contributing to this behavior was the position of the discharge on the west wall of the uptake. In the throat of the discharge, the air velocity was accelerated to about 8 times the superficial velocity in the upper section of the uptake. The importance of the discharge on the flow in the uptake was confirmed when its position was rotated 180° about the longitudinal axis. In this scenario the flow patterns in the uptake were turned around to yield a mirror image of the original case. Figure 5.1.7 shows typical dimensionless velocity profiles measured at different cross-sectional planes for both cases.

A small region of back flow was noted in the lower section of the uptake (plane P5) as the flow

accelerated up the west wall. This was a localized effect which was not noted in the upper section of the uptake. The tapered section of the uptake resulted in a slight acceleration of the air mass by a factor of about 1.4.

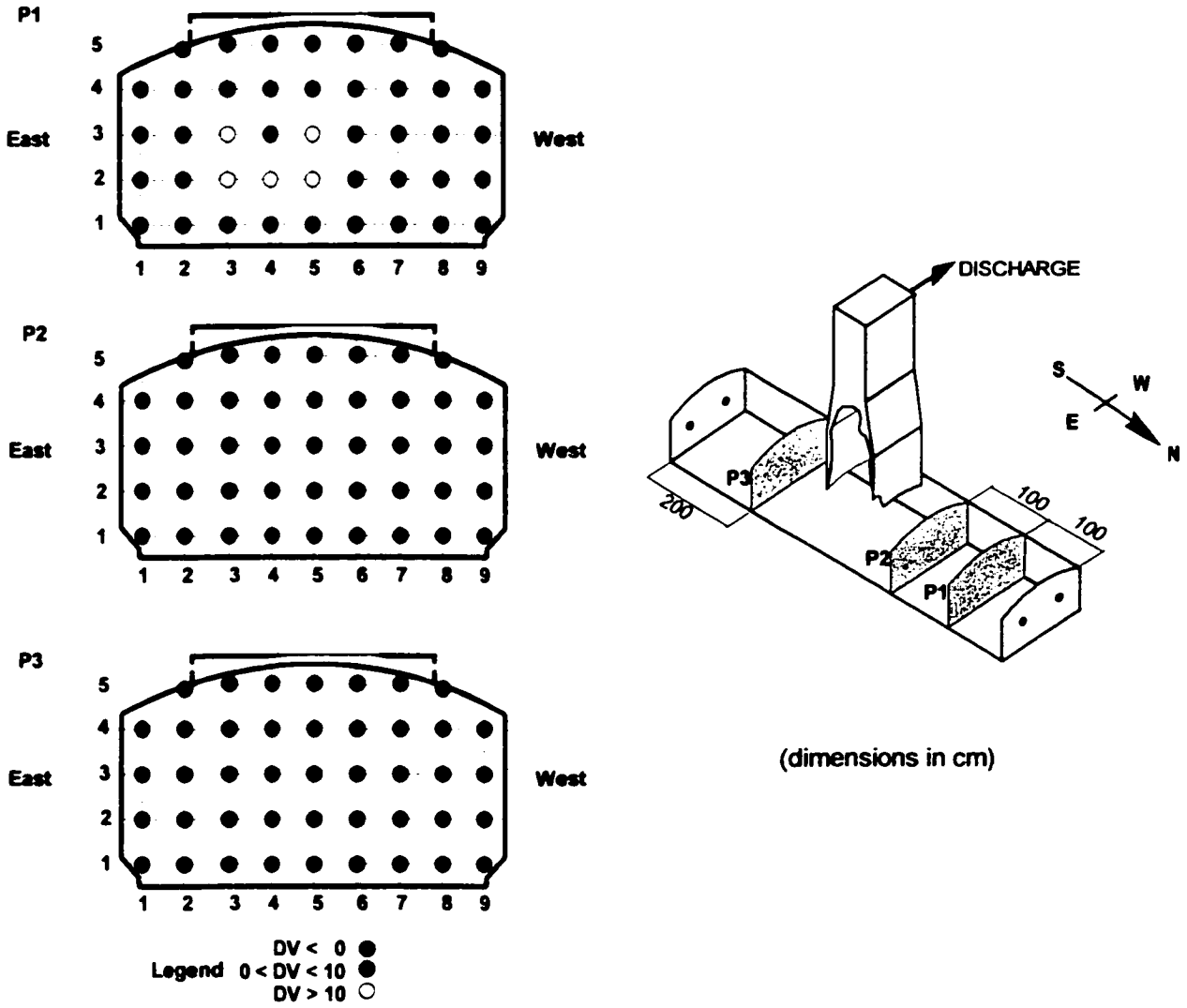

Figure 5.1.6 Typical Furnace Velocity Profiles Measure in Air Model (Test V1A)

(DV>0 ≡ flow toward uptake)

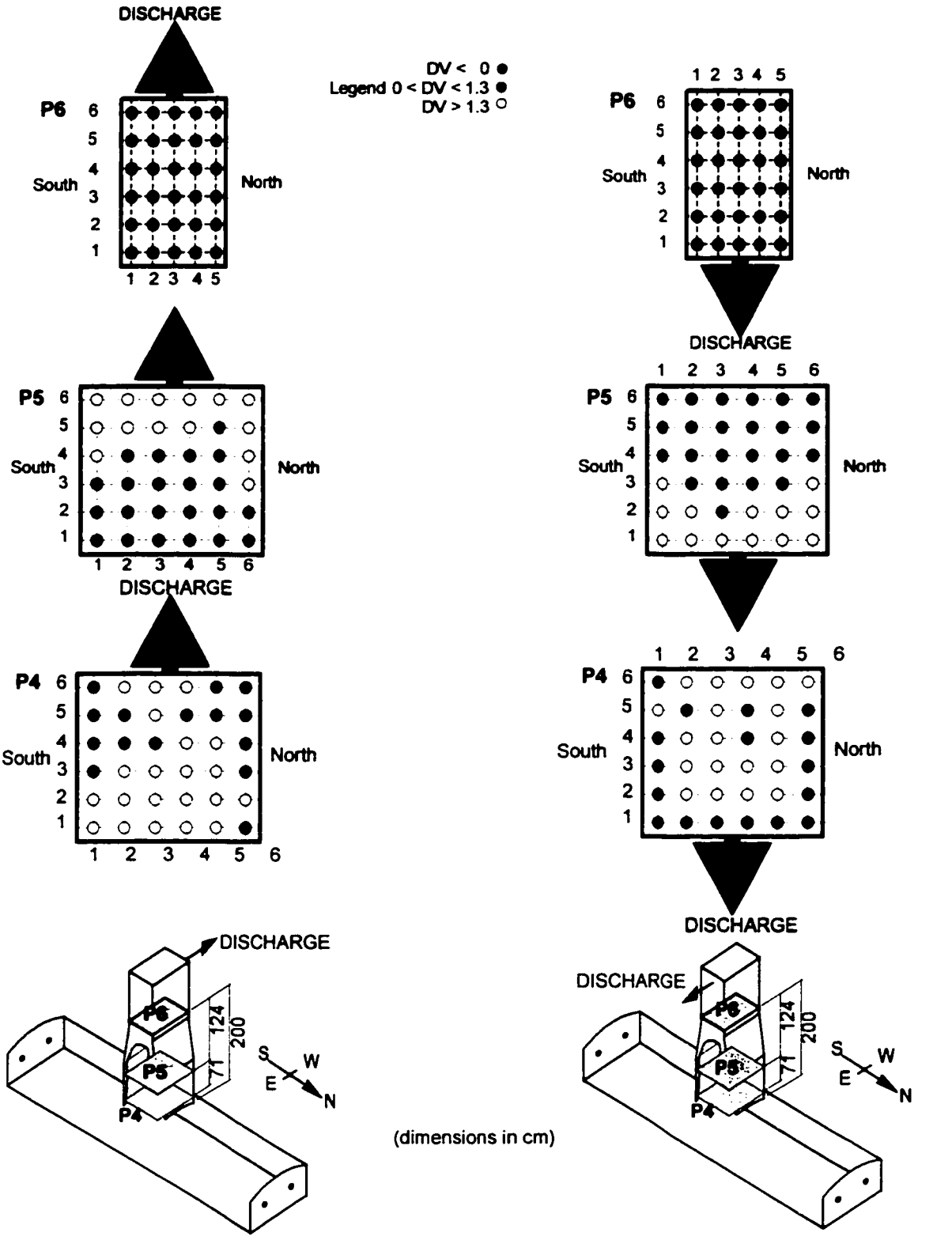

ORIGINAL (Test V1A)

UPTAKE ROTATED 180° (Test V1C)

Figure 5.1.7 Typical Uptake Velocity Profiles in Air Model (DV>0 ≡ upward flow)

5.1.3.2 Effect of Sampling Grid Density

In test V1A and V1B, the sensitivity of the velocity profile to the grid spacing was evaluated on planes P2, P3 and P5. By comparison, the grid density used in test V1B was increased by about 70%. The velocity profile measured on the denser grid (P2, P3 - 9x9; P5, 10x6) was no different than the velocity profile measured on the less dense grid (P2, P3 - 5x9; P5 - 6x6). Figure 5.1.8 shows the measured velocity profiles for the different grid spacing, while a direct comparison of the dimensionless velocities at three lateral positions across plane P2 is made in figure 5.1.9.

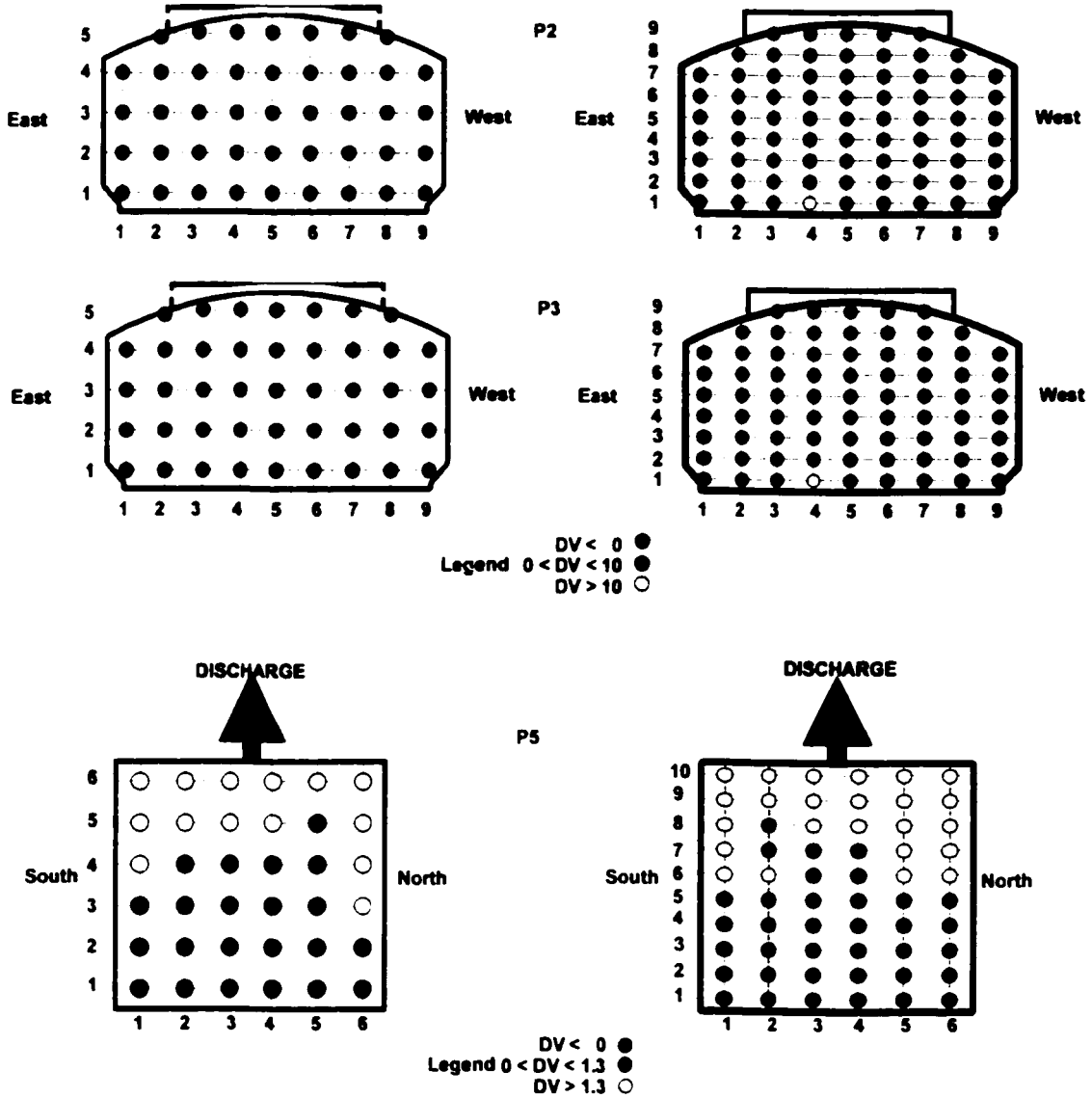

Figure 5.1.8 Sensitivity to Grid Spacing on Velocity Profiles in Air Model (Test V1A,B)

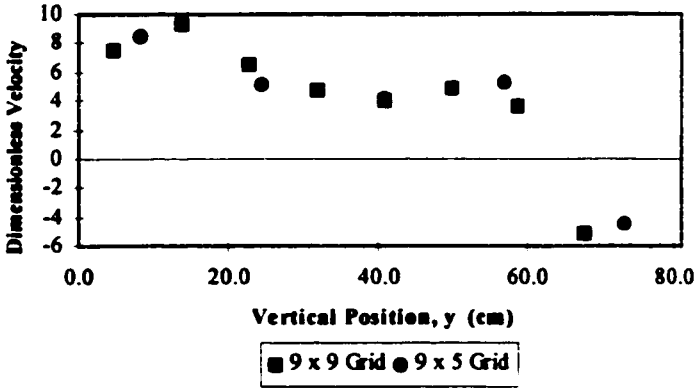

Column 2 (z = 23.61 cm)

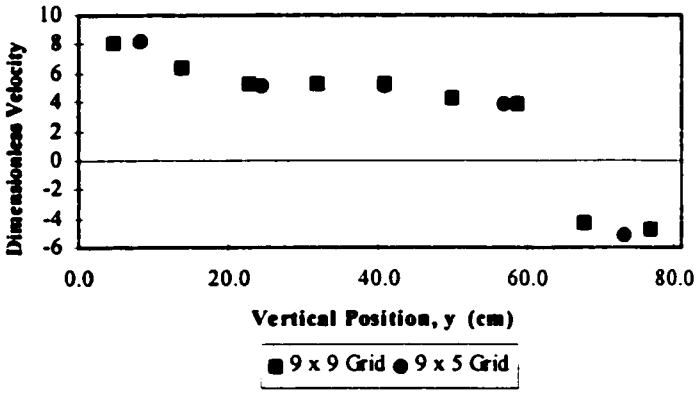

Column 5 (z = 70.81 cm)

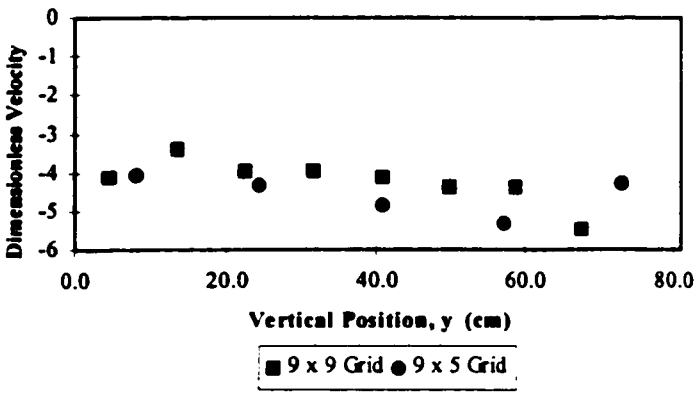

Column 8 (z = 118.05 cm)

Figure 5.1.9 Comparison of Dimensionless Velocities Measured on Different Grids in Air Model at Plane P2 (x = 200 cm from jets)

5.1.3.3 Effect of Burner Jet Velocity

The effect of burner jet velocity on the flow patterns in the furnace space was investigated at two different velocities, 19 m/s (test V2A-B) and 30 m/s (test V1A). The burner jet velocity had no effect on the flow patterns in the furnace and uptake. Figure 5.1.10 illustrates the effect of jet velocity on the flow patterns in the furnace at planes P1, P2 and P3.

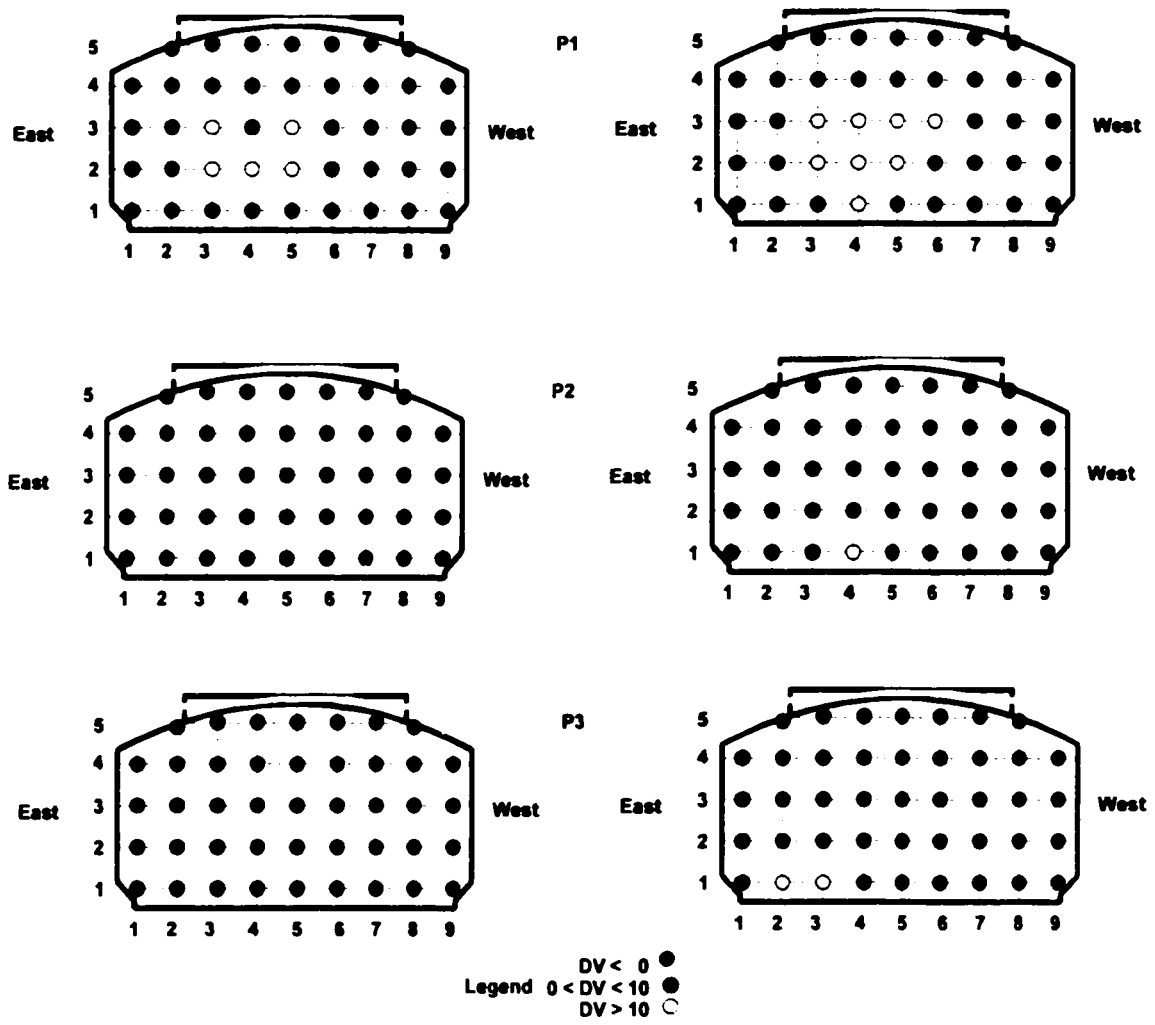

Figure 5.1.10 Effect of Burner Jet Velocity on Flow Patterns in Air Model

5.1.3.4 Effect of Burner Jet Size on Flow Patterns

When the kinetic energy of the jet was increased by decreasing the jet diameter, the flow patterns in the furnace space changed. This aspect was examined for two smaller jet sizes: 4.98 cm and 7.40 cm. By decreasing the jet size, the rate of kinetic energy dissipation for this flow through system was increased as was the dispersion number ratio. A comparison of the dispersion number ratio (equation 4.1.5) is given in table 5.1.6 for the air model using. This approach was taken because the proportionality constant required to calculate the turbulent dispersion number (equation 4.1.4) was not known.

Table 5.1.6 Comparison of the Dispersion Number Ratio for the 4.98, 7.40 and 9.80 cm Jets

Jet Size (cm)	Dispersion Number Ratio (equation 4.1.5)
4.98	1.88
7.40	1.10
9.80	0.76

The flow from both jets combined to form a single forward moving stream as in the case of the 9.80 cm jet. However, the dimensionless velocities were, depending on jet size, 1.5-2.5 times greater than in the case with the 9.80 cm jets. In addition, due to the increased rate of kinetic energy, the asymmetry observed with the 9.80 cm jets was not as pronounced in the case of the smaller jets (figure 5.1.11). The asymmetry was least noticeable with 4.98 cm jet. The net result was an increase in the amount of back flow measured in the model (section 5.1.3.7). In the case of the smaller jets, the back flow enveloped the combined jet stream along the sides and roof of the model.

In the uptake the flow pattern measured at plane P5 remained unchanged with a high velocity region along the west wall (side of the discharge) and a region of downward flow along the east wall.

Plane P2

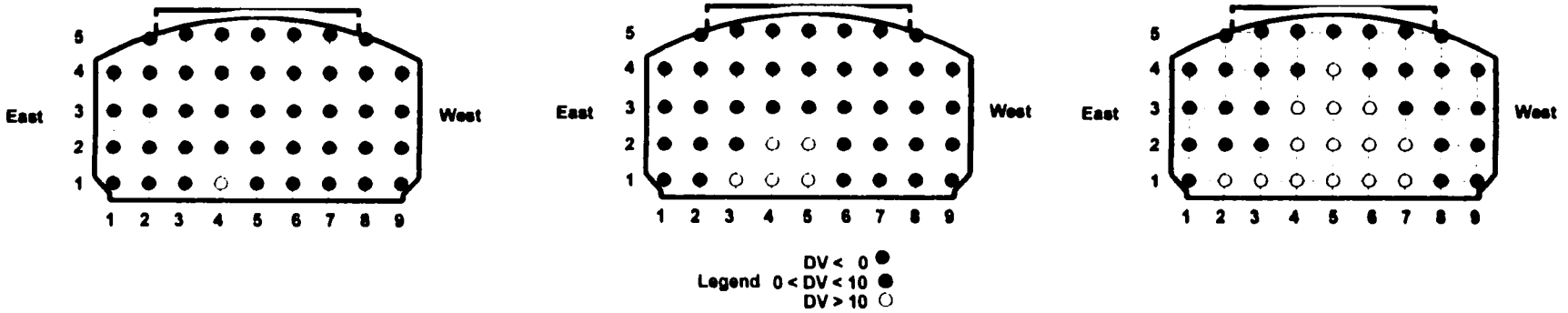

Plane P3

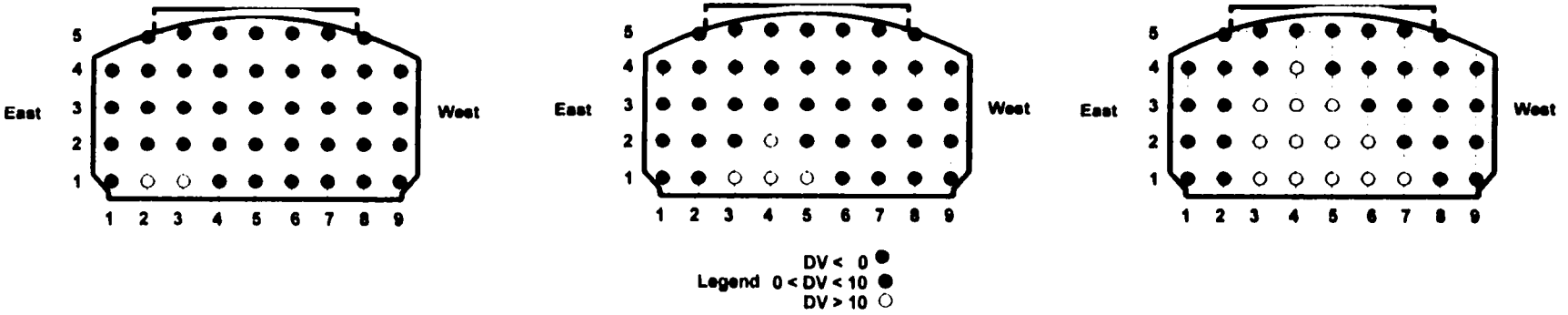

9.80 cm ∅ Burner Jet (Test V2A)

7.40 cm ∅ Burner Jet (Test V4A)

4.98 cm ∅ Burner Jet (Test V3A)

Figure 5.1.11 Effect of Burner Jet Diameter on Furnace Flow Patterns in Air Model

5.1.3.5 Effect of Afterburner Jets on Flow Patterns

The influence of afterburner jets on the flow patterns in the furnace and uptake was examined under two configurations (figure 5.1.12). One set of measurements were taken at planes P3, P4, P5 and P6 for each configuration under conditions which closely simulated the plant operation. The introduction of air through the afterburner jets in the uptake had no effect on the flow patterns in the furnace and at the entrance to the uptake. The furnace flow patterns remained unchanged which was expected as the flow through the uptake afterburner jets was a small fraction of the total flow through the burner jets, about 15%. Figure 5.1.13 shows a comparison of the velocity profiles measured with and without flow to the afterburner jets at planes P3 and P4.

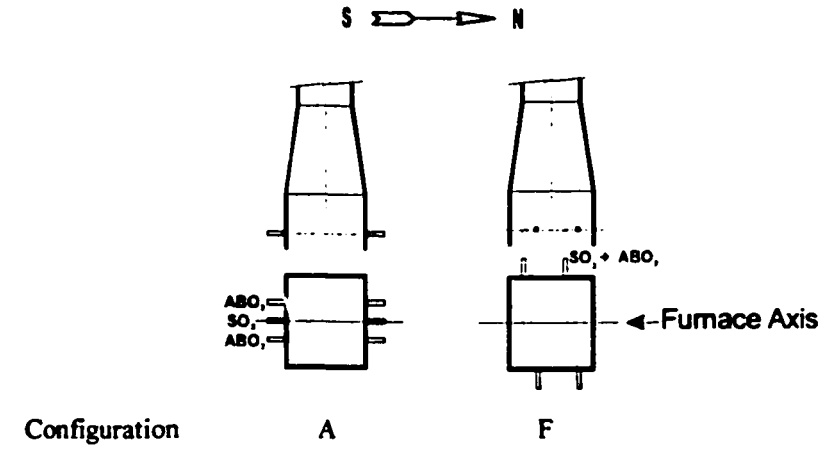

Figure 5.1.12 Afterburner Configurations - Air Model Velocity Tests

In the uptake, the trends were also similar with and without the flow of air through the afterburner jets. A region of higher velocity was established along the west wall of the uptake (i.e. the discharge side) although no significant region of back flow zone could be distinguished on plane P5 when the afterburner jets were turned on. When the afterburner jets were on, smoke tracer and yarn streamer tests revealed that the flow was highly three dimensional with no distinct pattern. Unlike the case without the afterburners, the flow was not uni-dimensional containing lateral velocity component of similar magnitude as the axial component, and the mass balance agreement between the measured flow to the jets and the measured velocity profile was not good on planes P5 and P6 (section 5.1.3.6).

Plane P3

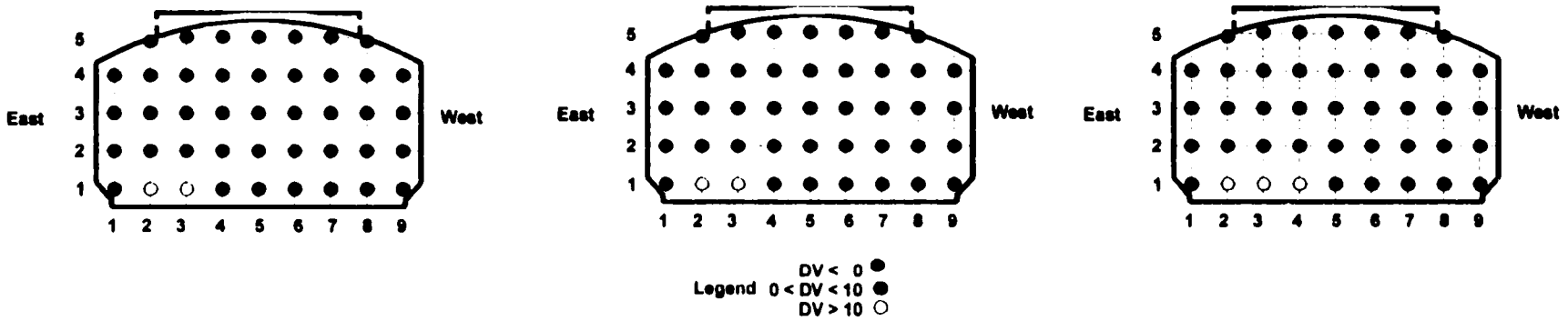

Plane P4

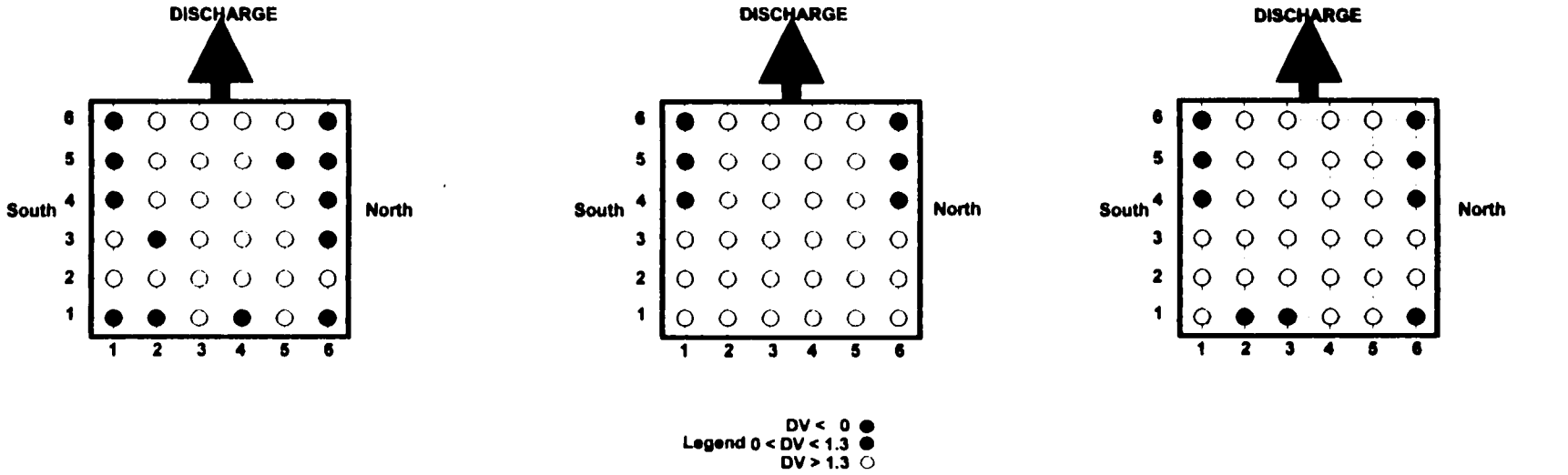

No Afterburner Jet Flow (Test V2A)

Afterburner Jet Configuration A (Test V2C)

Afterburner Jet Configuration F (Test V2D)

Figure 5.1.13 Influence of Afterburner Jets on Velocity Profiles Measured in the Air Model

5.1.3.6 Mass Balance Agreement Between Measured Burner Jet Flows and Estimates from the Velocity Profile Flow

There was reasonable agreement between the burner jet flows and the flows as determined by the integration of the velocity profiles. Agreement was considered to be good when there was no more than a 20% percent difference between the values. This was acceptable despite a) the high turbulence intensity measured in the flow field (section 5.1.3.8), b) the finite duration of the sampling period (60 seconds), and c) using measured point velocities in integrating the velocity field. Table 5.1.7 summarizes the mass balances for each experiment.

In all tests, a comparison of the flow rates on planes P2, P3 and P4 showed good agreement regardless of the flow conditions. By planes P2 and P3, the flow from the high velocity burner jets had dissipated, and the velocities in the main stream flowing towards the uptake were more uniform. This was not the case on plane P1 where a region of high velocity was observed in the center of the flow field.

In the uptake, the agreement between the flows and the flow rates determined by the measured velocity profiles was not consistent. There was good agreement only when the flow of air through the afterburner jets was turned off. However, with the exception of plane P4, the difference was significantly greater suggesting that the flow was no longer uni-dimensional in the presence of the afterburner jets. It was therefore concluded that the method described in chapter 4 for measuring velocities was not applicable to the cases when the afterburner jets were turned on. To overcome this problem, it would be necessary to a) improve the design shield by making it closer fitting to the anemometer tip, and b) measure all three velocity components.

The significance of grid spacing was also investigated in the air model (section 5.1.3.2). It is worth noting that the density of the sampling grid had no significant bearing on the agreement between measured jet flows and flows estimated from the velocity profiles.

Table 5.1.7 Mass Balance Agreement Between Measured Jet Flows and Flows Estimated from Velocity Profiles (L/min)

Test		V1A	V1B	V1C	V2A	V2B	V2C	V2D	V3A	V4A
Afterburner Configuration		----	----	----	----	----	A	F		
Plane P1	Furnace Flow[1], Q_f (L/min)	24210			23980					
	Flow through burner jets[2] (L/min)	27040			17580					
	% Difference[3]	-10.5			36.4					
Plane P2	Furnace Flow[1], Q_f (L/min)	26740	28150		20840	20440			18220	15870
	Flow through burner jets[2] (L/min)	27040	27000		17580	17390			17340	15180
	% Difference[3]	-1.1	4.3		18.5	17.5			5.1	4.5
Plane P3	Furnace Flow[1], Q_f (L/min)	25360	24830		17850	17640	18060	20870	14290	15830
	Flow through burner jets[2] (L/min)	26880	26880		17820	17270	17330	17420	16930	15110
	% Difference[3]	-5.7	-7.6		0.2	2.1	4.2	19.8	-15.6	4.8
Plane P4	Uptake Flow[1]· Q_u (L/min)	52180		47450	36150		38750	34620		
	Flow through burner jets[2] (L/min)	53920		54050	35400		34570	34650		
	% Difference[3]	-3.2		-12.2	2.1		12.1	-0.1		
Plane P5	Uptake Flow[1]· Q_u (L/min)	52780	53580	49920	40570	33400	68370	56650	32610	28760
	Flow through burner and uptake jets[2] (L/min)	53920	53880	54050	35400	34660	40740	39090	34270	30290
	% Difference[3]	-2.1	-0.6	-7.6	14.6	-3.6	67.8	44.9	-4.8	-5.1
Plane P6	Uptake Flow[1]· Q_u (L/min)	58680		53400	43330		50650	49450		
	Flow through burner and uptake jets[2] (L/min)	53920		54050	35400		40740	39090		
	% Difference[3]	8.8		-1.2	22.4		24.3	26.5		

Note 1: Flow calculated based on measured velocity profiles.
Note 2: Flow based on measured jet flows.

Note 3: $$\% \text{ difference} = \frac{(Q_{vp} - Q_j)}{Q_j} \times 100$$

5.1.3.7 Recirculation in the Furnace

In the furnace, as noted previously, the flow from adjacent burner jets converged forming a single stream, which was skewed to the east side of the model. The strong jet flows issuing from the end wall generated a large back flow of air which enveloped the main jet stream along the west side and roof line of the model. The flow of this air back towards the jets, close to those enclosing walls, was referred to as recirculation. The recirculating flow traveled in more or less plug flow having a rather uniform velocity.

The recirculation ratio, defined as the ratio between the recirculating air flow and the flow through the burner jets, was found to be inversely proportional to the jet diameter. By decreasing the jet size, the rate of kinetic energy dissipation in the furnace space was increased resulting in a greater amount of recirculation. The relationship between dispersion number ratio (equation 4.1.5) and recirculation ratio in the furnace space is seen in figure 5.1.14. The relationship was linear. As per the assumptions discussed in section 4.1.2.2, a ratio of 1 implies that the turbulent mixing behaviour in the model and the plant are similar. Therefore, from this plot, the recirculation ratio was estimated to be 2.85. In other words, the recirculating gas flow in the plant is about three times the furnace off-gas flow.

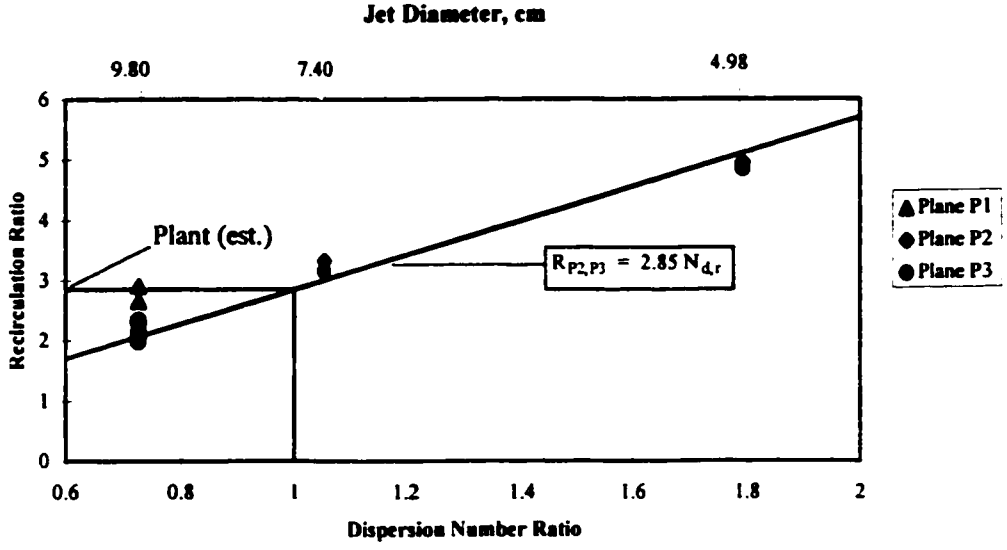

Figure 5.1.14 Recirculation Flow as a Function of Dispersion Number Ratio in the Air Model

The calculated recirculation ratio was greater on plane P1 measuring 2.6-2.9 compared with a value of 2.0-2.5 for planes P2 and P3. At plane P1, the rate of entrainment is greater than at plane P2 and P3 suggesting that there is more disentrainment occurring at plane P2.

The recirculation ratios calculated in the air model were less than the ratio calculated with the simplified model proposed by Thring and Newby (1953) which was based on a single jet centered in a cylindrical duct. The basis of the theory is that the jet entrains as a free jet up to the point where entrainment ceases and disentrainment begins. The Thring and Newby model is expressed by the simple correlation given by equation 5.1.3. Figure 5.1.15 compares the calculated and the measured recirculation ratios for the air model. In applying this theory to the air model, an effective jet diameter was employed to account for two jets, as defined in equation 5.1.3.

$$\frac{Q_r}{Q_j} = 0.47\ \theta^{-1} - 0.5; \text{ where } \theta = \frac{d_{eff}}{D_{hyd\ fce}} \qquad (5.1.3)$$

$$d_{eff} = \sqrt{2 \times d_j^2}$$

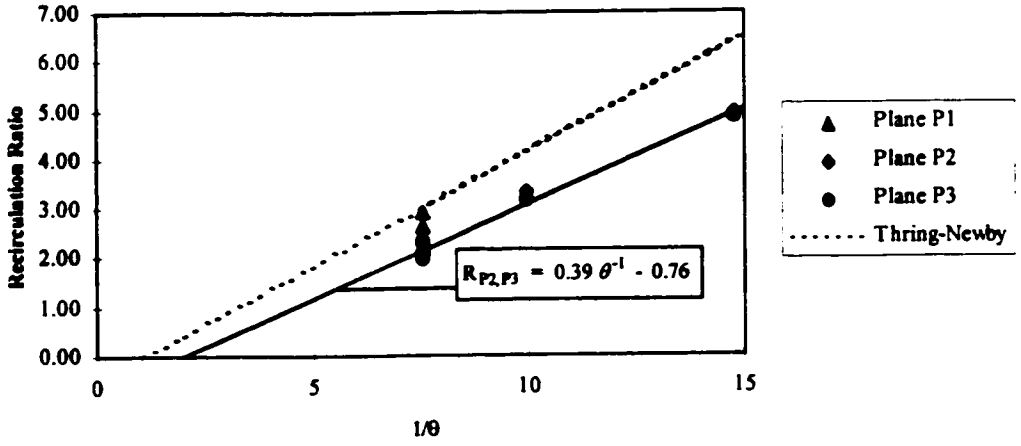

Figure 5.1.15 Recirculation Ratio - Measured vs Calculated

The difference between the calculated and measured recirculation ratio was attributed to several factors. First, the jets in the air model were angled inward and downward at an angle of 12° and were not centered in the end wall. The expansion was restricted along the floor of the model as

well as by the adjacent jet, which would affect the jet expansion. Second, the Thring and Newby theory does not account for the interaction between the two adjacent jets. Third, the theory assumes that the jet boundary would reach the enclosing duct walls, which was not the case in the air model. Therefore, the Thring and Newby theory provides only an approximation of the recirculation in the air model.

In addition to the recirculation attributed to the burner jets, there was a back flow at the entrance to the uptake. The back flow, measured on plane P4, could be observed by making the flow visible with smoke, and amounted to 20% of the total jet flow entering the uptake. As previously described the back flow region was located on the west side of the uptake along the north and south walls. This flow separation at the entrance was associated with vortex shedding produced by the high velocity stream flowing through the center of the uptake. The Thring and Newby model could not account for the back flow from the uptake.

5.1.3.8 Turbulence Intensity

The local rms turbulence intensity in the axial direction was computed from the variance of the velocities measured at each sampling node. It is worth noting that the data acquisition system recorded data from the anemometer module every 0.333 seconds; this was significantly slower than the turbulent time scale, which was on the order of 10^{-3} seconds. Therefore, the local rms turbulence intensity computed from this data provides only an approximation.

The local instantaneous velocities were observed to fluctuate in a quasi-random fashion. Figure 5.1.16 illustrates typical velocity fluctuations observed in the air model. Analysis of the data indicated that the flow exhibited two types of fluctuations - a high frequency fluctuation with a period between 0.3-1 Hz superimposed on a low frequency fluctuation. This behaviour was indicative of a temporal instability in the flow.

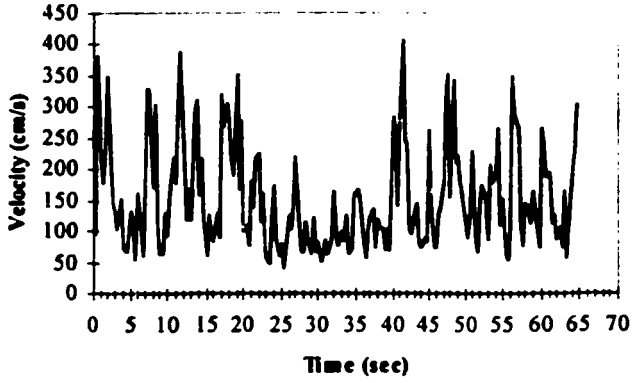

Cell (3,4), $\bar{v}_{3,4}$ = 153.8 cm/s, TI_{rms} = 0.54

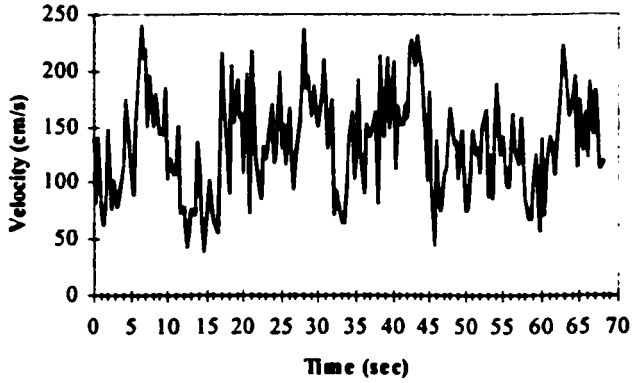

Cell (3,8), $\bar{v}_{3,4}$ = 136.4 cm/s, TI_{rms} = 0.33

Figure 5.1.16 Velocity Fluctuations Measured in Air Model - Test V2B Plane P2

Flow visualization with an NH_3-SO_2 reaction technique indicated that the impingement of the main streams from the burner jets produced instability in the centre of the model beneath the uptake. In these experiments, the ammonia and sulphur dioxide gases were introduced separately through burner jets at opposite ends of the model. Preliminary analysis has indicated that this instability oscillated with a frequency of 0.05-0.2 Hz as measured from observation of the flow. Similar qualitative observations were made in the water model using an acid-base reaction technique, where the acid and base were introduced through jets at opposite ends. Research in the field of jet impingement in a side-dump combustor, which operate at low jet Reynolds number (≈3000), has revealed similar instabilities but at higher oscillation frequencies (≈300 Hz) than those measured in the air model (Nossier and Behar, 1986).

Figure 5.1.16 also shows that the local instantaneous velocities varied from the average velocity at the corresponding points which lead to high values of turbulence intensity. This temporal instability in the flow was driven by cyclic imbalances of pressure in the system. Figure 5.1.17 illustrates the fluctuation of static pressure measured near the base of the uptake. The measured turbulence intensity was about 0.36 which was similar in magnitude to the values measured by Sutalo (1994) in his water model of the Outokumpu flash furnace. The average root mean square turbulence intensities measured on each sampling plane in the air model are summarized in table 5.1.8.

The high turbulent intensity values implied large velocity variances with a corresponding high degree of mixing of the incoming air with the air in the furnace and the lower section of the uptake. These elevated values of turbulence intensity were due to a flow-induced instability. The intensity was lower on plane P6 due the flow contraction in the uptake, which tended to dampen the fluctuations. The afterburner jets had no impact on the turbulence intensity.

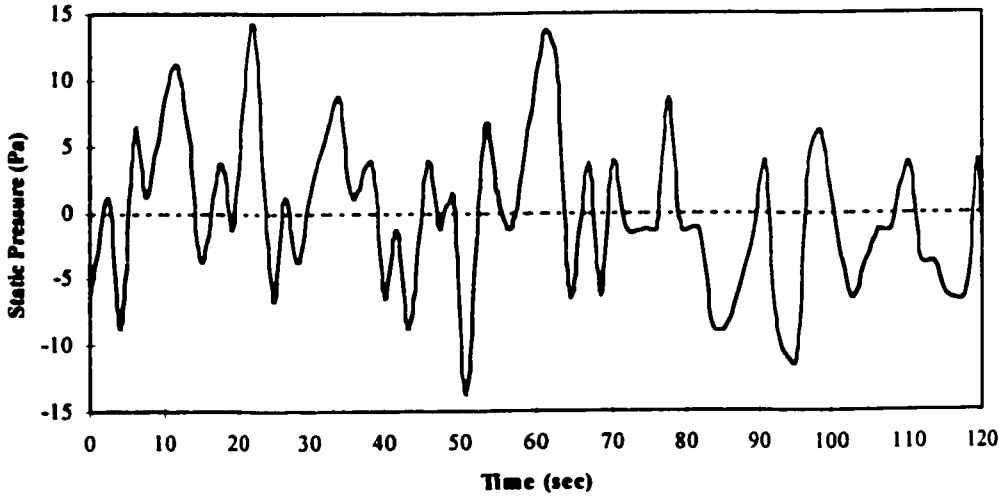

Figure 5.1.17 Pressure Fluctuations Measured Near the Base of the Uptake in the Air Model

Table 5.1.8 Average Root Mean Square Turbulence Intensity Measured in Air Model

	P1	P2	P3	P4	P5	P6
V1A	0.37	0.38	0.38	0.39	0.36	0.17
V1B		0.38	0.38		0.36	
V1C				0.38	0.36	0.18
V2A	0.36	0.38	0.37	0.40	0.36	0.16
V2B		0.40	0.39		0.39	
V2C			0.38	0.37	0.32	0.17
V2D			0.38	0.40	0.34	0.12
V3A		0.37	0.36		0.48	
V4A		0.39	0.34		0.41	

5.1.4 Summary of Bulk Flow Patterns

The bulk flow patterns in the furnace gas space were investigated in, first, the water model and, then, the air model using three different experimental techniques. A summary of the findings is given below.

- The residence time distribution tests revealed that the flow patterns could be represented by two flow regimes, a well mixed volume and a much smaller plug flow volume in series, as illustrated in figure 5.1.18.

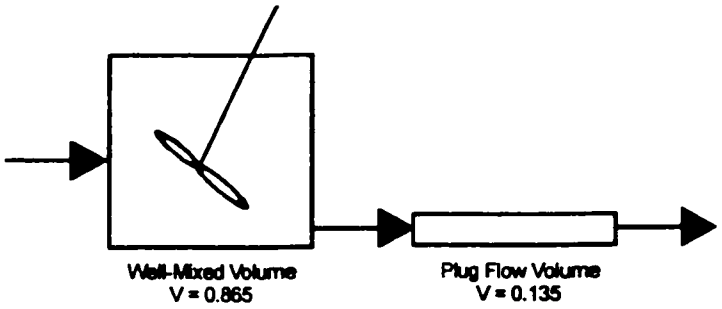

Figure 5.1.18 Schematic Representation of Flow Regimes in Water Model

- The velocity profiles measured in the air model were in agreement with the more qualitative observations made in the water model. The flow patterns and velocity profiles were unaffected by the flowrate through the main burner jets.

- In the furnace, the combined flow from adjacent jets was skewed to the east side of the model while a large back flow enveloped the jet flow along the west side and the roof line (figure 5.1.19). In the uptake, a region of higher velocity was established along the west wall of the uptake, i.e. the side of the discharge. The most significant factor contributing to this behavior was the position of the discharge on the west wall of the uptake. When the uptake was rotated 180° about its longitudinal axis so that the discharge was on the east wall, the flow patterns in the uptake were turned around. That is, the region of high velocity was now along the east wall where the discharge was located. Small regions of back flow were noted in the lower section of the uptake.

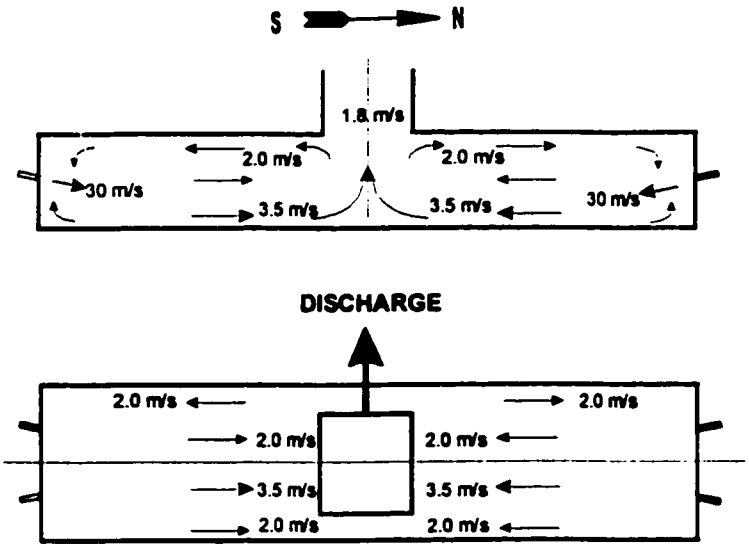

Figure 5.1.19 Typical Velocities Measured in Air Model (Test V1A)

- The flow of this air back towards the jets was referred to as recirculation. The recirculation ratio, defined as the ratio between the recirculating air flow and the flow through the burner jets, was found to be inversely proportional to the jet diameter. Decreasing the jet size increased the rate of kinetic energy dissipation in the furnace space resulting in a greater amount of recirculation. The relationship between recirculating flow and the dispersion number ratio (equation 4.1.5), a function of the jet diameter, was linear. From this plot, the recirculation ratio in the plant was estimated to be 2.85 based on a dispersion number ratio of 1 which implies that the turbulent mixing behaviour in the model and the plant were similar.

- The local instantaneous velocities were observed to fluctuate in a quasi-random fashion. Flow visualization with smoke indicated that the impingement of the main streams from the burner jets produced instability in the center of the model beneath the uptake. This instability oscillated with a frequency of 0.05-0.1 Hz that was measured from observation of the flow. The measured turbulence intensity was about 0.36. The high turbulence intensity values implied large velocity variances with a corresponding high degree of mixing of the incoming air with the air in the furnace and the lower section of the uptake.

5. 2 Mixing of Gases in the Uptake

The second objective of the modeling effort was to investigate the factors, which affect the mixing of afterburner and furnace gases in the uptake. The mixing conditions in the uptake were examined with different afterburner configurations in, first, the water model and, then, the air model. The degree of mixing was observed using flow visualization with acid-base reactions in the water model and measured using a tracer technique in both the water and air models.

5.2.1 Flow Visualization in Water Model - Acid-Base Reaction

The acid-base reaction experiments provided an excellent method for screening potential afterburner configurations and visually identifying the mixing and reaction zones within the water model. As discussed in section 4.2.2, acid-base reactions were selected to observe the mixing behaviour because they are extremely fast and are diffusion (mixing) controlled and can easily be made visible using indicators. In these experiments, the water model was operated with very dilute aqueous solutions of acid and base. The acid was introduced through the main burner jets and the base, marked with bromothymol blue indicator, was injected via the afterburner jets in the uptake. Mixing was evaluated qualitatively by observing the extent of neutralization of the base solution. Good mixing of the base with the acid stream was indicated by a yellow solution exiting the model. Poorly mixed conditions were identified by a blue solution of unmixed base in the discharged stream. In the model operated with excess acid, ideal mixing would be realized when the unmixed region appears only very near the afterburners.

A total of 6 afterburner configurations, labeled A through F, were screened using this method. The flow conditions, under which these configurations were examined, are given in table 5.2.1. A description and illustration of these configurations are given in table 5.2.2 along with a description of the observed flow patterns. Photographs illustrating the typical mixing conditions observed with configurations A through F can be found in Appendix A.

Table 5.2.1 Flow Visualization in Water Model - Experimental Conditions

Configuration		A	B	C	D	E	F
Burner	Flow (L/min/jet)	87.0	87.0	87.0	87.0	87.0	87.0
	Reynolds # (x 10^3)	92.6	92.6	92.6	92.6	92.6	92.6
	Velocity (m/s)	4.6	4.6	4.6	4.6	4.6	4.6
Furnace	Total Flow (L/min)	348	348	348	348	348	348
	Reynolds # (x 10^3)	10.8	10.8	10.8	10.8	10.8	10.8
	Superficial Velocity (cm/s)	4.0	4.0	4.0	4.0	4.0	4.0
Uptake	Entrance Reynolds # (x 10^3)	27.4	27.4	27.4	27.4	27.4	27.4
	Superficial Entrance Velocity (cm/s)	12.9	12.9	12.9	12.9	12.9	12.9
Afterburner Jet							
	Flow (L/min/jet)	1.96		1.96	1.96		
	Jet Diameter, Ø (cm)	0.3175		0.3175	0.3175		
	Velocity Ratio	31.9		31.9	31.9		
	Momentum Ratio	0.18		0.18	0.18		
	Reynolds # (x 10^3)	13.1		13.1	13.1		
SO_2 Recycle Jet							
	Flow (L/min/jet)	9.10					
	Jet Diameter, Ø (cm)	0.9525					
	Velocity Ratio	16.5					
	Momentum Ratio	0.43					
	Reynolds # (x 10^3)	20.3					
SO_2 Recycle + O_2 Jet							
	Flow (L/min/jet)		14.00	11.50	11.50	13.00	13.00
	Jet Diameter, Ø (cm)		0.9525	0.9525	0.9525	0.9525	0.9525
	Velocity Ratio		25.3	20.8	20.8	23.5	23.5
	Momentum Ratio		1.02	0.69	0.69	0.88	0.88
	Reynolds # (x 10^3)		31.2	25.6	25.6	29.0	29.0

Table 5.2.2 Flow Visualization in Water Model - Afterburner Configurations

Configuration	Schematic	Description of Afterburner Configuration	Flow Pattern Observed in Model
A	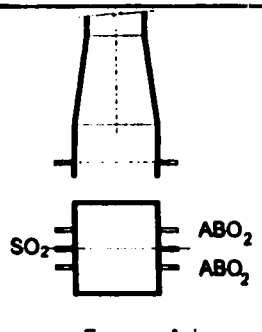	- original afterburner configuration - afterburner oxygen injected through 4 nozzles, two on each opposite wall of the uptake perpendicular to the longitudinal axis of the furnace - SO_2 recycle introduced via two jets, one on each opposite wall of the uptake perpendicular to the longitudinal axis of the furnace	- jet entrained surrounding reacting mixture and assumed a roughly conical shape before jet impingement - head-on impingement of two opposing jets was highly unstable, and jets oscillated along the jet axis due to their impingement and unstable bulk flow - jet-on-jet impingement produced a plume which did not dissipate completely prior to discharge, leading to the periodic discharging of unreacted base - intermittent downward pulsating flow along the uptake walls parallel to the furnace axis (generated at elevation of jets) resulted from temporal flow pattern changes at the furnace uptake transition - complete neutralization of base observed over short intervals primarily when the flow at the transition was downward
B	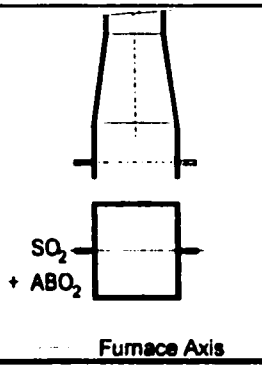	- injection of a blend of oxygen and SO_2 recycle through only two nozzles, one on each opposite wall of the uptake perpendicular to the longitudinal axis of the furnace (tested in plant) - blending oxygen and SO_2 recycle was intended to increase jet momentum and lower post-combustion flame temperature - potential for rapid commercial implementation	- jet behaviour was similar to configuration A with the exception of jet instability which was greater - less mixing of base was observed and the frequency of discharging unreacted base was greater than in configuration A - intermittent downward flow was more pronounced than in configuration A - complete neutralization was rarely observed

Table 5.2.2 (cont) Flow Visualization in Water Model - Afterburner Configurations

Configuration	Schematic	Description of Afterburner Configuration	Flow Pattern Observed in Water Model
C	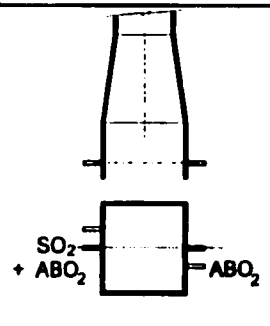	- injection of a blend of oxygen and SO_2 recycle through only two nozzles, one on each opposite wall of the uptake perpendicular to the longitudinal axis of the furnace (tested in plant) - balance of afterburner oxygen injected via two offset nozzles, one on each wall of the uptake perpendicular to the longitudinal axis of the furnace - intended to generate lateral circulation at the plane of injection into the uptake - potential for rapid commercial implementation	- jet behaviour was similar to configuration A with the exception of two afterburner oxygen jets which periodically impinged on the opposing walls of the uptake. -- about the same degree of mixing of base was observed as in configuration B, and the frequency of discharging unreacted base was also similar - frequency of intermittent downward flow was similar to configurations A and B and was confined to the corners. - complete neutralization was rarely observed
D	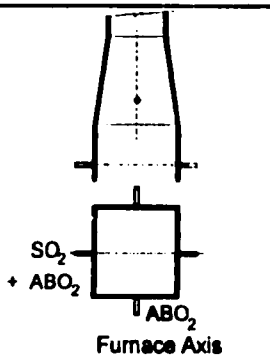	- injection of a blend of oxygen and SO_2 recycle through only two nozzles, one on each opposite wall of the lower section of the uptake perpendicular to the longitudinal axis of the furnace - balance of afterburner oxygen injected via two nozzles, one on each opposite wall of the mid section of the uptake perpendicular to the longitudinal axis of the furnace - intended to stage the post-combustion in the uptake and more uniformly dissipate the heat	- lower momentum of blend oxygen and SO_2 jets in the lower uptake prevented head-on impingement, although oscillation along the jet axis remained apparent due to the unstable flow at the furnace-uptake transition. - jets at higher elevation had insufficient time to thoroughly mix, thus resulting in the discharge of unreacted base. - intermittent downward flow was less obvious than in previous configurations - complete neutralization was not observed

Table 5.2.2 (cont) Flow Visualization in Water Model - Afterburner Configurations

Configuration	Schematic	Description of Afterburner Configuration	Flow Pattern Observed in Water Model
E	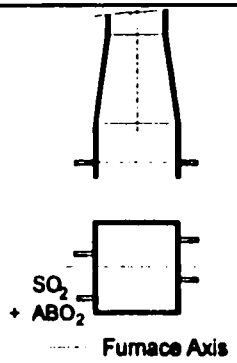	- injection of a blend of oxygen and SO_2 recycle through four nozzles, one on each opposite wall of the uptake perpendicular to the longitudinal axis of the furnace - nozzles were staggered to allow greater coverage of the uptake cross-section without jet-to-jet impingement	- jets were close enough to permit some interaction and periodic impingement of the jets on the opposing wall was noted. - jet oscillation along the jet axis remained apparent due to the unstable flow at the furnace-uptake transition. - frequency of intermittent downward flow was similar to configurations A and B but was primarily observed in the corners. - the frequency of discharging unreacted base was similar to the frequency observed in configuration A, and complete neutralization was observed occasionally
F	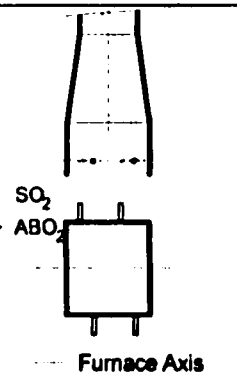	- injection of a blend of oxygen and SO_2 recycle through four nozzles, one on each opposite wall of the uptake parallel to the longitudinal axis of the furnace - nozzles were staggered to allow greater coverage of the uptake cross-section without jet-to-jet impingement - interaction between opposing jets helped induce mixing by creating a shearing effect. - geometry based on the configuration of after-fire jets in industrial waste wood boilers (MacCallum, 1983)	- jets were close enough to permit interaction and no impingement of the jets on the opposing wall was noted but was controlled by adjusting the jet momentum. - jet oscillation along the jet axis was less apparent - the frequency of the intermittent downward flow was less obvious than in previous configurations, and the downward flow lasted for a shorter period - the majority of the base is neutralized in the region above the jets, with the exception of the odd plug which moved straight through to the discharge

5.2.1.1 Incomplete Reaction - Configurations A, B C and D

Despite the addition of excess acid, the afterburner jet configurations A, B, and C involving jet-jet impingement were poorly mixed as evidenced by the predominantly incomplete discolouration of the base. Complete neutralization of the base in the uptake was only observed over short intervals when the flow at the transition had a downward component into the furnace.

The collision of the afterburner jets in the centre of the uptake produced a well-mixed plume of base. However, the dissipation and reaction of the combined plume in the uptake was neither uniform nor complete regardless of uptake jet configuration. Periodic discharging of unreacted base was related to the pulsating nature of the bulk flow at the furnace-uptake transition (section 5.2.2). Superimposed on this instability was the highly unstable head-on impingement of two opposing jets. The average period of oscillation was in the range of 2-5 seconds with configuration B having the shortest period.

Direct jet impaction on the opposing wall was prevented by the head-on collision of opposing jet. Although direct impaction was not observed, the head-on collision of the jets produced a plume, which typically climbed the transition along the east wall of uptake (opposite the discharge) and localized reaction zones resulted. Rising along the east wall, the velocity of the unreacted plume was between 14-16 cm/s which was in agreement with the findings of the particle tracer experiments. The slow-moving plume had little dispersion and did not mix thoroughly with the main flow.

Jets positioned farther up in the uptake (configuration D) did not allow sufficient time for the jet fluid to thoroughly mix with the main flow. The base solution from these jets short-circuited directly to the discharge. The impinging jets combined to produce a single plume rising approximately through the centre of the uptake.

5.2.1.2 Interlaced Jets - Configurations E and F

Configuration F with the staggered opposite pairs of jets flowing at 90° to the axis of the furnace produced the best mixing conditions. With the exception of very occasional slugs of base, which

reached the discharge, the majority of the base was neutralized in the region of the afterburner jets. The region above the afterburner jets remained "yellow" most of the time. This type of jet arrangement has been successfully implemented in industrial waste wood boilers (MacCallum, 1983) and was installed in the Inco plant in 1996.

The stitched afterburner jet arrangement in configuration F allowed for maximum coverage of the uptake cross-section while keeping the opposing jets close enough that they still interact. That is, the jet interaction helped induce mixing by creating a shearing effect. This mixing led to the neutralization of the base very near the afterburner jet region, typically less than 15 cm downstream of the injection point. However, the mixing was only effective when all four jets were in use.

The jet momentum was controlled so that the jet penetrated about 70% across the uptake, avoiding jet impingement on the opposing wall.. A jet momentum ratio of around 0.8 gave a penetration of 60-80% of the uptake width (section 5.2.3.1). This was difficult to assess exactly, because of the instability of the bulk flow and the oscillation of the jets with an average period of 4-6 seconds.

The frequency of the downward puffing of afterburner flow was dampened under configuration F (section 5.2.2). In contrast, configuration G with the staggered opposite pairs of jets flowing parallel to the axis of the furnace was not effective in dampening the downward slugging of base, and the afterburner flow was poorly mixed with the bulk flow.

5.2.1.3 Flow Visualization in the Air Model

Uptake gas mixing experiments were also carried out in the 1:5 scale air model, using an NH_3 - SO_2 reaction technique, to support the findings in the water model. In these experiments the flow was made visible by using a reaction between SO_2 and NH_3 gases. The NH_3 was injected with the air through the main burner jets while the SO_2 was mixed with air to the afterburner jets. These gases were added in a ratio of 3 NH_3:SO_2. The product of the reaction was a white ammonium sulfite powder, which was produced in the uptake. The mixing was examined qualitatively by visually observing the uniformity of air discolouration; regions, which were not well mixed,

appeared as voids. However, due to the size of the model and the opaqueness of the white powder, it was more difficult to evaluate the details of the mixing patterns in the air model than in the water model.

The air model experiments examined only the flow conditions under configuration A, B and F. These experiments confirmed that configuration F led to superior mixing of the afterburner jet flow and the bulk furnace flow. In both configurations A and B, voids were visible especially along the east walls of the uptake where the majority of the afterburner air flowed.

Although not a focus of this project, a concern expressed by Inco personnel was the formation of accretions, more commonly referred to as "horns", around the afterburner ports in the plant. This was briefly investigated in the air model and was later examined more extensively by Baird et al (1998) in the water model. The experiments carried out in the air model examined the impact of horns on the mixing in the uptake with afterburner configuration F. Extending the afterburner jet pipes into the uptake of the model simulated horns. These experiments revealed that when the afterburner pipe was extended beyond 15 cm into the uptake, the degree of mixing was compromised. As the horns extended they reached a point where the break up of the jet occurred on the opposing side wall of the uptake and there was little to no interaction between the jets in the center of the uptake. This observation suggested that unless the jets interacted, good mixing was not achieved in the uptake.

5.2.2 Flow Instability at the Furnace-Uptake Transition

The flow instability occurring at the transition between the furnace space and the uptake was examined primarily in the water model using the acid-base reaction technique. The instability of the flow at this transition produced a pulsating-type flow pattern. This behaviour was attributed to the eddy flow generated by the sharp change in direction of the bulk flow from the furnace to the uptake and resulted in intermittent downward puffing of the afterburner flow into the furnace. The downward puffing was most predominant in configurations A, B, C and E, significantly

affecting the mixing in the uptake. In contrast, the mixing under configuration F was least affected by the temporal flow instabilities. Good representation of the downward puffing could not be achieved with configuration D because the indicator concentration in the solution at the base of the uptake was insufficient to mark the bulk flow - in this configuration the afterburner flow was split between two elevations in the uptake.

In configurations A, B, C and E, the base solution was drawn down mainly along the east wall of the uptake (opposite the discharge) with the occasional plug drawn down along the west wall. The downward puffing shifted randomly between the north and the south corners of the east wall. In configuration F, the downward puffing, although less frequent, alternated randomly between both the east and west wall and was primarily confined to the corners. This behaviour was attributed to the asymmetric arrangement of the afterburner jets.

The frequency of the downward puffing was estimated from observations of a video of the uptake flow and was defined as the number of puffs over a period divided by the duration of the monitoring period. The periodicity of downward puffing varied over the monitoring period suggesting that the flow instabilities were quasi-random. The period ranged from 3 to 15 seconds in configurations A, B, C, and E and from 15 to 36 seconds in configuration F. In addition, the condition under which the flow was reversed lasted for periods of 2.5 ± 1 seconds with configuration A, B, C, and E and 1 ± 0.5 seconds with configuration F.

The instability at the entrance of the uptake was related to the phenomena of vortex shedding (Birkhoff and Zarantonello, 1957). In the models, large vortices or eddies were produced in the furnace space as well as at the entrance to the uptake. The frequency of the vortex shedding was related to the flow conditions by the Strouhal number. The Strouhal number is defined as

$$St = \frac{fd}{v} \quad ; \quad \text{where } d = \text{hydraulic diameter of uptake entrance} \qquad (5.2.1)$$

$$v = \text{superficial entrance velocity}$$

The calculated Strouhal numbers for the water model, the air model and the plant are summarized in table 5.2.3. In the air model, the flow was made visible by using a reaction between SO_2 and NH_3 gases (section 5.2.1.3), and the frequency of the downward puffing was determined in the same manner as in the water model. In the plant, the frequency was determined by observing puffing from an open port near the base of the uptake. Although the flow patterns could not be observed visually, this method provided a good indication of the flow instability in the entrance region. The frequency of puffing was determined by counting the number of puffs over a period divided by the duration of the time period.

Table 5.2.3 Frequency of Downward Pulsation at the Entrance of the Uptake

	Configuration	Superficial Entrance Velocity (cm/s)	Frequency, f (Hz)	Hydraulic Diameter (cm)	Strouhal Number	Reynolds Number
Water Model	A	8.9	0.10	21.2	0.24	18830
		12.9	0.15	21.2	0.25	27290
	B	8.9	0.10	21.2	0.24	18830
		12.9	0.14	21.2	0.23	27290
	F	8.9	0.03	21.2	0.07	18830
		12.9	0.05	21.2	0.08	27290
Air Model	A	90	0.33	84.6	0.31	50760
		130	0.50	84.6	0.33	73310
	B	90	0.36	84.6	0.34	50760
	F	90	0.22	84.6	0.21	50760
		130	0.33	84.6	0.21	73310
Plant [1]	A	170	0.45	423.0	1.12	53600
	F	180	0.40	423.0	0.94	56750

Note 1: In the plant tests, the superficial velocity was based on a) furnace gas flow calculated from a mass balance and b) no accretions on uptake walls.

Over the range of flow conditions tested in the water model, the Strouhal number remained approximately the same with the exception of configuration F. In the configuration F scenario, the frequency of downward puffing was dampened. The data suggested that the effectiveness of mixing in the uptake was inversely proportional to the Strouhal number.

The experiments in the air model produced the same trend to those conducted in the water model. The calculated Strouhal numbers were similar in both models. There was weak dependence between the Strouhal and Reynolds numbers in the range of Reynolds numbers tested. In the models, the range of Strouhal numbers was found to be between 0.2-0.35 for configurations A and B and between 0.05 - 0.2 for configuration F.

The values of the Strouhal number calculated from the plant findings were larger than those of the models, and no data was available to support the finding of the models with respect to the relationship between mixing in the uptake and the Strouhal number. Nevertheless, the significance of the observation was that flow instabilities as indicated by the puffing were present in both the plant and the models. It is worth noting that the plant Strouhal number was calculated based on the assumption of zero build-up on the uptake walls. That is, there was no reduction in cross-sectional area due to accretions. However, based on plant experience, this is not the case - in fact, accretions 30-90 cm in thickness are not uncommon. Although it was difficult to know the extent of the build-up at the time of these measurements, a simple example will illustrate the significance of build-up on the calculated Strouhal number. Assuming accretions of 60 cm, the calculated Strouhal number is reduced to between 0.55 and 0.7 which is closer to the values calculated from the modeling experiments. Other factors attributing to the difference between the modeling and plant observations could be a) the ingress of tramp air and b) the combustion instability of the flame due to fluctuations in oxygen purity.

5.2.3 Mixing Studies

The degree of mixing homogeneity in the uptake was determined in the models using a tracer technique originally proposed by Forney (1985). Most of the uptake mixing studies was carried out in the water model. Only select experiments were performed in the air model primarily to confirm the findings obtained in the water model. The modeling experiments focused on examining the mixing under configurations A, B and F, all of which were used in the plant (figure 5.2.1).

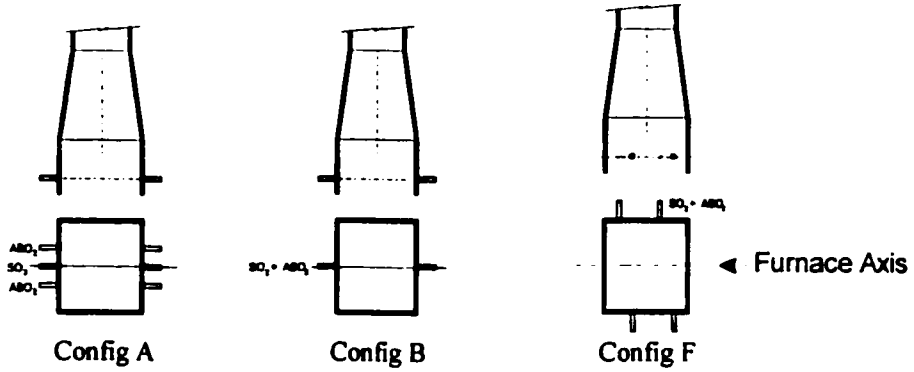

Figure 5.2.1 Uniformity of Mixing Experiments - Afterburner Configurations

Dimensional analysis by Forney (1985) suggested that the mixing conditions were related to the M_r, U_r, Re_j, Re_U, Fr_j and x/D_U (equation 4.2.5 in Chapter 4). A useful method of characterizing the uniformity of the mixture within the uptake was to calculate the second moment of the tracer concentration across the uptake (Uhl and Gray, 1966). The second moment measured the degree of lateral mixing at a given distance from the point of tracer injection. Details of the calculation of M are given in section 4.2.2.

$$M = f\left(M_r, U_r, Re_j, Re_U, Fr_j, \frac{x}{D_U}\right) \qquad (4.2.5)$$

The experiments carried out in the water model investigated the effect of dimensionless parameters, M_r, U_r, Re_j, Re_U, Fr_j and x/D_U. Each parameter, except for Fr_j, was varied within the range applicable to the operation of the plant uptake. In the plant, this range is limited by the

chemistry of the furnace off-gas, as it determines the afterburner oxygen requirements for the oxidation of combustible sulfur species and the recycle gas flow for controlling the operating temperature. Therefore, the range over which the parameters were varied in the water model was based on the upper and lower operating flows of afterburner oxygen and SO_2 recycle gas in the plant.

5.2.3.1 Salt Tracer Mixing Experiments in the Water Model

The degree of mixing homogeneity experiments performed provided a quantitative measure of the mixing in the uptake of the water. The experimental procedure involved an inert salt tracer, which was introduced through the afterburner jets. Then steady state local tracer concentrations were measured at various points in the uptake under different flow conditions. The flow conditions examined in the water modeling experiments are summarized in table 5.2.4.

Reproducibility of Experimental Results

The first step was to determine whether the experimental procedure used to measure the degree of mixing in the water model produced reproducible results. The reproducibility of the second moment, M, of the dimensionless local tracer concentrations measured on a given sampling plane in the uptake was examined for each afterburner configuration tested in the water model. The graphs presented in figure 5.2.2 show that the calculated second moments were repeatable. It is worth noting, however, that there was some variation in the local values of the dimensionless tracer concentration although the same general trend in tracer distribution was observed. The variations were attributed to the low frequency random pulsing of the flow patterns in the model.

Table 5.2.4 Uniformity of Mixing Experiments in Water Model - Test Conditions (Configurations A and B)

Test		1A	2A	3A	4A	5A	3B	4B	5B	6B	7B
Burner	Flow (L/min/jet)	31.5	60.0	87.0	87.0	87.0	87	87	87	60.0	31.5
	Reynolds # (x 10^3)	33.5	63.9	92.6	92.6	92.6	92.6	92.6	92.6	63.9	33.5
	Velocity (m/s)	1.68	3.2	4.6	4.6	4.6	4.6	4.6	4.6	3.2	1.68
Furnace	Flow (L/min)	126	240	348	348	348	348	348	348	240	126
	Reynolds # (x 10^3)	3.9	7.5	10.8	10.8	10.8	10.8	10.8	10.8	7.5	3.9
	Superficial Velocity (cm/s)	1.45	2.76	4.00	4.00	4.00	4.00	4.00	4.00	2.76	1.45
Uptake	Entrance Reynolds # (x 10^3)	9.9	18.9	27.4	27.4	27.4	27.4	27.4	27.4	18.9	9.9
	Superficial Entrance Velocity (cm/s)	4.68	8.92	12.93	12.93	12.93	12.93	12.93	12.93	8.92	4.68
Afterburner Jet											
	Flow (L/min/jet)	0.71	1.35	1.96	1.50	2.55					
	Velocity Ratio	31.9	31.9	31.9	24.4	41.5					
	Momentum Ratio	0.18	0.18	0.18	0.11	0.30					
	Reynolds # (x 10^3)	4.7	9.0	13.0	10.0	17.0					
	Modified Froude #	60	430	820	510	1380					
SO_2 Recycle Jet											
	Flow (L/min/jet)	3.3	6.3	9.1	9.1	9.1					
	Velocity Ratio	16.5	16.5	16.5	16.5	16.5					
	Momentum Ratio	0.43	0.43	0.43	0.43	0.43					
	Reynolds # (x 10^3)	7.4	14.0	20.3	20.3	20.3					
SO_2 Recycle + Oxygen Jet											
	Flow (L/min/jet)						14.00	9.25	18.00	9.70	5.10
	Velocity Ratio						25.3	16.7	32.6	25.4	25.5
	Momentum Ratio						1.02	0.44	1.68	1.03	1.03
	Reynolds # (x 10^3)						31.2	20.6	40.1	21.6	11.4
	Modified Froude #						1060	460	1710	490	140

Table 5.2.4 (cont) Uniformity of Mixing Experiments in Water Model - Test Conditions (Configuration F)

Test		1F	2F	3F	4F	5F	6F	7F	8F	9F	10F
Burner	Flow (L/min/jet)	87.0	87.0	87.0	87.0	87.0	87.0	87.0	87.0	87.0	87.0
	Reynolds # (x 10^3)	92.6	92.6	92.6	92.6	92.6	92.6	92.6	92.6	92.6	92.6
	Velocity (m/s)	4.6	4.6	4.6	4.6	4.6	4.6	4.6	4.6	4.6	4.6
Furnace	Flow (L/min)	348	348	348	348	348	348	348	348	348	348
	Reynolds # (x 10^3)	10.8	10.8	10.8	10.8	10.8	10.8	10.8	10.8	10.8	10.8
	Superficial Velocity (cm/s)	4.00	4.00	4.00	4.00	4.00	4.00	4.00	4.00	4.00	4.00
Uptake	Entrance Reynolds # (x 10^3)	27.4	27.4	27.4	27.4	27.4	27.4	27.4	27.4	27.4	27.4
	Superficial Entrance Velocity (cm/s)	12.93	12.93	12.93	12.93	12.93	12.93	12.93	12.93	12.93	12.93
SO_2 Recycle + Oxygen Jet											
	Flow (L/min/jet)	3.60	4.75	6.00	7.25	9.50	12.0	10.75	12.30	14.25	18.00
	jet diameter, ∅ (cm)	0.3175	0.3175	0.3175	0.6350	0.6350	0.6350	0.9525	0.9525	0.9525	0.9525
	Velocity Ratio	58.6	77.3	97.7	29.5	38.7	48.8	19.4	22.2	25.8	32.6
	Momentum Ratio	0.61	1.06	1.68	0.61	1.06	1.68	0.60	0.79	1.06	1.68
	Reynolds # (x 10^3)	24.1	31.7	40.1	24.2	31.7	40.1	24.0	27.4	31.7	40.1
	Modified Froude #	5380	9500	15100	1380	2400	3830	760	990	1330	2120

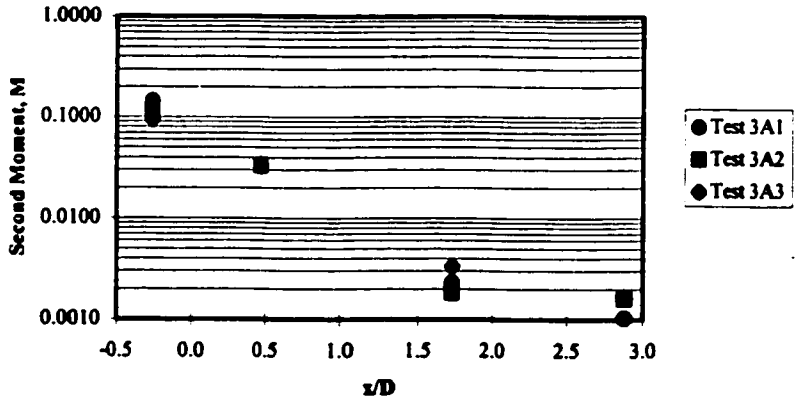

Configuration A

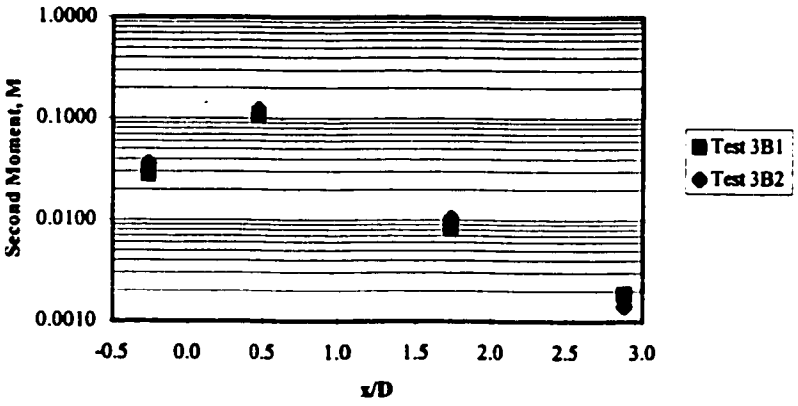

Configuration B

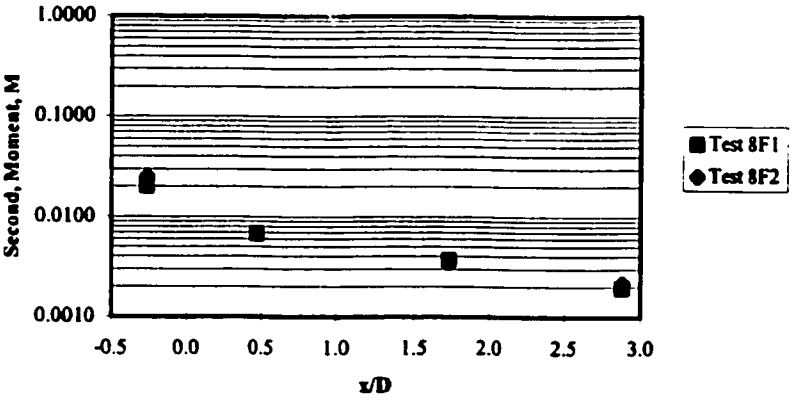

Configuration F

Figure 5.2.2 Reproducibility of Mixing Tests in Water Model

Effect of Buoyancy - Froude Number

In order to evaluate the effect of jet buoyancy, three experimental runs were conducted using configuration A. The objective of the experiments was to determine the minimum jet Froude number without introducing the effect of buoyancy. In the plant the jet buoyancy was not considered to be a factor in mixing as the computed value of the jet Froude number, defined in equation 5.2.1, was on the order of 10^4.

$$Fr_j = \frac{\rho_j u_j^2}{(\rho_j - \rho_{for\,gas}) g d_j} \qquad (5.2.1)$$

The experimental results suggested that jet buoyancy affected the mixing of the two streams in the water model and could not be ignored. It was noted that in the experiment with the less buoyant jets (Fr = 60), more tracer was measured below the afterburners. However, as seen in figure 5.2.3, the degree of mixing observed was similar when the jet Froude number was 100 or greater. This conclusion was in agreement with previous investigations of mixing in pipeline tees that predicted negligible effects of buoyancy for Froude numbers greater than 50 (O'Leary and Forney, 1985).

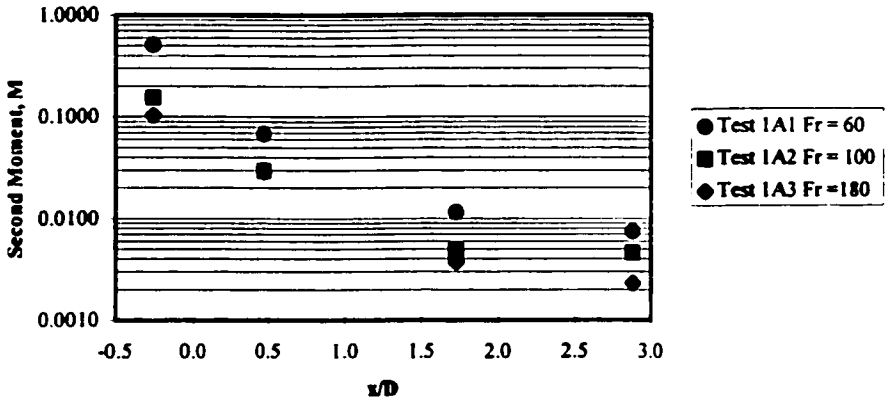

Figure 5.2.3 Effect of Froude Number on Jet Mixing in Water Model

Effect of Uptake Reynolds Number

The effect of uptake Reynolds numbers was investigated in the uptake of the water model operating with configurations A and B under constant jet momentum ratio. Figure 5.2.4 shows the results of the second moment analysis as applied at 0.471 and 1.728 diameters downstream from the point of injection. In the range of Reynolds numbers investigated, the degree of mixing uniformity was virtually insensitive to this parameter.

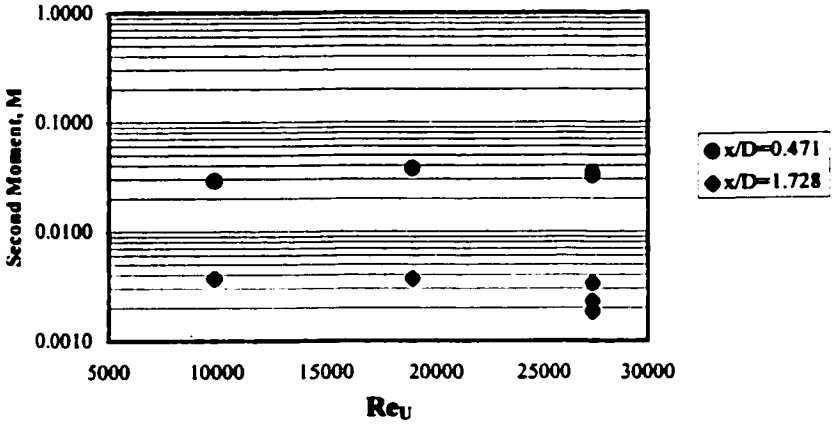

Configuration A

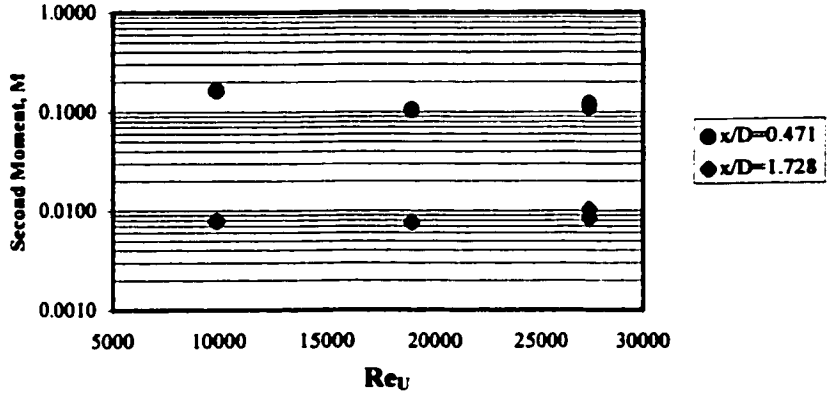

Configuration B

Figure 5.2.4 Effect of Reynolds Number on Mixing in Water Model

Effect of Jet Momentum/Velocity Ratio

Having established the effects of Reynolds number, the impact of jet momentum on the degree of mixing was evaluated in the model operating with configurations A, B and F at constant Reynolds number (27400). In configurations A and B with jet-jet impingement, the jet momentum had little effect on the mixing. The calculated jet momentum penetration, defined as the distance before the jet deflected over in the cross flow (equation 5.2.2), indicated that the jet-jet impingement occurred in the range of momentum ratios tested (Forney, 1989). In the model, the jet penetration was observed visually using the acid-base reaction technique in the water model. However, it should be noted that the jet penetration was not constant due to the pulsating behaviour of the bulk flow and the non-uniform velocity distribution in the uptake. Table 5.2.5 summarizes the calculated and observed jet momentum penetration distance. In configurations A and B, the calculated jet momentum penetration suggests that the jet plumes collided in the center of the uptake. Visual observation confirmed this behaviour although due to the unsteady flow the jet path oscillated back and forth.

$$\ell_m = d_j \frac{u_j}{u_o} \; ; \text{ where } u_o = \text{superficial uptake entrance velocity} \qquad (5.2.2)$$

In configuration F, the calculated jet penetration was always greater than the observed penetration, suggesting that the jet plume bent over in the cross flow within a short distance. This was attributed to the non- uniform velocity distribution in which there was a region of low velocity along the east wall (opposite the discharge) and a high velocity region along the west wall. The jet penetration was not constant but instead wavered back and forth across the uptake. In addition, the data indicated that jet impaction on the opposing wall occurred when the jet momentum ratio was greater than 1.0. In the plant, jet impaction was not desirable. Near the wall, the release of heat resulting from the reaction between the oxygen and the sulfide species in the furnace off-gas would prematurely cause the failure of the refractory lining in the uptake.

Table 5.2.5 Calculated and Observed Jet Momentum Penetration Distance

Configuration	Test	Jet Momentum Ratio	Jet Velocity Ratio	Jet Diameter (cm)	Jet Momentum Penetration Distance Calculated (cm)	Observed (cm)
A	4A	0.11	24.4	0.32	7.8	3-10
	3A	0.18	31.9	0.32	10.2	5-12
B	4B	0.44	16.7	0.95	15.9	6-13
	3B	1.02	25.3	0.95	24.1	8-16
F	1F	0.61	58.6	0.32	18.6	7-15
	4F	0.61	29.5	0.64	18.7	8-16
	5F	1.06	38.7	0.64	24.6	16-22
	7F	0.60	19.4	0.95	18.5	8-15
	8F	0.79	22.2	0.95	21.1	12-18
	9F	1.06	25.8	0.95	24.6	15-22
	10F	1.68	32.6	0.95	31.1	17-22

Note: Lower Section of Uptake L x W = 22.2 cm x 20.2 cm

The effect of jet momentum on the mixing in the uptake is shown in the graphs included in figure 5.2.5. The second moment of the dimensionless tracer concentration was measured at 0.471 and 1.728 diameters downstream from the point of injection. The experimental data indicate that the effects of jet momentum were very weak over the range of experimental conditions and can be neglected without introducing significant error. The relationship between jet momentum and mixing was moderate in the uptake with configuration B. In this configuration, the second moment of the dimensionless tracer concentration decreased steadily as the jet momentum was increased. The data suggests that the momentum with which the jet collided affected the degree of mixing in the uptake. In configurations A and F, no apparent trend in the second moment was seen.

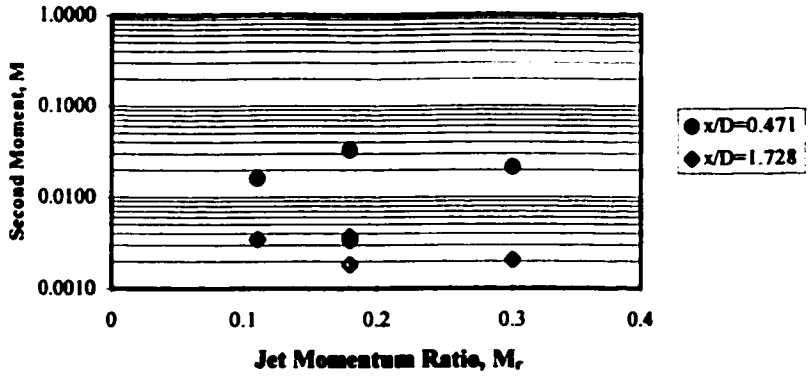

Configuration A

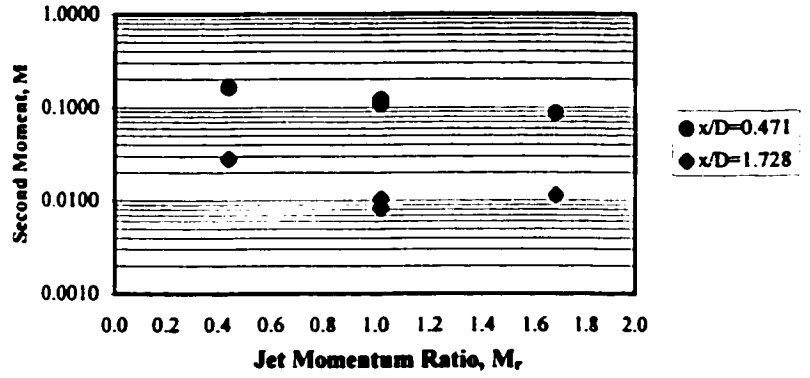

Configuration B

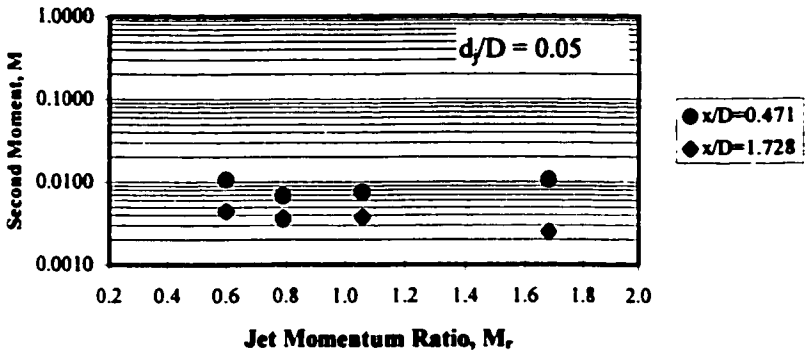

Configuration F

Figure 5.2.5 Effect of Jet Momentum Ratio on Mixing in Water Model

Jet-to-Uptake Diameter Ratio

The significance of jet-to-uptake diameter ratio was investigated for configuration F at a constant Reynolds number and jet momentum ratio. The jet-to-uptake diameter ratios examined ranged from 0.017 to 0.05. Table 5.2.6 summarizes the effect of this parameter on the mixing in the uptake. The second moment analysis was applied at 0.471 and 1.728 uptake diameters downstream from the point of tracer injection. The data showed a very weak relationship between jet-to-uptake diameter ratio and the degree of mixing in the uptake in the range examined.

Table 5.2.6 Effect of Jet-to-Uptake Diameter Ratio on Mixing in the Water Model

Test	Jet Momentum Ratio	Jet Diameter (cm)	Jet-to-Uptake Diameter Ratio	Jet Velocity Ratio	Second Moment x/D = 0.471	Second Moment x/D = 1.728
1F	0.61	0.318	0.017	58.6	0.0156	0.0044
4F	0.61	0.635	0.033	29.5	0.0139	0.0080
7F	0.60	0.953	0.050	19.4	0.0108	0.0045
2F	1.06	0.318	0.017	77.3	0.0127	0.0058
5F	1.06	0.635	0.033	38.7	0.0116	0.0047
9F	1.06	0.953	0.050	25.8	0.0075	0.0038
3F	1.68	0.318	0.017	97.7	0.0104	0.0059
6F	1.68	0.635	0.033	48.8	0.0130	0.0040
10F	1.68	0.953	0.050	32.6	0.0098	0.0019

Note: Uptake hydraulic diameter, D = 19.1 cm

Afterburner Jet Configuration

The rapid mixing of two fluids of the same phase is precursor to carrying out fluid phase reactions. In the preceding analysis, it became apparent that the configuration of the afterburner jets in the uptake cross flow was the most important parameter for rapid mixing. In general, increasing the rate of entrainment of the bulk flow into the jets decreases the mixing time and thus

improves the extent of reaction.

The afterburner jet configuration F yielded the most rapid mixing of the salt tracer in the water model, confirming the visual observations made using the acid-base reaction technique. Configuration B produced the least rapid mixing in the uptake. This observation suggested that staggering opposite pairs of jets was the most effective means of achieving rapid mixing. The stitched afterburner jet arrangement in configuration F with jets flowing at 90° to the furnace axis allowed for maximum coverage of the uptake cross-section and thus, maximum entrainment of the bulk flow. Figure 5.2.6 compares the degree of mixing, as defined by the second moment of the dimensionless tracer concentration, measured in configurations A, B and F.

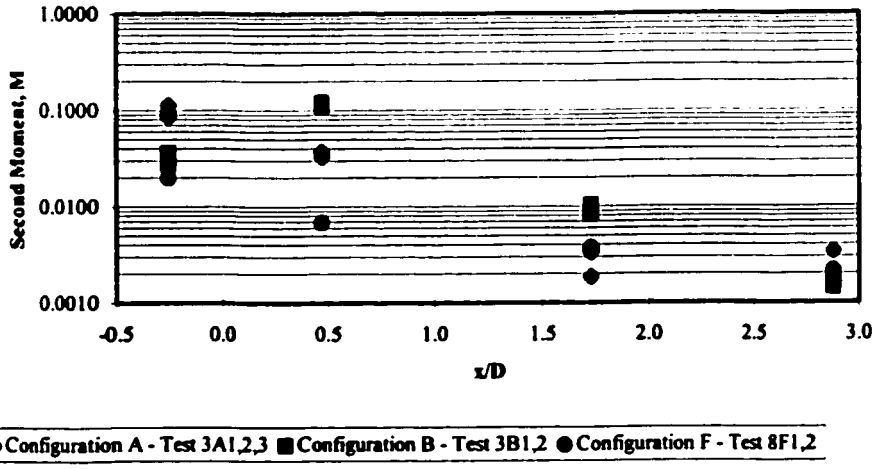

Figure 5.2.6 Effect of Afterburner Configuration on Mixing in the Water Model

Uptake Entrance Re = 27400; Uptake Entrance Superficial Velocity = 12.9 cm/s

It was evident that the degree of mixing homogeneity increased as the flow progressed towards the discharge of the model regardless of afterburner configurations. In all cases, the degree of mixing homogeneity was similar by the time the fluid reached the discharge. The progressive distribution of the tracer downstream of the afterburners approximately obeyed a first order decay.

5.2.3.2 Thermal Mixing in the Air Model

The experimental methodology used for the thermal mixing experiments simulated the uniformity of mixing experiments carried out in the water model with potassium chloride. In the air model, heated air was introduced through the afterburner jets and the steady state temperature rise was measured at various points in the uptake. These experiments were primarily focused on obtaining additional data for configuration F. Table 5.2.7 summarizes the flow conditions tested in the air model.

Table 5.2.7 Uniformity of Mixing Experiments in Air Model - Test Conditions

Test		M1	M2	M3	M4	M5	M6
Afterburner Configuration		F	F	F	F	A	B
Burner	Reynolds # (x 10^3)	133.5	137.4	144.5	196.4	141.0	137.7
	Velocity (m/s)	21.4	22.0	23.1	31.4	21.7	21.2
Furnace	Reynolds # (x 10^3)	20.2	20.8	21.9	29.7	20.6	20.1
	Superficial Velocity (cm/s)	30.5	31.4	33.0	44.8	31.0	30.3
Uptake	Entrance Reynolds # (x 10^3)	48.5	49.9	52.5	71.3	49.4	48.2
	Superficial Entrance Velocity (cm/s)	89.8	92.5	97.2	132.1	91.4	89.3
Afterburner O_2 Jet	Ø (cm)					1.59	
	Reynolds # (x 10^3)					24.5	
	Velocity Ratio					30.4	
	Momentum Ratio					0.25	
	Modified Froude # (x 10^3)					34.2	
SO_2 Recycle Jet	Ø (cm)					6.27	
	Reynolds # (x 10^3)					26.5	
	Velocity Ratio					9.1	
	Momentum Ratio					0.37	
SO_2 Recycle+O_2 Jet	Ø (cm)	3.81	3.81	3.81	3.81		6.27
	Reynolds # (x 10^3)	45.7	43.3	57.7	59.9		44.5
	Velocity Ratio	26.4	24.4	31.1	23.8		15.7
	Momentum Ratio	0.97	0.83	1.34	0.78		0.94
	Modified Froude # (x 10^3)	10.3	9.5	16.8	18.1		2.2

The results obtained from air model mixing experiments were in good agreement with those made in the water model, suggesting that model scale nor the fluid type were factors in the mixing of fluids in the uptake. A comparison of the results obtained in the models is given in table 5.2.8.

Table 5.2.8 Uniformity of Mixing Experiments - Comparison of Air vs Water Model

Configuration		A		B		F	
Test		3A1	M5	3B1	M6	8F1	M2
Model Type		Water	Air	Water	Air	Water	Air
Uptake	Entrance Reynolds # (x 10^3)	27.4	49.4	27.4	48.2	27.4	49.9
	Superficial Entrance Velocity (cm/s)	12.93	91.4	12.93	89.3	12.93	92.5
Afterburner O_2	Reynolds # (x 10^3)	13.0	24.5				
Jet	Velocity Ratio	31.9	30.4				
	Momentum Ratio	0.18	0.25				
	Modified Froude # (x 10^3)	0.8	34.2				
SO_2 Recycle	Reynolds # (x 10^3)	20.3	26.5				
Jet	Velocity Ratio	16.5	9.1				
	Momentum Ratio	0.43	0.37				
SO_2 Recycle+O_2	Ø (cm)			0.95	6.27	0.9525	3.81
Jet	Reynolds # (x 10^3)			31.2	44.5	2.9	43.3
	Velocity Ratio			25.3	15.7	22.2	24.4
	Momentum Ratio			1.02	0.94	0.79	0.83
	Modified Froude # (x 10^3)			1.1	2.2	1.0	9.5
Degree of Mixing, Second Moment							
	x/D = 0.47	0.0323	0.0199	0.1099	0.1195	0.0068	0.0126
	x/D = 1.80			0.0083	0.0016	0.0037	0.0030

Table 5.2.9 summarizes the effects of Reynolds number, jet momentum ratio and afterburner configuration on the degree of mixing in the air model. It is apparent that the most significant factor affecting the mixing was the afterburner configuration, although the amount of data was limited.

Table 5.2.9 Unifomity of Mixing in Air Model - Experimental Results

Effect of Reynolds Number (Configuration F)

Test	M2	M4
Uptake Reynolds Number ($x10^3$)	49.9	71.3
Degree of Mixing, Second Moment		
x/D = 0.475	0.0126	0.0115
x/D = 1.800	0.0030	0.0008

Effect of Jet Momentum Ratio (Configuration F)

Test	M1	M2	M3
Jet Momentum Ratio	0.97	0.83	1.34
Degree of Mixing, Second Moment			
x/D = 0.475	0.0126	0.0126	0.0131
x/D = 1.800	0.0009	0.0030	0.0006

Effect of Afterburner Configuration

Test	M5	M6	M2
Afterburner Configuration	A	B	F
Degree of Mixing, Second Moment			
x/D = 0.475	0.0199	0.1195	0.0126
x/D = 1.800		0.0016	0.0030

5.2.3.3 Afterburner Jet Flow Distribution

Typical tracer distributions in the water model are illustrated in figure 5.2.7 for the three afterburner configurations. Similar trends were observed in both the water and air models. Analysis of the data indicated two key flow characteristics regarding the distribution of tracer in the uptake:

- There was a strong downward draw of tracer along the east wall of the uptake (wall opposite the discharge. The amount of tracer drawn downward was greatest in configuration A and least with configuration F (section.5.2.3.4).
- The tracer distribution varied in concentration across the width of the uptake from east to west. The tracer concentration was greatest along the east side where the bulk flow

velocities were lowest, i.e. less dilution of the afterburner jet flow. This behaviour was most significant in configuration A. In these experiments, the jet-jet impingement seen with configuration A produced a plume, which typically climbed along the east wall of uptake (opposite the discharge) with little dispersion.

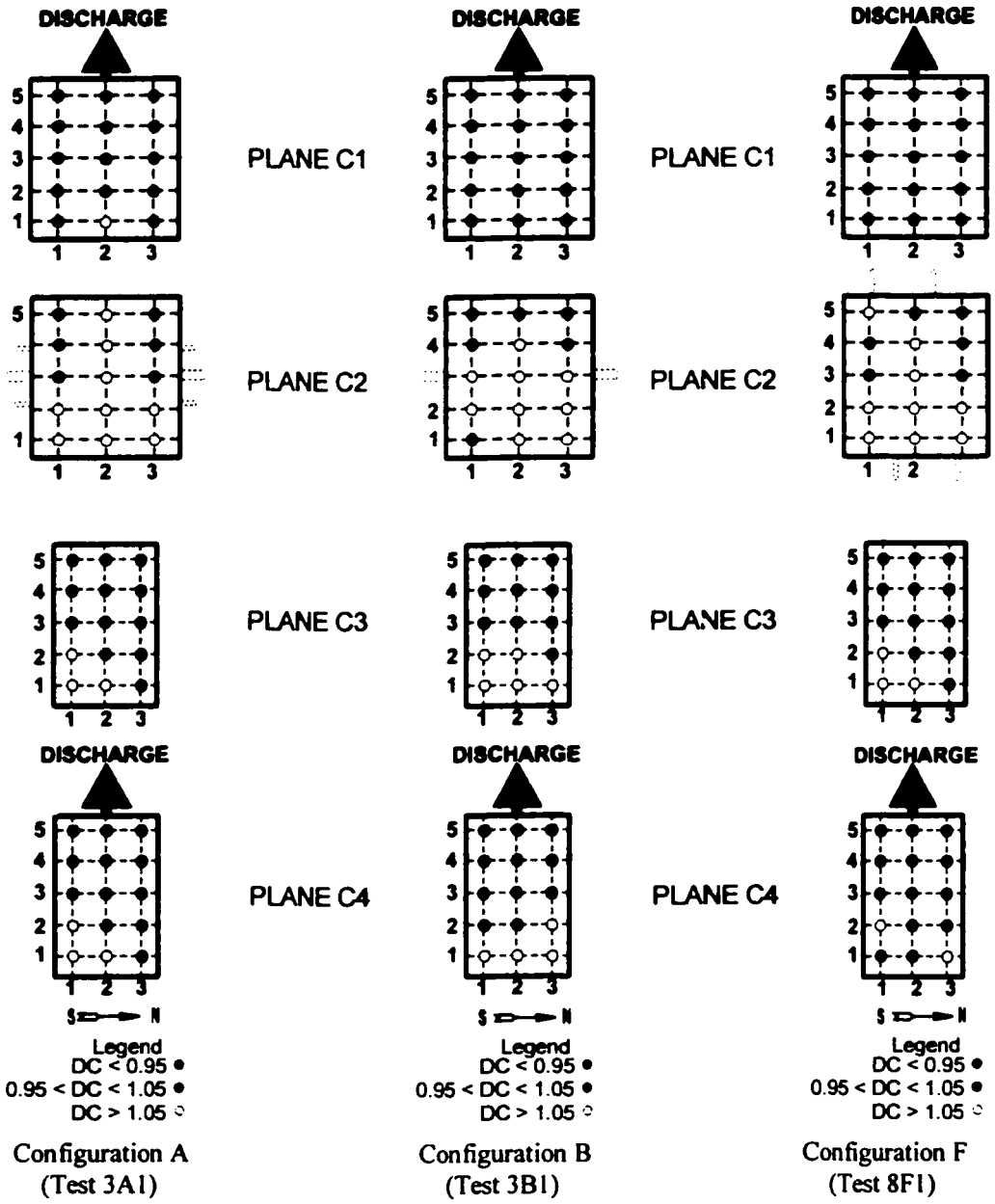

Figure 5.2.7 Typical Salt Tracer Distribution in the Water Model

5.2.3.4 Effect of Flow Instability at Furnace-Uptake Transition

In section 5.2.2, the significance of flow instability at the transition between the furnace and the uptake was discussed. Using the acid-base reaction technique, the flow instability in the water model was seen to produce a downward flow of afterburner jet fluid primarily along the east wall of the uptake. Visually it was noted that the afterburner jet configuration F was least affected by the pulsating nature of the flow.

A simplistic approach was proposed in section 4.2.2.3 to quantify the effect of the pulsating flow on the amount of tracer back mixing. A 1-dimensional transport model in the axial direction was developed to estimate axial dispersion coefficient, E, which indirectly is a measure of back mixing observed in the models. In this analysis, the tracer concentration profile was assumed to be laterally uniform upstream and downstream of the afterburner jets, and the velocity at the entrance of the uptake was assumed to be uniform. From the physical models, it is known that these assumptions were an oversimplification of the problem because the velocity and concentration profiles were observed to be non-uniform. (section 5.1.3.1 and 5.2.3.3).

The average values of E were obtained by fitting data obtained in the models for configurations A, B and F to equation 4.2.6. The axial dispersion numbers were calculated using equation 4.1.3 and were compared with the values obtained for a model developed by Levenspiel (1972), describing the dispersion of fluids flow in pipes. Table 5.2.10 gives the values of the axial dispersion coefficient and the axial dispersion number for each afterburner configuration. Although configuration F had the smallest value, the axial dispersion coefficients in the water model were of the same order of magnitude suggesting that the afterburner configuration had little effect on the bulk flow patterns in the uptake. The larger value calculated for configuration F in the air model was due to larger scale.

The values for the axial dispersion numbers, obtained from the experimental data were in good agreement with those of the Levenspiel model. The small values of the dispersion numbers suggested that the uptake flow was approaching plug flow behaviour. Therefore, in order to realize rapid mixing conditions, the afterburner configuration must uniformly spread the tracer across the injection plane.

Table 5.2.10 Measured Back Mixing of Tracer at Steady State in Models

	Configuration	Axial Dispersion Coefficient (cm2/s)	Superficial Uptake Entrance Velocity (cm/s)	Reynolds Number	Axial Dispersion Number	
					Experimental	Levenspiel Model
Water Model	A	87	12.9	27400	0.09	0.07
	B	55	12.9	27400	0.06	0.07
	F	47	12.9	27400	0.05	0.07
Air Model	F	2061	93.2	50300	0.07	0.07

5.2.4 Summary of Mixing in the Uptake

The mixing between the afterburner jet and bulk flows in the uptake was examined in both the water and air models. A summary of the experimental findings is given below.

- The water and air models produced similar results with respect to the mixing of two fluids of the same phase in the uptake.

- The afterburner jet configurations A, B, and C, involving jet-jet impingement were poorly mixed as evidenced by the predominantly incomplete discolouration of the base. Jets positioned farther up in the uptake (configuration D) did not allow sufficient time for the jet fluid to thoroughly mix with the main flow. Configuration F with the staggered opposite pairs of jets flowing at 90° to the axis of the furnace produced the best mixing conditions with the region above the afterburner jets remaining "yellow" most of the time. The stitched afterburner jet arrangement in configuration F allowed for maximum coverage of the uptake cross-section while keeping the opposing jets close enough that they still interact.

- The degree of mixing homogeneity in the uptake for configurations A, B and F was

determined in the models using a tracer technique originally proposed by Forney (1985). The experiments investigated the effect of Reynolds number, jet momentum and axial distance. In the range applicable to the plant operation, the effect of Reynolds number and jet momentum on the mixing was very weak. The most significant factor affecting the mixing was the afterburner configuration. The ranking of configurations starting with the "best mixing" results was:

$$F >> A > B$$

- There were two key flow characterisics regarding the distribution of tracer in the uptake:

    a) There was a strong downward draw of tracer along the east wall of the uptake (wall opposite the discharge). The amount of tracer drawn downward was greatest in configuration A and least with configuration F.
    b) The tracer distribution varied in concentration across the width of the uptake from east to west. The tracer concentration was greatest along the east side where the bulk flow velocities were lowest.

- The flow instability occurring at the transition between the furnace space and the uptake produced a pulsating-type flow pattern, which was attributed to the eddy flow generated by the sharp change in flow direction. Intermittent downward puffing of the afterburner flow into the furnace was most predominant in configurations A, B, C and E. In configurations A, B, C and E, the base solution was drawn down mainly along the east wall of the uptake (opposite the discharge). The instability at the entrance of the uptake was related to the eddy shedding. The Strouhal number related the frequency of the instability to the flow conditions. Over the range of flow conditions tested in the models, the Strouhal number remained approximately the same ranging between 0.2-0.35 for configurations A and B and between 0.05 - 0.2 for configuration F.

Chapter 6

NUMERICAL MODELING

As stated previously in Chapter 3, the objectives of the mathematical model, which has been developed for this study, were:

- to simulate, within a reasonable degree of error, the experimental data generated by the 1:5 linear scale air models of the furnace and uptake.

- to analyze the parameters that affected the flow patterns observed in the physical models.

- to evaluate the merits of numerical modeling as a design tool for recommending plant improvements.

In order to realize these objectives, the computational fluid dynamics code FLUENT v 4.5 was used to simulate the flow through the air model (FLUENT, 1996). FLUENT is a general purpose computer code for modeling fluid flow, heat transfer and chemical reaction.

6.1 FLUENT Model

The FLUENT v4.5 code was used to solve the Navier-Stokes equations for the conservation of mass, momentum and turbulent quantities in 3-dimensional body fitted coordinates (BFC). In

FLUENT, the governing partial differential transport equations are solved using a finite difference procedure which involves dividing the calculation domain into a finite number of control volumes. The partial differential equations are discretized over the control volume to obtain a set of simultaneous algebraic equations that are solved iteratively.

6.1.1 Governing Equations

The numerical simulation of the flow in the air model of the furnace was based on the solution of the steady-state, turbulent, time-average, Navier-Stokes partial differential equations. The conservation equations for turbulent flow are based on a time averaging procedure, such that the velocity at a point is considered as the sum of the mean ($\bar{u}_i$) and fluctuating (u_i') components. The turbulent fluctuations are assumed to be random so that the time averaged value of the fluctuations is zero (Tennekese and Lumley, 1992).

Conservation of Mass:

$$\frac{\partial}{\partial x_i}(\rho \bar{u}_i) = 0 \qquad (6.1.1)$$

Conservation of Momentum:

$$\frac{\partial}{\partial x_j}(\rho \bar{u}_i \bar{u}_j) = \frac{\partial}{\partial x_j}\left(\mu\left[\frac{\partial \bar{u}_i}{\partial x_j}+\frac{\partial \bar{u}_j}{\partial x_i}\right]-\left(\frac{2}{3}\mu\frac{\partial \bar{u}_l}{\partial x_l}\right)\delta_{ij}\right)-\frac{\partial \bar{P}}{\partial x_i}+\frac{\partial}{\partial x_j}(\rho\overline{u_i' u_j'}) \qquad (6.1.2)$$

Note that because the flow simulation was carried out for isothermal, single phase conditions, the gravitational acceleration and external body force terms have been neglected in the momentum equation . The "Reynolds stresses", $\rho\overline{u_i' u_j'}$, must be modeled to close equations 6.1.1 and 6.1.2.

6.1.2 Turbulence Model

The main task of the turbulence model is to provide expressions that allow the evaluation of the "Reynolds stresses" in terms of mean flow quantities. The turbulence closure model used in the analysis of the air model flow patterns was the $k-\varepsilon$ model (Launder and Spalding, 1974). The $k-\varepsilon$ model is an eddy-viscosity model in which the Reynolds stresses are assumed to be proportional to the mean velocity gradients via the Boussinesq hypothesis (6.1.3). In this relationship, the constant of proportionality is the turbulent viscosity, μ_t. In essence, the form of the Reynolds average momentum equations remains identical to the form of the laminar momentum equations except that μ is replaced by an effective viscosity, μ_{eff} (6.1.4)

$$\rho\overline{u_i'u_j'} = \mu_t\left(\frac{\partial u_i}{\partial x_j}+\frac{\partial u_j}{\partial x_i}+\frac{2}{3}\frac{\partial u_i}{\partial x_i}\partial_{ij}\right)-\frac{2}{3}\rho k\partial_{ij} \qquad (6.1.3)$$

$$\mu_{eff} = \mu+\mu_t \qquad (6.1.4)$$

The turbulent viscosity, μ_t, is obtained by assuming that it is proportional to the product of a turbulent velocity scale and length. In the $k-\varepsilon$ model, these velocity and length scales are obtained from the parameter k, the turbulent kinetic energy and ε, the dissipation rate of turbulence. The velocity scale is taken to be $\sqrt{k}$ and the length scale is given by $\sqrt{k^3}/\varepsilon$. The turbulent viscosity is therefore given by:

$$\mu_t = \rho C_\mu\frac{k^2}{\varepsilon}; \text{ where } C_\mu \text{ is an empirically derived constant } = 0.09 \qquad (6.1.5)$$

The values of k and ε required in equation 6.1.5 are obtained from the solution of the conservation equations for the turbulent kinetic energy and the dissipation rate of turbulence.

Conservation of Turbulent Kinetic Energy:

$$\frac{\partial}{\partial x_i}(\rho \bar{u}_i k) = \frac{\partial}{\partial x_i}\left(\frac{\mu_t}{\sigma_k}\frac{\partial k}{\partial x_i}\right) - \mu_t\left(\frac{\partial \bar{u}_j}{\partial x_i}+\frac{\partial \bar{u}_i}{\partial x_j}\right)\frac{\partial \bar{u}_i}{\partial x_i} - \rho\varepsilon \qquad (6.1.6)$$

Conservation of Dissipation Rate of Turbulence:

$$\frac{\partial}{\partial x_i}(\rho \bar{u}_i \varepsilon) = \frac{\partial}{\partial x_i}\left(\frac{\mu_t}{\sigma_\varepsilon}\frac{\partial \varepsilon}{\partial x_i}\right) + C_{1\varepsilon}\frac{\varepsilon}{k}\mu_t\left(\frac{\partial \bar{u}_j}{\partial x_i}+\frac{\partial \bar{u}_i}{\partial x_j}\right)\frac{\partial \bar{u}_i}{\partial x_i} - C_{2\varepsilon}\rho\frac{\varepsilon^2}{k} \qquad (6.1.7)$$

Note that the generation of turbulence due to buoyancy has been neglected. The coefficients σ_k and σ_ε are the "Prandtl" numbers governing the turbulent diffusion of k and ε. The coefficients $C_{1\varepsilon}, C_{2\varepsilon}, \sigma_k$ and σ_ε are empirically derived constants with values (Launder and Spalding, 1974):

$$C_{1\varepsilon} = 1.44, \quad C_{2\varepsilon} = 1.92, \quad \sigma_k = 1.0, \quad \sigma_\varepsilon = 1.3$$

The $k-\varepsilon$ model has two important shortcomings:

- the K-ε model is a semi-empirical model which requires several universal constants and it assumes isotropic turbulence through the turbulent viscosity, μ_t. Some investigators have found that the universal constants in the k-ε model are in fact variable (Moon and Rudinger, 1977; Tennankore and Steward, 1978). Isotropic turbulence implies that the velocity and length scales are the same in all directions. In flows with recirculation, the velocity and length scales can vary with direction.

- high generation of turbulent energy is simulated around impingement points and regions of high strain. This excess turbulent energy creates high levels of turbulent viscosity which tends to over-simulate mixing and under-simulate separation resulting from vortex shedding.

Despite these shortcomings, the $k-\varepsilon$ model has been widely used and validated and has the desirable properties of robustness and economy in terms of computing requirements (FLUENT, 1996).

6.1.3 Computational Domain

The FLUENT model was setup to take advantage of symmetry about the center of the air model. In cold model experiments, the flow for opposite end was observed to possess approximately mirror symmetry. The computational domain used in the numerical simulation is illustrated in figure 6.1.1 based on the geometrical features of the air model.

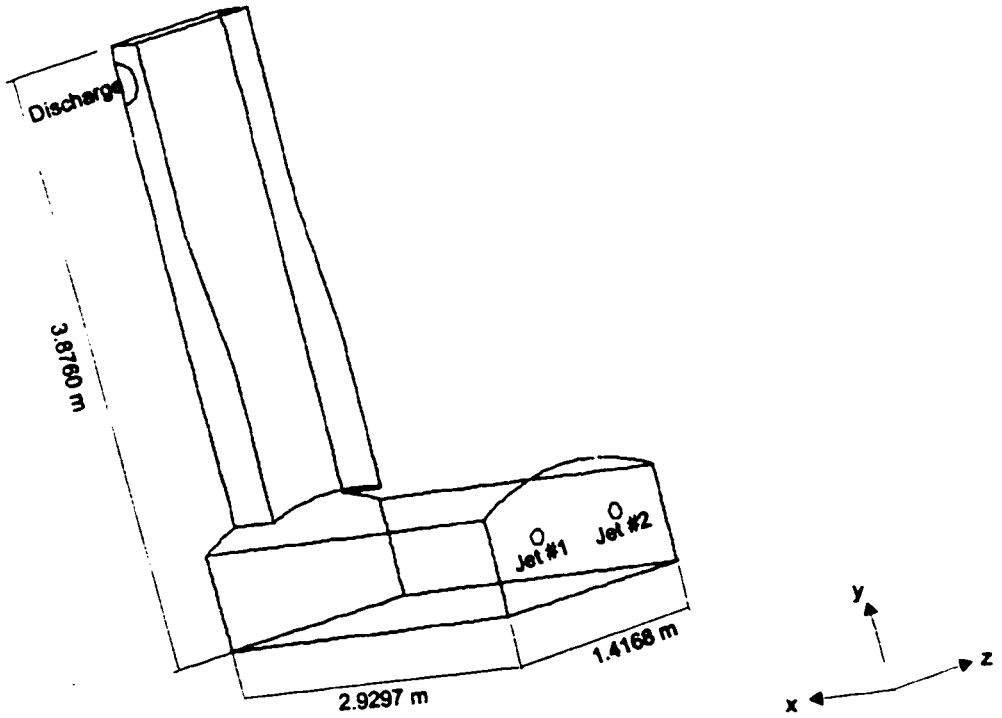

Figure 6.1.1 Outline of Computation Domain Used in FLUENT Model

The computational domain was defined by a curvilinear body-fitted coordinate system (BFC) in which the grid lines are determined by a coordinate system that conforms to the geometric boundary of the model. In generating a body-fitted grid, the geometric boundaries of the model were first defined in terms of points in Cartesian coordinates, curves and surfaces. The

computational grid was then generated by interpolating the grid points which were specified on the geometric boundaries.

The grid is a discrete representation of the continuous field phenomena that is being modeled. The grid size used in the numerical model was 50 x 60 x 34. A non-uniform grid distribution was employed. In this way, the grid spacing was reduced in regions where high gradients were expected, such as in the near jet region, at the transition between the furnace and the uptake and at the discharge, and increased in regions were the flow was relatively uniform. Figure 6.1.2 illustrates the grid spacing at the geometric boundaries.

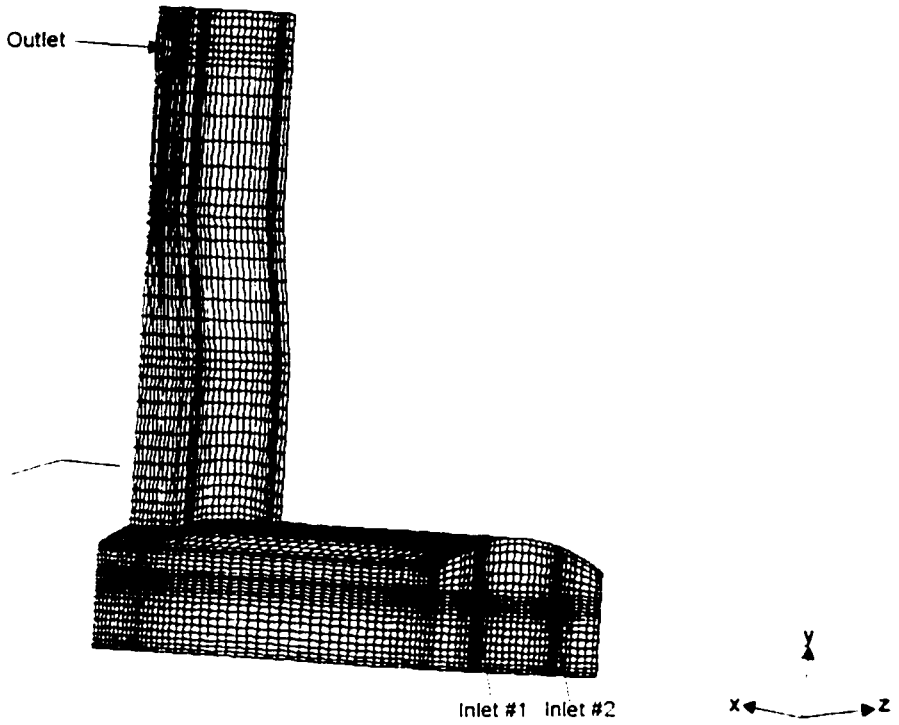

Figure 6.1.2 Computational Grid Spacing at the Geometric Boundaries (50x60x34)

Grid spacing was adjusted by defining a weighting factor to control the grid density at each end of a segment. In the setup of the computational grid, consideration was given to the cell aspect ratio and grid skewness. Excessive cell aspect ratios and grid skewness can lead to stability problems and convergence difficulties.

6.1.4 Boundary Conditions

The elliptical form of the conservation equations required that values of the dependent variables or their gradients be specified at the inlet and at each boundary of the computational domain. The inlet boundary conditions were specified separately for each jet assuming a uniform velocity profile. At the jet inlet, velocity magnitudes were given for each Cartesian coordinate direction. The magnitude of the velocity was positive when its vector pointed along the positive coordinate direction. Table 6.1.1 gives the inlet boundary conditions used in the model assuming jet velocities of 20 m/s and jet angles of 12° in and 12° down.

Table 6.1.1 FLUENT Modeling - Inlet Boundary Conditions

Inlet 1	v_x (m/s)	19.14
	v_y (m/s)	-4.16
	v_z (m/s)	4.08
	Turbulence Intensity, I (%)	10
	Characteristic Length, L (m)	0.098
Inlet 2	v_x (m/s)	19.14
	v_y (m/s)	-4.16
	v_z (m/s)	-4.08
	Turbulence Intensity, I (%)	10
	Characteristic Length, L (m)	0.098

To calculate the turbulent characteristics at the inlet boundaries, values of the turbulence intensity and the characteristic length were specified. These parameters are used by the code to derive inlet values for the turbulent kinetic energy, k, and for the dissipation rate of turbulence, ε. The values of k and ε were assumed to be uniform across each inlet zone. The turbulence intensity is defined as the ratio of the root mean square turbulent velocity fluctuations to the mean flow velocity $\left(u'/u_{avg}\right)$. The inlet value of k is calculated by FLUENT from the turbulence intensity, I, as follows for isotropic turbulence:

$$k = \frac{3}{2}\left(u_{avg} I\right)^2 \qquad (6.1.8)$$

In internal flows, the turbulence intensity at the inlet is dependent on the upstream history of the flow. The upstream flow leading to the jets involved flow turning around four elbows over a distance of less than 1.5 m. In fully developed pipe flow, the turbulence intensity at the core was estimated from an empirical correlation to be 3-4% (Hinze, 1975). Because the flow was not fully developed, a sensitivity analysis was carried out at turbulence intensity values of 10% and 50%. The value of 50% was derived from measured velocity data in the duct supplying the jets. Unfortunately, this data was recorded at 2 seconds intervals which was not representative of the turbulent time scale. Nevertheless, the data served to demonstrate that, macroscopically, the flow through the jets was unsteady.

The dissipation rate of turbulence is calculated based on the turbulence length scale, ℓ. This parameter is related to the size of the largest eddy that contains energy in turbulent flow. The inlet value of ε was determined from the relationship:

$$\varepsilon = C_\mu^{\frac{3}{4}} \frac{k^{\frac{3}{2}}}{\ell}; \quad \text{where } \ell = 0.07\,\mathrm{L} \qquad (6.1.9)$$

$$\mathrm{L} = \text{characteristic length}$$

This relationship for ℓ is based on fully developed duct flow wherein the value of ℓ is restricted by the duct size. Its value, 0.07 L, is based on the maximum value of the mixing length in fully developed turbulent flow and a characteristic length, L, equal to the jet diameter (Rodi, 1984).

At the wall boundaries, the no-slip condition was imposed on all velocity components. The shear stress on the fluid at the wall is simulated from the properties of the flow adjacent to the wall/fluid boundary. The standard wall functions were used to estimate the turbulent flows in the regions close to the walls (Launder and Spalding, 1974).

The flow in the air model was taken to be symmetric about the center of the model with the plane

of symmetry perpendicular to the longitudinal axis of the furnace (figure 6.1.2). At this plane, a zero flux of all transport quantities was assumed; i.e. there are no convective and diffusion fluxes across the boundary (zero normal velocity components and zero normal gradients of the flow variables at the symmetry plane).

The outlet boundary was modeled with a zero diffusion flux condition in the direction normal to the exit plane for all flow variables except pressure. In FLUENT, this means that the conditions at the outlet plane are extrapolated from within the computation domain and have no impact on the upstream flow. The zero diffusion flux condition is approached in fully developed flows in which the flow velocity profile remains unchanged in the flow direction. At this boundary, the convective effects are expected to dominate.

The physical properties of air were taken at room temperature of 20°C. The density and viscosity of air used in the calculations were 1.18 kg/m^3 and 1.8×10^{-5} Pa s, respectively.

6.1.5 Solution Convergence

FLUENT solves the governing partial differential equations by a finite difference scheme whereby the governing equations are discretized over the computation cells into which the domain is divided. A calculation is converged when all the governing equations are balanced at each point in the solution domain. In FLUENT, the progress of the solution towards convergence was evaluated via residual values. The residual for each flow variable provides a measure of the magnitude of the error in the solution after each iteration. The solution was considered converged when the sum of normalized residuals for each flow variable is on the order of 10^{-4}. As the solution approached this level, spot checks were made for convergence by examining the calculated flow field. If the solution remained essentially unchanged, it was considered to be converged.

The large number of computational cells and the complex flow physics containing several flow direction changes hindered the convergence of the solution. The solution convergence was very

dependent on the conversion rate of the pressure equation. The SIMPLE (Semi-Implicit Method for Pressure Linked Equations) algorithm which relates the velocity and pressure fields was used in the computational model (Patankar, 1980). Because the equations are coupled and non-linear, an iterative solution procedure is used which employed the Line Gauss-Seidel (LGS) "line-by-line" solver. In the LGS method, the linear equations are solved simultaneously for a line of cells, the direction of which is referred to as the "sweep direction". The sweep direction was set to the z-axis which was normal to the primary direction of flow. Despite the changes in flow direction throughout the computational domain, the primary direction of flow chosen was parallel to the longitudinal axis of the furnace. The direction in which the solution proceeds through the domain, that is the "marching direction", was set the same as the primary flow direction.

The convergence rate of this procedure was improved by adjusting the under-relaxation parameters, which determine how much the variables are allowed to change at each iteration. In these calculations, the values of this parameter were set at 0.1-0.5 for the velocity and turbulence variables and 0.2-0.5 for the pressure. The convergence rate of the pressure was slow. Therefore, to improve the convergence rate of the pressure, the number of sweeps of the pressure equation, that is the number of times the pressure equation is updated within a global iteration, was increased. The number of "sweeps" of the pressure equation was set at 5; this tended to reduce the instability of the pressure equation. In addition, the multigrid algorithm was used (Hutcheson and Raithby, 1986). The multigrid technique, which computes corrections to the current solution of the pressure field within successively coarser blocks of the control volumes, was effective in increasing the convergence rate.

The computations were carried out on an IBM compatible Pentium 128MB RAM computer. Depending upon the problem, the total CPU time varied between 10 and 14 hours despite efforts to improve the convergence rate of the model. Convergence was slowest when the jets were asymmetric.

6.2 Mathematical Model Simulations

The principal objective was to determine whether the mathematical model could successfully simulate the flow patterns observed in the air model. The model simulations were run with different burner jet flow and angle configurations to evaluate the impact on the furnace flow patterns. The addition of afterburner jet flow was not included in the FLUENT calculations.

6.2.1 Sensitivity Analysis

A sensitivity analysis was performed to evaluate the response of the model to changes in the grid density and in the inlet turbulence intensity. This analysis investigated the effects on the model simulations that were produced by large changes in the parameters, and hence provided an estimate of the reliability of the model simulations. In each case, all variables were maintained constant except for the variable being investigated.

6.2.1.1 Grid Density

The accuracy and numerical stability of the simulation depend on the choice of grid size. In other words, the distribution and density of the grid lines determines the accuracy with which the mathematical model represents the physical phenomena. The distribution of grid lines, previously discussed in section 6.1.3, was not investigated.

The effect of varying the global grid density has been examined. In the FLUENT calculations, the mesh size was set at 50 x 60 x 34 which was the maximum that could be handled by the computer. Since there was no benefit to testing a smaller grid size, the sensitivity analysis was carried out for a smaller computational domain, which included only one quadrant of the furnace space. In taking this approach, a direct comparison with experimental data could not be made. Therefore this effort compared only the effect of grid density on the model output.

The sensitivity of the simulations was evaluated based on a three-dimensional mesh dependency

test for two different sizes: 50 x 22 x 17 and 64 x 28 x 21. In the latter mesh size, the global grid density was doubled. The cross sectional plane selected for the comparison was an axial distance 1.92 m from the inlet jets. Comparisons of the axial velocity component and the velocity magnitude were made at two positions in the plane; z = 0.265 m away from the main jet stream and at z = 0.66 m close to center of the main jet stream. The dependency on mesh size is illustrated in figures 6.2.1 and 6.2.2. There was no significant difference in the profiles of the axial velocity component and the velocity magnitude. In the main jet stream, the calculated velocities were lower when modeling with the coarser mesh simulations due to relatively larger size of the control volume.

6.2.1.2 Inlet Turbulence Intensity

The significance of the inlet turbulence intensity was examined at two settings 10% and 50%. In the air model the measured root mean square of the jet velocity fluctuations was 50%. Although the data was recorded at a frequency of 0.5 Hz, it did provide an approximation of the turbulence intensity in the jet, which was significantly higher than the turbulence intensity in fully developed pipe flow. This data suggested that the flow through the jets was macroscopically unsteady.

To reduce the computational effort, the sensitivity analysis was performed with the 50x22x17 grid system used for the mesh dependency test. Comparisons of the axial velocity component, the velocity magnitude and the turbulence intensity were made on a plane 1.92 m from the jets (x-axis) at two positions; z = 0.265 m and z = 0.66 m. The inlet turbulence had no significant effect on the simulated values, having dissipated rapidly with distance from the burner jet (figure 6.2.3 and 6.2.4). Therefore, subsequent calculations of the FLUENT model were carried out with an inlet turbulence intensity of 10%.

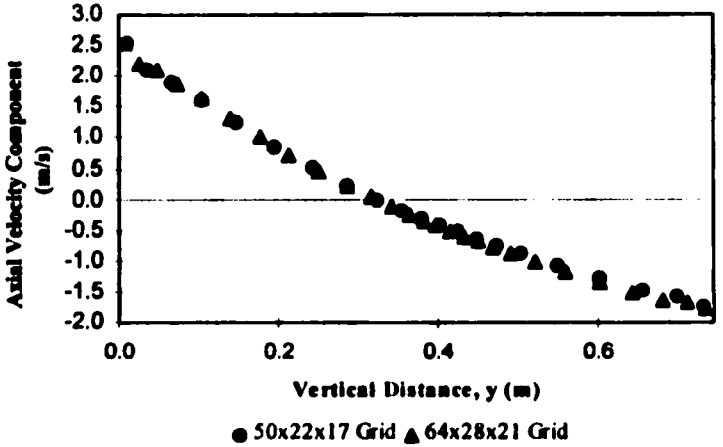

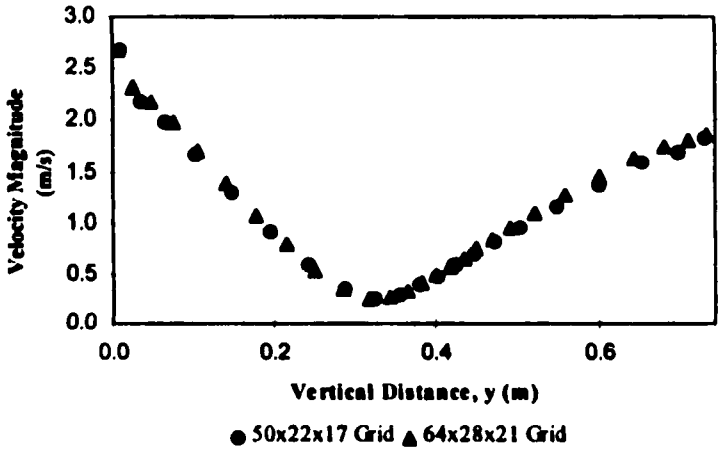

Figure 6.2.1 Grid Sensitivity at x = 1.92 m, z = 0.265 m

(Inlet Conditions: V_x=19.14 m/s, V_y=-4.16 m/s, V_z=4.08 m/s, Turb. Intensity=10%)

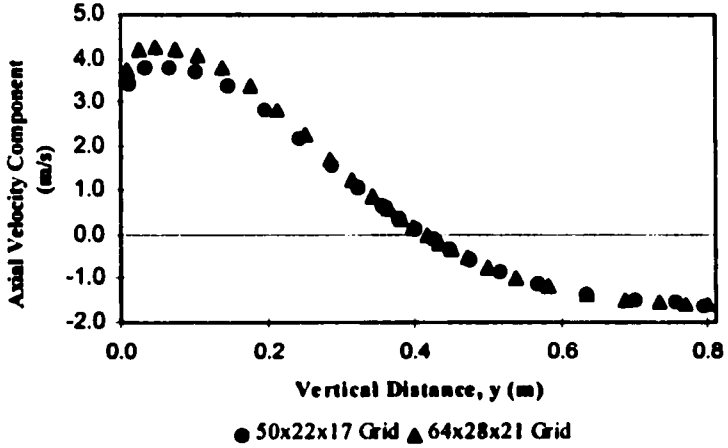

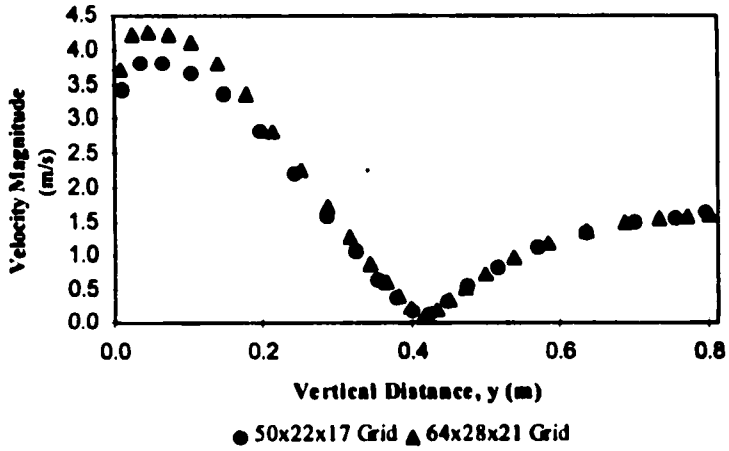

Figure 6.2.2 Grid Sensitivity at x = 1.92 m, z = 0.66 m

(Inlet Conditions: V_x=19.14 m/s, V_y=-4.16 m/s, V_z=4.08 m/s, Turb. Intensity=10%)

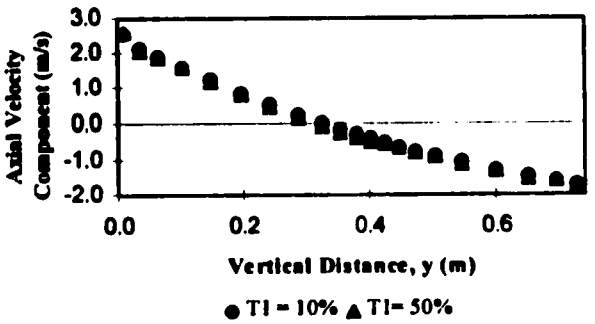

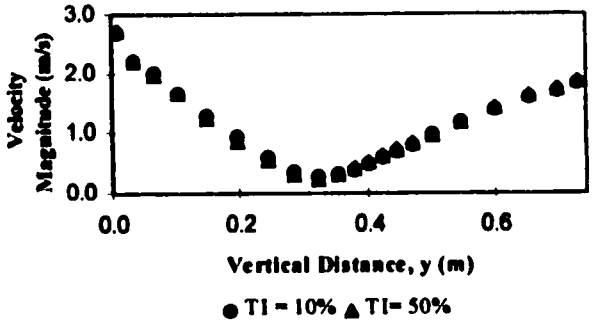

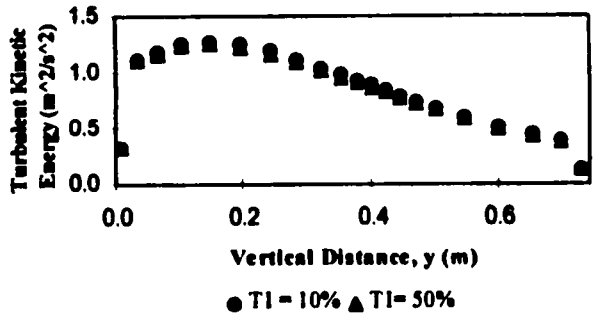

Figure 6.2.3 Effect of Inlet Turbulence Intensity

at x = 1.92 m and z = .265 m

(Inlet Conditions: V_x=19.14 m/s, V_y=-4.16 m/s, V_z=4.08 m/s)

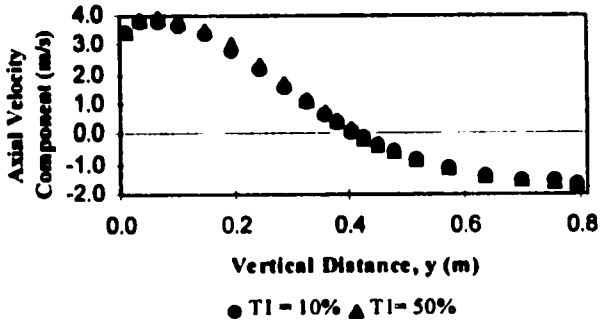

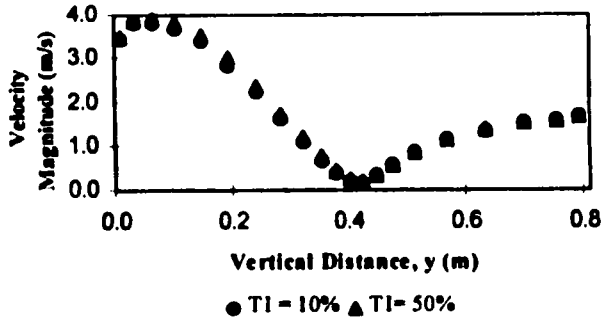

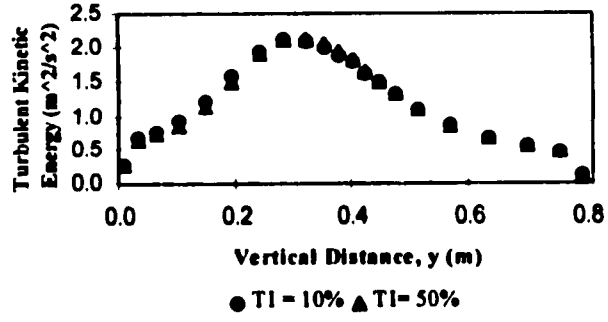

Figure 6.2.4 Effect of Inlet Turbulence Intensity

at x = 1.92 m and z = .66 m

(Inlet Conditions: V_x=19.14 m/s, V_y=-4.16 m/s, V_z=4.08 m/s)

6.2.2 FLUENT Simulated Flow Patterns

The FLUENT computation fluid dynamics code was used to simulate the flow through the scaled air model of the Inco flash furnace under different flow conditions. The flow conditions studied in FLUENT investigated the effect of the discharge position in the uptake, the effect of jet angle, both inclination and convergence, and the effect of jet tip velocity. In total, nine simulations were executed with the FLUENT model.

6.2.2.1 Symmetric Flows

The first simulations investigated the furnace and uptake flow patterns with the two burner jet configured symmetrically. The inlet flow conditions for the jets were summarized in table 6.1.1. Two simulations were carried out to illustrate the effect of the discharge position in the uptake on the flow patterns (west vs east) and are referred to as:

Case 1	Symmetrical Burner Configuration (12°/12°)[1] with a West Discharge
Case 2	Symmetrical Burner Configuration (12°/12°) with an East Discharge

For the same inlet flow conditions, the FLUENT model predicted that the furnace flow patterns remained unaffected by the position of the uptake discharge. Figure 6.2.5 compares a typical flow distribution in the furnace space for the two discharge configurations. The simulated flow patterns in the furnace space were symmetric about the center, which was unlike the flow patterns observed in the air model. It was apparent that other factors affected the flow behaviour of fluid in the furnace, such as the jet angles and tip velocities. These factors are explored further in the preceding sections.

As in the cold models, the jets flowed directly towards the floor forming a single, forward moving stream, which was enveloped on three (3) sides by zone of recirculation. The simulation predicted that the initial merging of jet flows occurred at a distance of 0.57 m from the end wall

[1] The two angles, 12°/12°, refer to the angles of convergence and inclination, respectively.

and the formation of a single, forward moving stream was determined to begin a distance of 0.90 m from the end wall. The forward moving stream propagated through the furnace with little vertical expansion. Figure 6.2.6 illustrates the development of the jet flows in the furnace space at several cross sectional planes from the burner jets (x = 0.57 m, 0.90 m and 2.0 m).

The flow patterns simulated by the FLUENT model showed that the axial velocity was the principal velocity component between x= 0.9 m and x=2.51 m. A similar observation was made in the air model. The change in direction of the furnace flow towards the uptake was predicted to develop directly beneath the mouth of the uptake, 2.51 m from the end wall. This can be seen in figure 6.2.7 where the vector of the velocity magnitude changes direction beneath the uptake.

In the uptake, the flow patterns in the lower section were also symmetric with a high velocity region formed in the center and no back flow along the walls. The position of the discharge was noted to affect the flow patterns in the upper section, starting 1.79 m from the base of the uptake. At this point, the velocity of the fluid was higher along the discharge side of the uptake. A region of recirculation was established in the upper corners of the uptake, opposite the discharge. The flow development in the uptake is illustrated in figure 6.2.8 at several cross-sectional planes in the uptake (y = 0.93 m, 1.79 m and 2.32 m).

Shifting the location of the uptake discharge from west to east produced flow patterns which were the mirror image of those described in figure 6.2.5. Under symmetric flow conditions, the furnace flow patterns were unaffected by the presence of the uptake. In the case of the east discharge, the high velocity region was noted along the east side and vice versa. Figure 6.2.9 gives a comparison of the velocity vectors on the plane of symmetry. This simulation is in agreement with the observations made in the air model.

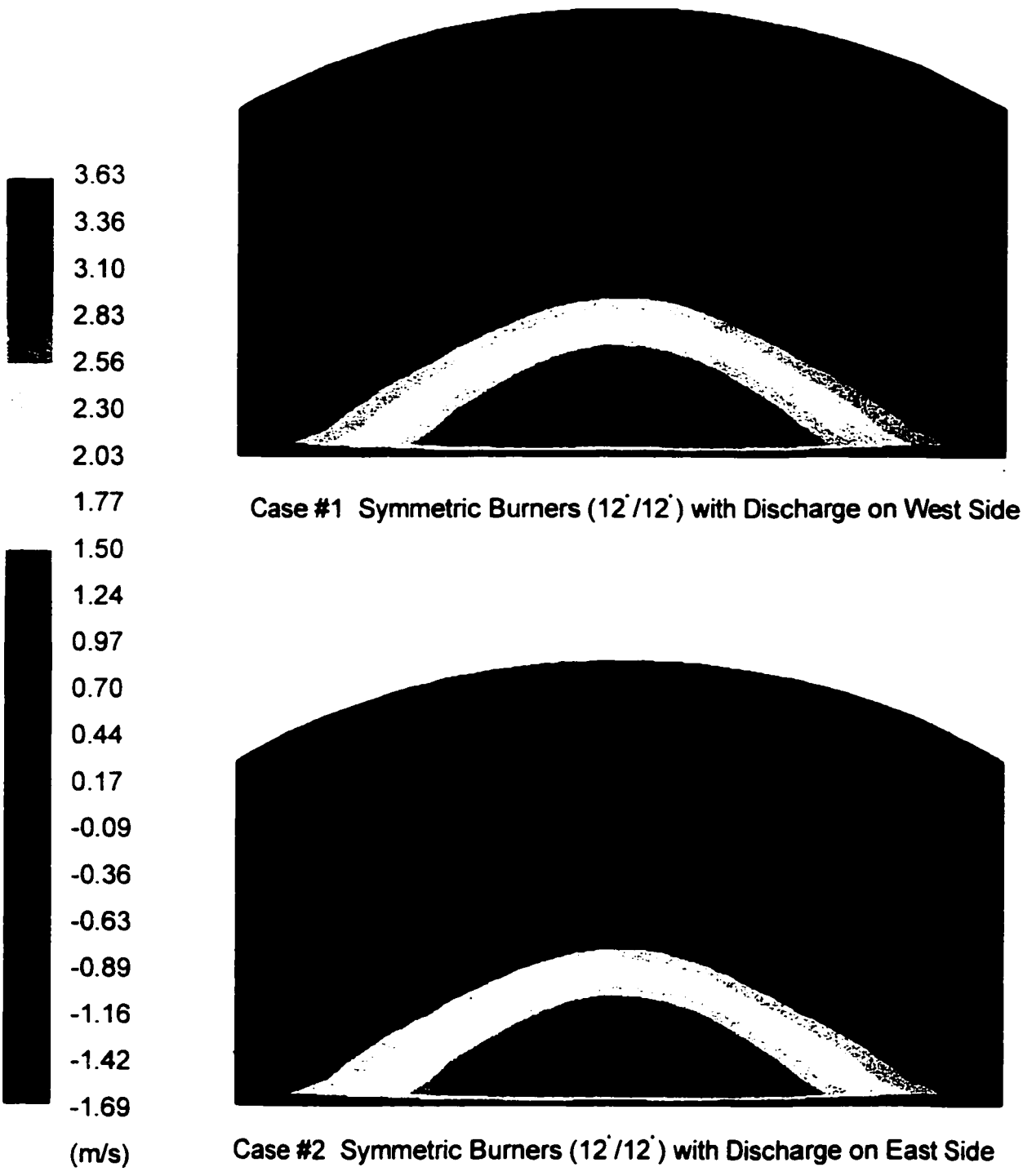

Figure 6.2.5 Effect of Uptake Discharge on Furnace Flow Pattern (FLUENT)

Axial Velocity Profile at x = 2.0 m

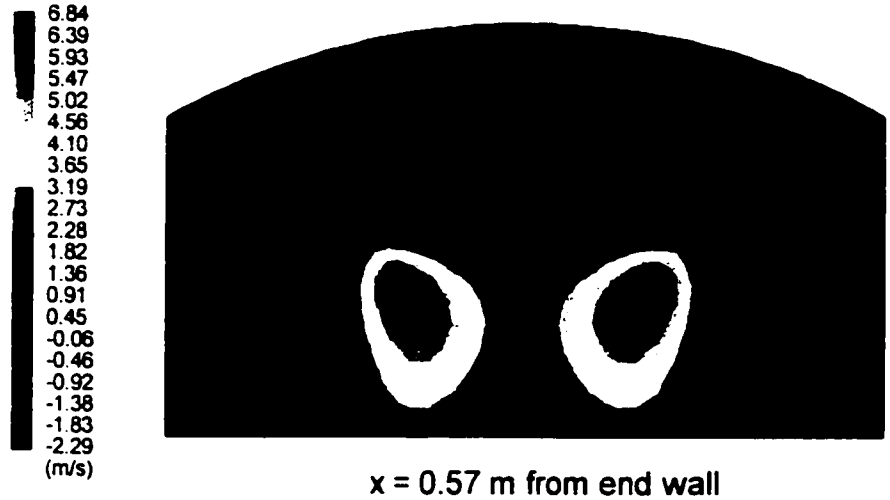

x = 0.57 m from end wall

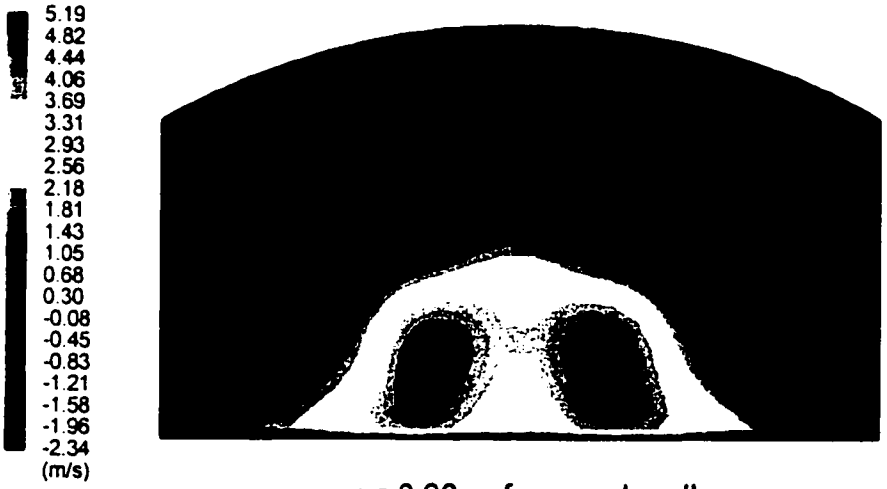

x = 0.90 m from end wall

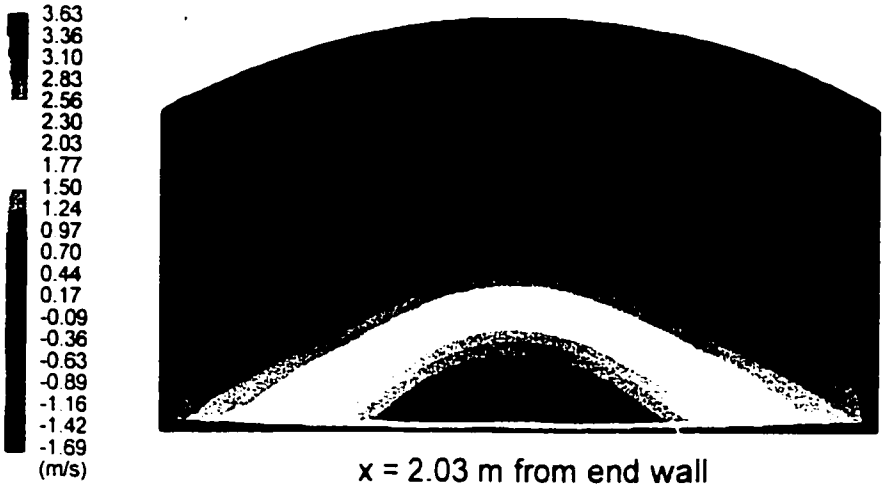

x = 2.03 m from end wall

Figure 6.2.6 Flow Development in Furnace Space - Axial Velocity Profile (FLUENT)

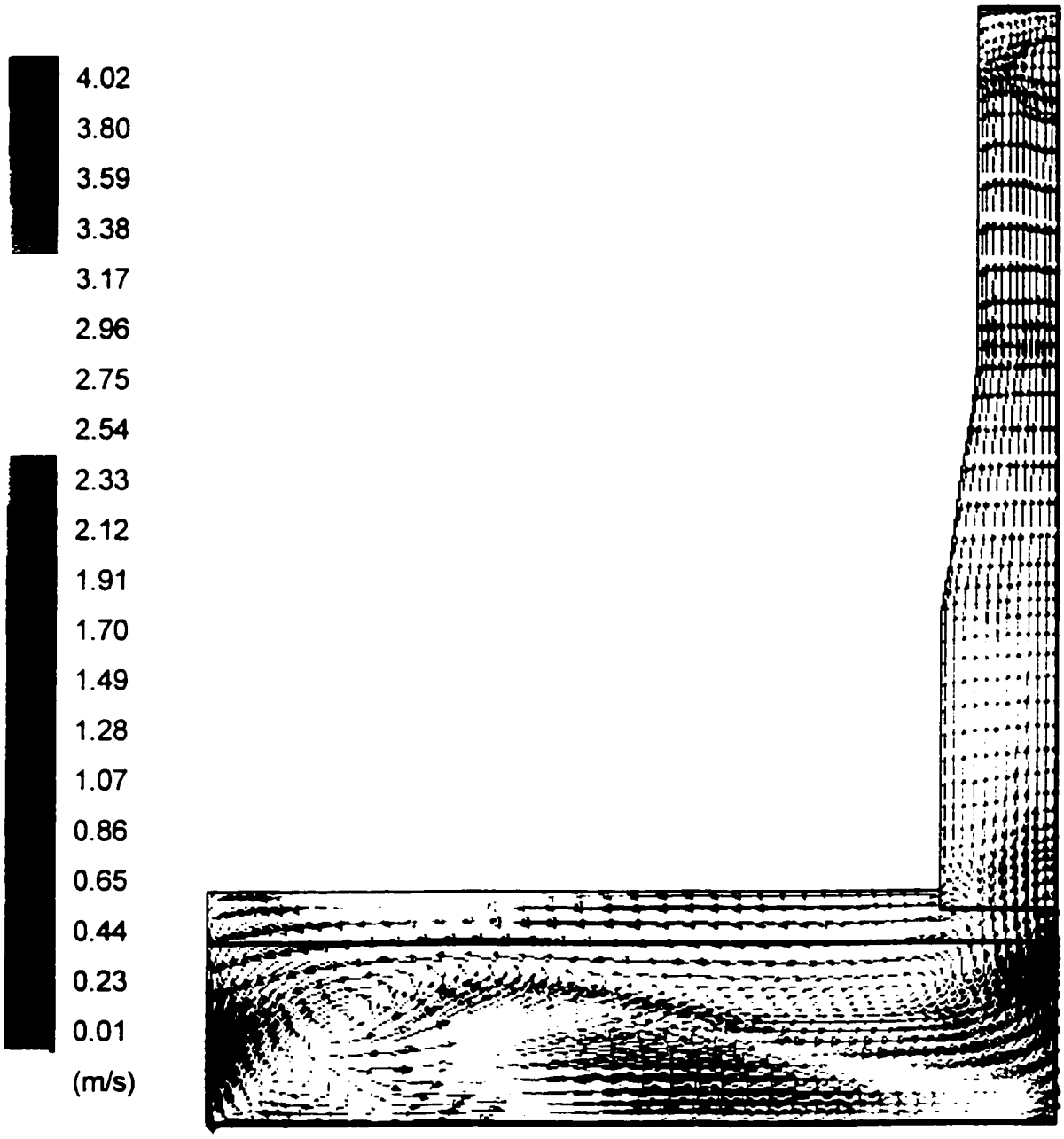

z = 0.71 m (longitudinal centerline of furnace space)

Figure 6.2.7 Velocity Vector Plot in Furnace Space (FLUENT)

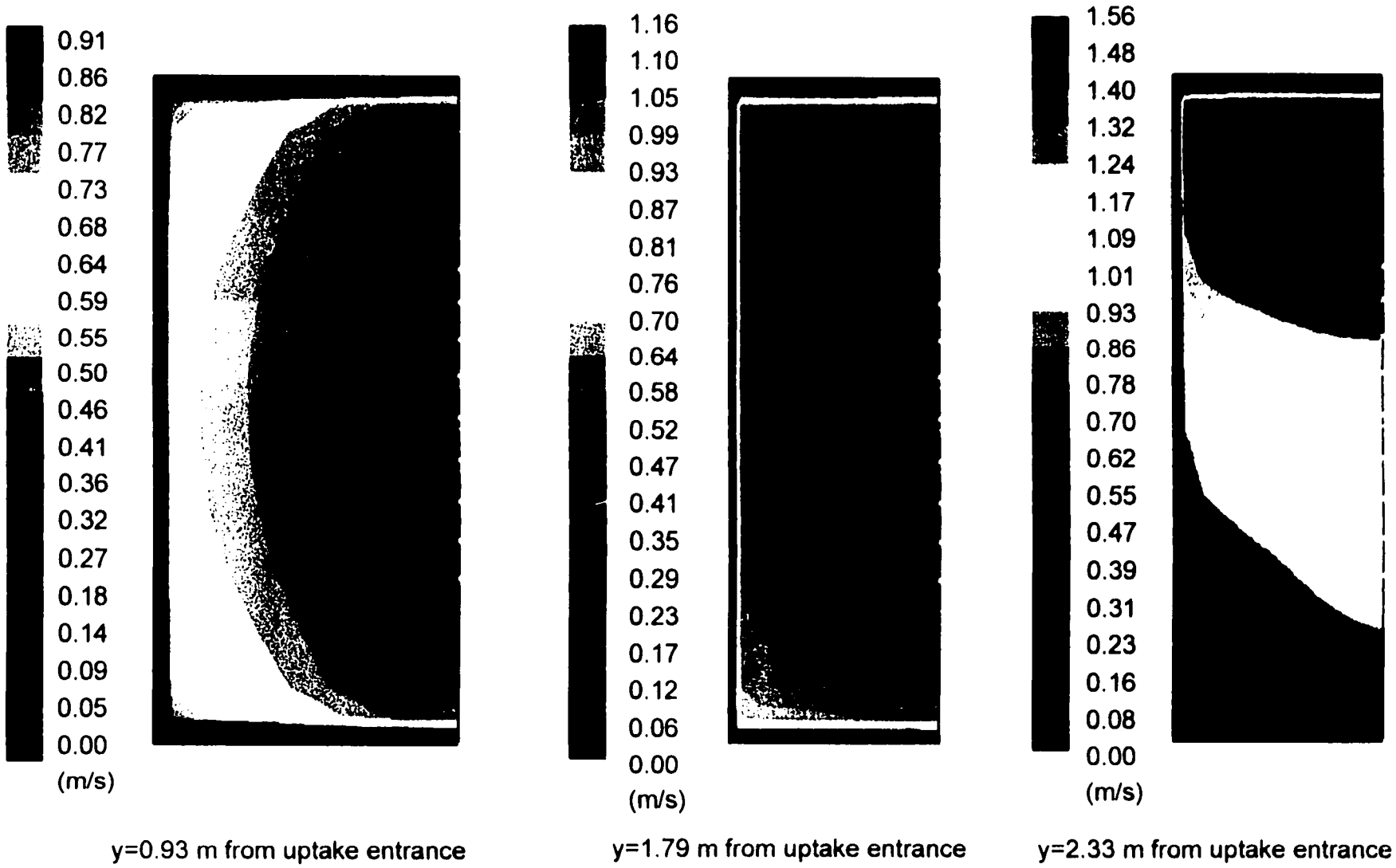

Figure 6.2.8 Flow Development in Uptake - Axial Velocity (FLUENT)

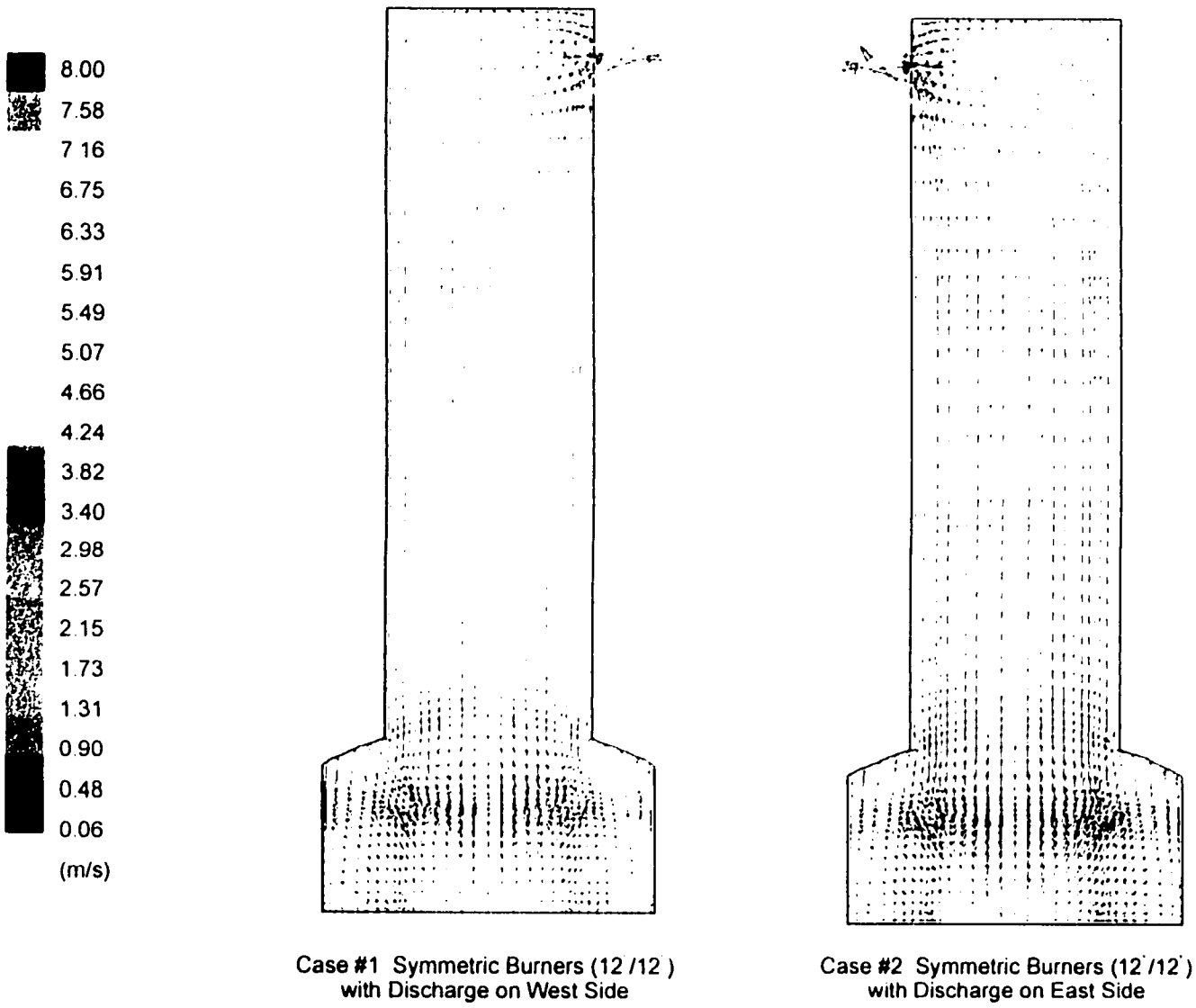

Figure 6.2.9 Velocity Vector Plot Along Symmetry Plane, x = 2.93 m (FLUENT)

6.2.2.2 Factors Affecting Furnace and Uptake Flow Patterns

The preceding section discussed symmetric flow patterns in the furnace space. However, as observed in the air model, the flows in the furnace space were not symmetric but skewed to one side. In this section, the factors that affect the flow behaviour of fluid in the furnace and uptake are discussed. These factors included the jet angles, both the convergence and inclination angles, as well as the jet tip velocities.

Seven additional runs were carried out using FLUENT. In these calculations, the changes to the inlet boundary conditions were made only to jet #2 while the conditions for jet #1 were maintained the same as given in table 6.1.1. Table 6.2.1 gives the inlet boundary conditions and the angles for jet #2, which were used in these computations.

Table 6.2.1 Description of Inlet Boundary Conditions for Jet #2 (FLUENT Cases 3-9)

Case #	Jet Angles	Inlet Boundary Velocity, m/s			Comment
	(α°/β°)	v_x	v_y	v_z	
3	(10.5°/12°)	19.24	-4.16	-3.57	
4	(11.5°/12°)	19.17	-4.16	-3.90	
5	(13.5°/12°)	19.02	-4.16	-4.57	
6	(12°/10.5°)	19.24	-3.65	-4.08	
7	(12°/13.5°)	19.02	-4.67	-4.04	
8	(12°/12°)	20.09	-4.37	-4.27	5% increase in flow
9	(12°/12°)	18.18	-3.95	-3.86	5% decrease in flow

1. Angle $\alpha \equiv$ Angle of convergence; Angle $\beta \equiv$ Angle of inclination
2. In all cases, the turbulence intensity and length were held constant at 10% and 0.098 m, respectively.

Significance of Jet Convergence Angle

Four burner convergence angle configurations are presented in this section: 10.5°, 11.5°, 12° and 13.5°. The convergence angle, α, is defined as the degree to which the jets are angled inward (figure 6.2.10). For example, as the angle of convergence decreases ($\alpha \rightarrow 0°$), the jet of air becomes parallel to the longitudinal axis of the furnace. In these calculations, the velocity components were adjusted to correspond to the different convergence angles.

When the angles of convergence were not set equal, the flow in the furnace was rendered asymmetric. The main flow in the furnace was directed toward the side of the furnace that had the jet with the smaller angle of convergence. The amount of flow deflection to one side was dependent on the convergence angle. A region of counter-flow enveloped the main flow along the opposite side. Figure 6.2.11 shows the position of the high velocity zone, relative to the furnace centerline, at a cross-sectional plane 2.0 m from the burner jets. The furnace flow was sensitive to the slightest change in angle, suggesting that the flow was very prone to become asymmetric, i.e. a small change results in a shift from symmetrical flows (Kirshner and Katz, 1975). It is apparent in figure 6.2.11 that a half degree change in convergence angle from 12° to 11.5° for jet #2 produced a significant deflection in the furnace flow.

In the uptake, the flow patterns in the lower section were also asymmetric. The furnace flow pattern significantly affected the uptake flow behaviour. The furnace flow entered the uptake forming a high velocity region along the same side that corresponded to the jet with the smaller angle of convergence. This high velocity stream quickly traveled toward the opposite side of the uptake and a separation region was established in the lower part of the uptake. The effect of the uptake discharge on the flow patterns was not as significant as in the symmetric case due to the asymmetry at the base of the uptake. Figure 6.2.12 gives a comparison of the velocity vectors on the plane of symmetry for each case.

Significance of Jet Inclination Angle

Three burner inclination angle configurations are presented in this section: 10.5°, 12° and 13.5°. The angle of inclination, β, is defined as the degree to which the jets are angled downward (figure 6.2.10). For example, as the angle of inclination decreases ($\alpha \rightarrow 0°$), the jet fires perpendicular to the end wall of the furnace, i.e. the jet axis becomes parallel to the furnace floor. In these calculations, adjustments to the velocity components were made to correspond to the different convergence angles.

A change in the angle of inclination had a similar effect on flow patterns in the furnace system as a change in the convergence angle but the extent to which the flow was asymmetric was less. When the angle of inclination was decreased, the main flow in the furnace was deflected toward the side that had the jet with the smaller angle setting. The jet with the steeper angle of inclination directed the flow away from itself as it impinged on the furnace floor first, at a distance that was closer to the furnace end wall. Figure 6.2.13 shows the position of the high velocity zone, relative to the furnace centerline, at a cross-sectional plane 2.0 m from the burner jets. It is apparent in figure 6.2.13 that the decreasing of the inclination angle had a more significant effect on the asymmetry of the main furnace flow, than did an increase in the angle.

The predicted asymmetry in the uptake varied in the same way as the asymmetry in the furnace, i.e. the more asymmetric the furnace flow pattern, the more asymmetric was the uptake flow pattern. The furnace flow entered the uptake with higher velocities along the same side that corresponded to the jet with the smaller angle of convergence, but rapidly traveled across to the opposing wall. A region of back flow was formed in the lower part of the uptake. Due to the asymmetry in the uptake flow, the discharge did not have a significant effect. Figure 6.2.14 gives a comparison of the velocity vectors on the plane of symmetry for each case.

Significance of Jet Velocity

The jet velocity impacted the furnace flow patterns in a similar manner to the jet angles. Two

cases are discussed in this section: a 5% increase and a 5% decrease in the flow to jet #2. Small changes in the jet velocity by 5% resulted in asymmetric flows in the furnace and uptake spaces. The momentum of the jet with the higher velocity shifted the furnace flow toward the side that had the jet with the lower velocity. Figure 6.2.15 shows the position of the high velocity zone, relative to the furnace centerline, at a cross-sectional plane 2.0 m from the burner jets. The simulation predicted mirror symmetry between the two cases. In the uptake, the flow behaviour was asymmetric, similar to the previously discussed cases. A zone of high velocity was formed in the lower uptake as was a flow separation zone.

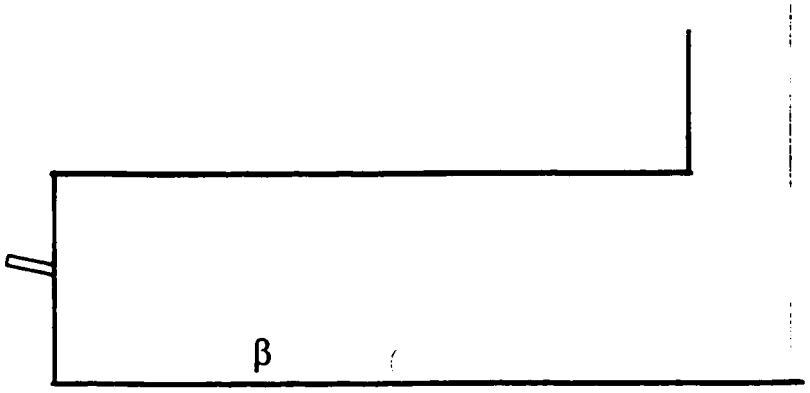

Angle of Inclination

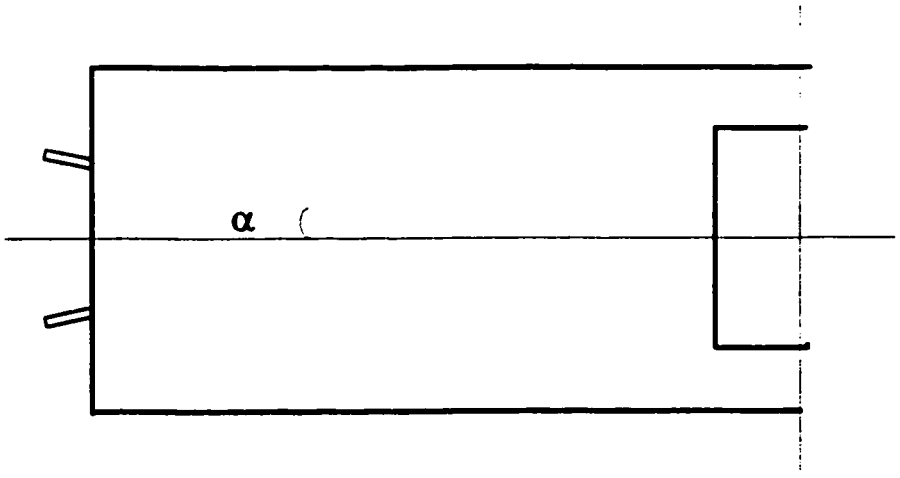

Angle of Convergence

Figure 6.2.10 Schematic of Jet Angles

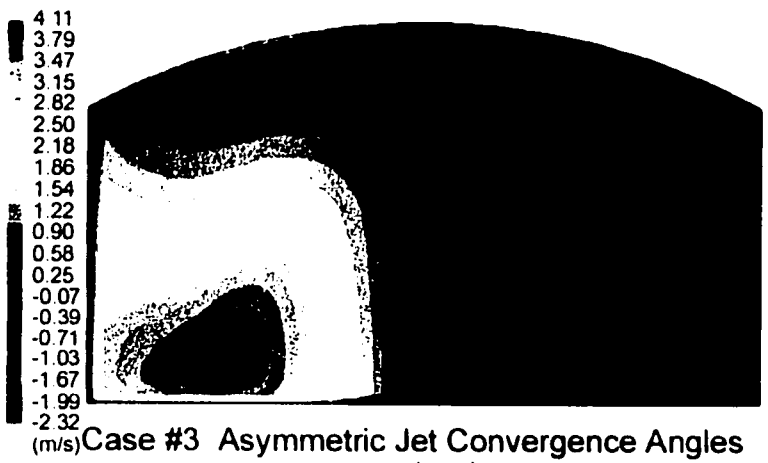

Case #3 Asymmetric Jet Convergence Angles (10.5°/12°)

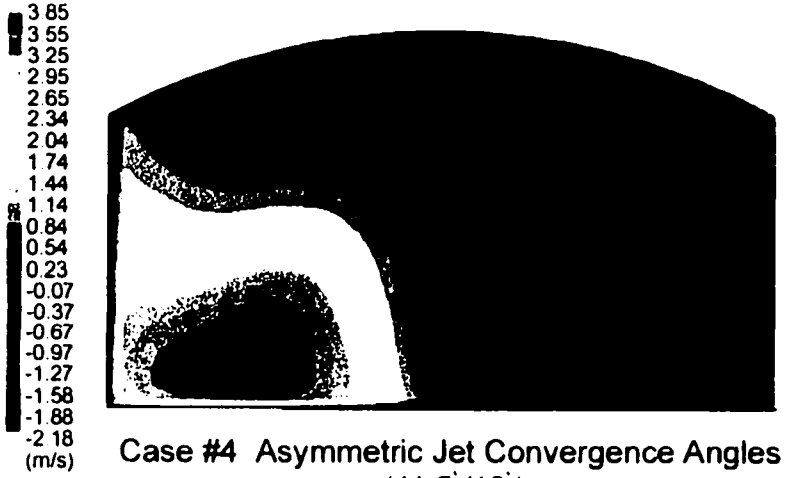

Case #4 Asymmetric Jet Convergence Angles (11.5°/12°)

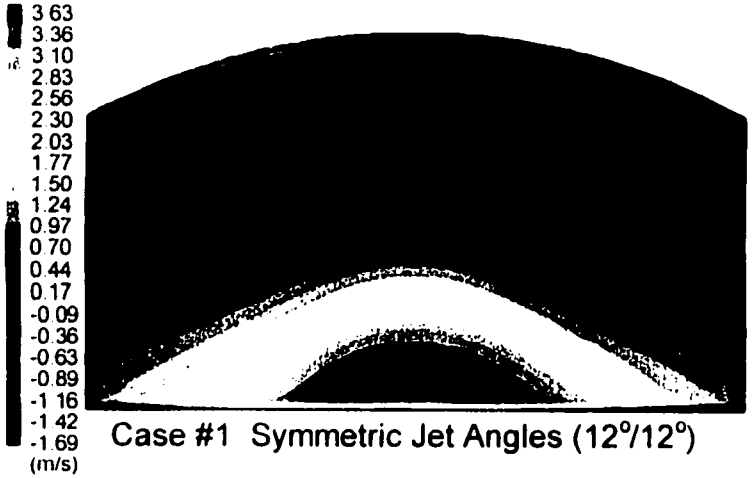

Case #1 Symmetric Jet Angles (12°/12°)

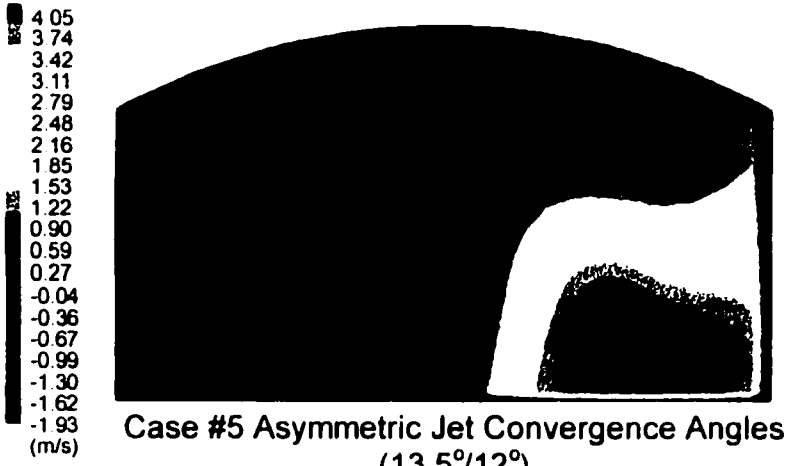

Case #5 Asymmetric Jet Convergence Angles (13.5°/12°)

Figure 6.2.11 Effect of Jet Convergence Angle on Furnace Flow - Axial Velocity Profile at x = 2.0 m (FLUENT)

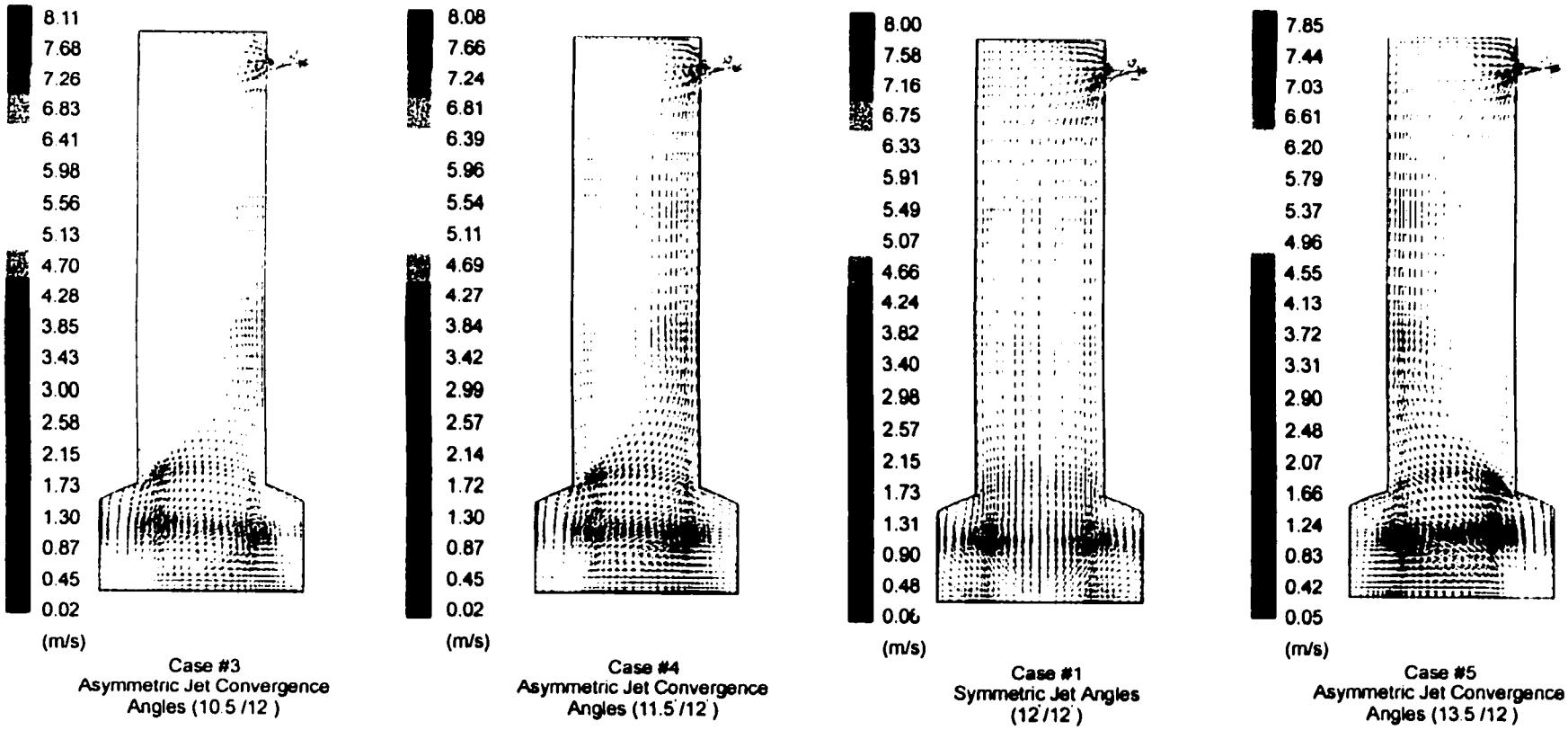

Figure 6.2.12 Effect of Jet Convergence Angle on Uptake Flow (FLUENT)

Velocity Vector Plot along Symmetry Plane at x = 2.93 m

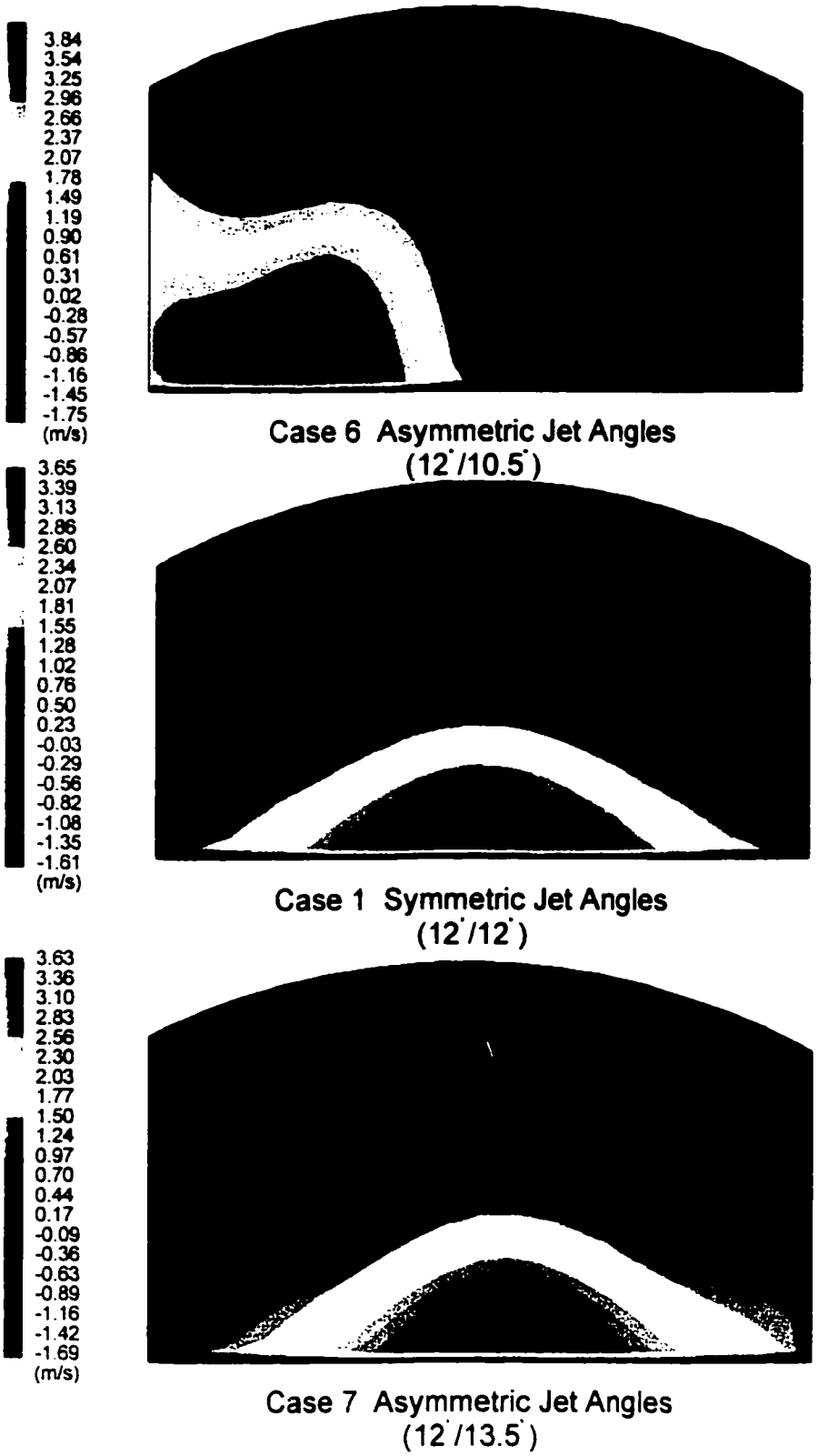

Figure 6.2.13 Effect of Jet Inclination Angle on Furnace Flow

Axial Velocity Profile at x = 2.0 m (FLUENT)

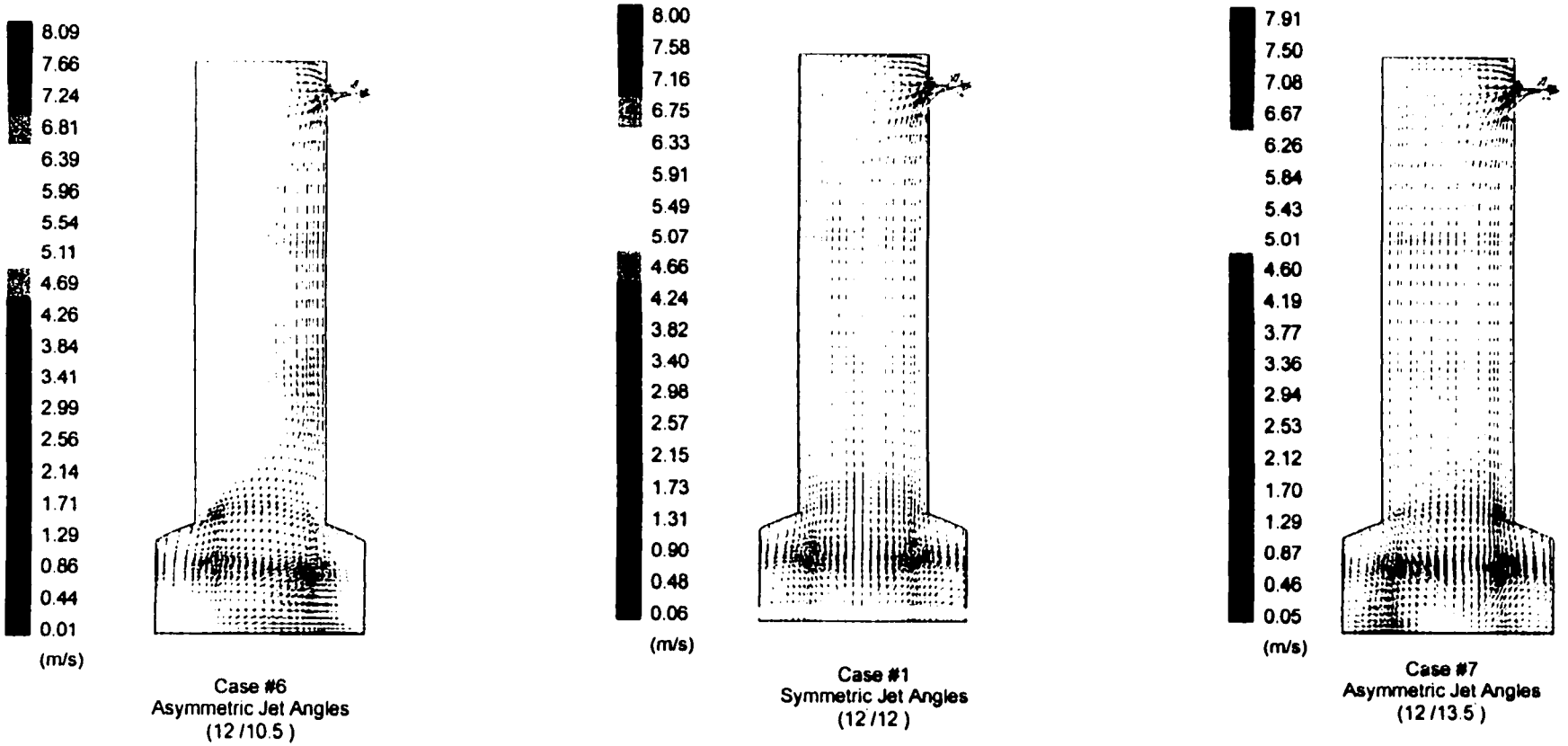

Figure 6.2.14 Effect of Jet Inclination Angle on Uptake Flow m (FLUENT)

- Velocity Vector Plot along Symmetry Plane at x = 2.93 m

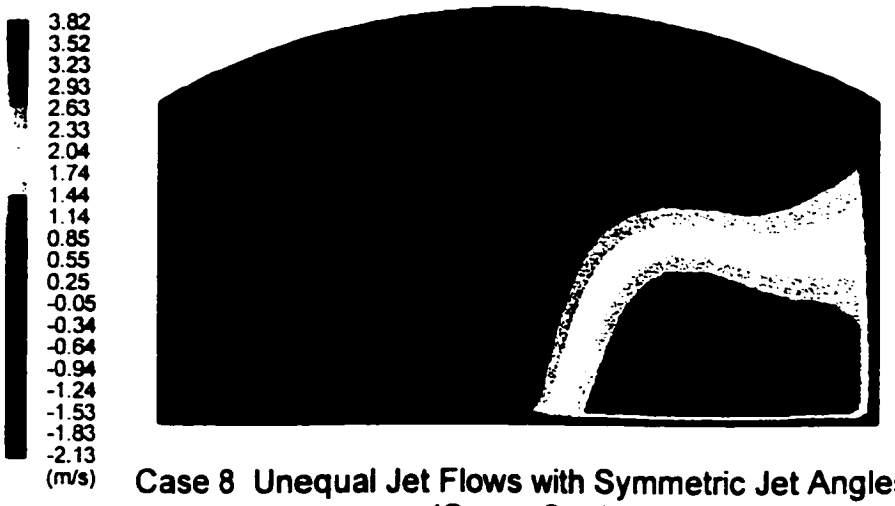

Case 8 Unequal Jet Flows with Symmetric Jet Angles
($Q_{...} > Q_{...}$)

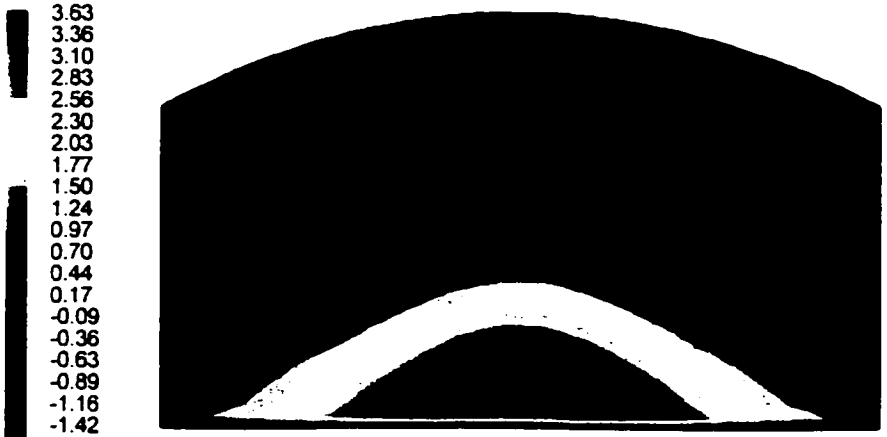

Case 1 Equal Jet Flows with Symmetric Jet Angles

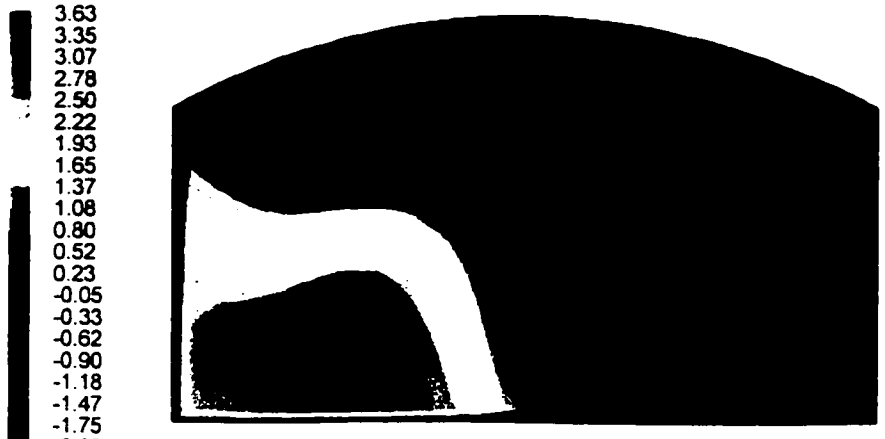

Case 9 Unequal Jet Flows with Symmetric Jet Angles
($Q_{...} < Q_{...}$)

Figure 6.2.15 Effect of a 5% Difference in Jet Velocity on Furnace Flow Axial Velocity Profile at x = 2.0 m (FLUENT)

6.3 Discussion of Mathematical Model Simulation

As previously stated, the principal objective of the mathematical modeling was to determine whether this technique could successfully simulate the flow patterns observed in the air model. The model simulations were run with different burner jet flow and angle configurations to evaluate the impact on the furnace flow patterns without the addition of afterburner jet flow to the uptake. A total of nine simulations were carried out using the FLUENT CFD code. In this section, the discussion will focus on comparing the mathematical model simulations with the experimental velocity data obtained in the air model.

6.3.1 Comparison of Simulations and Experimental Data

It was difficult to make a direct comparison between the simulated and experimental results. Although flow differences between jets were measured, the differences in jet angles, which could have contributed to the asymmetry observed in the air model, were not known. The mathematical model predictions suggested that the furnace flow is very prone to become asymmetric. It is known from the simulations that very small inequality in the jet angles or jet flows can lead to asymmetric flow, as observed in the air model. In the air modeling, the experimental findings indicated that the flow was aligned preferentially along one side (east) of the furnace. The flow asymmetry observed in the air model could be attributed to one or a combination of the factors examined with FLUENT.

The FLUENT modeling was effective in screening potential factors, which affect the fluid flow in the furnace. Of course, the steady state numerical model cannot account for the temporal flow instability at the transition between the furnace and uptake. The flow instability at this transition produced a pulsating-type flow pattern, which was driven by cyclic imbalances of pressure in the system (section 5.1.3.8). In addition to the factors evaluated using FLUENT, the flow instability could have contributed to the asymmetry by introducing a perturbation into the system which may momentarily bend a jet toward one wall (Kirshner and Katz, 1975).

Figure 6.3.1 provides a comparison of the FLUENT model predictions and the experimental data collected in the air model. The data is presented in terms of dimensionless velocities. There are significant discrepancies between the predicted and measured velocities, primarily in the region of the forward moving stream. For the same inlet flow rate, the mathematical model over-predicted the magnitudes of the measured time-averaged velocities. By comparison, it was evident that the velocities were of similar magnitude in the recirculation region of the measurement area.

The discrepancy in the velocity of the forward moving stream was likely to be due to:

a) the combined effect of jet angles and flow imbalances, which contributed to the asymmetry in the furnace flow, and

b) the observed temporal instability of the flow in the experimental model which tends to reduce the average velocity.

In unstable turbulent flow with high turbulence intensities, it is difficult to make a meaningful comparison between experimental averaged velocities and mean velocities calculated from numerical simulations. The average velocities, determined from the air model experiments, were measured over a finite period of time (60 seconds). Although this sampling time was deemed sufficient, average velocities measured over sampling periods of a longer duration should be made for comparison in future experiments.

The predicted asymmetric flow conditions and measured dimensionless fields were qualitatively similar. However, the FLUENT model showed more skew in the forward moving stream and did not predict the sharp transition between the forward and recirculating flow velocities at z-positions of 0.39 and 0.71m, observed in the air model. The reason for the sharp transition that was observed in the air model is not fully understood. One possible contributing factor could be the temporal instability in the flow causing rapid fluctuations in the local velocity, as seen in figure 5.1.16.

The predicted amount of recirculation flow was in good agreement with the measured values.

Table 6.3.1 compares the predicted and measure recirculation ratio, defined as the ratio between the recirculating air flow and the flow through the burner jets. The small difference between predicted values suggested that the factors of jet angle and flow had only a limited effect on the recirculation ratio.

Table 6.3.1 Comparison of Predicted and Measured Recirculation Flows at x = 2.0 m

Case #	Jet Angles ($\alpha°/\beta°$)	Recirculation Ratio
1	(12°/12°)	1.9
3	(10.5°/12°)	2.2
4	(11.5°/12°)	2.4
6	(12°/10.5°)	2.1
9	(12°/12°)	2.1
Exptl		2.0-2.4

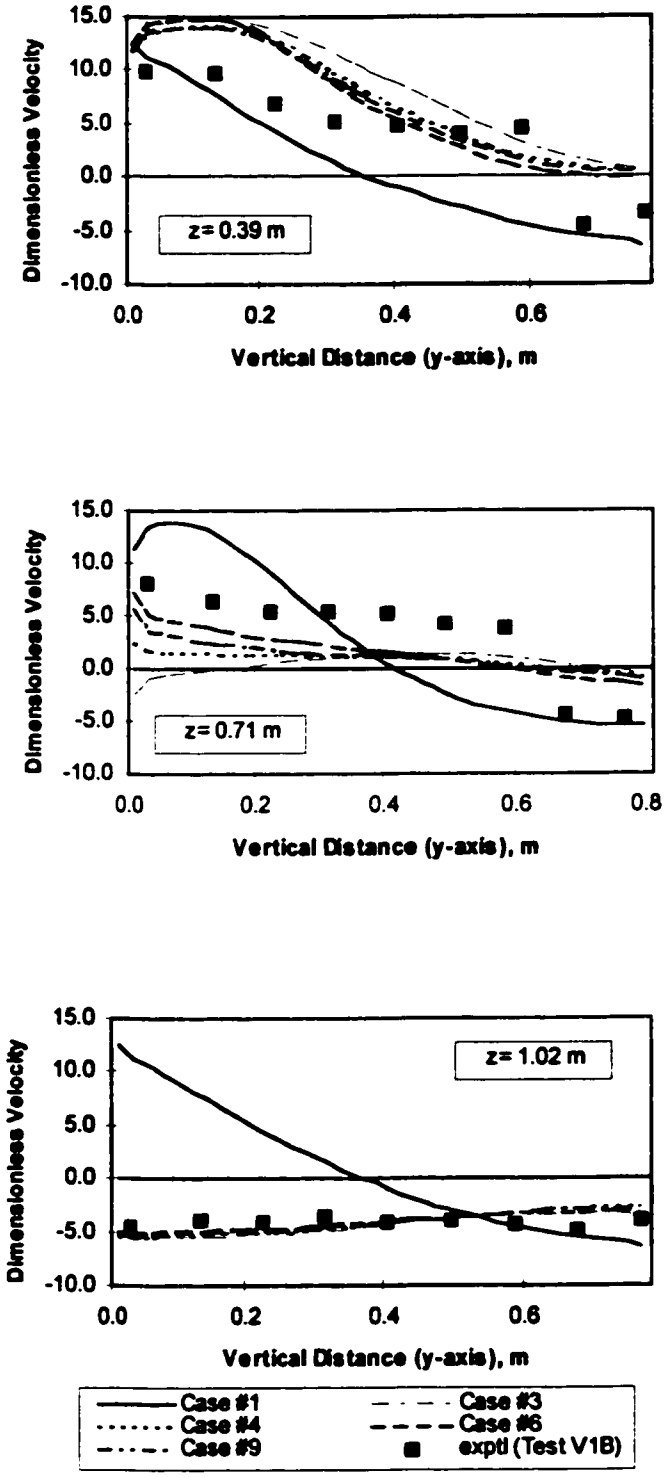

Figure 6.3.1 Comparison of Mathematical Predictions with Experimental Measurements

Axial Velocities at x = 2.0 m

Chapter 7

GENERAL DISCUSSION

In Chapters 5 and 6, the furnace flow patterns were examined under isothermal conditions by physical and numerical modeling techniques. The results of the modeling experiments and the numerical simulations provided insight into the gas flow patterns in the freeboard of the flash furnaces at Copper Cliff. Although these investigations were based on room temperature conditions, several inferences concerning the aspects of the plant operation can be drawn from the analysis of these flow patterns. In making these comparisons, reference is made to information collected from plant sampling campaigns (Appendix C) and annual plant inspections.

7.1 Flow Patterns in the Furnace

Given the close dynamic similarity between the physical models and the plant situation, the gas flow patterns were expected to be similar. The structure of the jet emerging the concentrate burners in the plant will, however, differ from the air and water jets used in the models. In the physical models, the kinetic energy of jets was scaled according the dispersion number ratio which accounted for the presence of uniformly distributed solids in the jet. Although the presence of particles will have a localized effect on the jet structure, this will not significantly alter the flow patterns in the furnace gas space.

In the plant, the jet structure is complicated by many factors, including the presence of particles, density changes caused by temperature and the effects of chemical reaction. A study conducted

by Melville and Bray (1979) suggested that the structure of a particle laden jet is primarily determined by two competing influences: inertia and turbulence. The inertia of the injected gas is dissipated by the effects of turbulent eddies. With increasing axial distance, the inertia of the gas is depleted as the jet entrains fluid and spreads under the influence of turbulence. However, the gas temperature and composition fields spread radially at higher rates than momentum (Szekely, 1979). This fact is reflected in numerical models by the turbulent Prandlt (Pr_g') number and turbulent Schimdt (Sc_g') having values less than unity (≈0.7) for round jets (Launder and Spalding, 1974).

The mechanism of the particulate dispersion is complex; due to their relatively small size the particles will tend to follow, to a certain extent, the turbulent radial fluctuations of the gas. However, the particles in the jet will not spread as rapidly as gas momentum, because the inertia of the particles reduces their tendency to follow the turbulent fluctuations of the gas. The effect of the solids burden in the jet is to damp the turbulence since the drag between the particles and the gas extracts energy from the turbulent fluctuations.

The particles are dispersed radially according to the time averaged turbulent velocity of the gas and depending on the turbulent particle diffusivity (D_p'). This diffusivity can be calculated from the turbulent particle Schmidt number (Sc_p') and an effective particle viscosity (ν_p'). It is worth noting that for very small (<1μm) completely following the turbulent fluctuations, the turbulent Schmidt number can be approximated to unity; for large particles failing to follow the turbulent fluctuations, it is less than unity. For the purpose of illustration, a constant value of 0.35 will be used as recommended by Smoot and Smith (1985). The "viscosity" is related to the effective gas viscosity (altered to account for particle effects) through the particle relaxation time (τ_p) and the turbulent time scale (t_t) as proposed by Melville and Bray (1979). From this information, the following relationship can be derived to describe the particle transport coefficient:

$$D_p^t = \frac{\nu_g^t}{Sc_p^t\left(1+\frac{\tau_p}{t_t}\right)};$$

where Sc_p^t = turbulent Schmidt number of particles = $\frac{\nu_p^t}{D_p^t}$ = 0.35 (7.1.1)

$$\nu_p^t = \nu_g^t \left(1 + \left(\frac{\tau_p}{t_t}\right)\right)^{-1}$$

τ_p = relaxation time of particles = $\frac{m_p}{6\pi r_p \mu_g}$

t_t = time scale of turbulence = 1-2 ms

Substituting into this equation gives a ratio of particle diffusivity to gas effective turbulent viscosity of less than unity for a 35μm particle (average size of concentrate particle). This ratio indicates that the diffusion of gas momentum is faster than the diffusion of the particles in the jet (Goldschmidt and Esinazi, 1966). Therefore, the structure of particle laden jet in a reacting flame, as is the case in the plant, will have less divergence than an isothermal gas jet (Field et al., 1967).

Qualitatively, under asymmetric jet configurations, the flow patterns and asymmetry observed in the physical models which operated with a single fluid phase would be similar to those in the plant with two phase (solids and gases) present. The sensitivity of jet deflection to changes in jet angles and flows as well as the magnitude to which the flow becomes asymmetric is more difficult to quantify under plant conditions.

7.1.1 Significance of Furnace Flow Patterns

In this study, the single most important factor affecting the flow behaviour of the flash furnace models is the configuration of the burner jets. In the air modeling, a single configuration of burner jet was used with jets angled 12° down and 12° in. The turbulent jets from adjacent nozzles flowed directly toward the model floor where they combined to form a single jet stream, regardless of jet angle.

The strong jet flow makes it inevitable that extensive separation from the side walls and roof occurs. The abrupt junction to the uptake amplifies the effect. The large stream circulates back toward the end wall between the edge of the jets and the walls of the model. Projecting the air model findings to the plant, the amount of recirculation was estimated to be about three times the flow through the burner jets (Chapter 5 Figure 5.1.14). In the air model study, the large recirculating stream is slow moving, having a velocity magnitude of about 5 times the superficial velocity. In the plant, this velocity would not be sufficient to present problems of side wall refractory erosion. However, the recirculating flow can carry entrained particulate (dust) which is not collected on the surface of the bath. The principal means of recovery of fine particles is by impingement on the molten bath. Sampling of the gas stream in the plant has indicated that the average size of the entrained particles was 10μm which was significantly smaller than the average size of the concentrate particles (35μm) (Appendix C Table C.4.10). However, as indicated in figure 7.1.1, this dust is extremely fine and is mainly composed of agglomerates of small spheres. The agglomerates had a mean particle size of about 10 μm, while the constituents of the agglomerates were much smaller (< 3μm).

According to equation 7.1.1, the diffusion of the finer particles is greater than that of the larger, thus the finer particles will propagate further toward the edge of the jet. The recovery of the fine material would be less, as they would have a tendency to be entrained by the recirculating flow. The concentrate contained a considerable quantity of very fine particles 3μm in diameter or less (approximately 10%). The entrained particulate in the recirculating flow is likely to originate from these finer concentrate particles. The chemical analysis of the entrained particles suggests that the source of these particles (Appendix C Table C.4.5,6,7) is primarily the very fine, less than 38μm, concentrate particles (Appendix C Table C.4.2). Interestingly, as table 7.1.1 shows, the nickel-to-iron mass ratio of the dust collected from the gas stream was in good agreement with that of the very fine concentrate particles.

X 5000

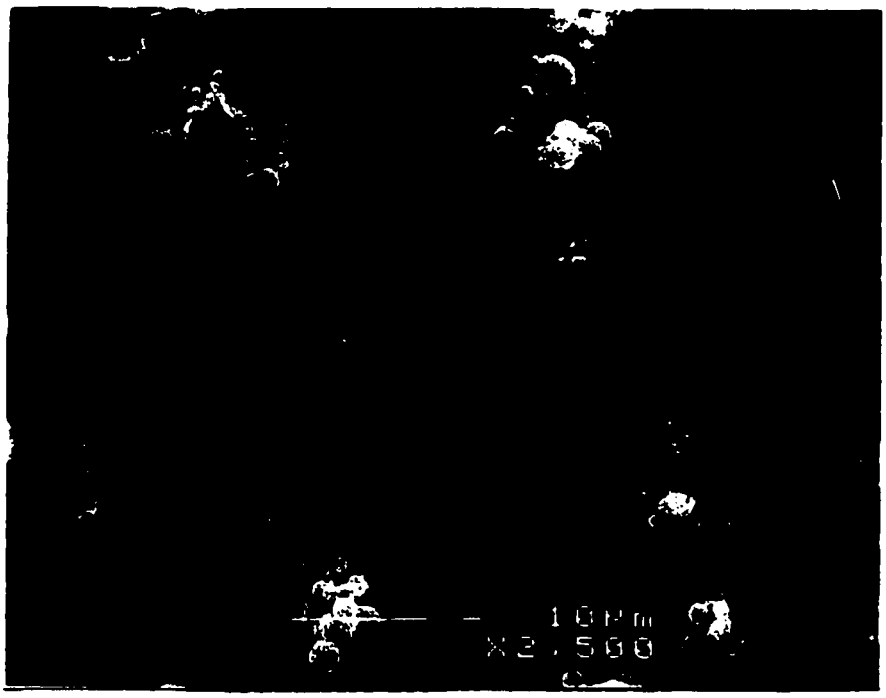

X 2500

Figure 7.1.1 Photomicrograph of Dust Collected from the Uptake

Table 7.1.1 Comparison of Ni/Fe Mass Ratio in Plant Samples

	Concentrate		Dust
	Composite	-38 μm	
Test 1	0.28	0.23	0.23 ± 0.01
Test 2	0.28	0.24	0.23 ± 0.01
Test 3	0.30	0.26	0.25 ± 0.01

On the basis of Stokes Law, the terminal velocity of a 35μm particle in the furnace gas atmosphere is only 0.06 m/s and that of a 10μm particle about 0.002 m/s. From the modeling studies, the velocity of the recirculating flow is two orders of magnitude greater than the terminal velocity of the particles. Thus, the very fine particles that are not collected on the surface of the molten bath, will not settle as readily from the furnace gases. Sampling of uptake gases has determined the solids loading to be about 200 g/Nm^3 of gas (Appendix C Table C.4.7). Although sampling could not be collected at iso-kinetic rates, this dust loading is in agreement with a 3% dust loss as previously reported in the literature (Humphris et al., 1997).

The entrained dust has a tendency to deposit on the walls and roof of the furnace. Inspections during annual plant outages reveal that the accretion profile varies from the center of the furnace, under the uptake, to the end walls. Deposited accretions measure 7 to 10 cm (3-4 in.) on the center side wall panels, increasing to 15 to 60 cm (6-24 in.) at the corners and on the end walls. Numerical modeling of the furnace patterns suggests that the velocity of the recirculating flow slows as it approaches the furnace end wall. This explains the increased accumulation of accretions in this region.

The numerical simulations showed that the flow patterns in the furnace gas space are very sensitive to small inequalities in the jet angles and/or jet flows, leading to asymmetric flow. This asymmetry was observed in the air modeling experiments. In the air modeling, the experimental findings indicated that the flow was skewed preferentially along one side (east) of the furnace. This flow phenomenon is attributed to one or more of the factors examined with the numerical model.

7.2 Flow Patterns in the Uptake

As in the furnace gas space, the flow pattern of gas in the uptake is influenced by the configuration of the burner jets but also the accumulation of accretions on the uptake walls in the plant. The mathematical model predictions suggested that the furnace flow is very prone to become asymmetric, as very small inequalities in the jet angles or jet flows led to asymmetric flow. The effects of the asymmetry in the furnace gas space were also seen in the uptake (Chapter 6 Figures 6.2.12 and 6.2.14).

The effect of wall accretions on the flow patterns and mixing in the uptake could not be investigated in the modeling experiments, as the configuration of the build-up was not well defined. From plant experience it is known that the amount and location of build-up in the uptake is, to certain extent, random and variable. This observation agrees with the finding that the furnace flow is very prone to become asymmetric. The accretions in the uptake can be expected to alter the mixing conditions in the uptake.

A typical schematic of the uptake accretions observed in the plant is given in figure 7.2.1, illustrating the stages of build-up accumulation. The basis for this schematic was visual inspections through a view port in the uptake roof. The accretion thickness on the uptake walls was estimated from thermographic studies of the uptake steel shell. The thermal conductivity of the accretions has been estimated to be 1.6 W/m/°C (Lee, 1995).

Periodic visual inspections in the plant revealed that the first accretions to form were around the afterburner ports near the base of the uptake. These accretions, more commonly referred to as "horns", formed due to the cooling effect caused by the introduction of oxygen and recycled scrubbed furnace gas through the port. In the air model, the impact of horns on the mixing in the uptake was significant, disrupting the uniformity of mixing achieved with the interlaced jet configuration (Chapter 5 Section 5.2.1.3). Experimental findings indicated that horn length in excess of 60 cm would adversely affect the degree of mixing achieved in the plant. Horn growth reached these lengths after 2-3 months of operations.

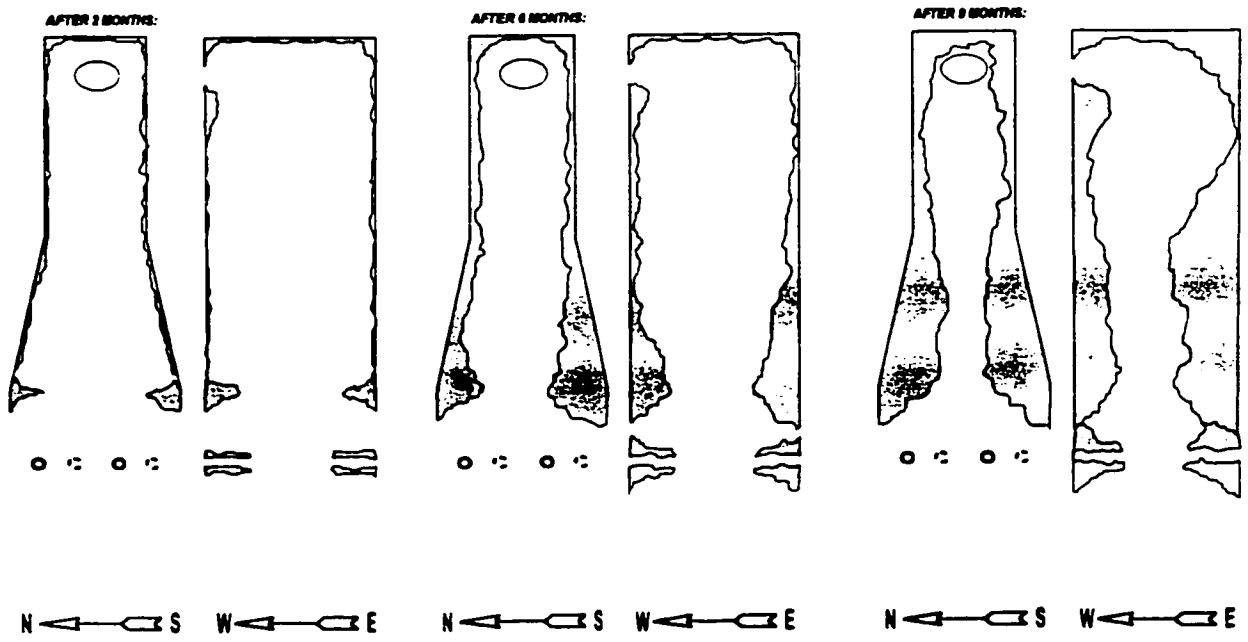

Figure 7.2.1 Schematic Representation of Uptake Accretions in the Plant

The next accretions to form were noted in the bottom corners of the tapered section of the uptake. In the physical modeling experiments, it was observed that a small zone of flow separation formed in these corners. A second flow separation zone was observed in the top corner of the uptake, resulting in the accumulation of build-up.

In the plant, the methods of controlling these accretions are by raising the operating temperature of the uptake or by physically removing the build-up that accumulates around the outlet. The normal operating temperature range for the uptake is 1280-1300°C. Laboratory experiments have revealed that the accretions in the uptake become fluid at temperatures in excess of 1325°C. This approach to removing build-up in the uptake has proven to be effective. However, as the build-up becomes fluid, it tends to be more corrosive to the castable lining used in the uptake. This observation led to a laboratory program aiming at finding a lining material which could better withstand the corrosive conditions prevailing in the uptake (Molino et al., 1997).

Although infrequent, physical removal of the accretions is required, especially, around the outlet of the uptake. This is accomplished with a mobile pneumatic hammer. Accretions in the upper

section of the uptake tend to accumulate preferentially along the discharge side, leading to the formation of a ledge and the eventual blockage of the outlet. This observation is in agreement with the modeling studies, which showed that the position of the outlet affected the flow patterns in the upper sections of the uptake (Chapter 6 Figure 6.2.8). The outlet induced higher velocities along the discharge side, which would tend to carry more entrained particulate.

7.2.1 Mixing in the Uptake

The physical modeling experiments illustrated that the most important factor affecting the mixing in the uptake was the configuration of the afterburner jets. The interlaced jet configuration, labeled configuration "F", produced the best mixing conditions between the afterburner jet gas and the furnace gas. Based on the results of the physical modeling studies, configuration F was selected for implementation in the plant in 1996.

The modifications to the plant resulted in effective temperature control and uniformity, thus indicating more effective furnace gas and afterburner gas mixing. Thermographic studies showed uptake shell temperature variations within 30°C versus 100°C for the previous uptake during the first few months of operation. The deposition of accretions on the uptake walls formed a thinner and more uniform layer. However, the formation of horns around the afterburner ports persisted, although the new afterburner configuration has permitted the development of a technique to control horn growth. This technique which involves shutting down the afterburner port was found to adversely affect the uniform mixing patterns produced with configuration F in the uptake and led to the accumulation of material on the walls. The significance of shutting down one jet was investigated in the water model by Baird (1998), confirming the plant observations.

In attempt to quantify the degree of combustion occurring in the plant, samples of gas and particulate were extracted from the uptake, using the sampling technique described in Appendix C. The samples were collected within the first few months of operation, prior to the accumulation of significant accretions on the uptake walls. The results, summarized in table 7.2.1, compare two

afterburner configurations (A and F) used in the plant, with respect to oxygen utilization and the degree of particle combustion.

The utilization of the afterburner oxygen was calculated based on the oxygen content of the gas stream after correcting for the background concentration. The background oxygen concentration was established by collecting samples during periods of no oxygen addition to the uptake. The high background oxygen content in the gas samples was at first rather worrying, possibly indicating severe contamination of the sample with air. However, the consistency of the gas analyses suggested that there was a systematic error in the sampling method. In all samples the oxygen content measured in the sample was very consistent (2.3-2.4 % O_2 v/v).

Based on this analysis, the utilization of the afterburner oxygen in the uptake was close to 100%. Although the data collected is limited, there is indication that the afterburner oxygen introduced via afterburner configuration F reacted more rapidly than with configuration A. These preliminary findings agree with the findings of the physical modeling experiments.

The degree of particle combustion was examined based on the mass ratio of iron-to-sulphur and nickel-to-sulphur in the dust samples. For this analysis the elements of iron and nickel were selected since the nickel-to-iron mass ratio remained very constant (table 7.1.1). In contrast, the copper-to-nickel and the copper-to-iron ratios in the dust were very much greater (20%) than the same ratio in the concentrate for all tests. This indicated that the copper was being preferentially concentrated in the dust by some mechanism. Munroe (1987) attributed the copper enrichment of the dust to either fragmentation of the copper particles in the concentrate or to the volatilization of copper, as reported by Jorgensen (1983).

In all tests, the value of the iron-to-sulphur and nickel-to-sulphur mass ratios increased significantly over the background ratio, as determined from the samples collected during periods of no oxygen addition to the uptake. As table 7.2.1 shows, the ratios increase steadily with elevation in the uptake, suggesting that the sulphur was being oxidized to form SO_2. The XRD analysis indicated the combustible sulphur in the samples was present as sulfide species and

elemental sulphur (Appendix C Table C.4.8). The elemental sulphur in the samples was assumed to have condensed from the gas phase during cooling in the sampling apparatus. In all test, the quantity of sulfide and elemental sulphur in the samples decreased along the uptake. In addition, there was an increase in the presence of a spinel phase suggesting that the iron was also being oxidized. The spinel phase was identified as magnetite.

Table 7.2.1 Oxygen Utilization and Degree of Combustion in the Uptake

		Sample Location [1]	Oxygen Utilization (%)	Degree of Particulate Combustion Fe/S Ratio	Ni/S Ratio
Configuration A					
Test 1	**$ABO_y/DSC = 0.00$**			0.67	0.15
	$ABO_y/DSC = 0.01$	**4.47 m**	79.0	0.84	0.18
	$ABO_y/DSC = 0.01$	**10.52 m**	94.7	1.06	0.25
Configuration F					
Test 2	**$ABO_y/DSC = 0.00$**			0.77	0.18
	$ABO_y/DSC = 0.013$	**4.47 m**	92.5	0.95	0.23
	$ABO_y/DSC = 0.013$	**4.47 m**	88.7	0.95	0.20
	$ABO_y/DSC = 0.013$	**10.52 m**	98.1	1.15	0.26
	$ABO_y/DSC = 0.013$	**10.52 m**	100.0	1.20	0.27
Test 3	**$ABO_y/DSC = 0.00$**			0.81	0.21
	$ABO_y/DSC = 0.00$			0.85	0.21
	$ABO_y/DSC = 0.01$	**4.47 m**	91.3	0.93	0.22
	$ABO_y/DSC = 0.01$	**10.52 m**	98.8	1.14	0.30

Note #1 The sample location is defined as the distance, in meters, from the afterburner jets.

Chapter 8

CONCLUSIONS

In the present work, the gas flow patterns of the Inco flash furnace have been investigated by physical modeling and numerical modeling techniques. The gas flow patterns in the furnace freeboard were first investigated in the water model and, later in the air model. The computational fluid dynamics code FLUENT v 4.5 was used to simulate the flow through the air model. The objective of this research was to determine the critical phenomena affecting the flow patterns and mixing behaviour in the furnace freeboard and uptake. The major findings of this study are as follows:

- The water and air models produced similar results with respect to the mixing of two fluids of the same phase in the uptake. The velocity profiles measured in the air model were in agreement with the more qualitative observations made in the water model. The flow patterns and velocity profiles were unaffected by the amount fluid flow through the models.

- The mathematical model predictions suggest that the furnace flow is very prone to become asymmetric. It was difficult to make a direct comparison between the simulated and experimental results, as the specific factor(s) causing the asymmetry observed in the air model is not known. The results of the numerical simulations indicated that a very small inequality between the angle and/or flow of the jets can lead to a dramatic asymmetry in the flow pattern. The predicted asymmetric flow conditions and measured dimensionless fields were qualitatively similar. Of course, the

steady state numerical model cannot account for the temporal flow instability at the transition between the furnace and uptake, as observed in the physical models. The flow instability at this transition produced a pulsating-type flow pattern, which was driven by cyclic imbalances of pressure in the system.

- The turbulent jets from adjacent nozzles flowed directly toward the model floor where they combined to form a single jet stream. The strong jets flow make it inevitable that extensive separation from the side walls and roof occurs. The abrupt junction to the uptake amplifies the effect. The large recirculating stream circulates back toward the end wall between the edge of the jets and the walls of the model. Projecting the air model findings to the plant, the amount of recirculation was estimated to be about three times the flow through the burner jets. The predicted amount of recirculation flow from the numerical simulation was in good agreement with the experimental values. The small difference between predicted values suggested that factors, such as jet angle and flow imbalances, had only minor effect on the amount of recirculation.

- The degree of mixing homogeneity in the uptake under different afterburner configurations investigated the effect of Reynolds number, jet momentum and axial distance. In the range applicable to the plant operation, the effect of Reynolds number and jet momentum on the mixing was very weak. The most significant factor affecting the mixing is the afterburner configuration. The afterburner configuration, which provided the best mixing conditions, had staggered opposite pairs of jets flowing at 90° to the axis of the furnace. The staggered jet arrangement allowed for maximum coverage of the uptake cross-section while keeping the opposing jets close enough that they still interact. This configuration was implemented in the plant at Copper Cliff in 1996.

8.1 Future Work

The present research has lead to new findings in the flow dynamics in the Inco flash smelting furnace. These new facts of flow instability, flow recirculation and sensitivity to small asymmetries provide a better understanding of the non-ideal flow behaviour occurring in the gas space of the furnace. In order to realize future productivity gains, further modeling is warranted to expand our knowledge of the transport phenomena specific to the Inco flash smelting furnace. In this effort, consideration should be given to process improvements with practical usefulness, for example:

- An increased smelting intensity, as characterized by the specific smelting rate (Kellogg and Diaz, 1992), would allow the possibility to construct smaller furnaces or make the current ones more efficient by increasing the smelting intensity.

- By reducing the flow instability at the furnace-uptake transition, an improved flow distribution in the uptake could be achieved which, according to the findings in the present study, would improve the mixing between afterburning and furnace gases.

- The concentrate burner design has a significant effect on the dust generation rate in the Outukumpu flash furnace, as demonstrated by Kemori et al. (1991). An improved burner design should be pursued to reduce the dust generation rate associated with nickel concentrate flash smelting. The optimal burner design, to reduce dusting and achieve uniform combustion of the concentrate particles, would be one in which the solids and the gas are dispersed at similar rates.

During the course of the present study, several other areas for additional research have been identified.

- There was qualitative agreement between predicted and experimental flow conditions. There was, however, limited experimental data available for defining the velocity field

in the furnace gas space. Experimental verification of the model predictions will be essential to better understand the interaction of adjacent jets.

- Qualitatively, a single phase system would behave in a similar manner to a two phase (solids-gas) system. However, the sensitivity of jet deflection and flow asymmetry should be quantified to simulate the conditions with a two phase system.

- The numerical model should be expanded to consider the effects of chemical reactions and the transport of mass and heat associated with the operation of the flash furnace. This model could be used to further our understanding of the mechanism for dust generation and accretion accumulations on the furnace and uptake walls.

REFERENCES

Antonioni, T.N., Church, A.D., Landolt, C.A. and Partelpoeg, E.H., "Operations on the INCO Flash Smelting Furnace with Recycle of Converter Slag", 18th Annual Conference of Metallurgists, CIM, Sudbury, Ontario, 1979.

ADM staff, "Flash Furnace Burner Model Study", report submitted to INCO, 1989.

ASARCO Staff, "Oxygen Furnace, Burner Study", Internal Report, 1987.

Baird, M.H.I. and Rice, R.G., "Axial Dispersion in Large Unbaffled Columns", The Chemical Engineering Journal, Volume 9, 1975, pp. 171-174.

Baird, M.H.I., Marcuson, S.W., Diaz, C.M. and Rohatgi, A., "Slag Mixing in the Inco Flash Furnace", in Proceedings of the Copper 91 - Cobre 91 International Symposium, C.M.Diaz, C.A.Landolt, A.Luraschi and C.J.Newman eds., Pergamon Press, Elmsford, New York, 1991, pp. 155-168.

Baird, M.H.I. and Rao, R., "Progress Report # 4: Burner Modeling", submitted to INCO, 1995.

Baird, M.H.I., Moruzi, P.G., Irons, G. A., Diaz, C.M. and Marcuson, S.W., "Simulation and Modelling of Slag Mixing in the Inco Flash Furnace", Canadian Metallurgical Quarterly, Vol 35, No.5, 1996, pp 451-462.

Baird, M.H.I. and Rao, R., "Progress Report # 5- Burner Modeling", submitted to Inco, 1996.

Baird, M.H.I and Moruzi, P.G., "Progress Report #2 - Mixing in Uptake of Water Model", submitted to Inco, 1998.

Birkhoff, G., Zarantonello, E.H., Jets, Wakes, and Cavities, Academic Press, 1957.

Biswas, A.K. and Davenport, W.G., Extractive Metallurgy of Copper, 3rd Edition, Elsevier Science Inc, New York, 1996.

Bohnet, M. and Wagenknecht, U., "Investigations of Flow Conditions in Gas/Solid - Injectors", German Chemical Engineering 1, 1978, pp. 298-304.

Boldt, J.R. and Queneau, P., The Winning of Nickel, Longmans Canada Limited, Toronto, 1967.

Chaubal, P.C. and Sohn, Y.H., "Intrinsic Kinetics of the Oxidation of Chalcopyrite Particles", Metallurgical Transactiond B. Vol. 17B, 1986, pp. 51-60.

Crowe, C.T., Sharma, M.P. and Stock, D.E., "The Particle-Source-In Cell (PSI-Cell) Model for Gas-Droplet Flows", Journal of Fluids Engineering, June, 1977, pp. 325-332.

Davenport, W.G. and Partelpoeg, E.H., Flash Smelting Analysis, Control and Optimization, Pergamon Press, Oxford, 1987.

Diaz, C.M. and Landolt, C.A., "Metallurgy of the INCO Flash Furnace with Converter Slag Recycle", Minerales, 41, 1986, pp. 175-186.

Doyle, C., "Inco Internal Report: Temperature Dependence of Attack by Build-up on the Castable Lining the Uptakes of the Flash Furnaces at the Copper Cliff Smelter", 1994.

Doyle, C., "Inco Internal Report: Evaluation of Candidate Flash Furnace Uptake Refractories", 1995.

Dunn, J.G. and Smith, T.N., "Flash Smelter Shaft Operation", Western Australian Mining and Petroleum Research Institute, Report No. 7, July, 1984

Elliot, B.J., Jorgensen, F.R. and Kemori, N., "Aspects of Burner Design for Flash Smelting", in Metallurgical Processes for Early Twenty-First Century, H.Y.Sohn ed., The Minerals, Metals and Materials society, 1994, pp. 943-962.

Field, M.A., Gill, D.W., Morgan, B.B. and Hawksley, P.G.W., Combustion of Pulversied Coal, The British Coal Utilisation Research Association, Cheney and Sons Ltd., Banbury, England, 1967.

FLUENT User's Manual, Version 4.5, 1996.

Fukunaka, Y., Nakashita, S., Asaki, Z. and Kondo, Y., :A Modeling on the Pyrite Smelting Process" World Mining and Metal Technology Proceedings of the Joint MMIJ-AIME Meeting, editor A.Weiss, Denver, Colorado, September, 1976, pp 481-504.

George, D.B., Gottling, R.J., Newman, C.J., "Modernization of the Kennecott Utah Copper Smelter", Volume IV - Pyrometallurgy of Copper, Proceedings of Copper 95 - Cobre 95 International Conference, W.J.Chen, C.Diaz, A.Luraschi and P.J.Mackey eds., 1995, pp. 41-52.

Goldschmidt, V. and Eskinazi, S., "Two-Phase Turbulent Flow in a Plane Jet", Journal of Applied Mechanics, December, 1966, pp. 735-747.

Gordon, J.R., Newman, G.H., Queneau, P., Sproule, W.K. and Young, C., U.S.Patent No. 2,668,107 issued 1954.

Gosman, A.D., Pun, W.M., Runchal, A.K., Spalding, D.B. and Wolfshtein, M., Heat and Mass Transfer in Turbulent Recirculating Flows, Academic Press, London, 1969.

Hahn, Y.B. and Sohn, H.Y., "Prediction of the Behaviour of a Particle-Laden Gas Jet as Related to the Flash-smelting Process", in Innovative Technology and reactor Design in Extractive Metallurgy, Proceedings of the R.Schuhmann Symposium, D.R.Gaskell, J.P.Hager, J.E.Hoffmann and P.J.Mackey eds., TMS-AIME, 1986, pp. 469-499.

Hahn, Y.B. and Sohn, H.Y., "The Trajectories and Distribution of Particles in a Turbulent Axisymmetric Gas Jet Injected into a Flash Furnace Shaft", Metallurgical Transactions B, Volume 19B, December, 1988, pp. 871-884.

Hahn, Y.B. and Sohn, H.Y., "Mathematical Modeling of Sulfide Flash Smelting Process: Part I. Model Development and Verification with Laboratory and Pilot Plant Measurements for Chalcopyrite Concentrate Smelting", Metallurgical Transactions B, Volume 21B, December, 1990, pp. 945-958.

Hahn, Y.B. and Sohn, H.Y., "Mathematical Modeling of Sulfide Flash Smelting Process: Part II. Quantitative Analysis of Radiative Heat Transfer", Metallurgical Transactions B, Volume 21B, December, 1990, pp. 959-966.

Hanniala, P., and Kojo, I.V. and Kyto, M., "The Kennecott-Outokumpu Flash Converting Process - Facts and Fiction", in Converting, Fire Refining and Casting, The Mineral, Metals and Materials Society, J.D.McCain and J.M.Floyd eds., 1993, pp 107-116.

Hinze, J.O., Turbulence, 2nd Edition, McGraw-Hill Book Company, New York, 1975

Humphris, M.J., "Inco Internal Report: Conical Diverging Burner Test", 1990.

Humphris, M.J., Carr, H., Longo, A., "The Smelting of Bulk Cu-Ni Concentrates at the Inco Copper Cliff Smelter", in Pyrometallurgical Operation, the Environment and Vessel Intergrity in Nonferrous Smelting and Converting, Proceeding of the Nickel-Cobalt 97 International Symposium - Volume III, 1997, pp 5-16.

Hutchinson, B.R. and Raithby, G.D., "A Multigrid Method Based on the Additive Correction Stradegy" Numerical Heat Transfer, Vol. 9, 1986, pp. 511-537.

INCO Staff, "The Oxygen Flash Smelting Process of the International Nickel Company", CIM Transactions, 58, 1955, pp. 158-166.

INCO Staff, "Oxygen Flash Smelting in a Converter", presented at the 106th AIME Annual Meeting, Atlanta, Georgia, March 7-11, 1977.

Jorgensen, F.R.A. and Segnit, E.R., "Copper Flash Smelting Simulation Experiments". Proceeding of the Australasian Institute of Mining and Metallurgy, No. 261, 1977, pp. 39-46.

Jorgensen, F.R.A., "The ignition Temperature of A Nickel Concentrate From Kambalda Under Simulated Flash Smelting Conditions", Proceeding of the Australasian Institute of Mining and Metallurgy, No. 268, December, 1978, pp. 47-55.

Jorgensen, F.R.A., "Heat Transfer Mechanism in Ignition of Nickel Sulphide Concentrate under Simulated Flash Smelting Conditions", Proceeding of the Australasian Institute of Mining and Metallurgy, No. 271, September, 1979, pp. 21-25.

Jorgensen, F.R.A., "Single-Particle Combustion of Chalcopyrite", Proceeding of the Australasian Institute of Mining and Metallurgy, No. 268, December, 1983, pp. 37-45.

Jorgensen, F.R.A, Moyle, F.J., and Wadsley, M.W., "The ignition of Chalcopyrite and Pyrite During Flash Smelting", in Flash Reaction Processes, D.G.C.Robertson, H.Y.Sohn, and N.J.Themelis ed., University of Utah, Salt Lake City, Utah, June 15-17, 1988, published by The Center For Pyrometallurgy, University of Missouri-Rolla, Rolla, Missouri, pp. 167-189.

Jorgensen, F.R.A. and Elliot, B.J., "Flash Furnace Reaction Shaft Evaluation Through Simulation", in Extractive Metallurgy of Gold and Base Metals, V.N.Misra, D.Halbe and D.J.Spottiswood eds., The Australasian Institute of Mining and Metallurgy, Publication Series No.9, 1992.

Kellog, H.H. and Diaz, C, "Bath Smelting Processes in Non-Ferrous Pyrometallury: an Overview", in Savard-Lee International Symoposium on Bath Smelting, J.K.Brimacombe, P.J.Mackey, G.J.W.Kor, C.Bickert and M.G.Ranade eds., TMS, Warrendale, Pennsylvania, 1992, pp 39-63.

Kemori, N., Ojima, Y. and Kondo, Y., "Variation of the Composition and Size of copper Concentrate Particles in the Reaction Shaft", in Flash Reaction Processes, D.G.C.Robertson, H.Y.Sohn, and N.J.Themelis ed., University of Utah, Salt Lake City, Utah, June 15-17, 1988, published by The Center For Pyrometallurgy, University of Missouri-Rolla, Rolla, Missouri, pp. 47-68.

Kemori, N., Akada, A. and Kondo, Y., "Development of a Concentrate Burner for Industrial Oxygen Flash Smelting", in Proceedings of the Copper 91 - Cobre 91 International Symposium, C.M.Diaz, C.A.Landolt, A.Luraschi and C.J.Newman eds., Pergamon Press, Elmsford, New York, 1991, pp. 141-154.

Kim, Y.H. and Themelis, N.J., "Effect of Phase Transformation and Particle Fragmentation on the Flash Reaction of Complex Metal Sulphides", in Innovative Technology and reactor Design in Extractive Metallurgy, Proceedings of the R.Schuhmann Symposium, D.R.Gaskell, J.P.Hager, J.E.Hoffmann and P.J.Mackey eds., TMS-AIME, 1986, pp.349-369

Kimura, T., Ojima, Y., Mori, Y. amd Ishii, Y., "Reaction Mechanism in a Flash Smelting Shaft", in The Reinhardt Schuhmann International Symposium on Innovative Technology and Reactor Design in Extractive Metallurgy, D.R.Gaskell, J.Phager, J.E.Hoffman and P.J.Mackey, Warrendale Pennsylvania, 1986, pp 403-418.

Kirshner, J.M. and Katz, S., Design Theory of Fluidic Components, Academic Press, New York, 1975.

Koh, P.T. and Taylor, R.N., "Mathematical Modelling of Heat Transfer in Flash-Smelting Burners", in Extractive Metallurgy of Gold and Base Metals, V.N.Misra, D.Halbe and D.J.Spottiswood eds., The Australasian Institute of Mining and Metallurgy, Publication Series No.9, 1992.

Launder, B.E. and Spalding, D.B., "The Numerical Computation of Turbulent Flow", Computer Methods in Applied Mechanics and Engineering, Vol. 3, 1974, pp. 269-289.

Lee, P, "Inco Internal Reoprt: Thermal Conductivity Measurements in #1 Flash Furnace Uptake", 1995.

Levenspiel, O., Chemical Reaction Engineering, 2nd ed., John Wiley and Sons Inc., New York, 1972.

Leys, J.A. and Leigh, E.T., "Aerodynamic Factors Associated with the Wear of Open-Hearth Furnace Roofs", The Journal of the Iron and Steel Institute, Vol. 170, April, 1952, pp. 336-342.

MacCallum, C., "Controlled Combustion-Zone Firing for Hogged Fuel in New and Retrofit Boiler Applications", The Journal of the Technical Association of the Pulp and Paper Industry, Volume 66, No.9, 1983.

Marcuson, S.W., "Flash Furnace Tracer Studies", INCO Limited, Internal Report, 1985.

Melville, W.K. and Bray, K.N.C., "The Two-Phase Turbulent Jet", International Journal of Heat and Mass Transfer, Volume 22, 1979, pp.279-287.

Mäkinen, T. and Kyto, M., "Pilot and Mini-Pilot Tests of Flash Reactions", in Flash Reaction Processes, D.G.C.Robertson, H.Y.Sohn, and N.J.Themelis Ed., University of Utah, Salt Lake City, Utah, June 15-17, 1988, published by The Center For Pyrometallurgy, University of Missouri-Rolla, Rolla, Missouri, pp. 69-98.

Molino, L., "Slag Mixing in the INCO Nickel Flash Furnace", M.Sc.Thesis, McMaster University, 1994.

Molino, L, Diaz, C.M., Doyle, C., Hrepic, J., Slayer, R., Carr, H., Baird, M.H.I., "Recent Design Improvements to the Inco Flash Furnace Uptake", in Pyrometallurgical Operation, the Environment and Vessel Intergrity in Nonferrous Smelting and Converting, Proceeding of the Nickel-Cobalt 97 International Symposium - Volume III, 1997, pp 527-537.

Moon, L.F. and Rudinger, G., "Velocity Distribution in an Abruptly Expanding Circular Duct", Journal of Fluids Engineering, Volume 99, March, 1977, pp.226-230.

Munro, N.D.H. and Themelis, N.J., "Rate Phenomena in a Laboratory Flash Smelting Reactor", Proceedings of the Copper 91 - Cobre 91 International Symposium, C.M.Diaz, C.A.Landolt, A.Luraschi and C.J.Newman eds., Pergamon Press, Elmsford, New York, 1991, pp. 475-494.

Munroe, N,D,H., "Simulation of Flash Smelting Phenomena in a Laboratory Reactor", Ph.D. Dissertation, Columbia University, 1987.

Nossier, N.S. and Behar, S., "Characteristics of Jet Impingment in a Side-Dump Combustor", American Institute of Aeronautics and Astronautics, Volume 24, November 1986, pp. 1752-1757.

Nguyen, T.V., Taylor, R.N. and Hall, T.P., " Fluid Flow Modelling in a Nickel Flash Smelter- A Simulation Study", in Extractive Metallurgy of Gold and Base Metals, V.N.Misra, D.Halbe and D.J.Spottiswood eds., The Australasian Institute of Mining and Metallurgy, Publication Series No.9, 1992.

O'Leary, C.D. and Forney, L.J., "Optimization of In-Line Mixing at a 90° Tee", Industrial and Engineering Chemistry Process Design and Development, Volume 24, 1985, pp. 332-338.

Otero, A., Brimacombe, J.K. and Richards, G.G., "Kinetics of the Flash Reaction of Copper Concentrates", in Proceedings of the Copper 91 - Cobre 91 International Symposium, C.M.Diaz, C.A.Landolt, A.Luraschi and C.J.Newman eds., Pergamon Press, Elmsford, New York, 1991, pp. 459-473.

Pannel, D.B., " A Survey of World Copper Smelters" in World Survey of Nonferrous Smelter, J.C.Taylor and H.Traulson ed., Pyrometallurgical Society of T.M.S., TMS-AIME meeting, Phoenix, January 25-29, 1988, pp. 3-118.

Partelpoeg, E.H., "Flash Smelting Reaction at the Phelps Dodge Hidalgo Smelter", in Flash Reaction Processes, Center for Pyrometallurgy Conference, University of Utah, Salt Lake City, Utah, June, 1988, pp. 35-45.

Patankar, S.V., Numerical Heat Transfer and Fluid Flow, Hemisphere Publishing Corporation, New York, 1980.

Rajaratnam, N., Turbulent Jet, Elsevier Scientific Publishing Company, New York, 1976

Robie, R.A, Hemingway, B.S. and Fisher, J.R, Thermodynamic Properties of Minerals and Related Substances at 1 Bar Pressure and at Higher Temerpatures, Unites States Government Printing Office, Washington, 1978

Rodi, W., Turbulence Models and Their Application in Hydraulics, 2nd Edition, Delft, Netherlands, 1984.

Ruottu, S., "The Description of a Mathematical Model for the Flash Melting of Cu-Concentrates", Combustion and Flame, 34, 1979, pp. 1-11.

Saffman, P.G., and Turner, J.S., " On the Collision of Drops in Turbulent Clouds", Journal of Fluid Mechanics, Vol. 1, 1956, pp. 16-30.

Smith, T.N., "Model Study of Gas Flow in Kalgoorlie Nickel Smelter", Fifth Australian IMM Extractive Metallurgy Conference, 1991, pp 245-250.

Smoot, L.D. and Smith, P.J., Coal Combustion and Gasification, The Plenum Chemical Engineering Series, Plenum Press, New York, 1985.

Solar, M.Y., Neal, R.J., Antonioni, T.N., Bell, M.C., "Smelting Nickel Concentrates in INCO's Oxygen Flash Furnace", Journal of Metals, 31 (1), 1979, pp.26-31.

Sridhar, R. and Dalvi, A, "Inco Report: Estimation of Heat of Formation of Pentlandite", 1975.

Sroka, L.M. and Forney, L.J., "Fluid Mixing with a Pipeline Tee: Theory and Experiment", American Institute of Chemical Engineering Journal, Vol. 35, No.3, March, 1989, pp. 406-414.

Sutalo, I.D., Harris, J.A., Jorgensen, F.R. and Gray, N.B., "Model Studies of Transient Flow Through a Flash Smelting Burner and Shaft", in Metallurgical Processes for Early Twenty-First Century, H.Y.Sohn ed., The Minerals, Metals and Materials society, 1994, pp. 823-839.

Szekely, J., Fluid Flow Phenomena in Metals Processing, Academic Press, New York, 1979.

Tennankore, K.N. and Steward, F.R., "Comparison of Several Turbulence Models For Predicting Flow Patterns within Confined Jets", Canadian Journal of Chemical Engineering, Volume 56, December, 1978, pp.673-678.

Tennekes, H. and Lumley, J.L., A First Course in Turbulence, The MIT Press, Cambridge, Massachusetts, 1992.

Themelis, N.J., Wu, L. and Jiao, Q., "Some Aspects of Mathematical Modelling of Flash Smelting Phenomena", Proceedings of the Copper 91 - Cobre 91 International Symposium, C.M.Diaz, C.A.Landolt, A.Luraschi and C.J.Newman eds., Pergamon Press, Elmsford, New York, 1991, pp. 263-285.

Thring, M.W., The Science of Flames and Furnaces, 2nd Edition, John Wiley and Sons Inc, New York, 1962.

Thring, M.W. and Newby, M.P., "Combustion Length of Enclosed Turbulent Jet Flames", in Fourth Symposium (International) on Combustion, B.Lewis, H.C.Hottel and A.J.Nerad eds., The Williams and Wlkins Company, Baltimore, 1952, pp. 789-796.

Uhl, V.W. and Gray, J.B., Mixing Theory and Practice, Vol. I, Academic Press, New York, 1966.

Victorovich, G.S., Diaz, C.M. and Raskauskas, J., "Impurity Distribution, Dusting and Control of Matte Grade in INCO Oxygen Flash Smelting", in Anales del Congresso Cincuentenario Mineria des Cobres Porfidicos, Vol. III, 1980, pp. 325-347.

Victorovich, G.S. and Timberg, L., "Factors Affecting Copper Losses and Magnetite Precipitation in the Flash Smelting Operation", INCO Limited, Internal Report, 1984.

Yasuda, Y. and Sohn, H.Y., "Particle Dispersion Phenomena in a Turbulent Gas Jet of the Flash Smelting Process", in EPD Congress 1994, G.Warren ed., The Minerals, Metals and Materials Society, 1994, pp. 753-777.

Appendix A

WATER MODEL EXPERIMENTAL CONDITIONS AND RAW DATA

To complete some of the experimental objectives described in the Chapter 3, a $^{1}/_{20}{}^{th}$ linear scale isothermal water model of the commercial furnace was constructed. The water model work was concentrated on describing the flow patterns in the uptake and relating the findings to plant observations. Similarity of the flow patterns in the uptake was expected between the model and the plant given the close agreement of the scaling criteria (Table 4.1.4). The techniques, employed to collect both qualitative and quantitative information about the flow conditions in the uptake, included: flow visualization, using acid-base reactions and neutrally buoyant particles, and chemical tracer studies, using inert tracers. A full description of the experimental techniques is given in section 4.2.2. This appendix summarizes the experimental conditions and the raw data collected from each experimental run.

A.1. Flow Visualization in Water Model - Acid-Base Reaction

As discussed in section 4.2.2.1, acid-base reactions were selected to observe the mixing behaviour because they are extremely fast and are diffusion (mixing) controlled. Similarly, the oxidation reactions occurring in the uptake are also known to be extremely fast and mixing controlled. It therefore seems probable that general similarity of the reaction zones in the uptake may be achieved with the model.

The acid and base solutions used in these experiments were 1 N hydrochloric acid solution (HCl) and 1 N caustic solution (NaOH). The hydrochloric acid solution was added continuously to the

main burner jets while the caustic solution was added to the afterburner jets. The hydrochloric acid solution was fed at a stoichiometric ratio of 1.5 with the caustic solution. The 1 N caustic solution was marked with bromothymol blue indicator so that the afterburner jets appeared dark blue in colour. When the alkaline afterburner jets mixed with the acidified bulk flow, the combined flow produced a yellow colour due to the excess acid (pH<6.6). In this way, good mixing of the base with the acidic stream was indicated by a yellow solution exiting the uptake. Under poorly mixed conditions, the base was not completely reacted, showing regions of blue solution exiting the uptake (pH>7.6).

Each experiment was recorded using both video and still photography techniques to permit careful observation of the mixing after the experiment. To simultaneously view both the front and side planes of the uptake, a mirror was positioned adjacent to the uptake at an angle of 45°.

The acid-base reaction experiments provided an excellent method for screening potential afterburner configurations. A total of 6 afterburner configurations were screened using this method; a description and illustration of these configurations and the observed flow patterns is given in table A1.1. The flow conditions, under which these configurations were examined, are tabulated in table A.1.2. Figures A1.1 to A1.6 comprise a series of sequential still photos taken at 0.5 second intervals which illustrate the typical mixing conditions observed in configurations A through F. In these back and white photos, the dark gray regions represent poorly mixed regions in which the base was not completely reacted. Conversely, the light gray regions illustrate well mixed regions wherein the base was completely neutralized.

Table A.1.1 Flow Visualization in Water Model - Afterburner Configurations

Configuration	Schematic	Description of Afterburner Configuration	Flow Pattern Observed in Water Model
A	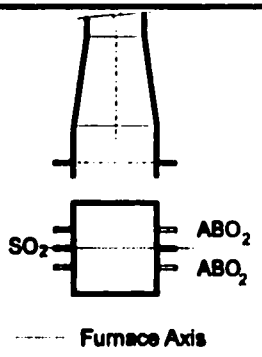	- original afterburner configuration - afterburner oxygen injected through 4 nozzles, two on each opposite wall of the uptake perpendicular to the longitudinal axis of the furnace - SO_2 recycle introduced via two jets, one on each opposite wall of the uptake perpendicular to the longitudinal axis of the furnace	- jet entrained surrounding reacting mixture and assumed a roughly conical shape before jet impingement - head-on impingement of two opposing jets was highly unstable, and jets oscillated along the jet axis due to their impingement and unstable bulk flow - jet-on-jet impingement produced a plume which did not dissipate completely prior to discharge, leading to the periodic discharging of unreacted base - intermittent downward pulsating flow along the uptake walls parallel to the furnace axis (generated at elevation of jets) resulted from temporal flow pattern changes at the furnace uptake transition - complete neutralization of base observed over short intervals primarily when the flow at the transition was downward
B	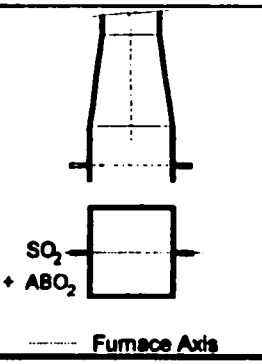	- injection of a blend of oxygen and SO_2 recycle through only two nozzles, one on each opposite wall of the uptake perpendicular to the longitudinal axis of the furnace (tested in plant) - blending oxygen and SO_2 recycle was intended to increase jet momentum and lower post-combustion flame temperature - potential for rapid commercial implementation	- jet behaviour was similar to configuration A with the exception of jet instability which was greater - less mixing of base was observed and the frequency of discharging unreacted base was greater than in configuration A - intermittent downward flow was more pronounced than in configuration A - complete neutralization was rarely observed

Table A.1.1 (cont) Flow Visualization in Water Model - Afterburner Configurations

Configuration	Schematic	Description of Afterburner Configuration	Flow Pattern Observed in Water Model
C	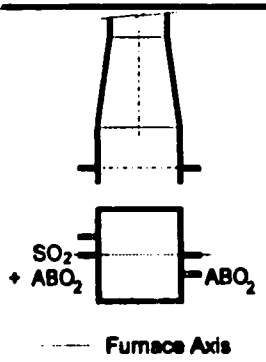	- injection of a blend of oxygen and SO_2 recycle through only two nozzles, one on each opposite wall of the uptake perpendicular to the longitudinal axis of the furnace (tested in plant) - balance of afterburner oxygen injected via two offset nozzles, one on each wall of the uptake perpendicular to the longitudinal axis of the furnace - intended to generate lateral circulation at the plane of injection into the uptake - potential for rapid commercial implementation	- jet behaviour was similar to configuration A with the exception of two afterburner oxygen jets which periodically impinged on the opposing walls of the uptake. -- about the same degree of mixing of base was observed as in configuration B, and the frequency of discharging unreacted base was also similar - frequency of intermittent downward flow was similar to configurations A and B and was confined to the corners. - complete neutralization was rarely observed
D	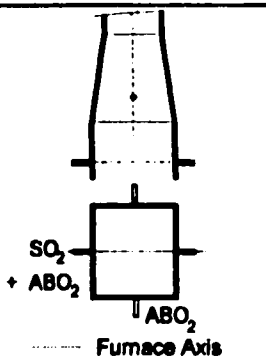	- injection of a blend of oxygen and SO_2 recycle through only two nozzles, one on each opposite wall of the lower section of the uptake perpendicular to the longitudinal axis of the furnace - balance of afterburner oxygen injected via two nozzles, one on each opposite wall of the mid section of the uptake perpendicular to the longitudinal axis of the furnace - intended to stage the post-combustion in the uptake and more uniformly dissipate the heat	- lower momentum of blend oxygen and SO_2 jets in the lower uptake prevented head-on impingement, although oscillation along the jet axis remained apparent due to the unstable flow at the furnace-uptake transition. - jets at higher elevation had insufficient time to thoroughly mix, thus resulting in the discharge of unreacted base. - intermittent downward flow was less obvious than in previous configurations - complete neutralization was not observed

Table A.1.1 (cont) Flow Visualization in Water Model - Afterburner Configurations

Configuration	Schematic	Description of Afterburner Configuration	Flow Pattern Observed in Water Model
E	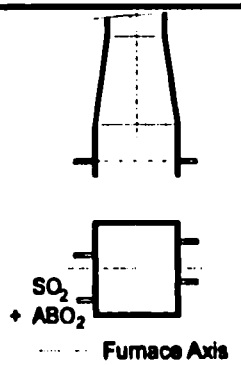	- injection of a blend of oxygen and SO_2 recycle through four nozzles, one on each opposite wall of the uptake perpendicular to the longitudinal axis of the furnace - nozzles were staggered to allow greater coverage of the uptake cross-section without jet-to-jet impingement	- jets were close enough to permit some interaction and periodic impingement of the jets on the opposing wall was noted. - jet oscillation along the jet axis remained apparent due to the unstable flow at the furnace-uptake transition. - frequency of intermittent downward flow was similar to configurations A and B but was primarily observed in the corners. - the frequency of discharging unreacted base was similar to the frequency observed in configuration A, and complete neutralization was observed occasionally
F	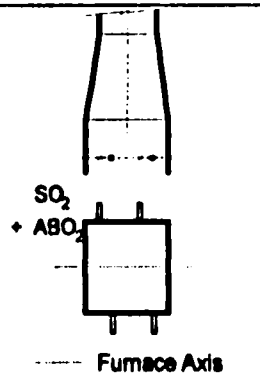	- injection of a blend of oxygen and SO_2 recycle through four nozzles, one on each opposite wall of the uptake parallel to the longitudinal axis of the furnace - nozzles were staggered to allow greater coverage of the uptake cross-section without jet-to-jet impingement - interaction between opposing jets helped induce mixing by creating a shearing effect. - geometry based on the configuration of after-fire jets in industrial waste wood boilers (MacCallum, 1983)	- jets were close enough to permit interaction and no impingement of the jets on the opposing wall was noted but was controlled by adjusting the jet momentum. - jet oscillation along the jet axis was less apparent - the frequency of the intermittent downward flow was less obvious than in previous configurations, and the downward flow lasted for a shorter period - the majority of the base is neutralized in the region above the jets, with the exception of the odd plug which moved straight through to the discharge

Table A.1.2 Flow Visualization in Water Model - Experimental Conditions

Configuration		A	B	C	D	E	F
Burner	Flow (L/min/jet)	87.0	87.0	87.0	87.0	87.0	87.0
	Reynolds # (x 10^3)	92.6	92.6	92.6	92.6	92.6	92.6
	Velocity (m/s)	4.6	4.6	4.6	4.6	4.6	4.6
Furnace	Total Flow (L/min)	348	348	348	348	348	348
	Reynolds # (x 10^3)	10.8	10.8	10.8	10.8	10.8	10.8
	Superficial Velocity (cm/s)	4.0	4.0	4.0	4.0	4.0	4.0
Uptake	Entrance Reynolds # (x 10^3)	27.4	27.4	27.4	27.4	27.4	27.4
	Superficial Entrance Velocity (cm/s)	12.9	12.9	12.9	12.9	12.9	12.9
Afterburner Jet							
	Flow (L/min/jet)	1.96		1.96	1.96		
	Velocity Ratio	31.9		31.9	31.9		
	Momentum Ratio	0.18		0.18	0.18		
	Reynolds # (x 10^3)	13.1		13.1	13.1		
SO_2 Recycle Jet							
	Flow (L/min/jet)	9.10					
	Velocity Ratio	16.5					
	Momentum Ratio	0.43					
	Reynolds # (x 10^3)	20.3					
SO_2 Recycle + O_2 Jet							
	Flow (L/min/jet)		14.00	11.50	11.50	13.00	13.00
	jet diameter, Ø (cm)		0.9525	0.9525	0.9525	0.9525	0.9525
	Velocity Ratio		25.3	20.8	20.8	23.5	23.5
	Momentum Ratio		1.02	0.69	0.69	0.88	0.88
	Reynolds # (x 10^3)		31.2	25.6	25.6	29.0	29.0

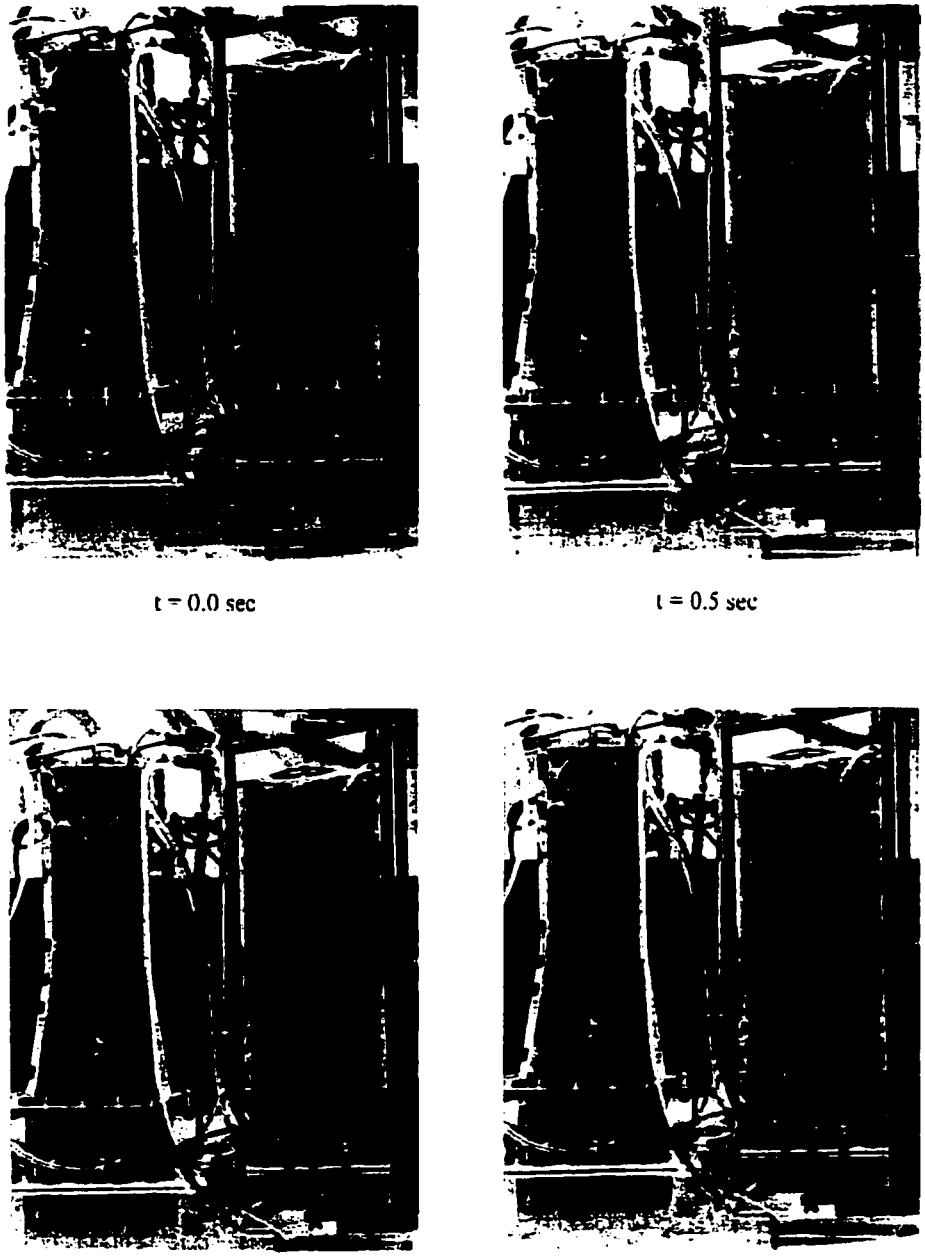

Figure A.1.1 Flow Visualization in Water Model Using an Acid-Base Reaction - Configuration A
(dark gray ≡ unreacted base; light gray ≡ reacted base)

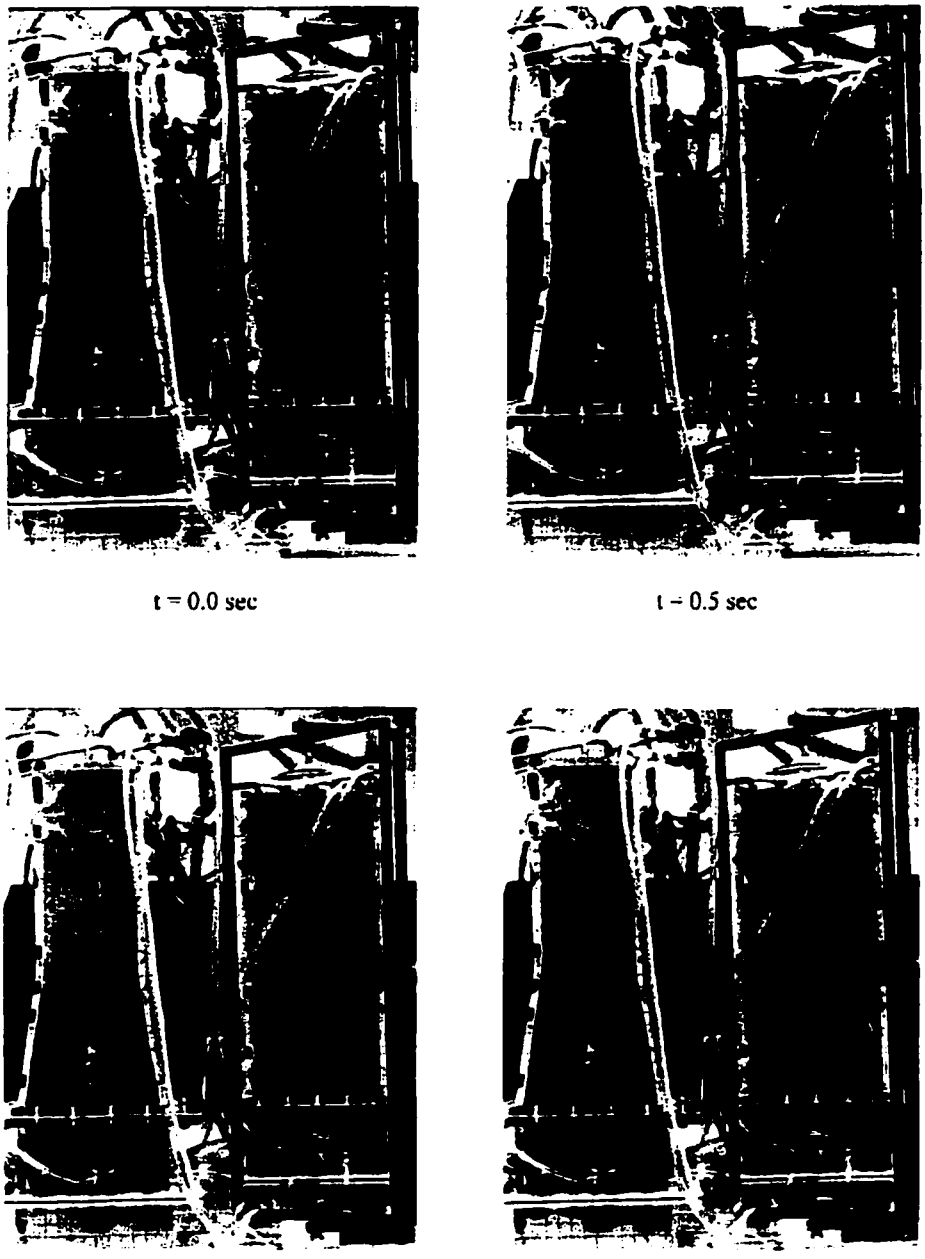

Figure A.1.2 Flow Visualization in Water Model Using an Acid-Base Reaction- Configuration B
(dark gray ≡ unreacted base; light gray ≡ reacted base)

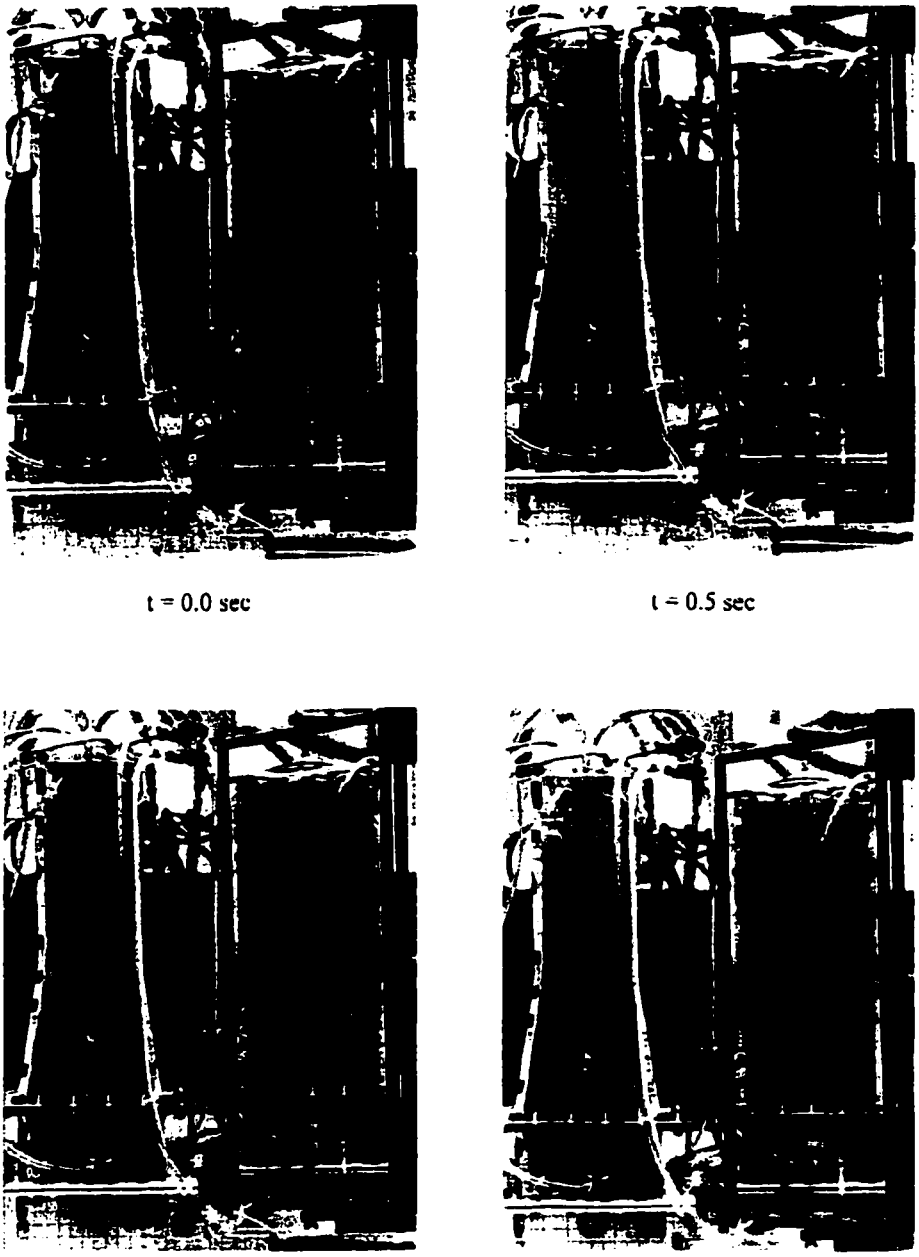

Figure A.1.3 Flow Visualization in Water Model Using an Acid-Base Reaction- Configuration C
(dark gray ≡ unreacted base; light gray ≡ reacted base)

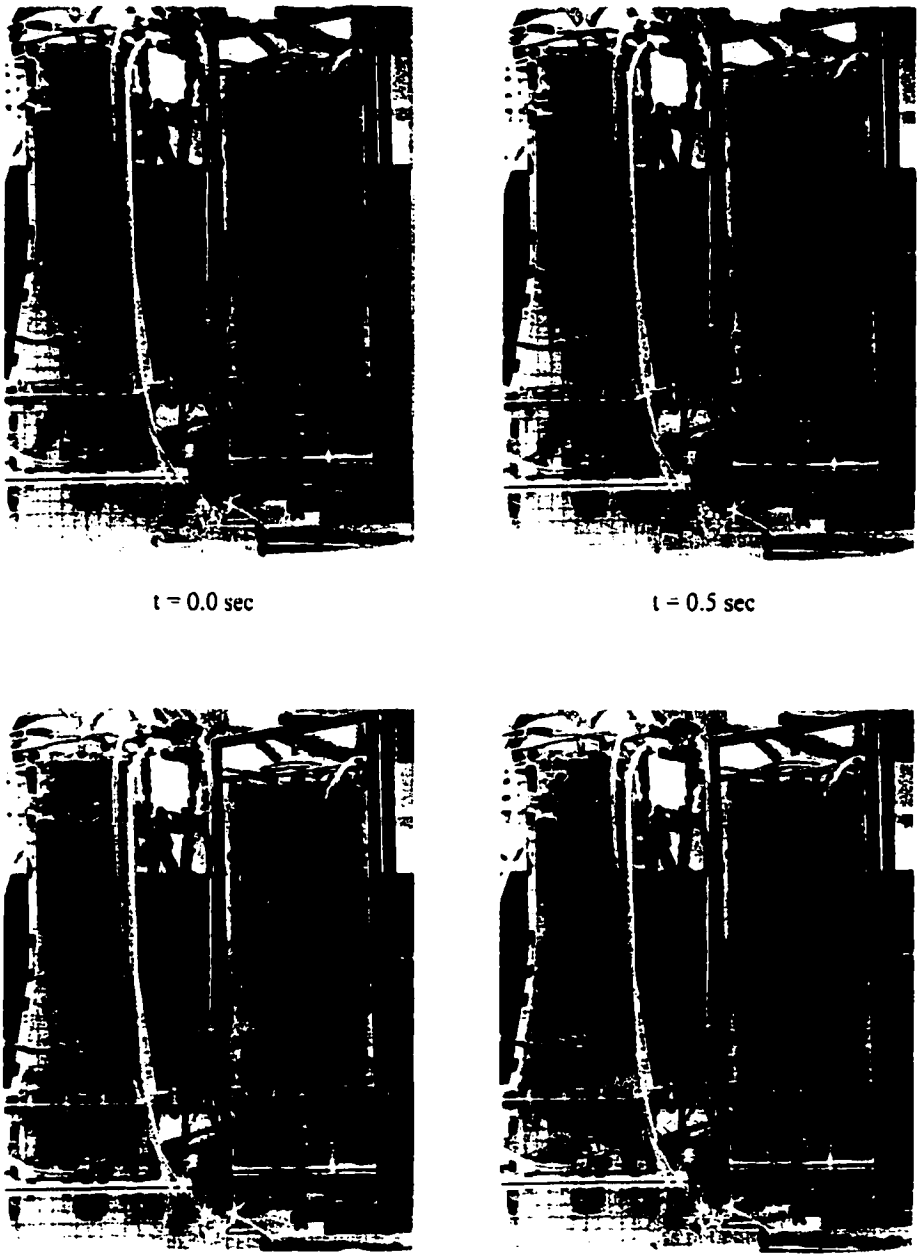

Figure A.1.4 Flow Visualization in Water Model Using an Acid-Base Reaction- Configuration D
(dark gray ≡ unreacted base; light gray ≡ reacted base)

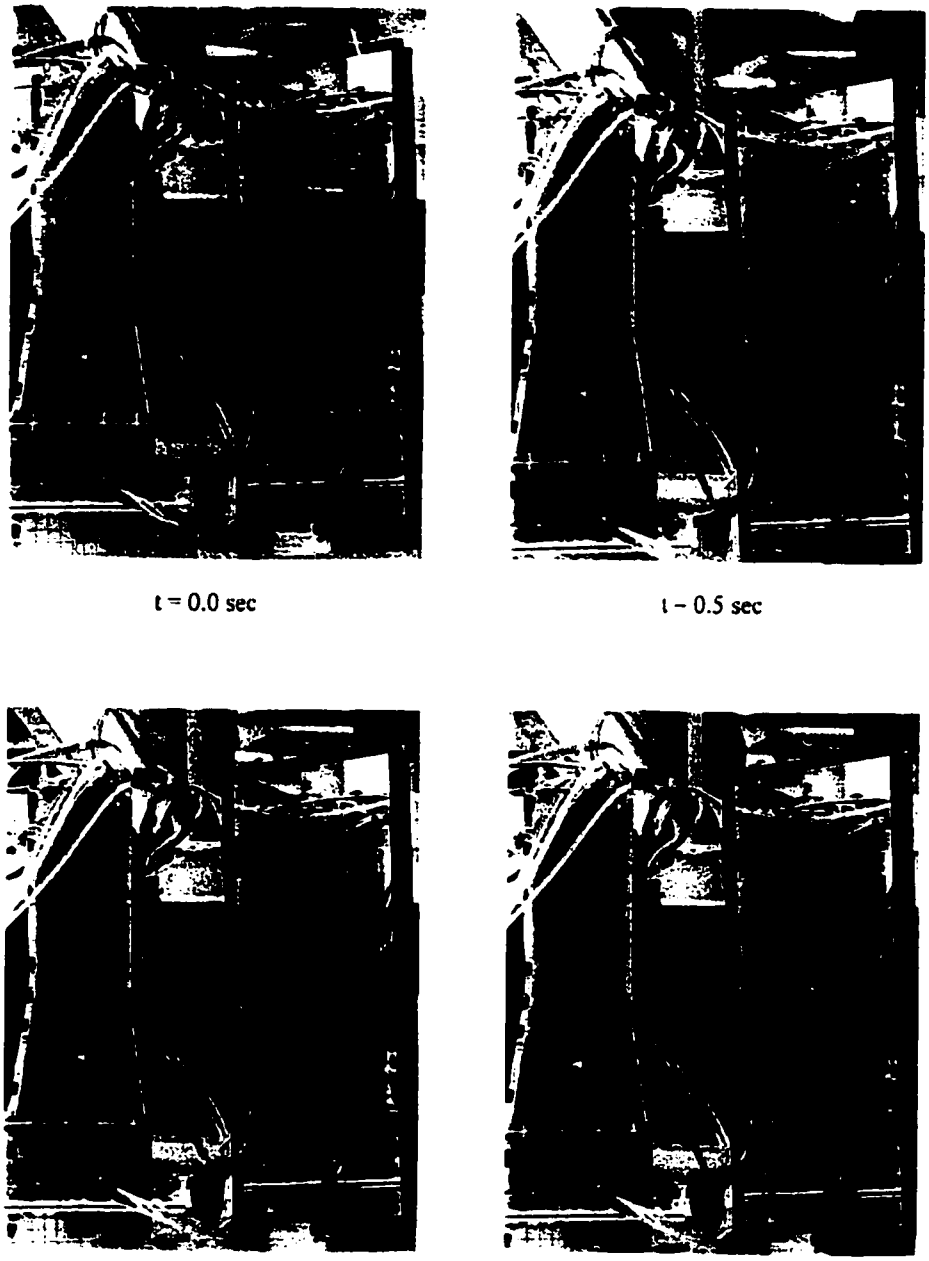

Figure A.1.5 Flow Visualization in Water Model Using an Acid-Base Reaction- Configuration E
(dark gray ≡ unreacted base; light gray ≡ reacted base)

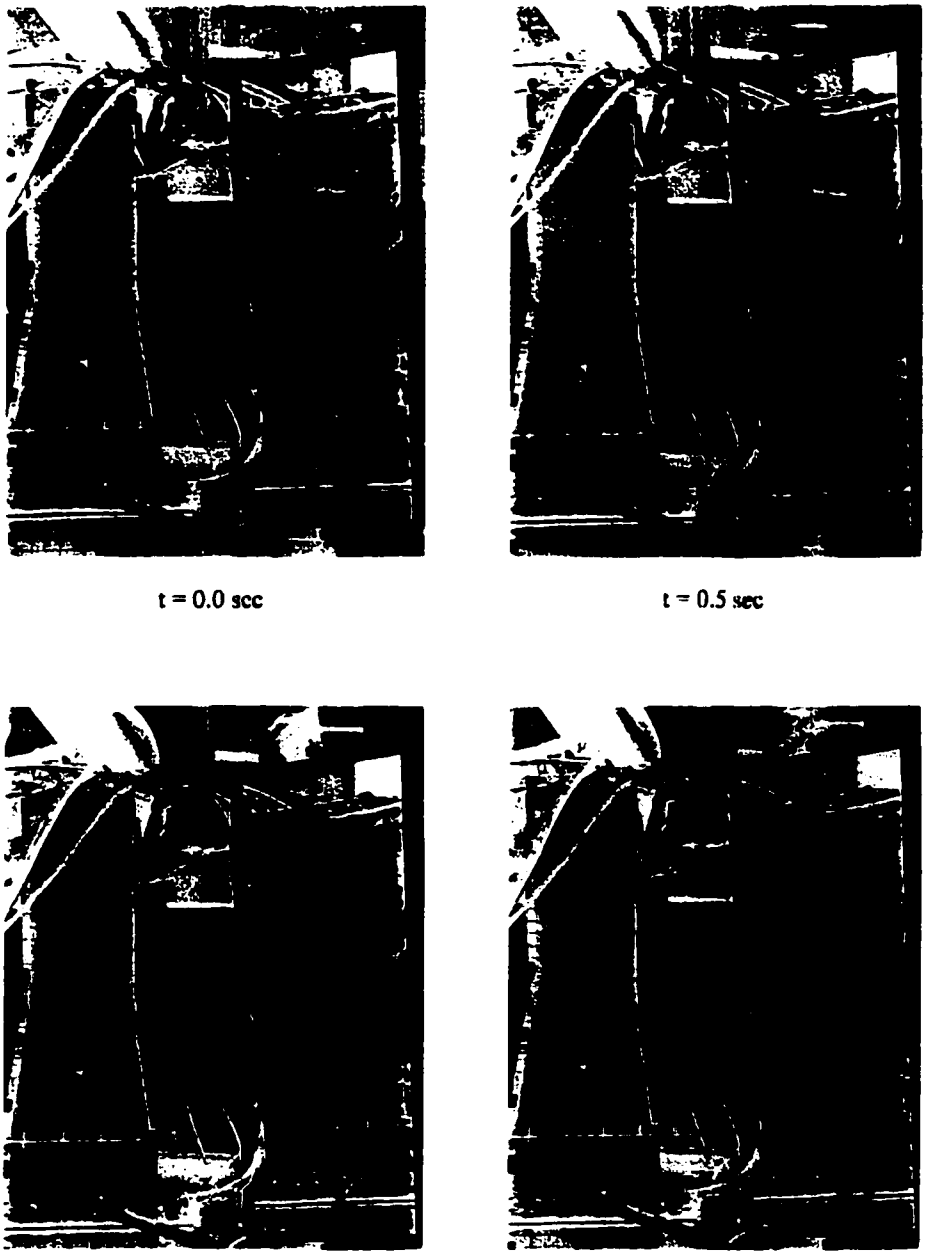

Figure A.1.6 Flow Visualization in Water Model Using an Acid-Base Reaction- Configuration F
(dark gray ≡ unreacted base; light gray ≡ reacted base)

A.2 Flow Visualization in Water Model - Particle Tracking

An alternative method for visually observing the flow patterns is to introduce neutrally buoyant particles into a model. In the water model, these experiments focused on examining the nature of the bulk flow patterns in the furnace and the uptake. These experiments were effective in demonstrating qualitatively the significant features of the flow patterns. Although it was difficult to obtain precise velocity measurements, estimates of the particles velocity were made by streak photography. No effort was made to obtain more accurate data by using elaborate lighting arrangements or laser techniques to illuminate the model.

The experimental conditions for which the particle tracking experiments were conducted are tabulated in table A2.1. The tracer particles, polystyrene spheres of specific gravity 0.98-1.02 and sphericity close to 1, were injected through one of the main burner jets. The polystyrene particles were in the size range of 1-3 mm in diameter. The experiments were carried out without the introduction of flow through the afterburner jets. Although these experiments can provide quantitative data, it was difficult to determine the exact position and trajectory of the particles.

Table A.2.1 Particle Tracking in Water Model - Test Conditions

Burner:	Flow	87 L/min
	Tip Velocity	467 cm/s
Furnace:	Total Flow, Q	348 L/min
	superficial velocity	4.0 cm/s
Uptake:	superficial entrance velocity	12.9 cm/s
	discharge velocity	183 cm/s

The experiment was observed using both video and still photography techniques. The still photographs were taken under continuous lighting with a 35 mm camera set for a shutter speed of 8 ($^1/_8$ second) and aperture opening (f-stop) of 4, and captured on 400 series Kodak film. The shutter speed was selected by trial methods until a streak, recording the path of the particle tracer,

was sufficiently long to be observed on a still photograph. A mirror was mounted on the model adjacent to the uptake to allow for the simultaneous viewing of both the side and front planes.

A white background with 2 cm square grids was mounted on two adjacent walls of the uptake. The grid provided a means of determining the approximate direction and velocity of individual particles but not their path of travel through the uptake. The trace appeared as comet-shaped object with the narrow end pointing in the direction of travel. Only approximate local velocities and flow directions were found from measurements of the trace lengths relative to the grid spacing. Streak lengths ranged from 0 to 25 mm and were measured with an accuracy of ± 0.5 mm. Nevertheless, this technique provided a simple means for observing the general flow pattern in the uptake.

The flow in the model was three-dimensional, making it difficult to position the tracer in the photograph. In the furnace, the tracer particles were positioned relative to the longitudinal (z-) and vertical (x-) axis. The curvature of the roof precluded the determination of the tracer position along the lateral (y-) axis. In the case of the uptake, the position of tracer particles in three dimensions were determined with the aid of a mirror mounted adjacent to the uptake at 45°. The coordinate system used for estimating the position of the tracer particle is shown in figure A.2.1. The coordinate 0,0,0 was located in the center of the model on the floor. The particle velocities measured in the model are given in tables A.2.2 and A.2.3 for the furnace and uptake, respectively. The measured particle velocities were made dimensionless with respect to the superficial velocity.

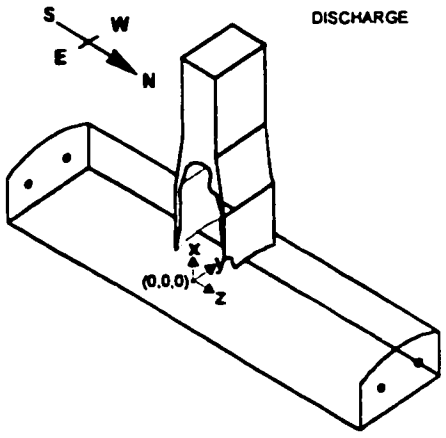

Figure A.2.1 Particle Tracking in Water Model - Coordinate System

Table A.2.2 Particle Tracking in Water Model - Axial Velocity in Furnace

Tracer Position x (cm)	Tracer Position z (cm)	Streak Length (mm)	Axial Velocity (cm/s)	Dimensionless Axial Velocity
4.0	-51	7.5	13.9	3.5
1.5	-46	7.5	13.9	3.5
5.5	-45	17.0	31.5	7.9
7.0	-44	14.0	25.9	6.5
9.5	-42	9.0	16.7	4.2
6.5	-41	7.0	13.0	3.2
2.0	-40	11.5	21.3	5.3
8.0	-39	8.5	15.7	3.9
3.0	-39	10.0	18.5	4.6
5.5	-38	16.0	29.6	7.4
3.0	-38	11.5	21.3	5.3
8.0	-38	7.0	13.0	3.2
6.5	-32	15.0	27.8	6.9
4.0	-32	9.5	17.6	4.4
4.5	-31	13.5	25.0	6.3
4.5	-31	13.0	24.1	6.0
7.0	-30	13.0	24.1	6.0
7.0	-30	12.0	22.2	5.6
7.0	-30	11.5	21.3	5.3
4.5	-29	14.0	25.9	6.5
4.5	-28	6.0	11.1	2.8
2.0	-24	11.0	20.4	5.1
4.5	-22	6.0	11.1	2.8
3.0	-22	5.5	10.2	2.5
2.5	-14	5.0	9.3	2.3
4.5	-13	9.0	16.7	4.2

Note: The axial velocity was measured relative to the longitudinal axis of the furnace (z - axis).
The axial velocity was measured for those particles moving toward the uptake.
The superficial velocity in the furnace was 4.0 cm/s.

Table A.2.3 Particle Tracking in Water Model - Axial Velocity in Uptake (Upper Section)

Tracer Position			Streak	Axial	Dimensionless
x	y	z	Length	Velocity	Axial
(cm)	(cm)	(cm)	(mm)	(cm/s)	Velocity
83	-6	6	0.0	0	0.00
80	7	-3	4.0	19	1.02
80	5	2	4.5	21	1.14
79	9	-4	3.5	17	0.89
79	-6	-4	3.0	14	0.76
78	9	0	5.0	24	1.27
78	-3	5	3.5	17	0.89
76	5	0	5.0	24	1.27
76	-2	-2	3.5	17	0.89
76	-5	5	2.0	9	0.51
75	7	5	4.5	21	1.14
74	5	1	4.0	19	1.02
74	-5	-4	3.0	14	0.76
73	7	2	5.0	24	1.27
73	-6	-3	3.0	14	0.76
73	-9	3	1.5	7	0.38
73	0	3	3.0	14	0.76
71	7	2	4.5	21	1.14
71	6	0	4.5	21	1.14
71	-5	3	3.5	17	0.89
71	-8	6	2.0	9	0.51
71	8	-5	3.5	17	0.89
71	-7	-3	3.0	14	0.76
70	-10	-5	3.0	14	0.76
69	3	-3	4.5	21	1.14
68	7	1	5.5	26	1.40
68	-7	1	3.0	14	0.76
68	9	5	5.5	26	1.40
68	9	-2	5.0	24	1.27
67	5	4	4.5	21	1.14
67	-4	2	2.5	12	0.63
67	9	-4	5.5	26	1.40
67	-1	2	4.0	19	1.02
66	6	0	4.5	21	1.14
66	4	3	5.0	24	1.27
66	0	-3	4.0	19	1.02
66	-2	-2	3.5	17	0.89

Note: The axial velocity was measured relative to the longitudinal axis of the uptake (x - axis).
The superficial velocity in the upper section of the uptake was 18.7 cm/s

A.3 Salt Tracer Mixing in Water Model (Uniformity of Mixing Experiments)

The mixing of the tracer in the uptake was hypothesized to be controlled by the turbulent characteristics of the jets and the main stream flow. A procedure, as proposed by Sroka and Forney (1989), was used to evaluate the degree of mixing homogeneity in the uptake. This experimental procedure provided a quantitative measure of the mixing in the uptake. In the model, an inert tracer, KCl, was introduced through the afterburner jets and the steady state tracer concentration was measured at various points both upstream and downstream of the afterburner jets.

The tracer solution was fed continuously to each afterburner jet using a metering pump. To measure the dilution of the afterburner jets, samples were extracted at 4 different elevations in the uptake (figure A.3.1). The grid system orientation used in these experiments is illustrated in figure A.3.2. Each sampling plane was sub-divided into 15 cells (5 x 3) of equal area to form a sampling grid (figure A.3.3). The samples, extracted from the centre of each cell, were collected after the model reached steady state conditions; these samples included feed and discharge waters to determine the baseline and well mixed concentrations of tracer, respectively. The samples were analyzed for the potassium ion (K^+) concentration by atomic absorption spectroscopy.

With the grid system described, the sampled average uptake concentration, c_{avg}, was calculated using equation A.3.1 and the well mixed concentration was given by equation A.3.2. The local dimensionless concentration, $C_{i,j}$, was corrected for the background level of potassium in the water and then normalized to the well-mixed tracer concentration (equation A.3.3).

$$c_{avg} = \frac{1}{A}\sum_{i=1}^{5}\sum_{j=1}^{3} c_{i,j}\,\Delta A \qquad \text{(A.3.1)}$$

$$\bar{c} = c_{well\ mixed} = c_o\left(\frac{q_{jets}}{Q_{total}}\right) \qquad \text{(A.3.2)}$$

$$DC_{i,j} = C_{i,j} = \frac{c_{i,j}}{\bar{c}} \qquad \text{(A.3.3)}$$

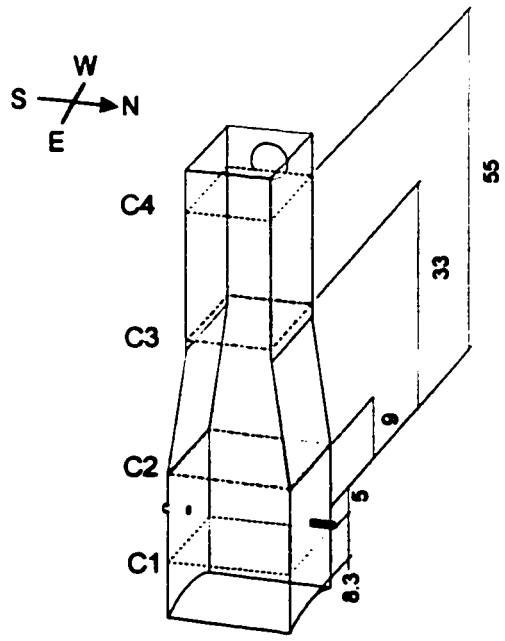

Figure A.3.1 Uniformity of Mixing Experiments in Water Model - Location of Sampling Planes

(dimensions in cm, measured relative to afterburner elevation)

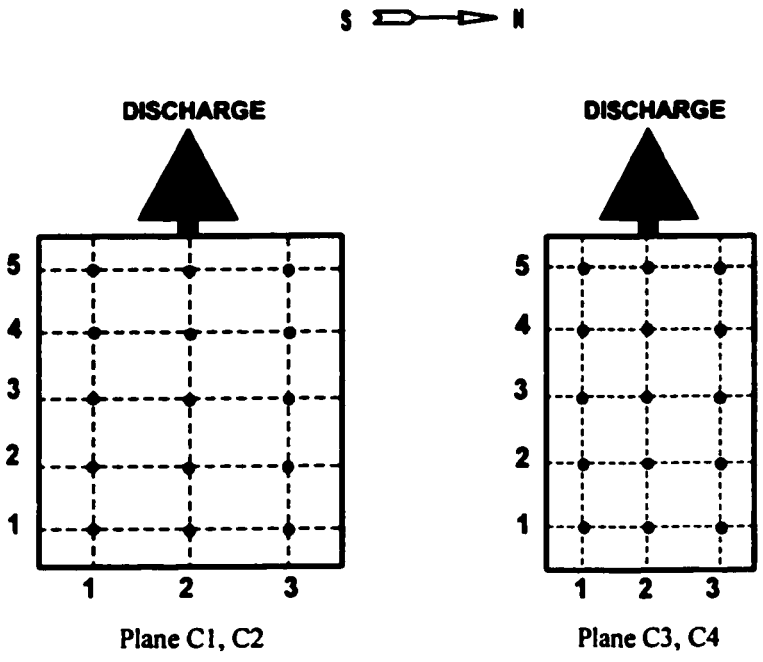

Figure A.3.2 Uniformity of Mixing Experiments in Water Model - Grid System Orientation

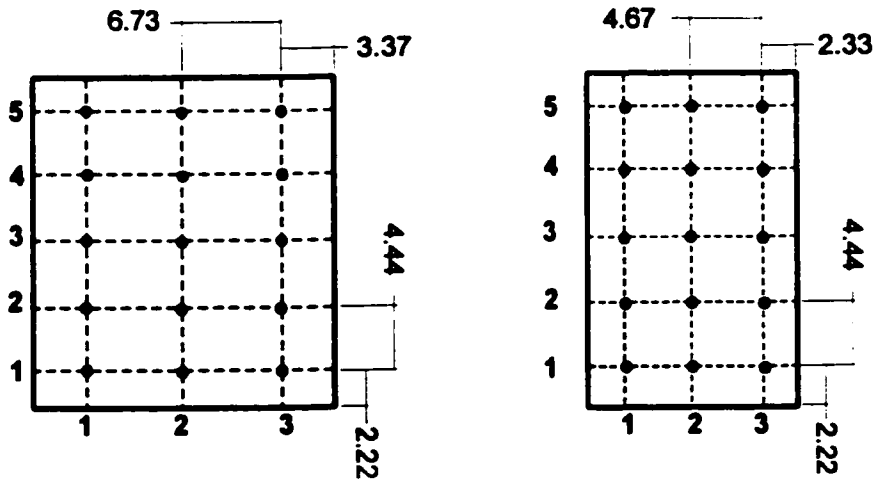

Figure A.3.3 Uniformity of Mixing Experiments in Water Model - Grid System Spacing

A useful method of characterizing the uniformity of the mixture within the uptake was to calculate the second moment of the tracer concentration across the uptake (Gray, 1986). Thus the second moment, M, was defined in the form:

$$M = \frac{1}{A}\sum_{i=1}^{5}\sum_{j=1}^{3}\left(C_{i,j}-1\right)^2 \Delta A \qquad \text{(A.3.4)}$$

Dimensional analysis by Forney (1986) suggested that the mixing conditions were related to the M_r, U_r, Re_j, Re_U, Fr_j and x/D_U. In water model, the jet buoyancy effects was not significant provided that the modified Froude number, Fr_j, was maintained in the range of 10^2 - 10^3. Thus, the second moment of the tracer concentration was written as:

$$M = f\left(M_r, U_r, \mathrm{Re}_j, \mathrm{Re}_U, \frac{x}{D_U}\right) \qquad \text{(A.3.5)}$$

The experimental conditions are given in tables A.3.1 to A.3.3, and a summary of the data collected is provided in tables A.3.4 to A.3.6. The afterburner configurations tested are illustrated in figure A.3.4. The tracer concentration distributions measured in the water model are illustrated

in figures A.3.5 to A.3.33.

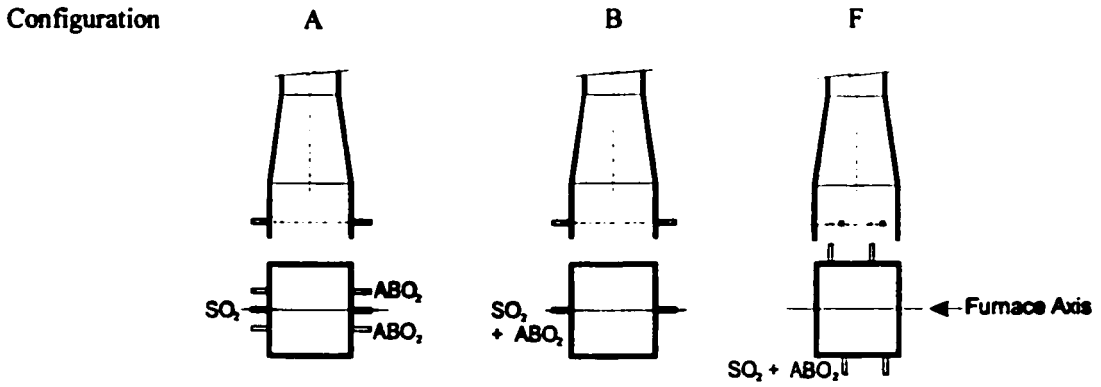

Figure A.3.4 Uniformity of Mixing Experiments in Water Model - Afterburner Configurations

The rise in tracer concentration measured on plane C1, upstream of the afterburner jets, provided a measure of the amount of tracer drawn downward due to backmixing (tables A.3.4 to A.3.6). The axial dispersion coefficient, E_c, which is a measure of the amount of backmixing, was estimated from a 1-dimensional transport model in the axial direction. In this model, the tracer concentration profile was assumed to be laterally uniform upstream and downstream of the afterburner jets, and the velocity at the entrance of the uptake was assumed to be uniform. Although this was an over-simplification of the problem, it provided a simple assessment of the degree of backmixing. Upstream of the jets, the net flux of tracer was zero and was given by equation A.3.5.

$$u\,c - E_c \frac{dc}{dx} = 0; \qquad \text{b.c. } x = 0 \text{ cm}, \; c = \bar{c} \tag{A.3.5}$$

$$\text{Hence: } c = \bar{c} \exp\left(u x / E_c\right) \text{ for } x < 0$$

The value of E was obtained by fitting data to equation A.3.5, and the axial dispersion number was calculated using equation A.3.6. The axial dispersion number was compared with the model developed by Levenspiel (1972), describing the dispersion of fluids flow in pipes (figure A.3.34).

$$N_d = \frac{E_c}{u\ell} \tag{A.3.6}$$

Table A.3.1 Uniformity of Mixing Experiments in Water Model - Test Conditions (Configuration A)

Test		1A1	1A2	1A3	2A1	3A1	3A2	3A3	4A1	5A1
Burner	Flow (L/min/jet)	31.5	31.5	31.5	60.0	87.0	87.0	87.0	87.0	87.0
	Reynolds # (x 10^3)	33.5	33.5	33.5	63.9	92.6	92.6	92.6	92.6	92.6
	Velocity (m/s)	1.68	1.68	1.68	3.2	4.6	4.6	4.6	4.6	4.6
Furnace	Total Flow (L/min)	126	126	126	240	348	348	348	348	348
	Reynolds # (x 10^3)	3.9	3.9	3.9	7.5	10.8	10.8	10.8	10.8	10.8
	Superficial Velocity (cm/s)	1.45	1.45	1.45	2.76	4.00	4.00	4.00	4.00	4.00
Uptake	Entrance Reynolds # (x 10^3)	9.9	9.9	9.9	18.9	27.4	27.4	27.4	27.4	27.4
	Superficial Entrance Velocity (cm/s)	4.68	4.68	4.68	8.92	12.93	12.93	12.93	12.93	12.93
Afterburner Jet										
	Flow (L/min/jet)	0.71	0.71	0.71	1.35	1.96	1.96	1.96	1.50	2.55
	Velocity (m/s)	1.5	1.5	1.5	2.8	4.1	4.1	4.1	3.2	5.4
	Velocity Ratio	31.9	31.9	31.9	31.9	31.9	31.9	31.9	24.4	41.5
	Momentum Ratio	0.18	0.18	0.18	0.18	0.18	0.18	0.18	0.11	0.30
	Reynolds # (x 10^3)	4.7	4.7	4.7	9.0	13.0	13.0	13.0	10.0	17.0
	Modified Froude #	60	100	180	430	820	820	820	510	1380
SO_2 Recycle Jet										
	Flow (L/min/jet)	3.3	3.3	3.3	6.3	9.1	9.1	9.1	9.1	9.1
	Velocity (m/s)	0.8	0.8	0.8	1.5	2.1	2.1	2.1	2.1	2.1
	Velocity Ratio	16.5	16.5	16.5	16.5	16.5	16.5	16.5	16.5	16.5
	Momentum Ratio	0.43	0.43	0.43	0.43	0.43	0.43	0.43	0.43	0.43
	Reynolds # (x 10^3)	7.4	7.4	7.4	14.0	20.3	20.3	20.3	20.3	20.3

Table A.3.2 Uniformity of Mixing Experiments in Water Model - Test Conditions (Configuration B)

Test		1B1	2B1	3B1	3B2	4B1	5B1	6B1	7B1
Burner	Flow (L/min/jet)	31.5	60.0	87	87	87	87	60.0	31.5
	Reynolds # (x 10^3)	33.5	63.9	92.6	92.6	92.6	92.6	63.9	33.5
	Velocity (m/s)	1.68	3.2	4.6	4.6	4.6	4.6	3.2	1.68
Furnace	Total Flow (L/min)	126	240	348	348	348	348	240	126
	Reynolds # (x 10^3)	3.9	7.5	10.8	10.8	10.8	10.8	7.5	3.9
	Superficial Velocity (cm/s)	1.45	2.76	4.00	4.00	4.00	4.00	2.76	1.45
Uptake	Entrance Reynolds # (x 10^3)	9.9	18.9	27.4	27.4	27.4	27.4	18.9	9.9
	Superficial Entrance Velocity (cm/s)	4.68	8.92	12.93	12.93	12.93	12.93	8.92	4.68
SO_2 Recycle + Oxygen Jet									
	Flow (L/min/jet)	4.00	9.00	14.00	14.00	9.25	18.00	9.70	5.10
	Velocity (m/s)	0.9	2.1	3.3	3.3	2.2	4.2	2.3	1.2
	Velocity Ratio	20.0	23.6	25.3	25.3	16.7	32.6	25.4	25.5
	Momentum Ratio	0.63	0.89	1.02	1.02	0.44	1.68	1.03	1.03
	Reynolds # (x 10^3)	8.9	20.1	31.2	31.2	20.6	40.1	21.6	11.4
	Modified Froude #	100	440	1060	1060	460	1710	490	140

Table A.3.3 Uniformity of Mixing Experiments in Water Model - Test Conditions (Configuration F)

Test		1F1	2F1	3F1	4F1	5F1	6F1
Burner	Flow (L/min/jet)	87.0	87.0	87.0	87.0	87.0	87.0
	Reynolds # (x 10^3)	92.6	92.6	92.6	92.6	92.6	92.6
	Velocity (m/s)	4.6	4.6	4.6	4.6	4.6	4.6
Furnace	Flow (L/min)	348	348	348	348	348	348
	Reynolds # (x 10^3)	10.8	10.8	10.8	10.8	10.8	10.8
	Superficial Velocity (cm/s)	4.00	4.00	4.00	4.00	4.00	4.00
Uptake	Entrance Reynolds # (x 10^3)	27.4	27.4	27.4	27.4	27.4	27.4
	Superficial Entrance Velocity (cm/s)	12.93	12.93	12.93	12.93	12.93	12.93
SO_2 Recycle + Oxygen Jet							
	Flow (L/min/jet)	3.60	4.75	6.00	7.25	9.50	12.0
	jet diameter, Ø (cm)	0.3175	0 3175	0.3175	0.6350	0.6350	0.6350
	Velocity (m/s)	7.6	10.0	12.6	3.8	5.0	6.3
	Velocity Ratio	58.6	77.3	97.7	29.5	38.7	48.8
	Momentum Ratio	0.61	1.06	1.68	0.61	1.06	1.68
	Reynolds # (x 10^3)	24.1	31.7	40.1	24.2	31.7	40.1
	Modified Froude #	5380	9500	15100	1380	2400	3830

Table A.3.3 (cont) Uniformity of Mixing Experiments in Water Model - Test Conditions (Configuration F)

Test		7F1	8F1	8F2	9F1	10F1	10F1
Burner	Flow (L/min/jet)	87.0	87.0	87.0	87.0	87.0	87.0
	Reynolds # (x 10^3)	92.6	92.6	92.6	92.6	92.6	92.6
	Velocity (m/s)	4.6	4.6	4.6	4.6	4.6	4.6
Furnace	Flow (L/min)	348	348	348	348	348	348
	Reynolds # (x 10^3)	10.8	10.8	10.8	10.8	10.8	10.8
	Superficial Velocity (cm/s)	4.00	4.00	4.00	4.00	4.00	4.00
Uptake	Entrance Reynolds # (x 10^3)	27.4	27.4	27.4	27.4	27.4	27.4
	Superficial Entrance Velocity (cm/s)	12.93	12.93	12.93	12.93	12.93	12.93
SO_2 Recycle + Oxygen Jet							
	Flow (L/min/jet)	10.75	12.30	12.30	14.25	18.00	18.00
	jet diameter, Ø (cm)	0.9525	0.9525	0.9525	0.9525	0.9525	0.9525
	Velocity (m/s)	2.5	2.9	2.9	3.3	4.2	4.2
	Velocity Ratio	19.4	22.2	22.2	25.8	32.6	32.6
	Momentum Ratio	0.60	0.79	0.79	1.06	1.68	1.68
	Reynolds # (x 10^3)	24.0	27.4	27.4	31.7	40.1	40.1
	Modified Froude #	760	990	990	1330	2120	2120

Table A.3.4 Uniformity of Mixing Experiments in Water Model - Summary of Findings (Configuration A)

Test		1A1	1A2	1A3	2A1	3A1	3A2	3A3	4A1	5A1
Dimensionless Concentration - Average										
Plane C1	L/D = -0.261	0.965	0.608	0.509	0.457	0.518	0.470	0.458	0.474	0.457
Plane C2	L/D = 0.471	1.222	1.134	1.091	1.049	1.100	1.119	1.155	1.072	1.102
Plane C3	L/D = 1.728	1.060	1.066	0.990	1.010	1.018	1.020	1.012	0.999	1.001
Plane C4	L/D = 2.880	1.016	0.982	1.002	1.010	1.038	1.000	1.016	0.994	1.009
$C_{WELL\ MIXED}$ (ppm) [1]		401	269	147	242	158	172	168	168	172
Second Moment (Variance), M										
Plane C1	L/D = -0.261	0.5083	0.1534	0.1031	0.0852	0.1430	0.1133	0.0954	0.1238	0.0965
Plane C2	L/D = 0.471	0.0681	0.0292	0.0290	0.0372	0.0323	0.0327	0.0340	0.0160	0.0212
Plane C3	L/D = 1.728	0.0115	0.0048	0.0037	0.0037	0.0023	0.0020	0.0023	0.0035	0.0020
Plane C4	L/D = 2.880	0.0074	0.0046	0.0023	0.0034	0.0010	0.0013	0.0016	0.0014	0.0009

Note: L base on distance from afterburner jets
D based on hydraulic diameter of uptake = 19.1 cm
Grid Size = 5 x 3
Second Moment based on Forney's paper (1989)

Axial Dispersion Number, E/uL										
Fully Developed Turbulent Flow in Pipe		0.13	0.13	0.13	0.09	0.07	0.07	0.07	0.07	0.07
1-D Transport Model		1.84	0.13	0.10	0.08	0.10	0.09	0.08	0.09	0.08

Note: Thermal dispersion number calculated for fully developed turbulent flow in pipes was based on Levenspiel's dispersion model (Levenspiel, 1972). See figure A.3.34
L_{uptake} = 75.6 cm
d_t based on hydraulic diameter of uptake = 19.1 cm

Table A.3.5 Uniformity of Mixing Experiments in Water Model - Summary of Findings (Configuration B)

Test		1B1	2B1	3B1	3B2	4B1	5B1	6B1	7B1
Dimensionless Concentration - Average									
Plane C1	L/D = -0.261	0.360	0.257	0.262	0.304	0.371	0.304	0.284	0.410
Plane C2	L/D = 0.471	1.220	1.187	1.123	1.038	1.200	1.080	1.237	1.295
Plane C3	L/D = 1.728	1.051	1.060	0.990	0.992	1.019	1.056	0.999	0.995
Plane C4	L/D = 2.880	1.017	1.034	1.010	1.012	0.996	1.000	1.065	1.021
$C_{WELL\ MIXED}$ (ppm) [1]		534	288	223	162	170	122	216	450
Second Moment (Variance), M									
Plane C1	L/D = -0.261	0.0394	0.0359	0.0278	0.0358	0.0564	0.0222	0.0384	0.0582
Plane C2	L/D = 0.471	0.1128	0.1458	0.1099	0.1212	0.1636	0.0855	0.1041	0.1643
Plane C3	L/D = 1.728	0.0123	0.0093	0.0083	0.081	0.0281	0.0114	0.0077	0.0079
Plane C4	L/D = 2.880	0.0030	0.0031	0.0018	0.0014	0.0094	0.0041	0.0063	0.0039

Note: L base on distance from afterburner jets
D based on hydraulic diameter of uptake = 19.1 cm
Grid Size = 5 x 3
Second Moment based on Forney's paper (1989)

Axial Dispersion Number, E/uL								
Fully Developed Turbulent Flow in Pipe	0.13	0.09	0.07	0.07	0.07	0.07	0.08	0.13
1-D Transport Model	0.06	0.05	0.05	0.06	0.07	0.06	0.05	0.07

Note: Thermal dispersion number calculated for fully developed turbulent flow in pipes was based on Levenspiel's dispersion model (Levenspiel, 1972). See figure A.3.34
L_{uptake} = 75.6 cm
d_t based on hydraulic diameter of uptake = 19.1 cm

Table A.3.6 Uniformity of Mixing Experiments in Water Model - Summary of Findings (Configuration F)

Test		1F1	2F1	3F1	4F1	5F1	6F1
Dimensionless Concentration - Average							
Plane C1	L/D = -0.261	0.305	0.343	0.286	0.289	0.238	0.326
Plane C2	L/D = 0.471	1.107	1.036	1.039	1.012	1.005	1.025
Plane C3	L/D = 1.728	1.002	0.998	1.034	1.067	0.999	0.995
Plane C4	L/D = 2.880	1.003	1.001	0.999	1.030	1.014	1.031
$C_{WELL\ MIXED}$ (ppm) [1]		132	139	147	126	158	122
Second Moment (Variance), M							
Plane C1	L/D = -0.261	0.0371	0.0435	0.0401	0.0396	0.0255	0.0383
Plane C2	L/D = 0.471	0.0156	0.0127	0.0104	0.0139	0.0116	0.0130
Plane C3	L/D = 1.728	0.0044	0.0058	0.0059	0.0080	0.0047	0.0040
Plane C4	L/D = 2.880	0.0019	0.0013	0.0018	0.0020	0.0016	0.0015
Axial Dispersion Number, E/uL							
Fully Developed Turbulent Flow in Pipe		0.07	0.07	0.07	0.07	0.07	0.07
1-D Transport Model		0.06	0.06	0.05	0.05	0.05	0.06

Note: L base on distance from afterburner jets
D based on hydraulic diameter of uptake = 19.1 cm
Grid Size = 5 x 3
Second Moment based on Forney's paper (1989)

Note: Thermal dispersion number calculated for fully developed turbulent flow in pipes was based on Levenspiel's dispersion model (Levenspiel, 1972). See figure A.3.34
L_{uptake} = 75.6 cm
d_t based on hydraulic diameter of uptake = 19.1 cm

Table A.3.6 (cont) Uniformity of Mixing Experiments in Water Model - Summary of Findings (Configuration F)

Test		7F1	8F1	8F2	9F1	10F1	10F2
Dimensionless Concentration - Average							
Plane C1	L/D = -0.261	0.238	0.220	0.241	0.230	0.282	0.313
Plane C2	L/D = 0.471	1.068	1.060	1.100	1.018	1.006	1.014
Plane C3	L/D = 1.728	1.005	1.016	1.041	1.016	0.997	0.994
Plane C4	L/D = 2.880	1.010	0.995	1.016	0.995	1.016	0.992
$C_{WELL\ MIXED}$ (ppm) [1]		141	143	166	145	124	160
Second Moment (Variance), M							
Plane C1	L/D = -0.261	0.0291	0.0199	0.0249	0.0301	0.0332	0.0326
Plane C2	L/D = 0.471	0.0108	0.0068	0.0068	0.0075	0.0105	0.0108
Plane C3	L/D = 1.728	0.0045	0.0037	0.0035	0.0038	0.0025	0.0024
Plane C4	L/D = 2.880	0.0026	0.0019	0.0021	0.0012	0.0008	0.0011
Axial Dispersion Number, E/uL							
Fully Developed Turbulent Flow in Pipe		0.07	0.07	0.07	0.07	0.07	0.07
1-D Transport Model		0.05	0.04	0.05	0.04	0.05	0.06

Note: L base on distance from afterburner jets

D based on hydraulic diameter of uptake = 19.1 cm

Grid Size = 5 x 3

Second Moment based on Forney's paper (1989)

Note: Thermal dispersion number calculated for fully developed turbulent flow in pipes was based on Levenspiel's dispersion model (Levenspiel, 1972).

L_{uptake} = 75.6 cm

d_t based on hydraulic diameter of uptake = 19.1 cm

			1	2	3
		5	0.243	0.286	0.790
		4	0.314	0.357	0.495
Plane C1	x/D = -0.261	3	0.514	0.486	2.943
		2	1.067	1.086	1.705
		1	1.157	1.657	1.371

			1	2	3
		5	0.767	1.371	0.933
		4	1.133	1.419	0.752
Plane C2	x/D = 0.471	3	1.219	1.610	1.038
		2	1.419	1.610	1.086
		1	1.419	1.324	1.229

			1	2	3
		5	1.014	1.038	0.829
		4	1.014	1.005	0.890
Plane C3	x/D = 1.728	3	1.148	1.133	0.990
		2	1.133	1.210	1.076
		1	1.086	1.248	1.086

			1	2	3
		5	1.000	0.943	0.943
		4	1.048	0.990	0.833
Plane C4	x/D = 2.880	3	1.090	1.038	0.919
		2	1.110	1.086	0.924
		1	1.124	1.133	1.057

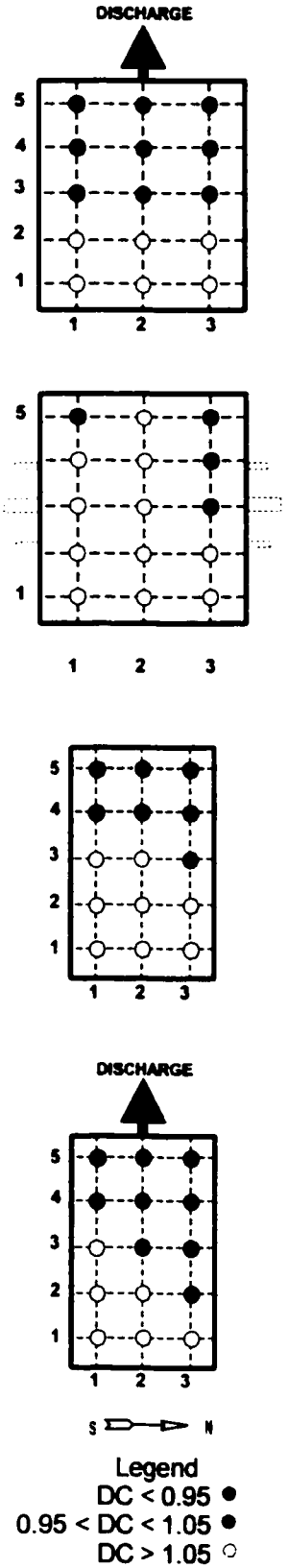

Figure A.3.5 Uniformity of Mixing in Water Model - Test 1A1 Dimensionless Concentrations

			1	2	3
		5	0.113	0.163	0.241
		4	0.184	0.270	0.369
Plane C1	x/D = -0.261	3	0.348	0.667	0.631
		2	0.681	1.156	1.043
		1	0.837	1.333	1.085

			1	2	3
		5	0.922	1.262	0.816
		4	1.085	1.326	1.064
Plane C2	x/D = 0.471	3	1.050	1.376	1.099
		2	1.121	1.496	1.199
		1	0.972	1.135	1.092

			1	2	3
		5	1.000	1.149	0.979
		4	1.050	1.113	1.113
Plane C3	x/D = 1.728	3	0.986	1.021	1.135
		2	1.028	1.014	1.177
		1	1.028	1.014	1.184

			1	2	3
		5	0.887	1.050	1.050
		4	0.851	1.021	1.050
Plane C4	x/D = 2.880	3	0.872	0.957	1.050
		2	0.929	0.965	1.028
		1	1.021	0.965	1.035

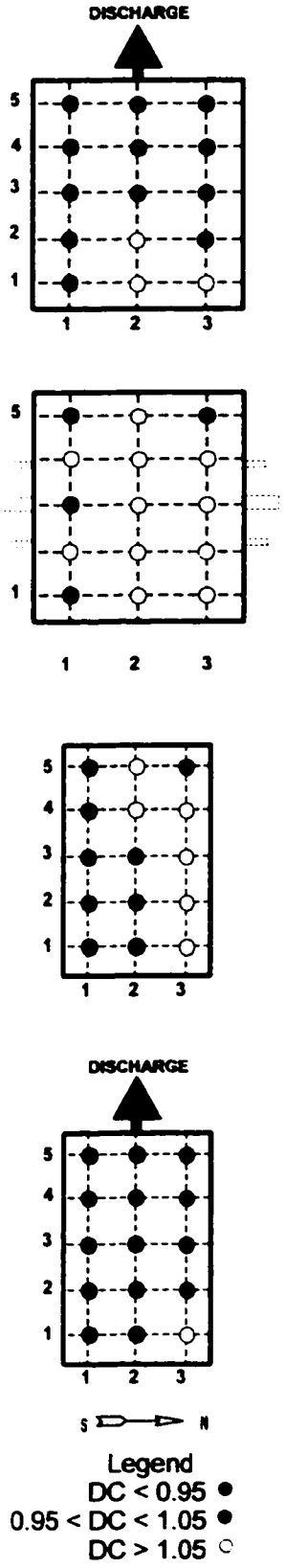

Figure A.3.6 Uniformity of Mixing in Water Model - Test 1A2 Dimensionless Concentrations

			1	2	3
		5	0.169	0.130	0.260
		4	0.208	0.234	0.312
Plane C1	x/D = -0.261	3	0.364	0.338	0.455
		2	0.818	0.584	0.909
		1	1.013	0.688	1.156

			1	2	3
		5	0.792	1.039	0.935
		4	0.896	1.091	1.208
Plane C2	x/D = 0.471	3	0.948	1.182	1.221
		2	1.039	1.455	1.169
		1	0.935	1.325	1.130

			1	2	3
		5	0.974	0.974	0.896
		4	0.987	0.974	1.026
Plane C3	x/D = 1.728	3	0.935	0.987	1.117
		2	0.922	0.987	1.078
		1	0.935	0.974	1.091

			1	2	3
		5	0.961	0.974	1.013
		4	1.013	0.935	1.039
Plane C4	x/D = 2.880	3	0.987	0.974	1.117
		2	0.987	0.974	1.065
		1	0.935	1.000	1.052

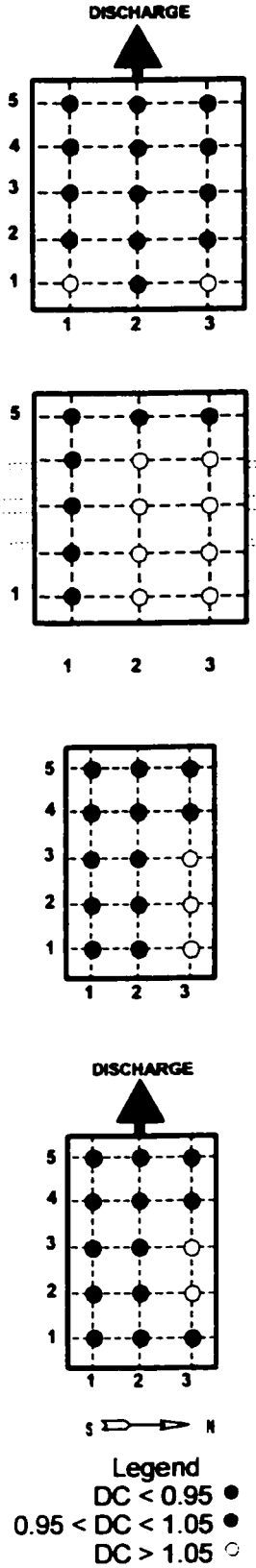

Figure A.3.7 Uniformity of Mixing in Water Model - Test 1A3 Dimensionless Concentrations

			1	2	3
		5	0.142	0.260	0.194
		4	0.173	0.291	0.134
Plane C1	x/D = -0.261	3	0.283	0.283	0.307
		2	0.591	0.598	0.575
		1	0.917	0.987	0.940

			1	2	3
		5	0.995	1.189	0.872
		4	0.969	1.323	0.950
Plane C2	x/D = 0.471	3	0.984	1.354	0.943
		2	1.087	1.567	1.261
		1	1.265	1.331	1.221

			1	2	3
		5	0.961	0.992	0.990
		4	1.008	0.992	0.911
Plane C3	x/D = 1.728	3	1.031	0.992	0.890
		2	1.024	1.063	1.006
		1	1.087	1.102	1.108

			1	2	3
		5	0.992	0.984	1.008
		4	0.992	0.984	0.976
Plane C4	x/D = 2.880	3	0.976	0.937	1.010
		2	0.961	1.045	1.134
		1	0.992	1.006	1.157

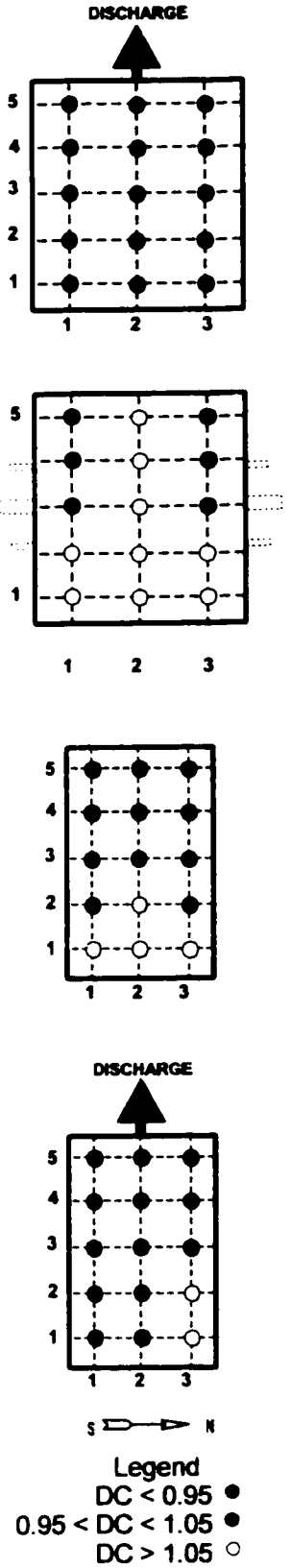

Figure A.3.8 Uniformity of Mixing in Water Model - Test 2A1 Dimensionless Concentrations

			1	2	3
		5	0.157	0.145	0.108
		4	0.301	0.217	0.133
Plane C1	x/D = -0.261	3	0.386	0.313	0.337
		2	0.916	0.964	0.687
		1	0.916	1.337	0.855

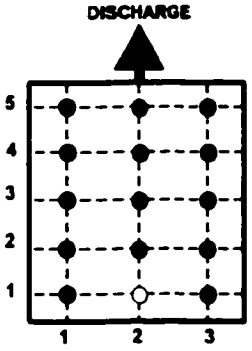

			1	2	3
		5	0.964	1.229	0.831
		4	0.964	1.446	0.867
Plane C2	x/D = 0.471	3	0.988	1.289	0.952
		2	1.084	1.277	1.096
		1	1.012	1.373	1.133

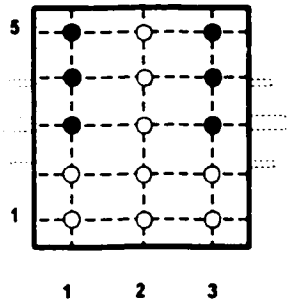

			1	2	3
		5	1.000	1.036	0.904
		4	1.024	1.048	0.964
Plane C3	x/D = 1.728	3	1.048	1.036	0.952
		2	1.072	1.048	0.964
		1	1.060	1.060	1.048

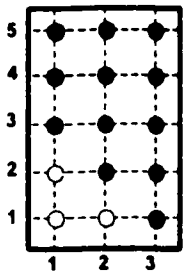

			1	2	3
		5	1.024	0.988	1.048
		4	1.036	1.012	1.036
Plane C4	x/D = 2.880	3	1.048	1.048	1.024
		2	1.060	1.012	1.012
		1	1.060	1.133	1.024

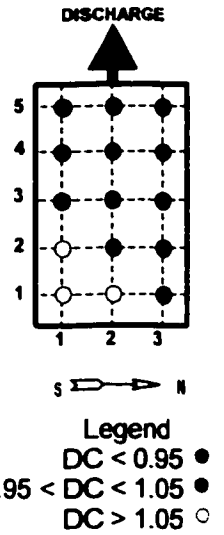

Figure A.3.9 Uniformity of Mixing in Water Model - Test 3A1 Dimensionless Concentrations

			1	2	3
		5	0.156	0.178	0.122
		4	0.211	0.211	0.144
Plane C1	x/D = -0.261	3	0.333	0.411	0.256
		2	0.656	0.811	0.533
		1	1.122	1.100	0.800

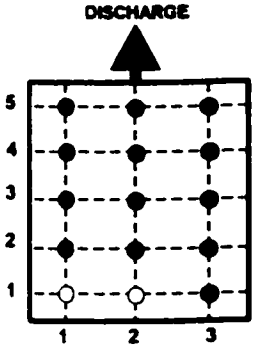

			1	2	3
		5	0.800	1.289	1.000
Plane C2		4	0.933	1.278	0.844
	x/D = 0.471	3	1.033	1.200	1.011
		2	1.222	1.344	1.156
		1	1.322	1.367	0.978

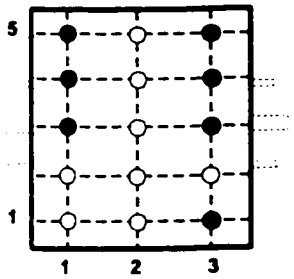

			1	2	3
		5	1.000	0.911	0.967
		4	1.044	0.967	1.022
Plane C3	x/D = 1.728	3	1.022	0.956	0.989
		2	1.056	1.022	1.067
		1	1.056	1.056	1.056

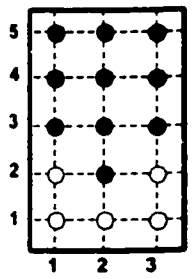

			1	2	3
		5	0.967	1.011	0.989
		4	0.978	0.978	1.000
Plane C4	x/D = 2.880	3	0.989	0.967	1.044
		2	0.989	1.033	0.922
		1	1.022	1.056	1.056

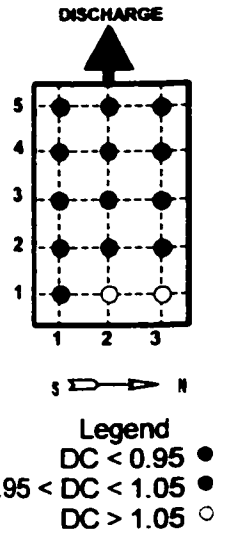

Figure A.3.10 Uniformity of Mixing in Water Model - Test 3A2 Dimensionless Concentrations

			1	2	3
		5	0.341	0.125	0.148
		4	0.273	0.182	0.182
Plane C1	x/D = -0.261	3	0.250	0.330	0.352
		2	0.466	0.750	0.727
		1	0.602	1.159	0.989

			1	2	3
		5	0.955	1.216	0.955
		4	1.114	1.295	0.932
Plane C2	x/D = 0.471	3	1.114	1.091	0.864
		2	1.227	1.318	1.045
		1	1.489	1.477	1.227

			1	2	3
		5	1.023	0.977	0.932
		4	1.011	0.977	0.955
Plane C3	x/D = 1.728	3	1.045	0.966	0.977
		2	1.080	1.055	1.011
		1	1.091	1.077	1.000

			1	2	3
		5	0.977	1.023	0.989
		4	1.000	0.966	0.966
Plane C4	x/D = 2.880	3	1.034	0.966	0.989
		2	1.068	1.023	1.023
		1	1.080	1.091	1.045

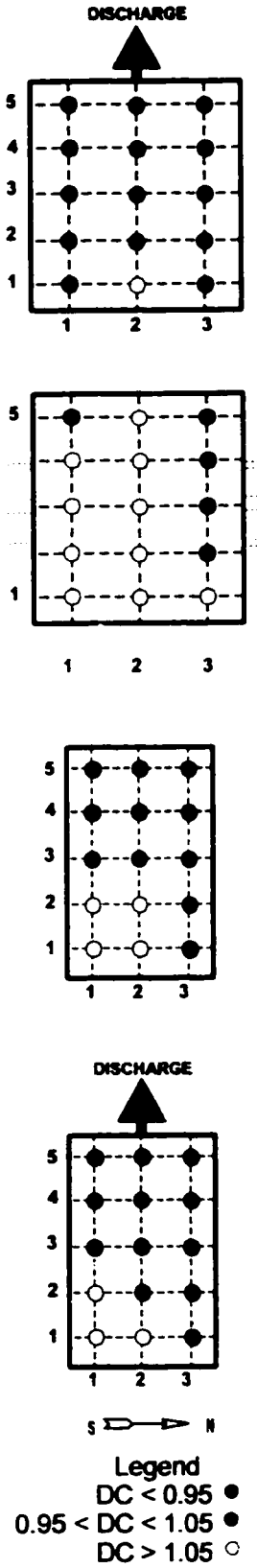

Figure A.3.11 Uniformity of Mixing in Water Model - Test 3A3 Dimensionless Concentrations

			1	2	3
		5	0.159	0.148	0.125
		4	0.216	0.193	0.159
Plane C1	x/D = -0.261	3	0.330	0.364	0.330
		2	0.636	0.841	0.682
		1	0.739	1.398	0.795

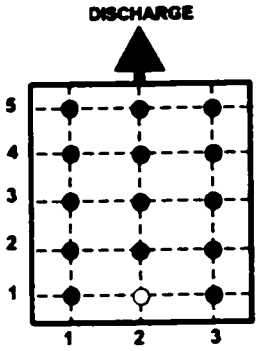

			1	2	3
		5	0.886	1.127	0.898
		4	0.934	1.193	0.920
Plane C2	x/D = 0.471	3	0.957	1.216	0.955
		2	1.102	1.250	1.193
		1	1.191	1.125	1.136

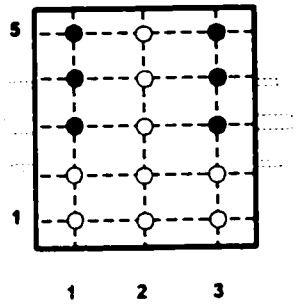

			1	2	3
		5	0.966	1.023	0.875
		4	0.955	1.034	0.898
Plane C3	x/D = 1.728	3	0.989	1.023	0.966
		2	0.966	1.045	1.068
		1	1.045	1.057	1.080

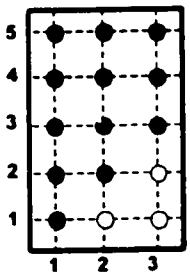

			1	2	3
		5	1.023	0.966	0.986
		4	0.966	0.989	0.920
Plane C4	x/D = 2.880	3	1.000	1.023	0.920
		2	1.011	1.034	1.020
		1	1.023	1.045	0.989

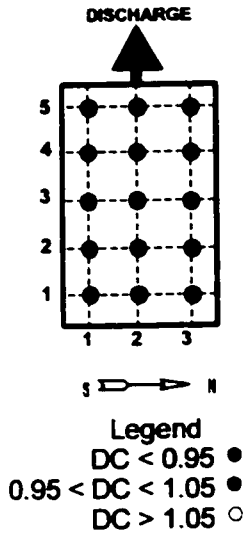

Figure A.3.12 Uniformity of Mixing in Water Model - Test 4A1 Dimensionless Concentrations

			1	2	3
		5	0.122	0.156	0.178
		4	0.189	0.189	0.189
Plane C1	x/D = -0.261	3	0.300	0.311	0.322
		2	0.667	0.811	0.644
		1	0.922	1.033	0.822

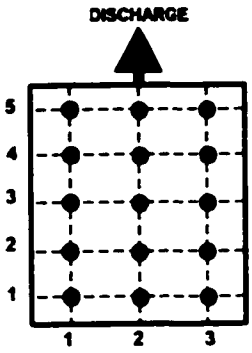

			1	2	3
		5	0.856	1.256	0.867
		4	1.000	1.344	1.000
Plane C2	x/D = 0.471	3	0.978	1.133	0.967
		2	1.122	1.200	1.133
		1	1.178	1.289	1.211

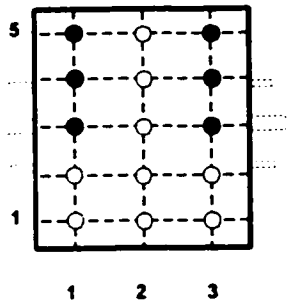

			1	2	3
		5	0.922	0.967	0.933
		4	0.978	0.989	1.000
Plane C3	x/D = 1.728	3	1.044	0.978	0.978
		2	1.067	1.033	1.000
		1	1.089	1.044	0.989

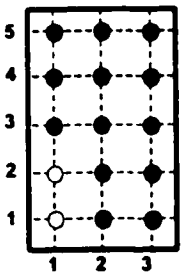

			1	2	3
		5	0.933	0.983	0.989
		4	0.972	0.983	1.033
Plane C4	x/D = 2.880	3	1.033	1.011	1.033
		2	1.000	1.033	1.033
		1	1.011	1.033	1.044

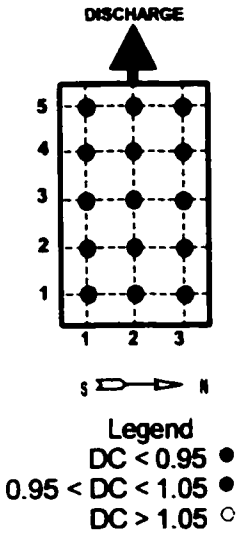

Figure A.3.13 Uniformity of Mixing in Water Model - Test 5A1 Dimensionless Concentrations

			1	2	3
		5	0.179	0.100	0.129
		4	0.239	0.236	0.193
Plane C1	x/D = -0.261	3	0.289	0.414	0.293
		2	0.404	0.721	0.371
		1	0.557	0.779	0.500

			1	2	3
		5	0.550	0.736	0.664
		4	1.000	1.414	1.250
Plane C2	x/D = 0.471	3	1.193	1.700	1.707
		2	1.321	1.436	1.479
		1	1.357	1.250	1.243

			1	2	3
		5	0.950	0.964	0.814
		4	1.036	0.943	0.921
Plane C3	x/D = 1.728	3	1.143	1.121	1.014
		2	1.229	1.186	1.100
		1	1.157	1.114	1.071

			1	2	3
		5	0.921	1.029	0.943
		4	0.971	1.014	1.000
Plane C4	x/D = 2.880	3	0.943	1.050	1.014
		2	0.993	1.064	1.057
		1	1.050	1.129	1.071

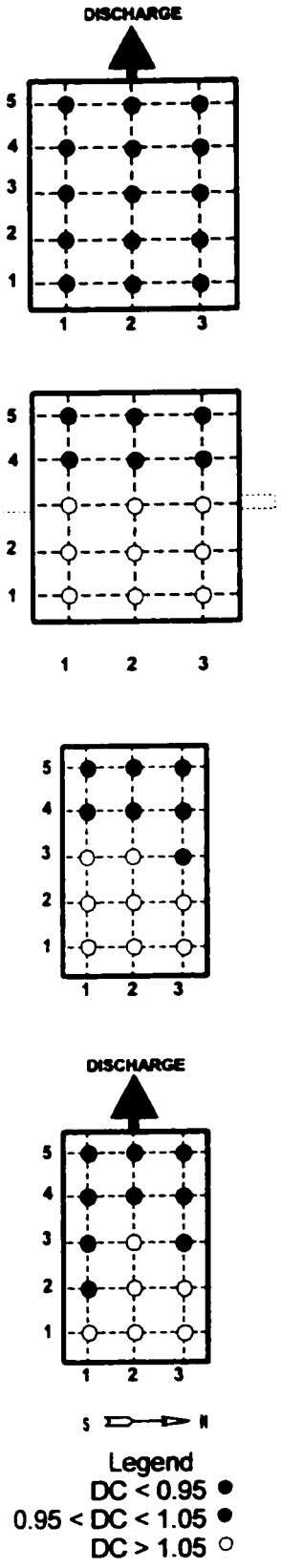

Figure A.3.14 Uniformity of Mixing in Water Model - Test 1B1 Dimensionless Concentrations

			1	2	3
		5	0.066	0.093	0.079
		4	0.093	0.152	0.132
Plane C1	x/D = -0.261	3	0.185	0.338	0.166
		2	0.285	0.536	0.265
		1	0.371	0.781	0.318

			1	2	3
		5	0.391	0.715	0.748
		4	0.901	1.391	1.205
Plane C2	x/D = 0.471	3	1.258	1.974	1.497
		2	1.325	1.642	1.397
		1	1.099	1.205	1.060

			1	2	3
		5	0.848	0.940	0.934
		4	0.987	1.046	1.020
Plane C3	x/D = 1.728	3	1.079	1.099	1.053
		2	1.152	1.152	1.073
		1	1.166	1.205	1.139

			1	2	3
		5	1.079	1.046	0.934
		4	1.046	1.033	0.940
Plane C4	x/D = 2.880	3	1.026	1.126	0.947
		2	1.053	1.086	1.007
		1	1.026	1.099	1.060

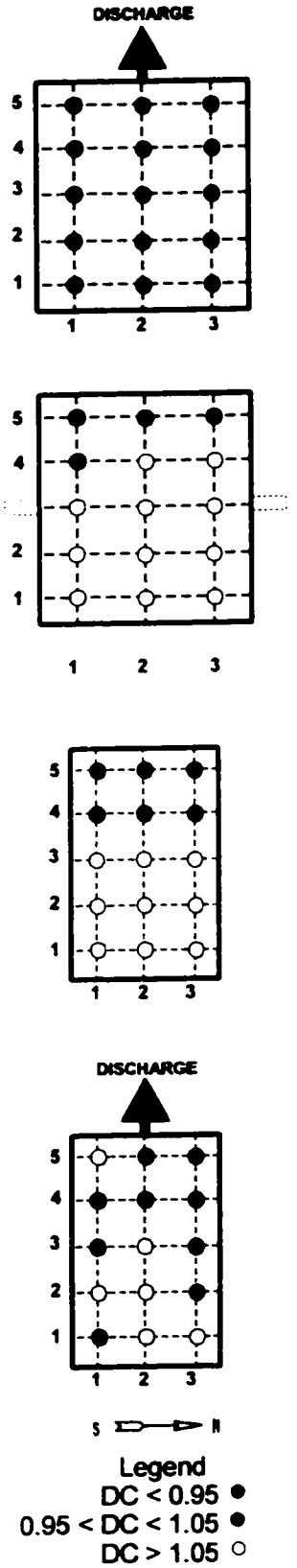

Figure A.3.15 Uniformity of Mixing in Water Model - Test 2B1 Dimensionless Concentrations

			1	2	3
		5	0.068	0.077	0.103
		4	0.111	0.128	0.103
Plane C1	x/D = -0.261	3	0.179	0.299	0.231
		2	0.333	0.462	0.325
		1	0.410	0.607	0.496

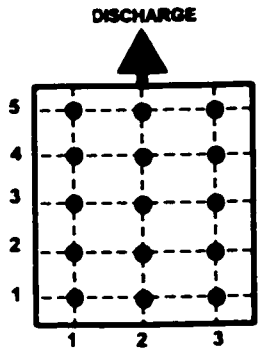

			1	2	3
		5	0.641	0.624	0.632
		4	1.034	1.325	1.017
Plane C2	x/D = 0.471	3	1.350	1.778	1.376
		2	1.128	1.556	1.197
		1	0.812	1.299	1.077

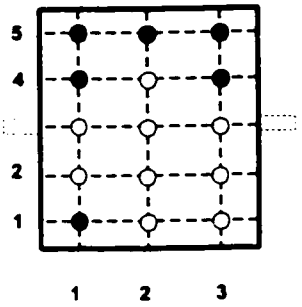

			1	2	3
		5	0.812	0.863	0.915
		4	0.855	0.932	1.000
Plane C3	x/D = 1.728	3	0.966	1.034	1.034
		2	1.060	1.077	1.034
		1	1.094	1.077	1.103

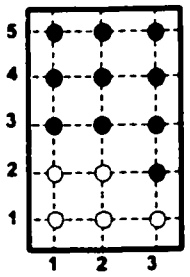

			1	2	3
		5	0.949	0.949	0.974
		4	0.966	0.980	1.017
Plane C4	x/D = 2.880	3	0.991	0.990	1.017
		2	1.039	1.009	1.050
		1	1.100	1.059	1.059

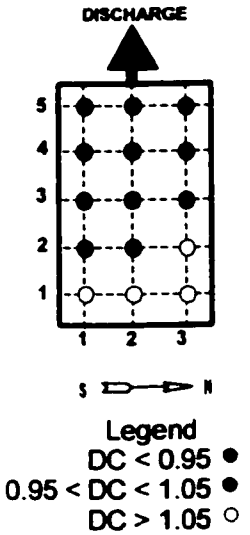

Figure A.3.16 Uniformity of Mixing in Water Model - Test 3B1 Dimensionless Concentrations

			1	2	3
		5	0.094	0.118	0.106
		4	0.176	0.188	0.141
Plane C1	x/D = -0.261	3	0.412	0.424	0.224
		2	0.565	0.482	0.329
		1	0.682	0.588	0.435

			1	2	3
		5	0.588	0.800	0.600
		4	0.988	1.588	0.965
Plane C2	x/D = 0.471	3	1.224	1.800	1.529
		2	1.059	1.400	1.271
		1	0.871	1.012	0.824

			1	2	3
		5	0.863	0.863	0.918
		4	0.918	0.918	0.988
Plane C3	x/D = 1.728	3	0.965	0.918	0.965
		2	1.106	1.056	1.094
		1	1.118	1.082	1.106

			1	2	3
		5	0.968	0.966	0.988
		4	0.961	0.995	0.999
Plane C4	x/D = 2.880	3	0.993	0.988	1.012
		2	1.024	1.035	1.029
		1	1.082	1.056	1.082

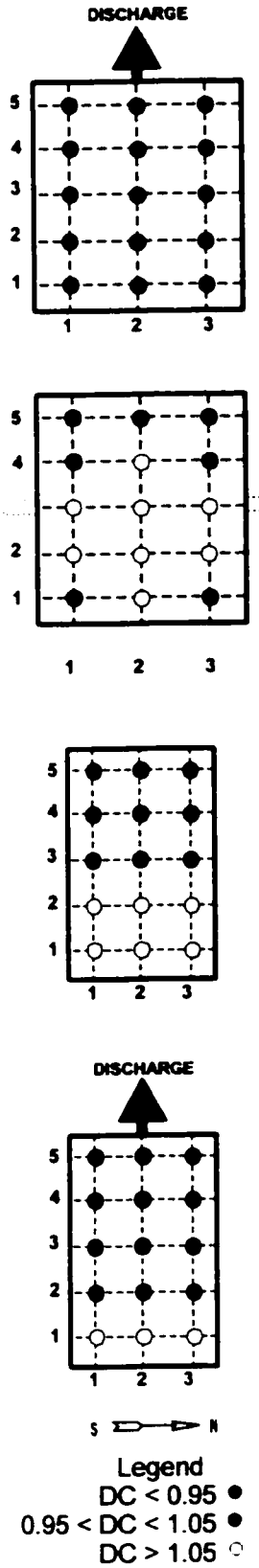

Figure A.3.17 Uniformity of Mixing in Water Model - Test 3B2 Dimensionless Concentrations

			1	2	3
		5	0.135	0.101	0.112
		4	0.180	0.146	0.191
Plane C1	x/D = -0.261	3	0.292	0.236	0.292
		2	0.506	0.652	0.584
		1	0.764	0.742	0.629

			1	2	3
		5	0.404	0.820	0.618
		4	1.157	1.618	1.135
Plane C2	x/D = 0.471	3	1.596	1.989	1.539
		2	1.247	1.562	1.202
		1	1.124	1.135	0.854

			1	2	3
		5	0.966	0.955	0.697
		4	1.112	1.045	0.787
Plane C3	x/D = 1.728	3	1.202	1.135	0.899
		2	1.247	1.157	0.854
		1	1.202	1.180	0.854

			1	2	3
		5	1.022	1.090	0.820
		4	1.045	1.034	0.809
Plane C4	x/D = 2.880	3	1.101	0.989	0.888
		2	1.112	1.022	0.910
		1	1.112	1.034	0.944

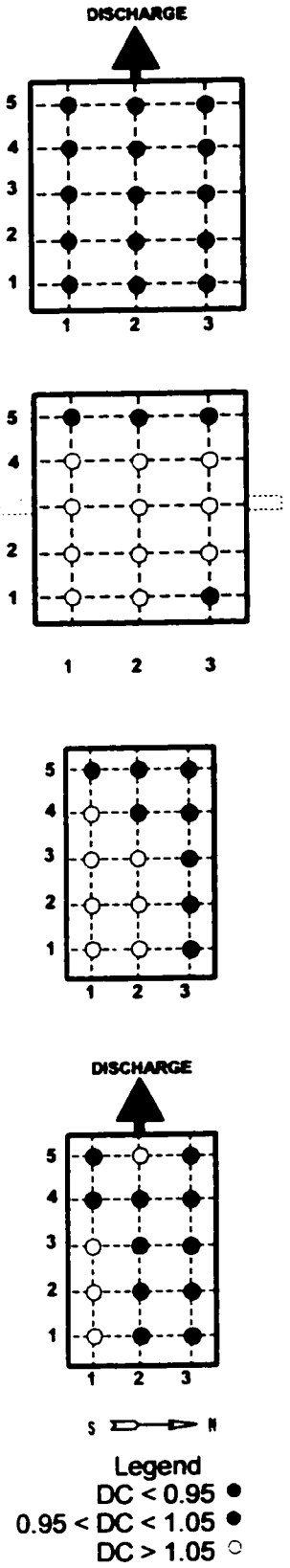

Figure A.3.18 Uniformity of Mixing in Water Model - Test 4B1 Dimensionless Concentrations

			1	2	3
		5	0.078	0.328	0.109
		4	0.094	0.453	0.172
Plane C1	x/D = -0.261	3	0.188	0.563	0.234
		2	0.328	0.391	0.359
		1	0.516	0.313	0.438

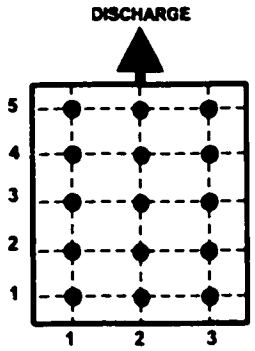

			1	2	3
		5	0.516	0.844	0.734
		4	0.969	1.313	0.984
Plane C2	x/D = 0.471	3	1.219	1.781	1.219
		2	1.078	1.453	1.094
		1	0.953	1.125	0.922

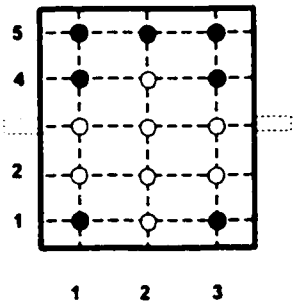

			1	2	3
		5	0.797	0.953	0.875
		4	0.906	0.922	0.953
Plane C3	x/D = 1.728	3	0.969	1.031	1.109
		2	1.016	1.031	1.172
		1	1.094	1.109	1.172

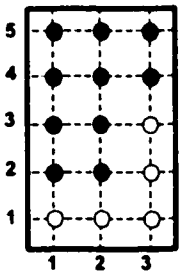

			1	2	3
		5	0.913	0.906	1.047
		4	0.944	0.953	1.063
Plane C4	x/D = 2.880	3	0.944	1.000	1.094
		2	0.956	1.016	1.094
		1	0.953	1.047	1.078

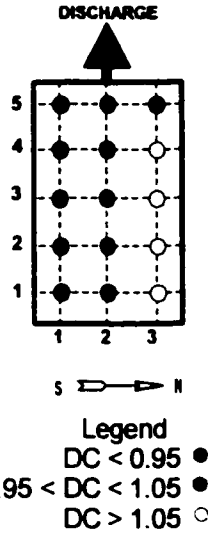

Figure A.3.19 Uniformity of Mixing in Water Model - Test 5B1 Dimensionless Concentrations

			1	2	3
		5	0.062	0.106	0.080
		4	0.097	0.177	0.115
Plane C1	x/D = -0.261	3	0.142	0.354	0.230
		2	0.274	0.566	0.451
		1	0.363	0.673	0.575

			1	2	3
		5	0.664	0.823	0.646
		4	1.168	1.496	1.186
Plane C2	x/D = 0.471	3	1.416	1.823	1.522
		2	1.345	1.513	1.496
		1	1.159	1.106	1.186

			1	2	3
		5	0.770	1.009	0.850
		4	0.956	0.982	0.956
Plane C3	x/D = 1.728	3	1.018	1.000	1.035
		2	1.088	1.027	1.088
		1	1.115	1.044	1.053

			1	2	3
		5	0.965	1.027	0.956
		4	1.106	1.018	1.009
Plane C4	x/D = 2.880	3	1.168	1.062	0.982
		2	1.195	1.106	0.991
		1	1.204	1.115	1.071

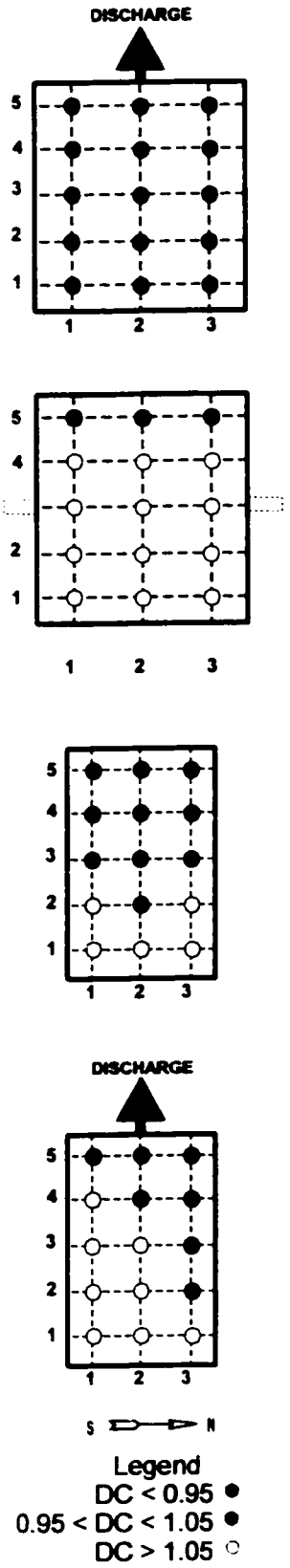

Figure A.3.20 Uniformity of Mixing in Water Model - Test 6B1 Dimensionless Concentrations

			1	2	3
		5	0.161	0.263	0.093
		4	0.208	0.381	0.131
Plane C1	x/D = -0.261	3	0.449	0.424	0.237
		2	0.767	0.492	0.415
		1	1.008	0.576	0.547

			1	2	3
		5	0.602	0.653	0.678
		4	1.331	1.593	1.407
Plane C2	x/D = 0.471	3	1.771	1.941	1.602
		2	1.373	1.669	1.381
		1	1.322	1.246	0.856

			1	2	3
		5	0.881	0.873	0.864
		4	0.966	0.992	0.941
Plane C3	x/D = 1.728	3	0.907	1.076	1.008
		2	0.992	1.076	1.127
		1	0.992	1.119	1.119

			1	2	3
		5	0.975	0.941	0.924
		4	1.034	0.975	0.932
Plane C4	x/D = 2.880	3	1.068	0.992	0.992
		2	1.093	1.076	1.042
		1	1.119	1.110	1.042

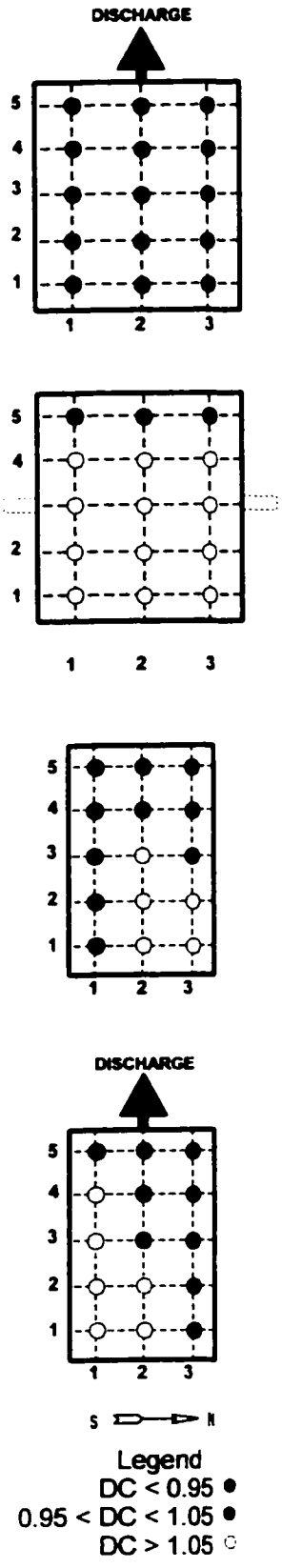

Figure A.3.21 Uniformity of Mixing in Water Model - Test 7B1 Dimensionless Concentrations

			1	2	3
		5	0.116	0.145	0.145
		4	0.101	0.188	0.174
Plane C1	x/D = -0.261	3	0.174	0.290	0.188
		2	0.391	0.507	0.333
		1	0.652	0.725	0.449

			1	2	3
		5	0.971	0.986	0.884
		4	1.029	1.116	1.000
Plane C2	x/D = 0.471	3	1.145	1.246	1.116
		2	1.232	1.275	1.029
		1	1.348	1.159	1.072

			1	2	3
		5	1.043	0.899	0.913
		4	1.014	0.942	0.971
Plane C3	x/D = 1.728	3	1.072	0.957	0.957
		2	1.101	0.986	0.986
		1	1.145	1.043	1.000

			1	2	3
		5	1.043	0.913	0.959
		4	1.058	0.970	0.959
Plane C4	x/D = 2.880	3	1.058	0.970	0.986
		2	1.029	1.000	0.986
		1	1.058	1.043	1.014

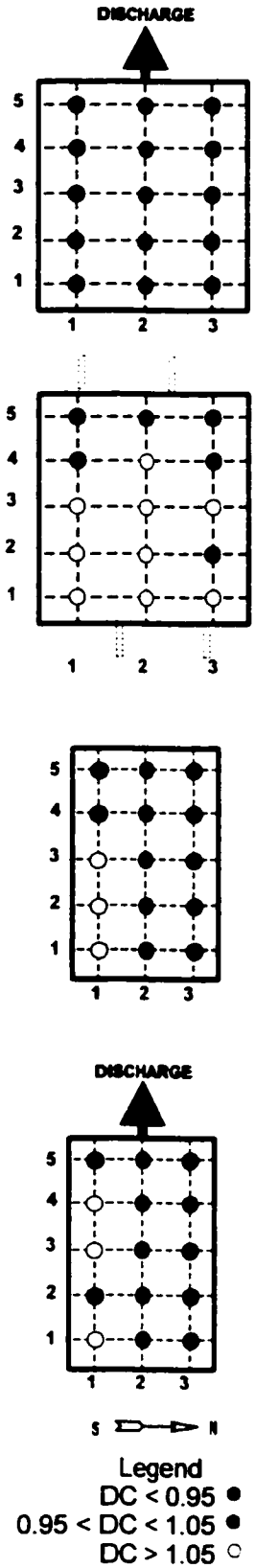

Figure A.3.22 Uniformity of Mixing in Water Model - Test 1F1 Dimensionless Concentrations

			1	2	3
		5	0.192	0.137	0.123
		4	0.151	0.164	0.548
Plane C1	x/D = -0.261	3	0.178	0.329	0.384
		2	0.315	0.521	0.151
		1	0.521	0.808	0.630

			1	2	3
		5	1.082	0.890	0.753
		4	1.014	0.890	0.959
Plane C2	x/D = 0.471	3	1.055	1.014	1.137
		2	1.151	1.123	1.096
		1	1.151	1.110	1.110

			1	2	3
		5	1.041	0.904	0.849
		4	1.027	0.918	0.918
Plane C3	x/D = 1.728	3	1.096	0.959	0.945
		2	1.055	1.027	1.000
		1	1.123	1.055	1.055

			1	2	3
		5	1.027	0.973	0.986
		4	1.041	0.978	0.945
Plane C4	x/D = 2.880	3	1.041	0.973	0.945
		2	1.055	0.973	1.000
		1	1.059	1.014	1.000

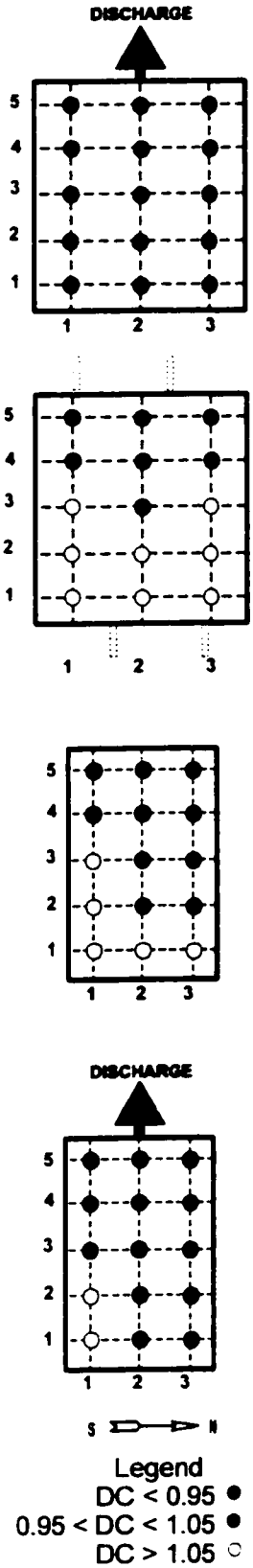

Figure A.3.23 Uniformity of Mixing in Water Model - Test 2F1 Dimensionless Concentrations

			1	2	3
		5	0.160	0.200	0.093
		4	0.093	0.120	0.107
Plane C1	x/D = -0.261	3	0.133	0.213	0.187
		2	0.293	0.413	0.400
		1	0.507	0.747	0.627

			1	2	3
		5	1.133	1.133	0.920
		4	1.120	1.053	0.840
Plane C2	x/D = 0.471	3	1.120	1.040	0.893
		2	1.160	1.013	0.960
		1	1.200	1.000	1.000

			1	2	3
		5	1.040	1.027	0.880
		4	0.933	0.987	1.013
Plane C3	x/D = 1.728	3	0.960	1.093	1.027
		2	1.093	1.080	1.013
		1	1.200	1.133	1.027

			1	2	3
		5	1.053	0.980	0.980
		4	1.067	0.980	0.980
Plane C4	x/D = 2.880	3	1.040	0.933	0.947
		2	1.053	0.960	0.973
		1	1.067	0.987	0.987

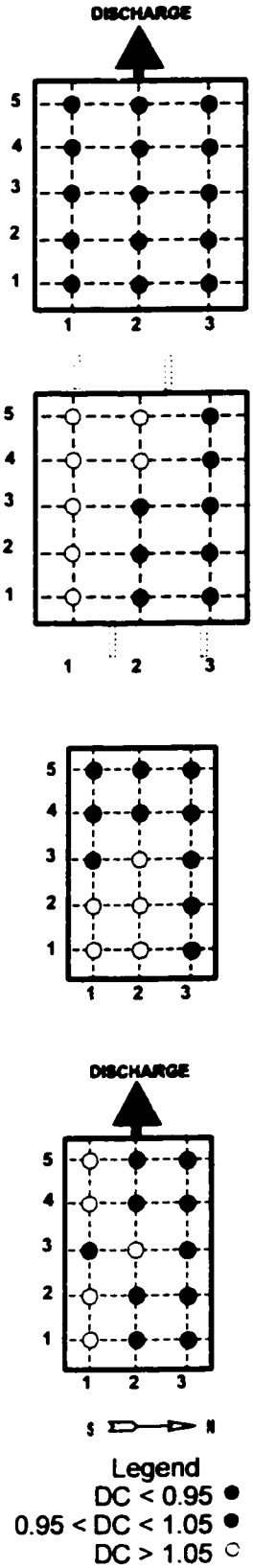

Figure A.3.24 Uniformity of Mixing in Water Model - Test 3F1 Dimensionless Concentrations

			1	2	3
		5	0.167	0.121	0.106
		4	0.212	0.152	0.121
Plane C1	x/D = -0.261	3	0.258	0.288	0.167
		2	0.455	0.500	0.288
		1	0.727	0.697	0.455

			1	2	3
		5	1.061	1.015	0.864
		4	1.106	1.182	1.015
Plane C2	x/D = 0.471	3	1.182	1.242	1.091
		2	1.258	1.242	1.015
		1	1.333	1.152	1.076

			1	2	3
		5	1.106	1.045	0.879
		4	1.106	1.061	0.939
Plane C3	x/D = 1.728	3	1.121	1.030	1.015
		2	1.167	1.000	1.106
		1	1.227	1.015	1.182

			1	2	3
		5	1.076	0.970	0.979
		4	1.076	1.000	0.990
Plane C4	x/D = 2.880	3	1.106	0.999	0.990
		2	1.091	1.024	1.030
		1	1.091	1.009	1.015

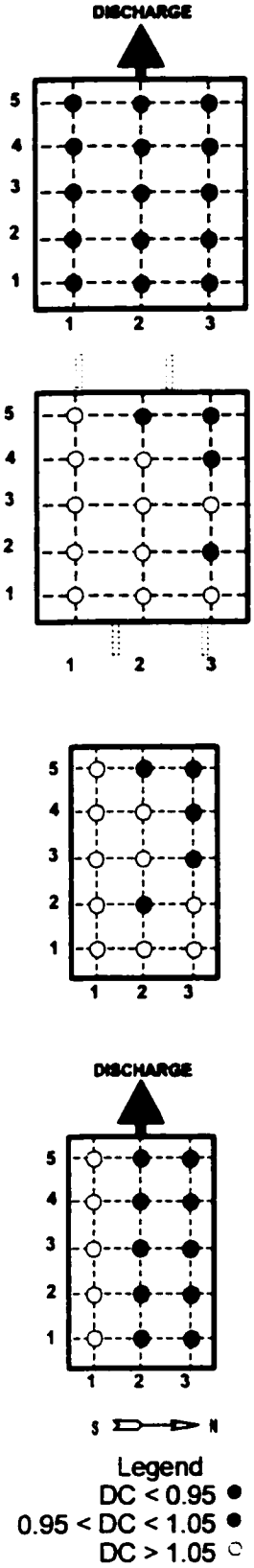

Figure A.3.25 Uniformity of Mixing in Water Model - Test 4F1 Dimensionless Concentrations

			1	2	3
		5	0.120	0.169	0.120
		4	0.096	0.120	0.096
Plane C1	x/D = -0.261	3	0.133	0.145	0.157
		2	0.289	0.229	0.289
		1	0.554	0.542	0.506

			1	2	3
		5	0.876	1.036	0.928
		4	0.871	0.964	0.988
Plane C2	x/D = 0.471	3	0.871	1.036	1.036
		2	0.843	1.072	1.072
		1	1.136	1.181	1.169

			1	2	3
		5	0.964	1.000	0.940
		4	0.855	1.000	0.976
Plane C3	x/D = 1.728	3	0.904	1.036	1.012
		2	0.940	1.048	1.096
		1	1.036	1.072	1.108

			1	2	3
		5	0.992	1.060	1.036
		4	0.944	1.024	1.036
Plane C4	x/D = 2.880	3	0.958	1.012	1.000
		2	0.966	1.012	1.088
		1	1.000	1.000	1.076

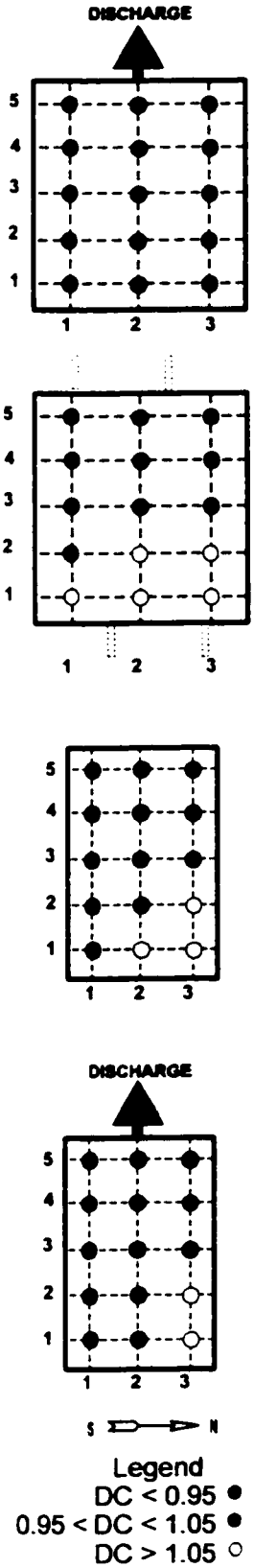

Figure A.3.26 Uniformity of Mixing in Water Model - Test 5F1 Dimensionless Concentrations

			1	2	3
		5	0.310	0.264	0.195
		4	0.149	0.138	0.138
Plane C1	x/D = -0.261	3	0.172	0.184	0.207
		2	0.333	0.345	0.425
		1	0.667	0.609	0.759

			1	2	3
		5	0.967	1.069	1.111
		4	1.046	0.897	0.908
Plane C2	x/D = 0.471	3	0.954	0.885	0.897
		2	1.181	0.966	0.943
		1	1.161	1.203	1.183

			1	2	3
		5	1.057	1.023	1.000
		4	1.069	0.954	0.954
Plane C3	x/D = 1.728	3	1.034	0.908	0.966
		2	1.103	0.954	0.977
		1	1.138	1.046	1.080

			1	2	3
		5	1.057	0.989	1.034
		4	1.046	0.989	1.011
Plane C4	x/D = 2.880	3	1.057	0.977	1.023
		2	1.103	0.977	1.046
		1	1.103	1.011	1.046

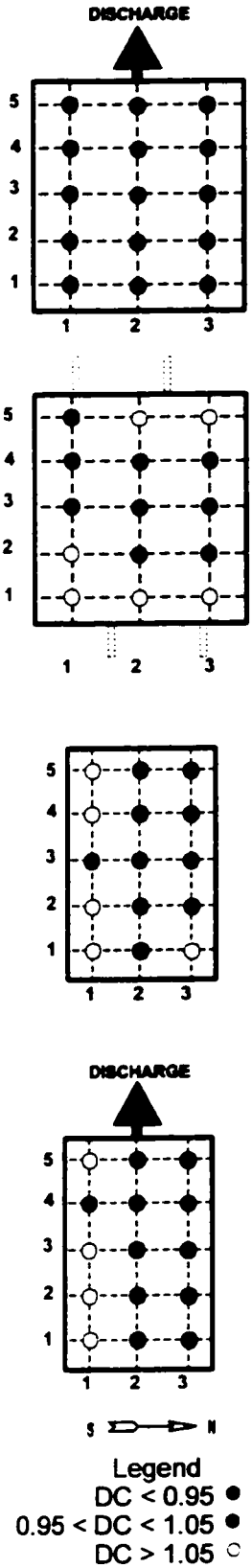

Figure A.3.27 Uniformity of Mixing in Water Model - Test 6F1 Dimensionless Concentrations

			1	2	3
		5	0.068	0.081	0.095
		4	0.081	0.122	0.135
Plane C1	x/D = -0.261	3	0.108	0.162	0.230
		2	0.216	0.351	0.378
		1	0.378	0.622	0.541

			1	2	3
		5	0.932	1.027	0.838
		4	0.932	1.068	1.027
Plane C2	x/D = 0.471	3	1.027	1.149	1.203
		2	1.081	1.135	1.176
		1	1.068	1.135	1.216

			1	2	3
		5	0.946	0.973	0.919
		4	0.946	0.959	0.919
Plane C3	x/D = 1.728	3	0.959	1.014	0.959
		2	1.086	1.081	1.027
		1	1.086	1.108	1.095

			1	2	3
		5	0.946	0.946	0.946
		4	0.973	0.973	0.972
Plane C4	x/D = 2.880	3	0.973	1.027	1.000
		2	1.086	1.054	1.027
		1	1.081	1.068	1.081

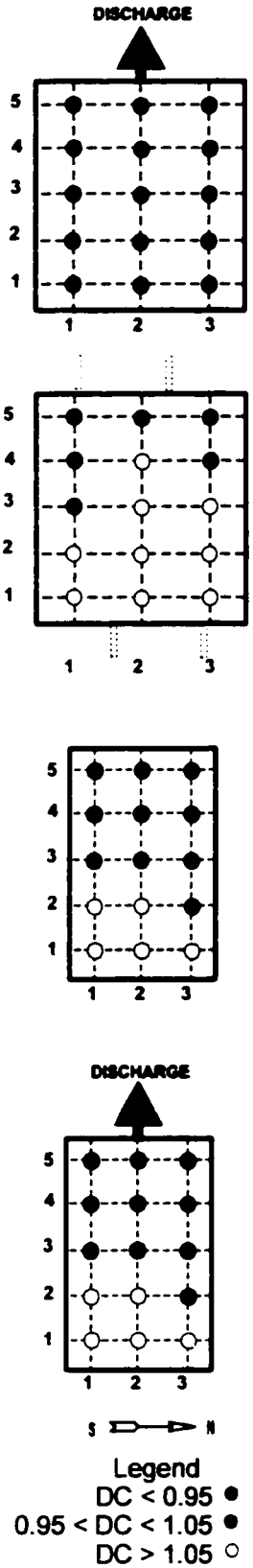

Figure A.3.28 Uniformity of Mixing in Water Model - Test 7F1 Dimensionless Concentrations

			1	2	3
		5	0.107	0.107	0.080
		4	0.107	0.107	0.093
Plane C1	x/D = -0.261	3	0.133	0.160	0.173
		2	0.240	0.280	0.320
		1	0.453	0.493	0.453

			1	2	3
		5	1.067	1.040	0.907
		4	0.933	1.067	0.960
Plane C2	x/D = 0.471	3	1.000	1.120	1.027
		2	1.080	1.160	1.067
		1	1.147	1.213	1.107

			1	2	3
		5	0.920	0.960	0.947
		4	1.027	1.000	0.960
Plane C3	x/D = 1.728	3	1.040	1.013	1.013
		2	1.067	1.013	1.013
		1	1.187	1.067	1.013

			1	2	3
		5	0.920	0.973	0.933
		4	0.987	0.973	0.947
Plane C4	x/D = 2.880	3	0.960	0.987	0.987
		2	1.067	1.040	1.013
		1	1.040	1.040	1.053

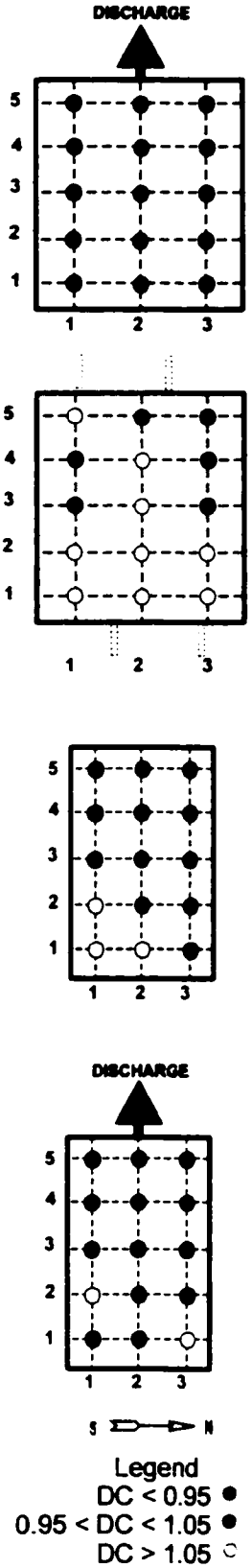

Figure A.3.29 Uniformity of Mixing in Water Model - Test 8F1 Dimensionless Concentrations

			1	2	3
		5	0.149	0.103	0.115
		4	0.092	0.092	0.138
Plane C1	x/D = -0.261	3	0.126	0.172	0.195
		2	0.241	0.322	0.287
		1	0.471	0.552	0.552

			1	2	3
		5	1.069	1.011	0.943
		4	1.011	1.046	1.057
Plane C2	x/D = 0.471	3	1.069	1.126	1.161
		2	1.103	1.126	1.126
		1	1.218	1.276	1.161

			1	2	3
		5	1.011	1.011	0.943
		4	1.046	0.977	0.966
Plane C3	x/D = 1.728	3	1.092	1.000	1.034
		2	1.149	1.023	1.080
		1	1.149	1.057	1.080

			1	2	3
		5	0.989	0.989	0.954
		4	0.954	0.989	0.943
Plane C4	x/D = 2.880	3	1.080	0.989	1.046
		2	1.057	1.034	1.069
		1	1.092	1.023	1.034

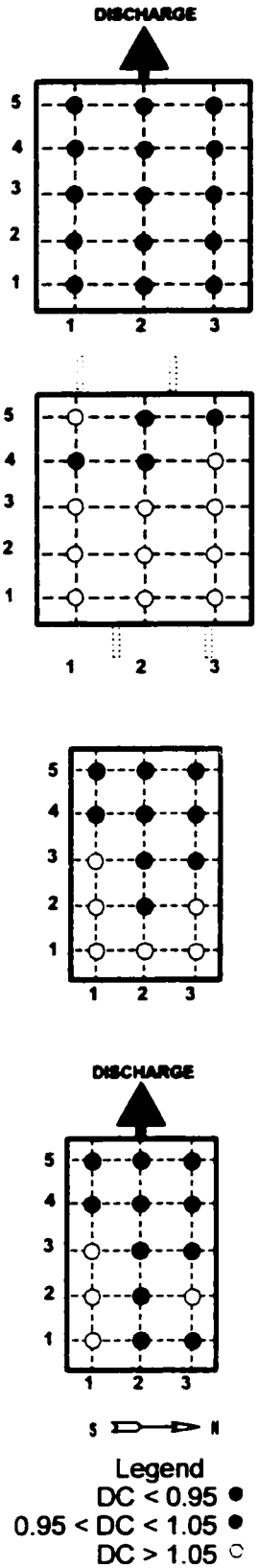

Figure A.3.30 Uniformity of Mixing in Water Model - Test 8F2 Dimensionless Concentrations

			1	2	3
		5	0.105	0.105	0.092
		4	0.132	0.132	0.079
Plane C1	x/D = -0.261	3	0.145	0.132	0.105
		2	0.250	0.316	0.211
		1	0.605	0.592	0.447

			1	2	3
		5	1.092	1.079	0.934
		4	0.921	0.987	0.882
Plane C2	x/D = 0.471	3	0.882	1.053	0.987
		2	0.974	1.079	1.026
		1	1.092	1.184	1.105

			1	2	3
		5	1.013	1.026	0.947
		4	0.987	0.961	0.988
Plane C3	x/D = 1.728	3	0.961	0.987	0.982
		2	1.000	1.039	1.105
		1	1.105	1.171	0.974

			1	2	3
		5	0.987	0.961	1.000
		4	0.961	0.987	1.000
Plane C4	x/D = 2.880	3	0.961	1.000	0.961
		2	0.974	1.026	0.961
		1	1.039	1.079	1.026

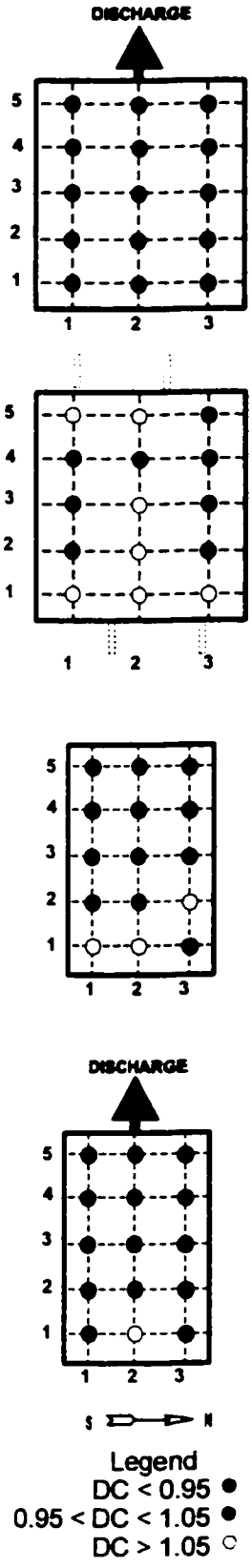

Figure A.3.31 Uniformity of Mixing in Water Model - Test 9F1 Dimensionless Concentrations

			1	2	3
		5	0.169	0.246	0.200
		4	0.123	0.154	0.123
Plane C1	x/D = -0.261	3	0.138	0.138	0.200
		2	0.262	0.246	0.369
		1	0.615	0.554	0.692

			1	2	3
		5	1.092	1.062	0.954
		4	0.923	0.954	0.915
Plane C2	x/D = 0.471	3	0.962	0.923	0.931
		2	0.923	0.954	0.938
		1	1.223	1.154	1.177

			1	2	3
		5	1.092	1.046	1.000
		4	0.969	0.985	0.938
Plane C3	x/D = 1.728	3	0.954	0.938	0.938
		2	1.031	0.954	0.969
		1	1.077	1.015	1.046

			1	2	3
		5	1.015	1.015	1.000
		4	1.031	1.000	0.985
Plane C4	x/D = 2.880	3	1.015	1.015	0.969
		2	1.015	1.015	1.000
		1	1.077	1.015	1.077

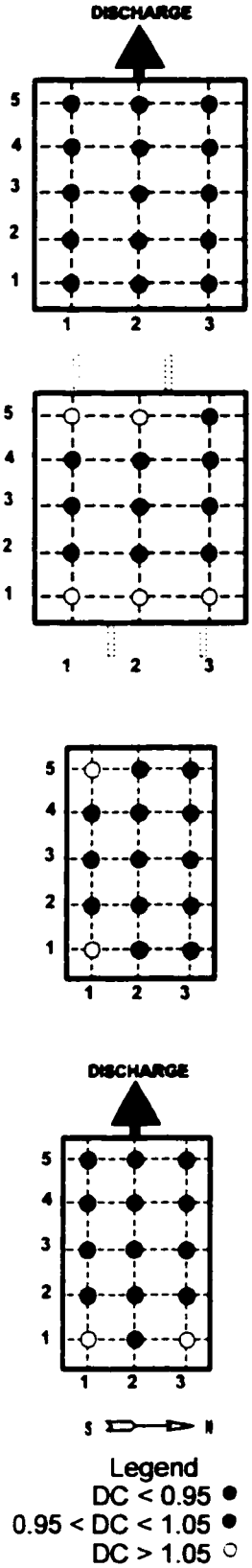

Figure A.3.32 Uniformity of Mixing in Water Model - Test 10F1 Dimensionless Concentrations

			1	2	3
		5	0.277	0.215	0.200
		4	0.138	0.154	0.169
Plane C1	x/D = -0.261	3	0.154	0.185	0.215
		2	0.277	0.369	0.431
		1	0.585	0.631	0.692

			1	2	3
		5	1.036	1.048	0.988
		4	0.869	0.952	0.910
Plane C2	x/D = 0.471	3	0.945	0.893	0.910
		2	1.093	1.052	0.988
		1	1.195	1.119	1.219

			1	2	3
		5	1.012	0.988	1.000
		4	0.976	0.929	0.929
Plane C3	x/D = 1.728	3	0.940	0.905	0.981
		2	1.029	1.040	1.029
		1	1.024	1.071	1.060

			1	2	3
		5	1.000	0.976	0.976
		4	1.000	0.964	0.976
Plane C4	x/D = 2.880	3	0.964	0.964	0.940
		2	1.000	1.012	0.964
		1	1.060	1.024	1.060

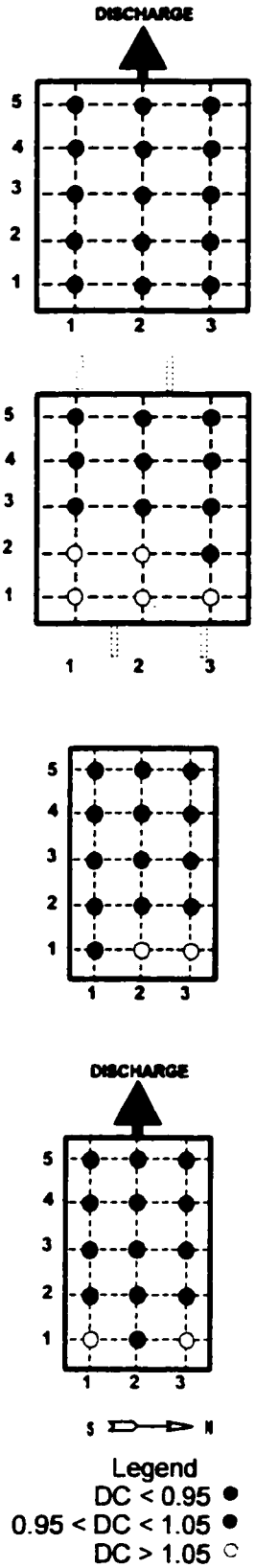

Figure A.3.33 Uniformity of Mixing in Water Model - Test 10F2 Dimensionless Concentrations

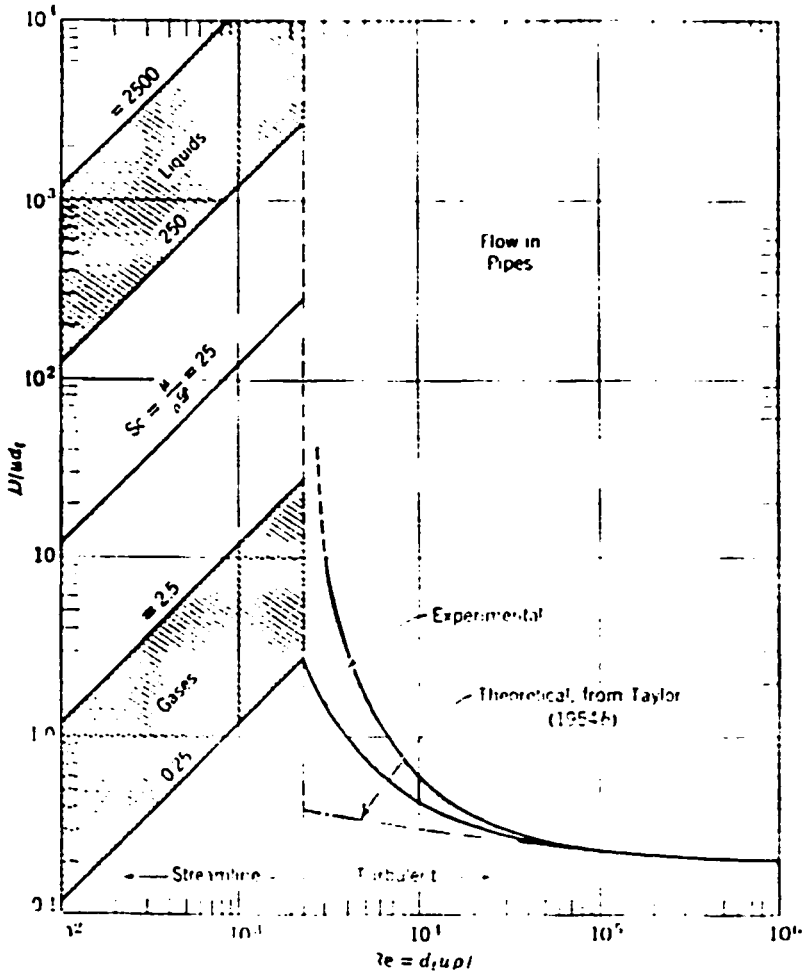

Figure A.3.34 Correlation for Dispersion of Fluids in Pipes, Adapted from Levenspiel (1972)

A.4. Salt Tracer Mixing in Water Model (Residence Time Distribution Experiments)

To evaluate the mixing conditions in the model, two exploratory experiments were carried in the water model using the residence time distribution technique. The objective of these experiments was examine the bulk flow patterns in the model with no of flow to the afterburners. The residence time distribution was measured under two flow conditions (table A.4.1 and A.4.2). In these experiments, a pulse injection of an inert tracer (20% NaCl solution) was introduced through a main burner jet in the furnace and the tracer concentration was measured at the discharge of the uptake. The actual residence time and the dispersion number were determined using the method described by Levenspiel (1972). The apparent residence time was equivalent to the plug flow residence time as defined by $\tau = V/Q$.

The tracer concentration was indirectly determined by measuring the conductivity of the water. In these studies, a Yokagawa (Model SC82) conductivity meter equipped with a titanium electrode was used to measure the change in the solution conductivity at the point of discharge from the model. During the residence time distribution experiments, the readings on the display screen of the Yogagawa conductivity meter were recorded with a video camera. Recording the data in this manner, unfortunately, limited the precision of the recorded measurement, especially in measuring the concentration decay. The conductivity was displayed with a $\pm$ 0.001 mS cm^{-1} accuracy, which was equivalent to $\pm$ 0.7 ppm NaCl. More details have been given in Section 4.2.2.4.

Table A.4.1 Residence Time Distribution Experiment in Water Model - RTD -1

Injection Point: #2 Burner Jet
Measuring Point: Discharge of Uptake
Test Conditions:

Flow	Burner	31.5 L/min x 4
Tracer	Conc	20 % w/w
	Net wt	96 g
	Vol	90 mL

Time (sec)	Temperature Corrected Net Conductivity (mS cm^{-1})	Tracer Concentration (ppm)	Dimensionless Time	Dimensionless Concentration
0	0.000	0.0	0.000	0.000
1	0.000	0.0	0.015	0.000
2	0.000	0.0	0.031	0.000
3	0.000	0.0	0.046	0.000
4	0.000	0.0	0.062	0.000
5	0.000	0.0	0.077	0.000
6	0.000	0.0	0.093	0.000
7	0.000	0.0	0.108	0.000
8	0.000	0.0	0.124	0.000
9	0.000	0.0	0.139	0.000
10	0.007	4.4	0.155	0.036
11	0.096	62.6	0.170	0.508
12	0.214	140.4	0.186	1.139
13	0.231	151.1	0.201	1.226
14	0.227	148.6	0.216	1.206
15	0.225	147.3	0.232	1.196
16	0.221	144.8	0.247	1.175
17	0.217	142.3	0.263	1.155
18	0.214	139.7	0.278	1.134
23	0.193	126.4	0.356	1.026
28	0.176	115.1	0.433	0.934
33	0.160	105.0	0.510	0.852
38	0.146	95.5	0.588	0.775
43	0.132	86.6	0.665	0.703
48	0.121	79.0	0.742	0.641
53	0.110	72.1	0.819	0.585
58	0.100	65.8	0.897	0.534
68	0.083	54.4	1.051	0.441
78	0.070	45.5	1.206	0.369
88	0.058	37.9	1.361	0.308
98	0.047	31.0	1.515	0.251
108	0.040	25.9	1.670	0.210
118	0.033	21.5	1.824	0.174
128	0.027	17.7	1.979	0.144
138	0.022	14.5	2.134	0.118
148	0.019	12.6	2.288	0.103
158	0.016	10.7	2.443	0.087
168	0.014	8.9	2.597	0.072
178	0.011	7.0	2.752	0.056
188	0.009	5.7	2.907	0.046
198	0.008	5.1	3.061	0.041
208	0.007	4.4	3.216	0.036
218	0.005	3.2	3.371	0.026
228	0.004	2.5	3.525	0.021
248	0.003	1.9	3.834	0.015
268	0.002	1.3	4.144	0.010
288	0.001	0.6	4.453	0.005
308	0.000	0.0	4.762	0.000

Apparent Residence Time:	64.0 sec	Dimensionless Variance:	0.59
Actual Residence Time:	64.7 sec	Dispersion Numer:	0.56
Variance:	2477 sec2	Tracer Recovery:	87.5 %

Table A.4.2 Residence Time Distribution Experiment in Water Model - RTD -2

Injection Point:	#2 Burner Jet			
Measuring Point:	Discharge of Uptake			
Test Conditions:	Flow	Burner	87	L/min x 4
	Tracer	Conc	20	% w/w
		Net wt	102	g
		Vol	96	mL

Time (sec)	Temperature Corrected Net Conductivity ($mS\ cm^{-1}$)	Tracer Concentration (ppm)	Dimensionless Time	Dimensionless Concentration
0	0.000	0.0	0.000	0.000
1	0.000	0.0	0.042	0.000
2	0.000	0.0	0.085	0.000
3	0.000	0.0	0.127	0.000
4	0.036	23.4	0.170	0.173
5	0.242	158.7	0.212	1.174
6	0.248	162.5	0.255	1.202
7	0.239	156.2	0.297	1.155
8	0.227	148.6	0.340	1.099
9	0.214	139.7	0.382	1.033
10	0.204	133.4	0.424	0.987
11	0.192	125.8	0.467	0.931
12	0.185	120.8	0.509	0.893
13	0.174	113.8	0.552	0.842
14	0.164	107.5	0.594	0.795
19	0.128	83.5	0.806	0.617
24	0.099	64.5	1.019	0.477
29	0.076	49.9	1.231	0.369
34	0.059	38.6	1.443	0.285
39	0.045	29.7	1.655	0.220
44	0.035	22.8	1.867	0.168
49	0.027	17.7	2.079	0.131
54	0.021	13.9	2.292	0.103
59	0.016	10.7	2.504	0.079
69	0.010	6.3	2.928	0.047
79	0.006	3.8	3.353	0.028
89	0.003	1.9	3.777	0.014
99	0.002	1.3	4.201	0.009
109	0.001	0.6	4.626	0.005
129	0.000	0.0	5.474	0.000

Apparent Residence Time:	23.2 sec	Dimensionless Variance:	0.6
Actual Residence Time:	23.6 sec	Dispersion Numer:	0.56
Variance:	333 sec2	Tracer Recovery:	92.4 %

Appendix B

AIR MODEL EXPERIMENTAL CONDITIONS AND RAW DATA

The primary objectives of the air modelling work were to define the flow fields and mixing characteristics in the furnace and uptake and to relate the findings to the operation of the prototype and the water model. The flow patterns of the air model are expected to closely approximate those of the plant, given the agreement of the similarity criterion. The experimental techniques involved flow visualization using smoke tests, velocity distributions and thermal mixing. This appendix summarizes the experimental conditions and the raw data collected from each experimental run.

B.1 Velocity Distribution in Air Model

The air model provided a direct means of obtaining the distribution, magnitude and direction of the flow at any cross-sectional plane. These experiments primarily focused on examining the bulk flow patterns in the furnace and uptake and were carried with and without the introduction of flow through the afterburner jets. A hot wire anemometer was used to measure the magnitude of the velocity, and a yarn streamer, attached to the tip of anemometer probe, indicated the predominant direction of the flow. The axial component of the mean velocity and the rms turbulence intensity were measured on a grid of points lying in three horizontal planes through the furnace and three vertical planes in the uptake (figure B.1.1). The grid system spacing used for the measuring local velocities in the furnace and the uptake is illustrated in figures B.1.2 and B.1.3.

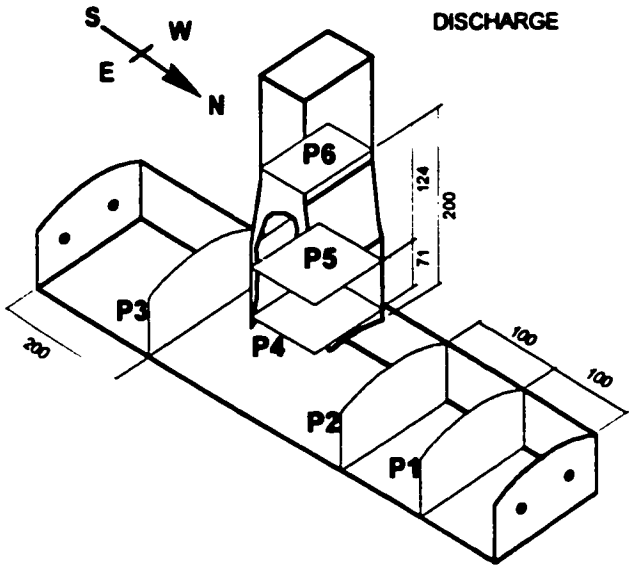

Figure B.1.1 Velocity Distribution in Air Model - Sampling Planes
(dimensions in cm)

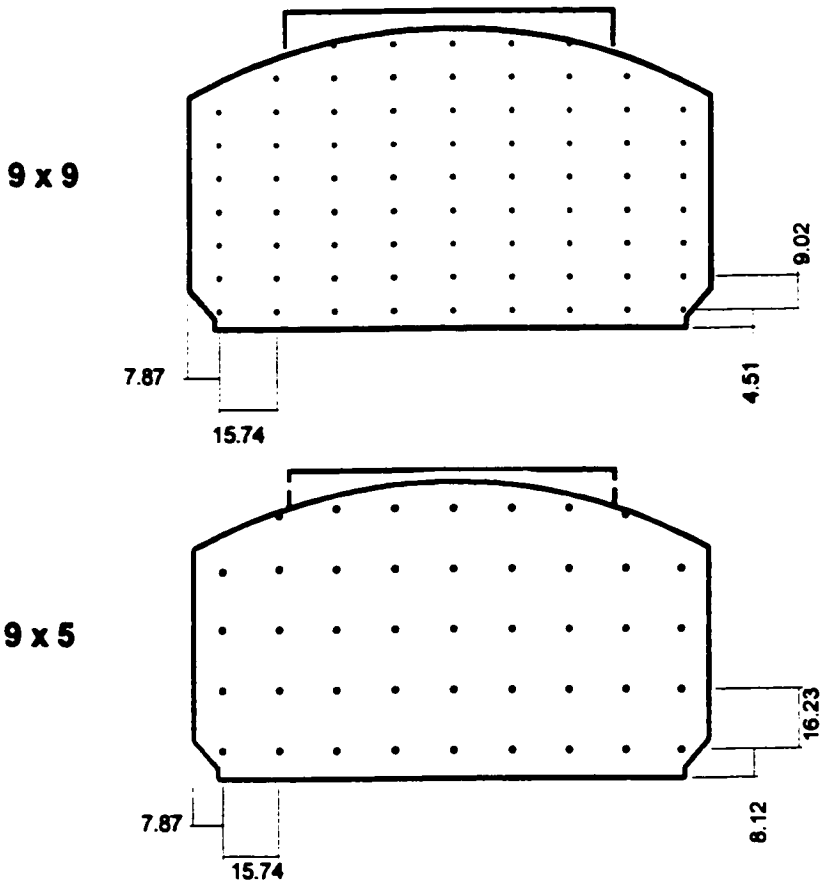

Figure B.1.2 Velocity Distribution in Air Model - Furnace Sampling Grid Spacing (P1, P2, P3)
(dimensions in cm)

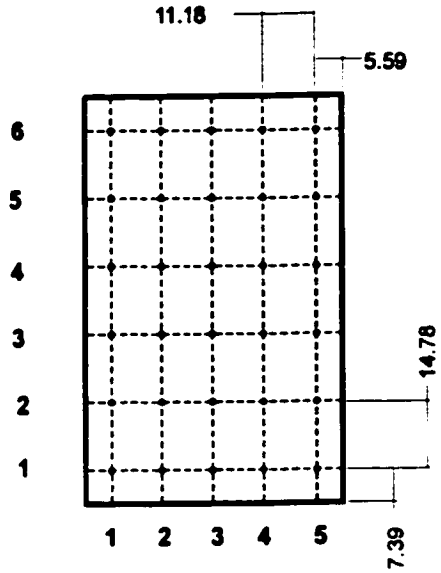

P6

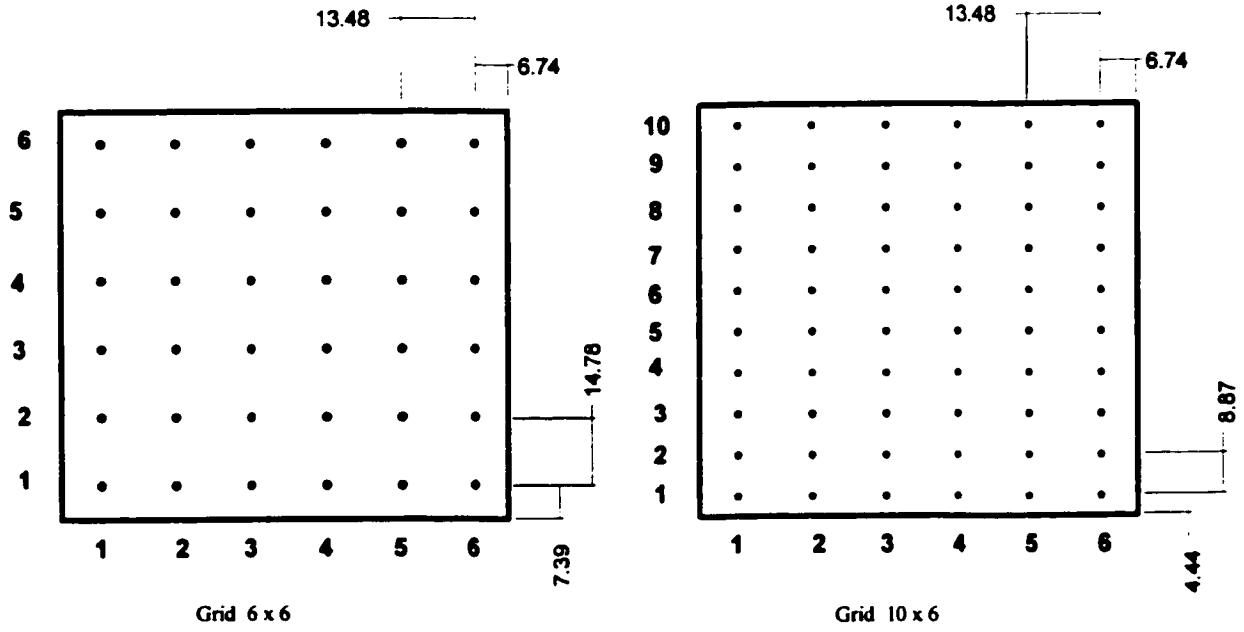

P4, P5

Figure B.1.3 Velocity Distribution in Air Model - Uptake Sampling Grid Spacing (dimensions in cm)

The average local axial velocity was calculated using equations B.1.1 and made dimensionless (equation B.1.2) with respect to the superficial velocity, $\bar{v}_{\text{measured flows to jets}}$, based on the measured flows to the jets (equation B.1.3). The superficial velocity, $\bar{v}_{\text{velocity profile}}$, based on the average local axial velocities (equation B.1.4), was found to be in close agreement to the superficial velocity calculated from the measured flows to the jets. The local rms turbulence intensity, TI, in the axial direction was computed from the variance of the data points (equation B.1.5).

$$\bar{v}_{i,j} = \frac{1}{n}\sum_{n=1}^{n} v_{i,j} \quad ; \text{where n = number of measurements} \tag{B.1.1}$$

$$\bar{V}_{i,j} = DV_{i,j} = \frac{\bar{v}_{i,j}}{\bar{v}} \tag{B.1.2}$$

$$\bar{v}_{\text{measured flows to jets}} = \frac{\sum_{m=1}^{m} q_m}{A} \quad ; \text{ where m = number of jets} \tag{B.1.3}$$

$$\bar{v}_{\text{velocity profile}} = \frac{1}{A}\sum_{i=1}^{I}\sum_{j=1}^{J} \bar{v}_{i,j}\,\Delta A_{i,j} \tag{B.1.4}$$

$$TI_{rms} = \frac{\sqrt{\dfrac{\sum_{n=1}^{n}\left(v_{i,j} - \bar{v}_{i,j}\right)^2}{n}}}{\bar{v}_{i,j}} \tag{B.1.5}$$

The experimental conditions are given in table B.1.1 an B.1.2, and a summary of the data collected is provided in table B.1.3. In table B.1.3, the furnace flow, Q, was calculated using equation B.1.6. The recirculating flow in the model was defined as the flow of air having a negative velocity, which in the furnace was the air stream moving toward the end wall away from the uptake. The numbering sequence used for the main burner and afterburner jets is shown in figure B.1.4. The velocity distributions measured in the air model are tabulated in table B.1.4 to

B.1.47 and illustrated in figures B.1.6 to B.1.49. In test V1B, the sensitivity to grid density was examined, while in test V1C the uptake was rotated 180^0 around its longitudinal axis, to evaluate the impact of the direction of the exhaust on the bulk flow patterns. Two test V2C and V2D were carried out to investigate the effect of the afterburners on the bulk flow patterns. The afterburner configurations tested are illustrated in figure B.1.5. In tests V3A, V3B, V4A, V4B and V5A, the effect of burner jet size on the furnace flow patterns was investigated - tests V3A, V3B, V4A and V4B were conducted with a 5 cm diameter jet while test V5A was carried out with a 7.4 cm jet.

$$Q = \sum_{i} \sum_{j} \bar{v}_{i,j} \Delta A_{i,j} \qquad \text{(B.1.6)}$$

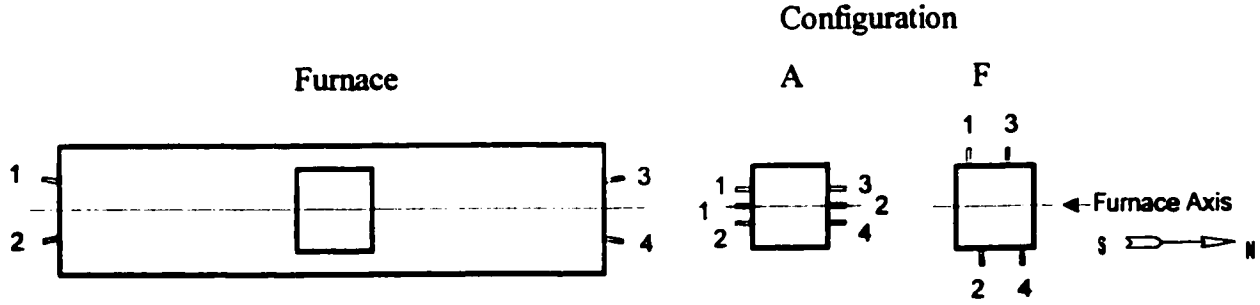

Figure B.1.4 Jet Numbering Sequence in Air Model

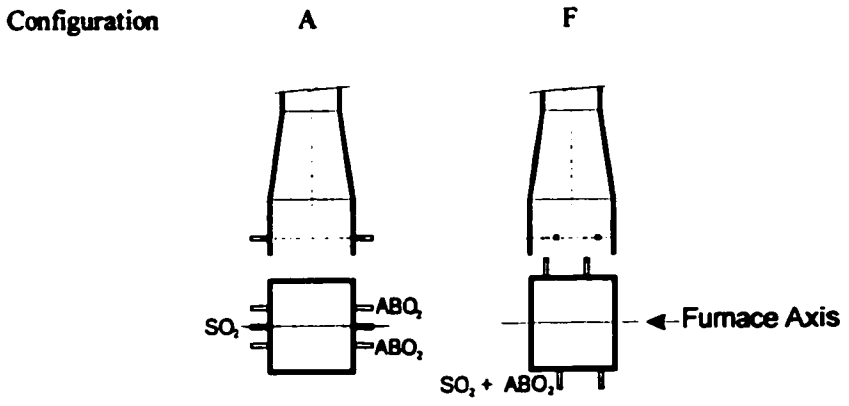

Figure B.1.5 Velocity Distribution in Air Model - Afterburner Configurations Tested

Table B.1.1 Velocity Distribution in Air Model - Experimental Conditions Based on Jet Flows

Test		V1A	V1B	V1C	V2A	V2B	V2C	V2D	V3A	V4A
Afterburner Configuration		----	----	----	----	----	F	A	----	----
Burner	Ø (cm)	9.80	9.80	9.80	9.80	9.80	9.80	9.80	4.98	7.40
	Reynolds # (x 10^3)	194.7	194.6	195.2	127.8	125.2	124.8	125.1	243.7	144.6
	Velocity (m/s)	29.8	29.8	29.9	19.6	19.2	19.1	19.2	73.4	29.3
Furnace	Grid Density	5 x 9	9 x 9	5 x 9	5 x 9	5 x 9	5 x 9	5 x 9	5 x 9	5 x 9
	Reynolds # (x 10^3)	29.4	29.4	29.5	19.3	18.9	18.9	18.9	18.7	16.5
	Superficial Velocity (cm/s)	42.5	42.5	42.6	27.9	27.3	27.3	27.3	27.0	23.9
Uptake	Grid Density - Lower	6 x 6	10 x 6	6 x 6	6 x 6	6 x 6	6 x 6	6 x 6	6 x 6	6 x 6
	- Upper	6 x 5		6 x 5	6 x 5		6 x 5	6 x 5		
	Entrance Reynolds # (x 10^3)	70.7	70.6	70.8	46.4	45.4	45.3	45.4	44.9	33.5
	Superficial Entrance Velocity (cm/s)	125.3	125.2	125.6	82.3	80.6	80.3	80.5	79.6	59.5
Afterburner O_2 Jet	Reynolds # (x 10^3)							25.4		
	Velocity (m/s)							24.0		
SO_2 Recycle Jet	Reynolds # (x 10^3)							37.2		
	Velocity (m/s)							8.9		
SO_2 Recycle+O_2 Jet	Ø (cm)						3.81			
	Reynolds # (x 10^3)						57.3			
	Velocity (m/s)						22.6			

Note 1: In test V1C, the uptake was rotated 180° around its longitudinal axis.
Note 2: Superficial velocity calculated based on measured flow to the jets (equation B.1.3).

Table B.1.2 Velocity Distribution in Air Model - Jet Flows

Test		Burner Jets				Afterburner O_2 Jets				SO_2 Recycle Jets		SO_2 Recycle+O_2 Jets			
		1	2	3	4	1	2	3	4	1	2	1	2	3	4
V1A	Flow (L/min)	13360	13520	13640	13400										
	Velocity (m/s)	29.5	29.9	30.2	29.6										
	Reynolds # (x 10^3)	193.0	195.3	197.0	193.6										
V1B	Flow (L/min)	13370	13510	13600	13400										
	Velocity (m/s)	29.6	29.9	30.1	29.6										
	Reynolds # (x 10^3)	193.1	195.2	196.5	193.6										
V1C	Flow (L/min)	13420	13580	13620	13430										
	Velocity (m/s)	29.7	30.0	30.1	29.7										
	Reynolds # (x 10^3)	193.9	196.2	196.7	194.0										
V2A	Flow (L/min)	8750	9070	8820	8760										
	Velocity (m/s)	19.3	20.1	19.5	19.4										
	Reynolds # (x 10^3)	126.4	131.0	127.4	126.5										
V2B	Flow (L/min)	8510	8760	8630	8760										
	Velocity (m/s)	18.8	19.4	19.1	19.4										
	Reynolds # (x 10^3)	122.9	126.5	124.7	126.5										
V2C	Flow (L/min)	8700	8630	8470	8770							1570	1560	1530	1510
	Velocity (m/s)	19.2	19.1	18.7	19.4							23.0	22.8	22.4	22.1
	Reynolds # (x 10^3)	125.7	124.7	122.4	126.7							58.3	57.9	56.8	56.1
V2D	Flow (L/min)	8730	8690	8440	8790	300	280	290	270	1650	1650				
	Velocity (m/s)	19.3	19.2	18.7	19.4	25.3	23.6	24.4	22.7	8.9	8.9				
	Reynolds # (x 10^3)	126.1	125.5	121.9	127.0	26.8	25.0	25.9	24.1	37.2	37.2				

Table B.1.2 (cont) Velocity Distribution in Air Model - Jet Flows

Test		Main Burner Jets				Afterburner O_2 Jets				SO_2 Recycle Jets		SO_2 Recycle+O_2 Jets			
		1	2	3	4	1	2	3	4	1	2	1	2	3	4
V3A	Flow (L/min)	8690	8240	8370	8970										
	Velocity (m/s)	74.5	70.6	71.7	76.9										
	Reynolds # (x 10^3)	247.2	234.4	238.1	255.2										
V4A	Flow (L/min)	7600	7510	7690	7490										
	Velocity (m/s)	29.4	29.1	29.8	29.0										
	Reynolds # (x 10^3)	145.1	143.4	146.8	143.0										

Table B.1.3 Velocity Distribution in Air Model - Summary of Findings

Test		V1A	V1B	V1C	V2A	V2B	V2C	V2D	V3A	V4A
Burner Jet Diameter (cm)		9.80	9.80	9.80	9.80	9.80	9.80	9.80	4.98	7.40
Afterburner Configuration		----	----	----	----	----	A	F	----	----
Plane P1	Superficial Furnace Velocity (cm/s)	38.2			37.8					
	Furnace Flow (L/min)	24210			23980					
	Flow through burner jets (L/min)	27040			17580					
	Recirculating Flow, Qr (L/min)	-71480			-51100					
Plane P2	Superficial Furnace Velocity (cm/s)	42.2	44.4		32.9	32.2			28.7	26.1
	Furnace Flow (L/min)	26740	28150		20840	20440			18220	15870
	Flow through burner jets (L/min)	27040	27000		17580	17390			17340	15180
	Recirculating Flow, Qr (L/min)	-58430	-55420		-40110	-36110			-85810	-50370
Plane P3	Superficial Furnace Velocity (cm/s)	40.0	39.2		28.2	27.8	28.5	32.9	22.5	25.0
	Furnace Flow (L/min)	25360	24830		17850	17640	18060	20870	14290	15830
	Flow through burner jets (L/min)	26880	26880		17820	17270	17330	17420	16930	15110
	Recirculating Flow, Qr (L/min)	-53850	-54120		-41840	-34040	-43080	-43900	-82020	-47610
Plane P4	Superficial Uptake Velocity (cm/s)	121.3		110.3	84.0		90.1	80.4		
	Uptake Flow, Qu (L/min)	52180		47450	36150		38750	34620		
	Flow through burner jets (L/min)	53920		54050	35400		34570	34650		
	Recirculating Flow, Qr (L/min)	-10370		-11770	-7200		-8650	-8170		
Plane P5	Superficial Uptake Velocity (cm/s)	122.6	124.5	116.0	94.3	77.6	158.9	131.7	75.8	66.9
	Uptake Flow, Qu (L/min)	52780	53580	49920	40570	33400	68370	56650	32610	28760
	Flow through burner and uptake jets (L/min)	53920	53880	54050	35400	34660	40740	39090	34270	30290
	Recirculating Flow, Qr (L/min)	-5300	-4760	-5550	-4130	-3450	----	----	-1580	-3220
Plane P6	Superficial Uptake Velocity (cm/s)	197.5		179.8	145.9		170.5	166.5		
	Uptake Flow, Qu (L/min)	58680		53400	43330		50650	49450		
	Flow through burner and uptake jets (L/min)	53920		54050	35400		40740	39090		

Table B.1.4 Test V1A - Velocity Profile at Plane P1

Average Furnace Velocity				42.7 cm/s	(based on measured flows to the main burner jets)				
				38.2 cm/s	(based on velocity profile)				
Dimensionless Velocity, DV									
	1	2	3	4	5	6	7	8	9
5		-1.97	-4.49	-4.08	-5.01	-4.79	-5.53	-5.13	
4	-4.12	-4.06	4.21	6.17	7.53	-5.32	-5.63	-6.77	-6.52
3	3.61	4.46	10.58	6.60	10.99	8.93	-5.86	-6.98	-6.70
2	3.81	5.97	11.73	12.16	10.11	7.49	-5.48	-5.71	-6.14
1	3.27	3.76	5.13	6.50	6.39	7.49	-4.91	-4.46	-5.66
Root Mean Square, RMS									
	1	2	3	4	5	6	7	8	9
5		0.40	0.40	0.50	0.35	0.38	0.32	0.31	
4	0.52	0.41	0.36	0.41	0.50	0.50	0.30	0.24	0.23
3	0.44	0.34	0.36	0.43	0.30	0.49	0.31	0.24	0.26
2	0.52	0.47	0.30	0.26	0.25	0.49	0.33	0.33	0.27
1	0.41	0.48	0.30	0.30	0.38	0.49	0.30	0.36	0.35

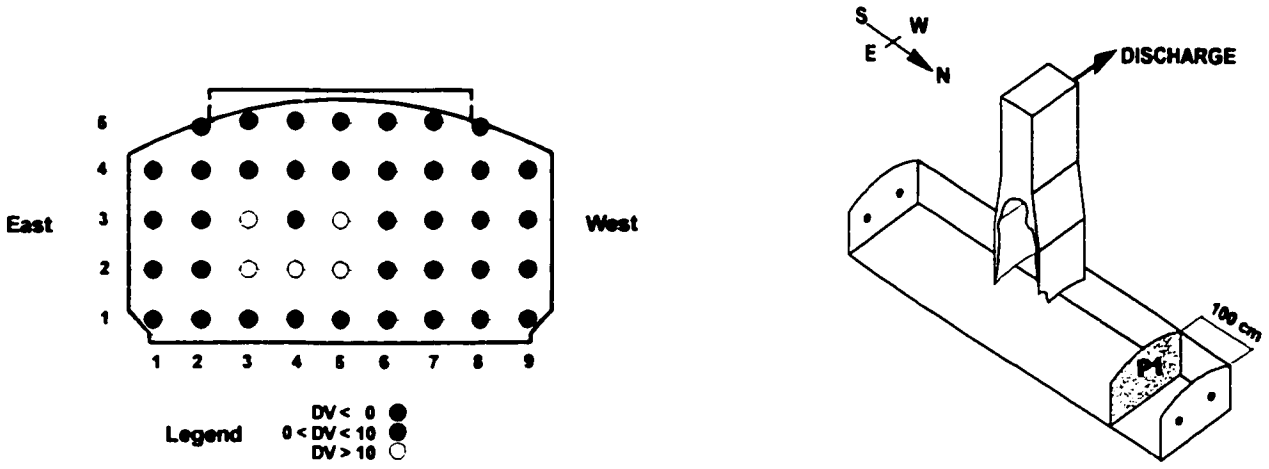

Figure B.1.6 Test V1A - Velocity Profile at Plane P1
(DV > 0 ≡ flow towards uptake)

Table B.1.5. Test V1A - Velocity Profile at Plane P2

Average Furnace Velocity				42.7 cm/s	(based on measured flows to the main burner jets)				
				42.2 cm/s	(based on velocity profile)				
Dimensionless Velocity, DV									
	1	2	3	4	5	6	7	8	9
5		-4.47	-4.47	-3.94	-5.12	-5.03	-5.69	-4.30	
4	-4.58	5.28	4.15	4.75	3.87	-4.15	-4.82	-5.34	-4.94
3	5.51	4.15	5.99	6.33	5.09	4.08	-4.58	-4.85	-4.63
2	6.07	5.14	7.32	7.31	5.18	4.11	-3.65	-4.33	-4.65
1	5.61	8.40	9.90	9.16	8.13	5.73	-4.50	-4.09	-4.44
Root Mean Square, RMS									
	1	2	3	4	5	6	7	8	9
5		0.27	0.35	0.42	0.27	0.33	0.27	0.34	
4	0.45	0.39	0.34	0.41	0.36	0.31	0.26	0.31	0.37
3	0.45	0.39	0.42	0.46	0.40	0.44	0.40	0.29	0.32
2	0.43	0.43	0.36	0.38	0.43	0.56	0.37	0.33	0.40
1	0.65	0.36	0.33	0.32	0.29	0.41	0.42	0.32	0.36

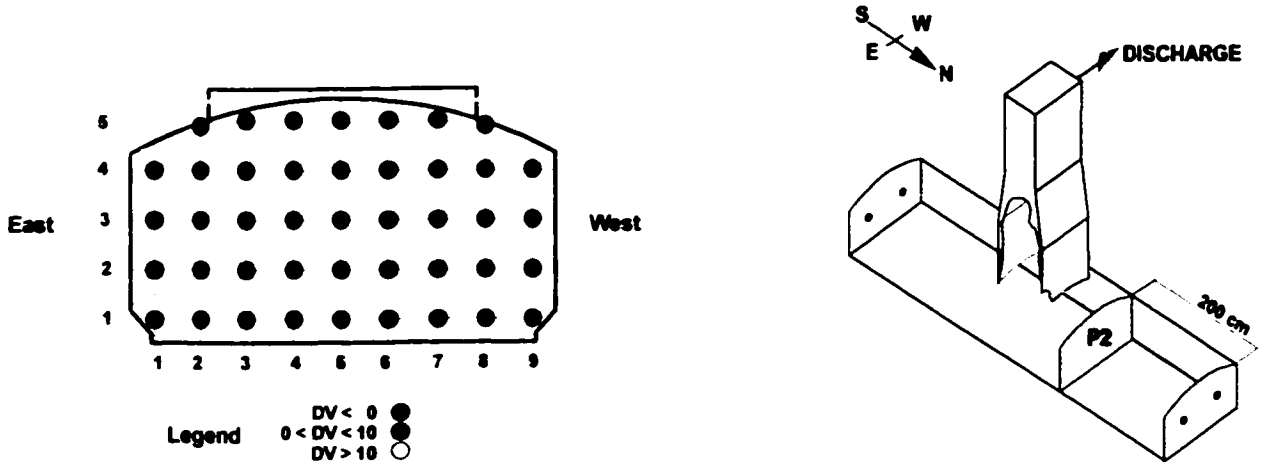

Figure B.1.7 Test V1A - Velocity Profile at Plane P2
(DV > 0 ≡ flow towards uptake)

Table B.1.6 Test V1A - Velocity Profile at Plane P3

Average Furnace Velocity				42.4 cm/s	(based on measured flows to the main burner jets)				
				40.0 cm/s	(based on velocity profile)				
Dimensionless Velocity, DV									
	1	2	3	4	5	6	7	8	9
5		-2.12	-4.26	-4.06	-4.55	-4.34	-5.66	-1.85	
4	3.50	3.93	4.00	3.59	-3.24	-4.23	-4.01	-5.23	-5.98
3	4.32	4.51	4.45	4.59	3.69	-3.53	-4.57	-4.32	-5.11
2	6.22	5.40	7.24	7.57	5.53	3.53	-3.48	-3.68	-4.98
1	9.61	6.51	8.78	9.07	7.13	5.93	4.19	-4.23	-4.18
Root Mean Square, RMS									
	1	2	3	4	5	6	7	8	9
5		0.28	0.45	0.40	0.32	0.32	0.27	0.20	
4	0.46	0.37	0.41	0.45	0.42	0.31	0.35	0.28	0.27
3	0.46	0.42	0.45	0.51	0.39	0.40	0.26	0.33	0.47
2	0.40	0.41	0.40	0.39	0.42	0.44	0.41	0.34	0.35
1	0.25	0.54	0.41	0.28	0.39	0.44	0.41	0.36	0.40

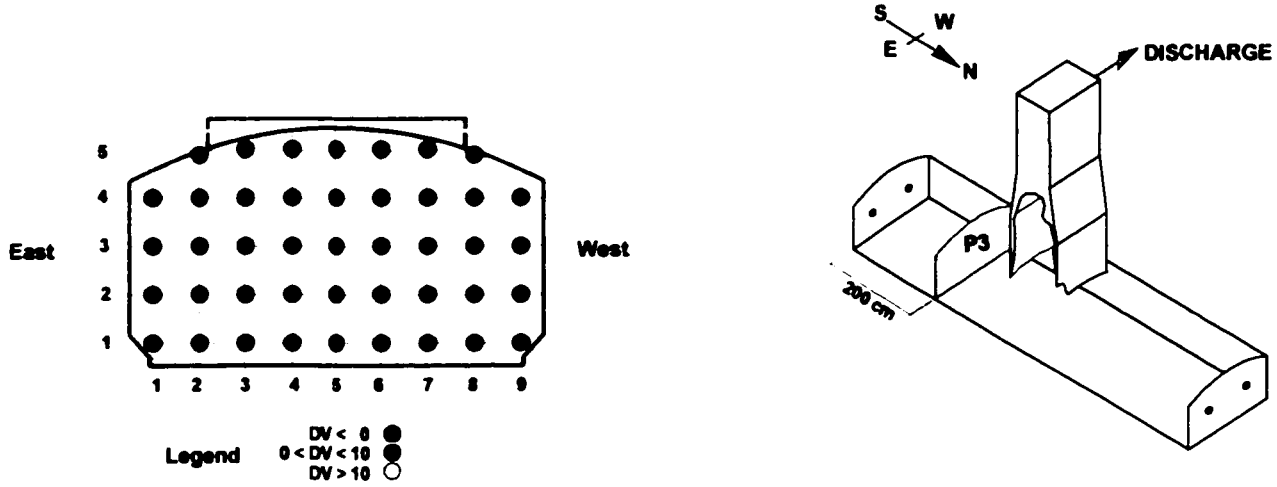

Figure B.1.8 Test V1A - Velocity Profile at Plane P3
(DV > 0 ≡ flow towards uptake)

Table B.1.7. Test V1A - Velocity Profile at Plane P4

Average Uptake Velocity				125.3 cm/s	(based on measured flows to the main burner jets)	
				121.3 cm/s	(based on velocity profile)	

Dimensionless Velocity, DV

	1	2	3	4	5	6
6	-1.07	1.32	1.50	1.45	1.27	-1.11
5	-1.23	1.13	1.38	1.27	1.15	-0.98
4	-1.28	1.27	1.28	1.30	1.44	-1.27
3	1.14	1.53	1.61	1.54	1.39	1.17
2	1.41	1.53	1.67	1.60	1.47	1.67
1	1.59	1.14	1.56	1.59	1.25	1.12

Root Mean Square, RMS

	1	2	3	4	5	6
6	0.46	0.39	0.37	0.38	0.38	0.43
5	0.45	0.36	0.35	0.29	0.39	0.36
4	0.48	0.40	0.32	0.34	0.34	0.41
3	0.45	0.35	0.34	0.30	0.38	0.36
2	0.58	0.33	0.33	0.32	0.38	0.40
1	0.38	0.45	0.40	0.38	0.43	0.49

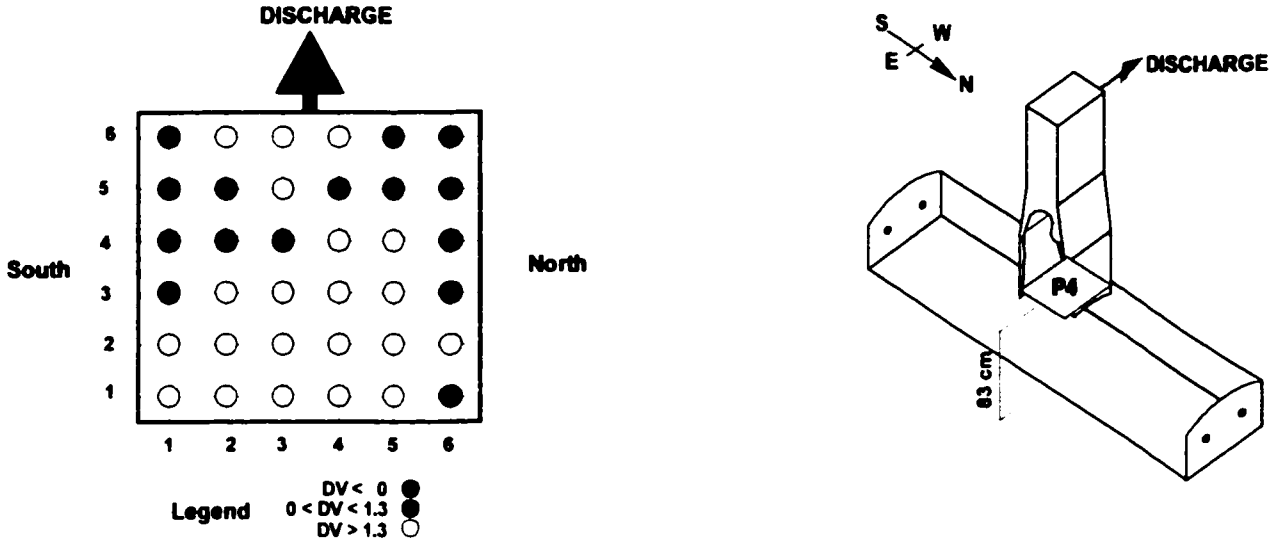

Figure B.1.9 Test V1A - Velocity Profile at Plane P4
(DV > 0 ≡ upward flow)

Table B.1.8 Test V1A - Velocity Profile at Plane P5

Average Uptake Velocity				125.3 cm/s	(based on measured flows to the main burner jets)	
				122.6 cm/s	(based on velocity profile)	

Dimensionless Velocity, DV

	1	2	3	4	5	6
6	1.71	1.66	1.51	1.41	1.41	1.32
5	1.59	1.32	1.41	1.48	1.29	1.36
4	1.46	1.24	1.28	1.08	1.06	1.46
3	1.17	1.02	1.08	0.89	1.06	1.34
2	1.12	0.94	0.85	0.79	0.86	0.91
1	-0.99	-0.73	0.79	0.88	-0.91	-0.92

Root Mean Square, RMS

	1	2	3	4	5	6
6	0.26	0.28	0.34	0.24	0.31	0.32
5	0.26	0.33	0.34	0.28	0.25	0.32
4	0.33	0.40	0.29	0.34	0.34	0.34
3	0.43	0.38	0.36	0.36	0.38	0.39
2	0.44	0.38	0.40	0.36	0.43	0.53
1	0.42	0.42	0.41	0.41	0.40	0.53

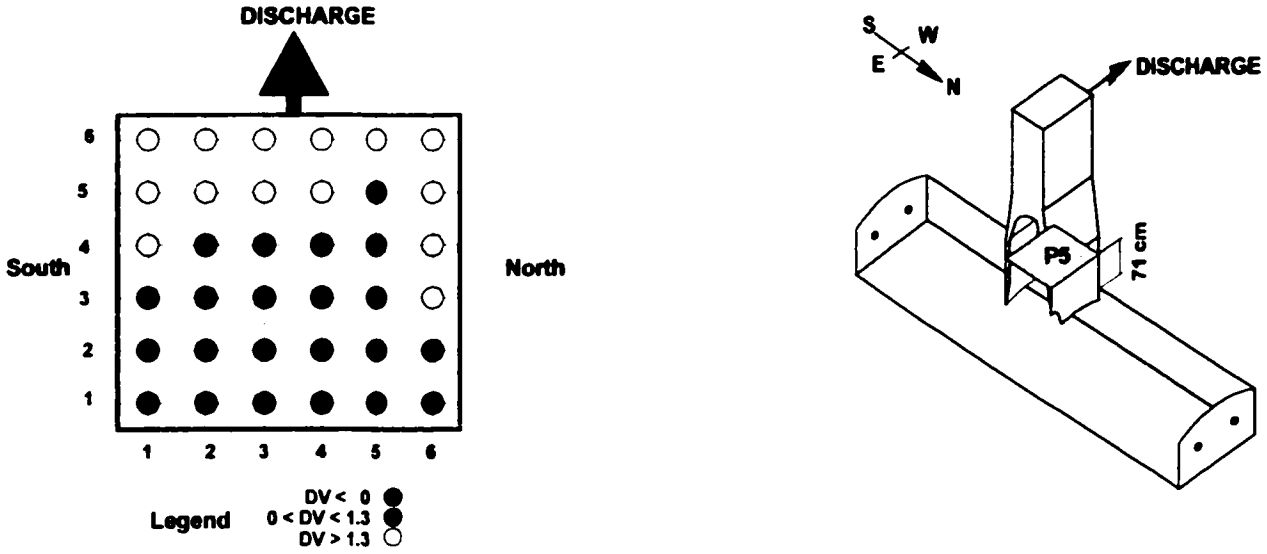

Figure B.1.10 Test V1A - Velocity Profile at Plane P5
(DV > 0 ≡ upward flow)

Table B.1.9 Test V1A - Velocity Profile at Plane P6

Average Uptake Velocity	181.4 cm/s	(based on measured flows to the main burner jets)
	197.5 cm/s	(based on velocity profile)

Dimensionless Velocity, DV

	1	2	3	4	5
6	1.26	1.25	1.20	1.25	1.27
5	1.25	1.24	1.15	1.23	1.24
4	1.18	1.08	1.06	1.11	1.10
3	0.98	1.03	0.98	1.02	1.09
2	1.08	0.98	0.98	0.95	0.94
1	0.92	0.96	0.97	0.98	0.95

Root Mean Square, RMS

	1	2	3	4	5
6	0.12	0.19	0.14	0.10	0.16
5	0.25	0.14	0.16	0.14	0.16
4	0.16	0.14	0.11	0.13	0.15
3	0.25	0.15	0.14	0.18	0.15
2	0.14	0.17	0.17	0.17	0.16
1	0.24	0.15	0.34	0.15	0.21

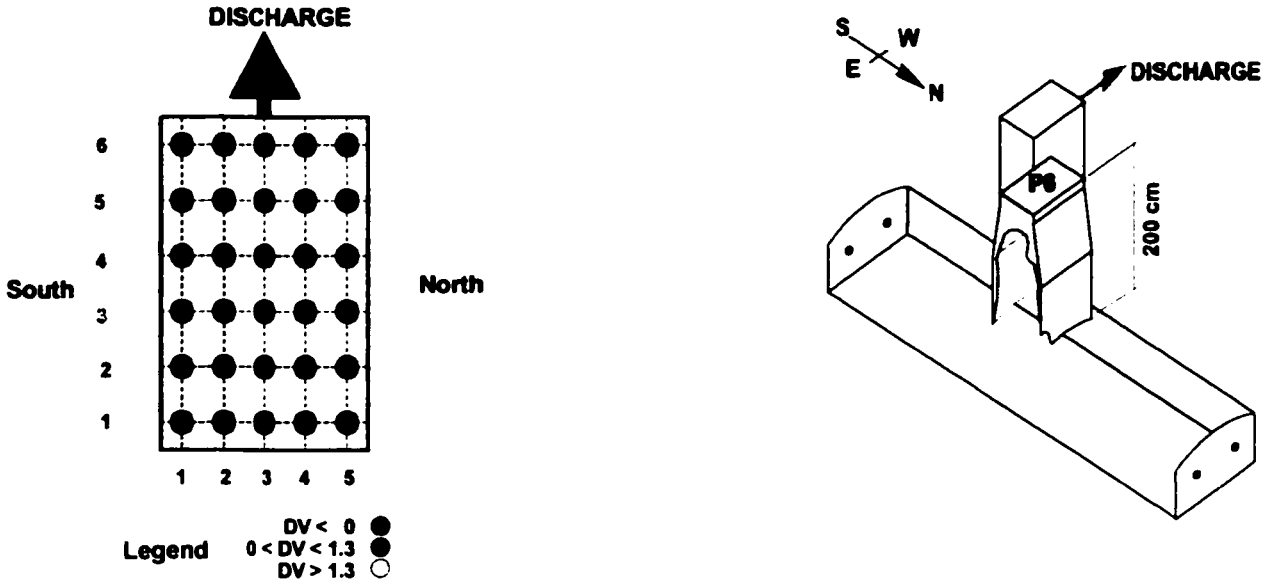

Figure B.1.11 Test V1A - Velocity Profile at Plane P6
(DV > 0 ≡ upward flow)

Table B.1.10 Test V1B - Velocity Profile at Plane P2

Average Furnace Velocity 42.6 cm/s (based on measured flows to the main burner jets)
44.4 cm/s (based on velocity profile)

Dimensionless Velocity, DV

	1	2	3	4	5	6	7	8	9
9			-3.40	-4.48	-4.79	-5.21	-4.01		
8		-5.12	-4.57	-3.63	-4.38	-4.14	-4.95	-5.46	
7	-4.36	3.57	4.51	4.14	3.94	-4.20	-4.31	-4.38	-5.61
6	4.51	4.81	4.07	4.35	4.24	-3.86	-3.97	-4.41	-4.37
5	5.65	4.01	4.72	6.17	5.24	4.65	-4.10	-4.11	-3.97
4	4.47	4.75	5.22	7.56	5.29	4.26	-3.62	-3.97	-4.40
3	4.66	6.46	6.77	7.63	5.29	4.21	-4.05	-3.94	-4.72
2	7.90	9.29	9.63	9.10	6.44	4.57	-3.86	-3.40	-3.83
1	8.66	7.47	9.85	10.27	8.04	6.66	-4.44	-4.11	-3.72

Root Mean Square, RMS

	1	2	3	4	5	6	7	8	9
9			0.44	0.41	0.38	0.34	0.37		
8		0.40	0.40	0.37	0.38	0.30	0.30	0.31	
7	0.42	0.39	0.48	0.38	0.36	0.36	0.32	0.34	0.32
6	0.38	0.46	0.51	0.47	0.38	0.38	0.29	0.31	0.32
5	0.41	0.44	0.50	0.45	0.44	0.35	0.31	0.38	0.40
4	0.35	0.41	0.40	0.38	0.41	0.37	0.35	0.37	0.45
3	0.45	0.39	0.40	0.33	0.41	0.42	0.46	0.29	0.35
2	0.47	0.22	0.30	0.28	0.43	0.37	0.36	0.35	0.36
1	0.40	0.45	0.32	0.26	0.36	0.35	0.44	0.37	0.38

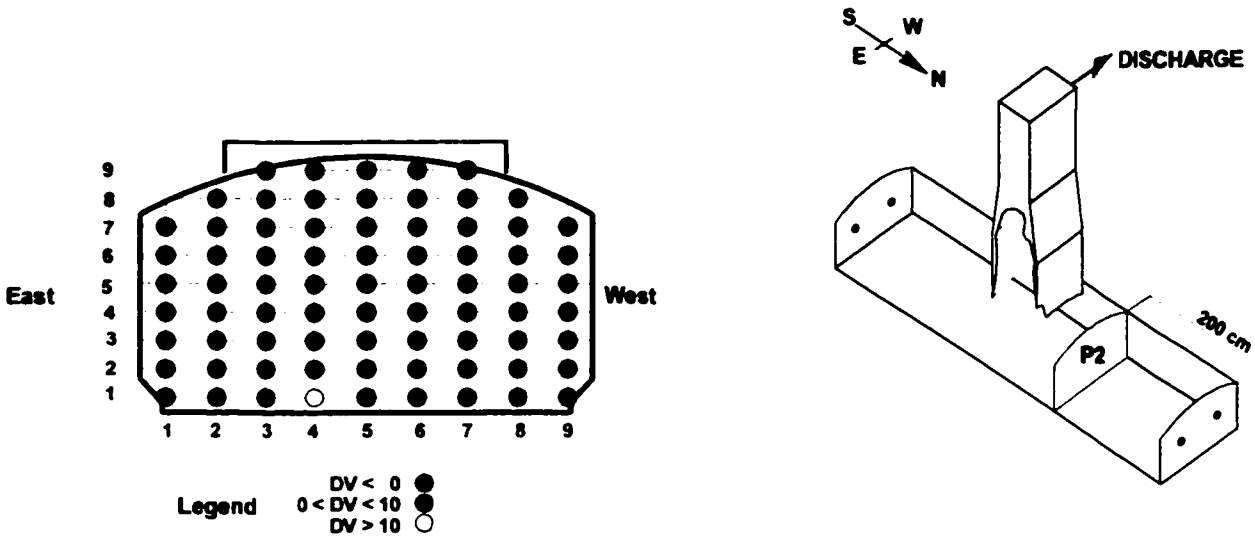

Figure B.1.12 Test V1B - Velocity Profile at Plane P2
(DV > 0 ≡ flow towards uptake)

Table B.1.11 Test V1B - Velocity Profile at Plane P3

Average Furnace Velocity				42.4 cm/s	(based on measured flows to the main burner jets)				
				39.2 cm/s	(based on velocity profile)				
Dimensionless Velocity, DV									
	1	2	3	4	5	6	7	8	9
9			-3.73	-4.01	-4.70	-4.79	-4.51		
8		-4.06	-4.04	-3.49	-3.94	-4.69	-5.99	-5.85	
7	3.94	3.66	3.55	3.82	-3.53	-4.54	-5.02	-5.15	-6.27
6	3.83	3.49	4.47	4.52	4.16	-4.18	-5.02	-4.79	-5.16
5	3.88	3.99	4.88	5.31	4.15	-3.34	-4.24	-4.42	-5.13
4	3.70	5.20	6.81	6.17	4.09	3.52	-3.68	-4.34	-5.19
3	5.25	6.22	6.87	6.81	5.44	3.78	3.47	-3.56	-3.96
2	6.48	7.35	9.13	8.79	6.15	4.78	3.85	-3.82	-4.67
1	5.88	6.27	8.68	9.29	7.56	6.03	4.81	-3.93	-4.10
Root Mean Square, RMS									
	1	2	3	4	5	6	7	8	9
9			0.46	0.46	0.28	0.38	0.28		
8		0.41	0.37	0.34	0.32	0.29	0.25	0.31	
7	0.43	0.40	0.41	0.39	0.33	0.33	0.29	0.32	0.19
6	0.41	0.46	0.53	0.47	0.42	0.29	0.30	0.31	0.35
5	0.40	0.47	0.50	0.44	0.47	0.34	0.33	0.33	0.39
4	0.39	0.37	0.39	0.47	0.45	0.40	0.32	0.38	0.44
3	0.51	0.40	0.34	0.42	0.44	0.41	0.35	0.33	0.39
2	0.34	0.41	0.25	0.27	0.32	0.45	0.34	0.31	0.37
1	0.56	0.44	0.36	0.27	0.33	0.41	0.47	0.41	0.41

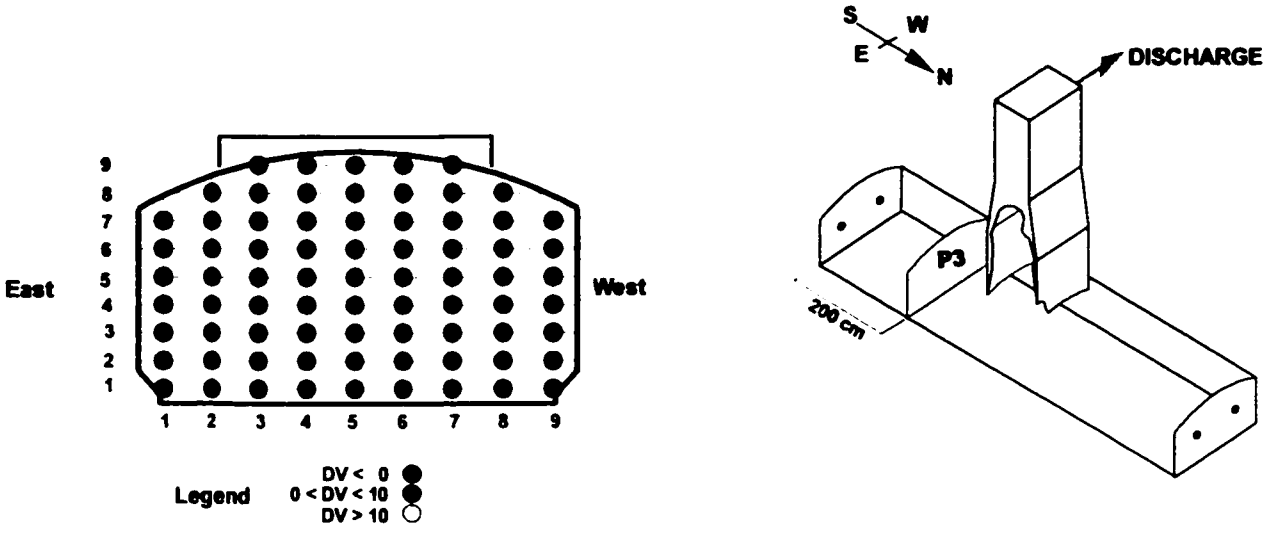

Figure B.1.13 Test V1B - Velocity Profile at Plane P3
(DV > 0 ≡ flow towards uptake)

Table B.1.12 Test V1B - Velocity Profile at Plane P5

Average Uptake Velocity 125.2 cm/s (based on measured flows to the main burner jets)
124.5 cm/s (based on velocity profile)

Dimensionless Velocity, DV

	1	2	3	4	5	6
10	1.50	1.30	1.47	1.50	1.34	1.44
9	1.57	1.45	1.75	1.46	1.54	1.58
8	1.35	1.29	1.38	1.50	1.33	1.38
7	1.50	1.29	1.21	1.19	1.31	1.42
6	1.62	1.32	1.10	1.04	1.45	1.50
5	1.20	1.16	0.89	1.05	1.17	1.21
4	1.19	1.05	0.78	0.89	0.88	1.10
3	1.00	0.74	0.97	0.86	0.97	0.94
2	-1.00	0.77	0.81	0.72	0.95	-1.01
1	-0.65	-0.83	0.82	0.79	-0.95	-0.87

Root Mean Square, RMS

	1	2	3	4	5	6
10	0.30	0.30	0.27	0.28	0.27	0.30
9	0.23	0.28	0.26	0.26	0.32	0.24
8	0.30	0.29	0.28	0.30	0.32	0.36
7	0.31	0.27	0.36	0.33	0.35	0.38
6	0.31	0.29	0.35	0.41	0.29	0.32
5	0.40	0.31	0.29	0.42	0.38	0.37
4	0.43	0.41	0.40	0.44	0.34	0.50
3	0.49	0.42	0.33	0.36	0.41	0.41
2	0.46	0.42	0.48	0.44	0.47	0.49
1	0.59	0.45	0.43	0.39	0.39	0.48

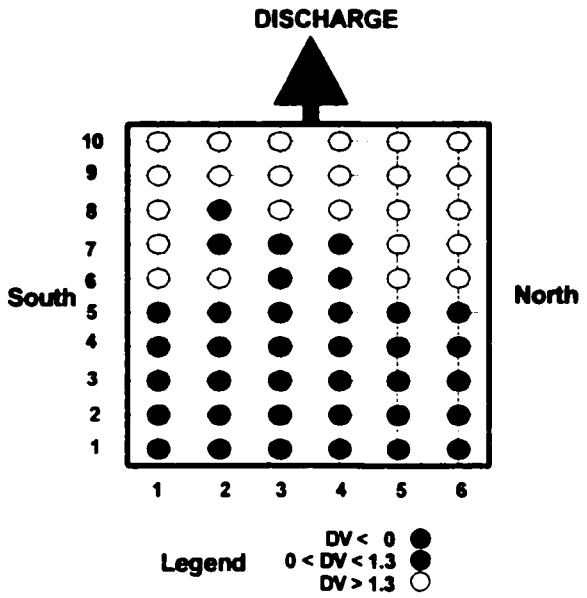

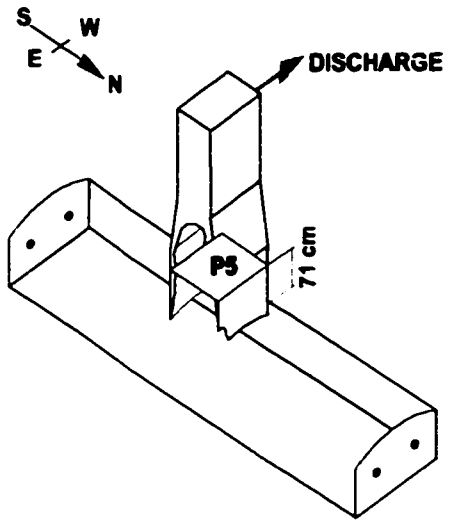

Figure B.1.14 Test V1B - Velocity Profile at Plane P5
(DV > 0 ≡ upward flow)

Table B.1.13 Test V1C - Velocity Profile at Plane P4

Average Uptake Velocity			125.6 cm/s	(based on measured flows to the main burner jets)		
			110.3 cm/s	(based on velocity profile)		

Dimensionless Velocity, DV

	1	2	3	4	5	6
6	1.29	1.33	1.43	1.51	1.34	1.32
5	1.34	1.13	1.33	1.19	1.42	1.22
4	1.28	1.30	1.31	1.26	1.52	1.10
3	-1.31	1.39	1.52	1.33	1.30	-1.38
2	-1.61	1.40	1.61	1.45	1.59	-1.37
1	-1.17	0.99	0.91	1.21	1.12	-1.00

Root Mean Square, RMS

	1	2	3	4	5	6
6	0.37	0.37	0.30	0.29	0.43	0.42
5	0.33	0.36	0.31	0.36	0.32	0.36
4	0.42	0.37	0.25	0.37	0.37	0.41
3	0.43	0.37	0.30	0.30	0.36	0.43
2	0.42	0.41	0.28	0.27	0.35	0.50
1	0.53	0.40	0.40	0.46	0.52	0.51

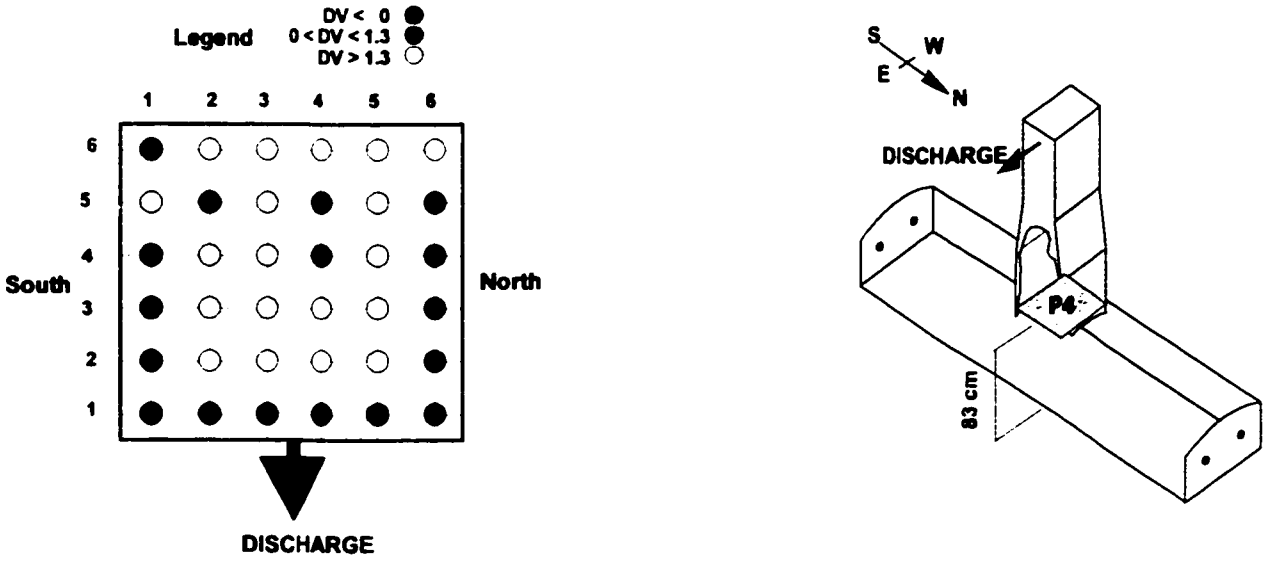

Figure B.1.15 Test V1C - Velocity Profile at Plane P4
(DV > 0 ≡ upward flow)

Table B.1.14 Test V1C - Velocity Profile at Plane P5

Average Uptake Velocity	125.6 cm/s	(based on measured flows to the main burner jets)
	116.0 cm/s	(based on velocity profile)

Dimensionless Velocity, DV

	1	2	3	4	5	6
6	-0.86	-0.87	0.75	0.75	-0.99	-0.98
5	1.08	0.73	0.77	0.66	0.75	1.03
4	1.18	1.00	0.90	0.84	0.98	1.24
3	1.42	1.15	1.13	1.08	1.23	1.34
2	1.42	1.36	1.27	1.41	1.30	1.49
1	1.45	1.37	1.30	1.58	1.48	1.50

Root Mean Square, RMS

	1	2	3	4	5	6
6	0.36	0.43	0.37	0.22	0.31	0.26
5	0.29	0.36	0.42	0.24	0.29	0.26
4	0.31	0.41	0.32	0.41	0.36	0.33
3	0.36	0.25	0.37	0.40	0.47	0.37
2	0.45	0.25	0.26	0.39	0.51	0.50
1	0.48	0.29	0.25	0.40	0.45	0.50

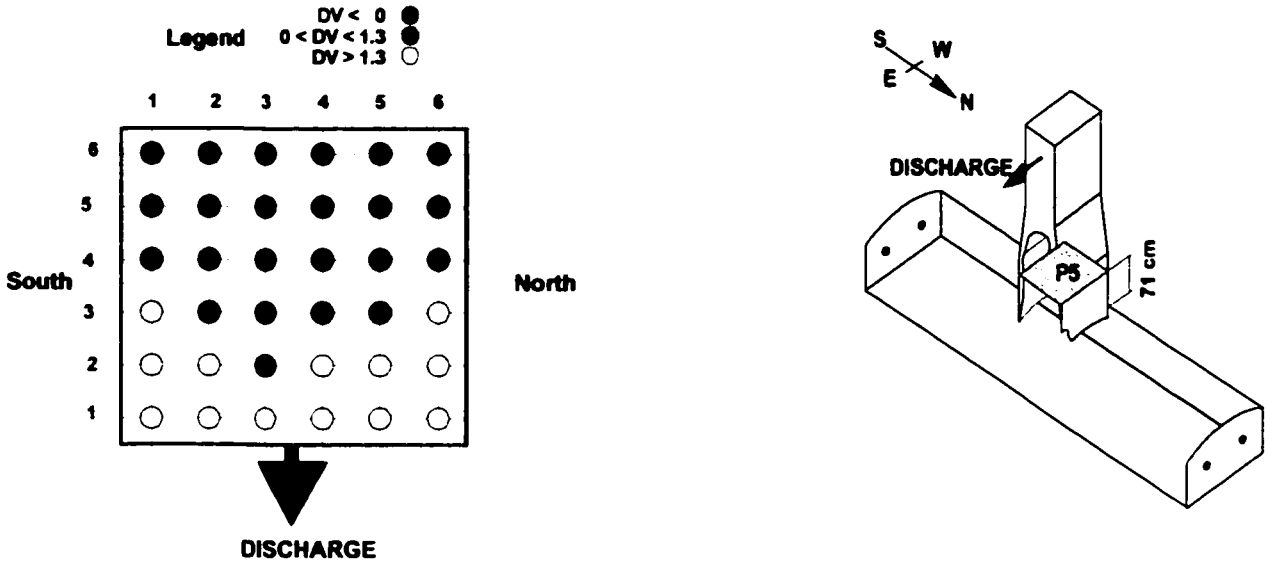

Figure B.1.16 Test V1C - Velocity Profile at Plane P5
(DV > 0 ≡ upward flow)

Table B.1.15 Test V1C - Velocity Profile at Plane P6

Average Uptake Velocity	181.3 cm/s	(based on measured flows to the main burner jets)
	179.8 cm/s	(based on velocity profile)

Dimensionless Velocity, DV

	1	2	3	4	5
6	1.04	1.11	1.08	1.16	1.06
5	1.10	1.02	0.95	0.95	1.10
4	1.05	0.92	0.96	0.98	0.90
3	0.96	0.98	0.92	0.91	0.96
2	0.96	1.01	0.92	0.93	1.05
1	0.85	1.04	1.00	0.97	0.94

Root Mean Square, RMS

	1	2	3	4	5
6	0.19	0.13	0.18	0.18	0.19
5	0.16	0.16	0.17	0.18	0.17
4	0.19	0.22	0.15	0.17	0.21
3	0.25	0.14	0.15	0.19	0.18
2	0.18	0.15	0.17	0.15	0.16
1	0.29	0.17	0.15	0.16	0.14

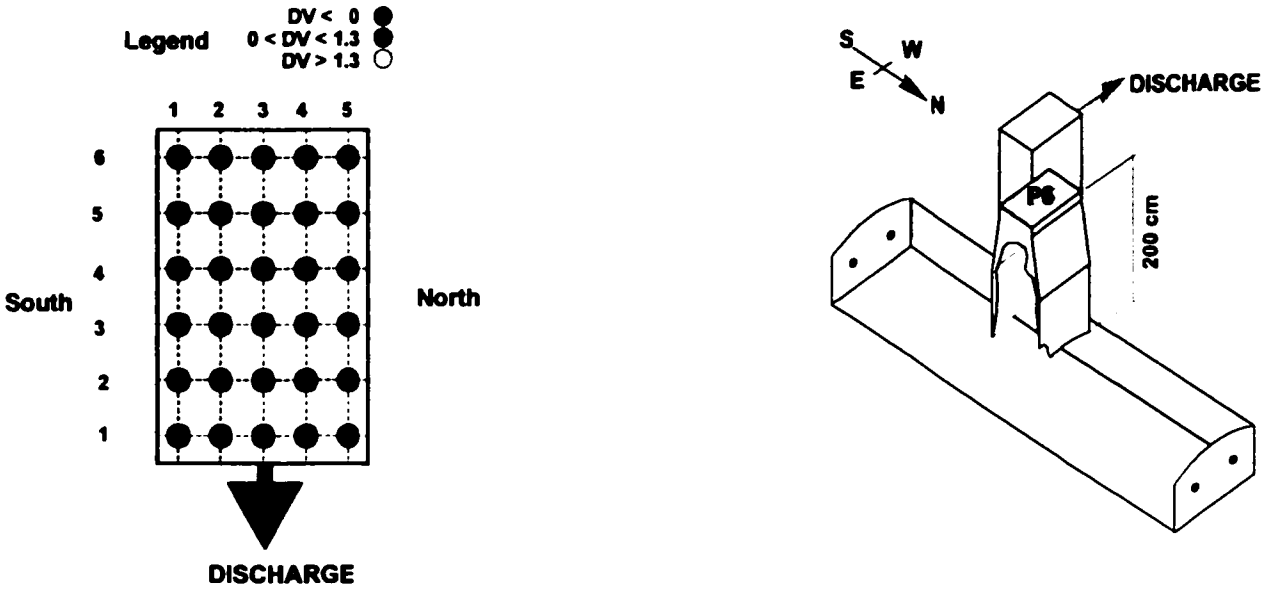

Figure B.1.17 Test V1C - Velocity Profile at Plane P6
(DV > 0 ≡ upward flow)

Table B.1.16 Test V2A - Velocity Profile at Plane P1

Average Furnace Velocity				27.7 cm/s	(based on measured flows to the main burner jets)				
				37.8 cm/s	(based on velocity profile)				
Dimensionless Velocity, DV									
	1	2	3	4	5	6	7	8	9
5		-6.31	-5.81	-6.14	-5.46	-5.70	-6.96	-2.92	
4	-3.74	4.11	4.75	6.17	7.76	6.03	-6.10	-8.69	-8.71
3	-3.36	3.83	11.26	14.27	13.74	10.51	-6.78	-8.40	-6.78
2	4.09	5.16	15.09	14.59	11.83	9.12	5.68	-6.92	-6.62
1	4.80	5.39	6.37	7.33	5.07	5.28	5.30	-5.50	-6.94
Root Mean Square, RMS									
	1	2	3	4	5	6	7	8	9
5		0.23	0.43	0.36	0.40	0.35	0.35	0.26	
4	0.37	0.42	0.39	0.52	0.51	0.41	0.40	0.17	0.19
3	0.37	0.38	0.40	0.32	0.29	0.45	0.31	0.21	0.29
2	0.43	0.30	0.30	0.22	0.31	0.44	0.35	0.27	0.29
1	0.55	0.42	0.39	0.30	0.52	0.44	0.47	0.40	0.26

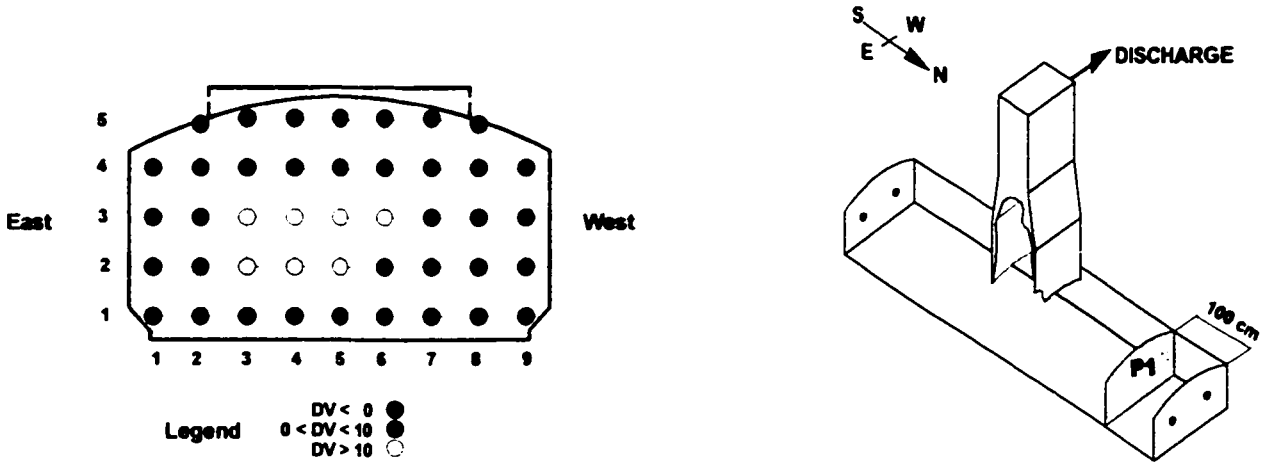

Figure B.1.18 Test V2A - Velocity Profile at Plane P1
(DV > 0 ≡ flow towards uptake)

Table B.1.17 Test V2A - Velocity Profile at Plane P2

Average Furnace Velocity				27.7 cm/s	(based on measured flows to the main burner jets)				
				32.9 cm/s	(based on velocity profile)				
Dimensionless Velocity, DV									
	1	2	3	4	5	6	7	8	9
5		-3.08	-5.99	-4.13	-5.14	-5.32	-6.40	-4.57	
4	-5.40	-5.38	4.46	5.46	4.16	-5.32	-5.08	-5.07	-7.21
3	5.08	3.83	4.66	7.01	4.46	3.56	-4.81	-4.04	-5.82
2	4.84	6.22	7.02	9.24	7.78	4.58	4.29	-4.21	-4.61
1	9.56	7.78	9.35	10.76	8.61	7.06	5.24	-4.08	-5.36
Root Mean Square, RMS									
	1	2	3	4	5	6	7	8	9
5		0.36	0.30	0.34	0.35	0.27	0.25	0.27	
4	0.40	0.48	0.47	0.45	0.34	0.27	0.31	0.35	0.23
3	0.45	0.38	0.52	0.43	0.46	0.34	0.36	0.41	0.37
2	0.47	0.44	0.46	0.36	0.40	0.46	0.41	0.33	0.49
1	0.36	0.44	0.36	0.22	0.31	0.41	0.40	0.45	0.39

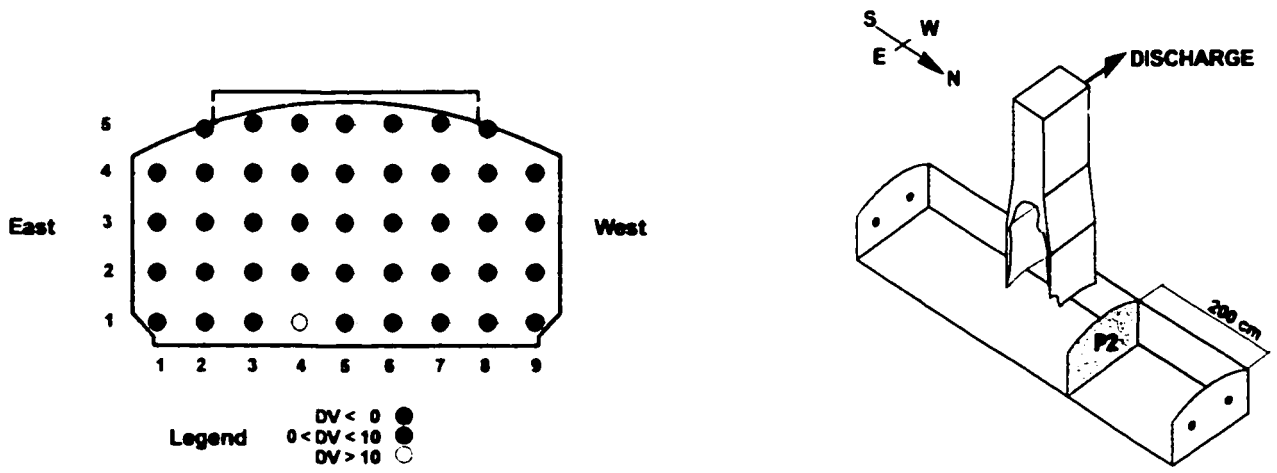

Figure B.1.19 Test V2A - Velocity Profile at Plane P2
(DV > 0 ≡ flow towards uptake)

Table B.1.18 Test V2A - Velocity Profile at Plane P3

Average Furnace Velocity				28.1 cm/s	(based on measured flows to the main burner jets)				
				28.2 cm/s	(based on velocity profile)				
Dimensionless Velocity, DV									
	1	2	3	4	5	6	7	8	9
5		-5.09	-4.68	-4.79	-4.64	-4.89	-6.11	-5.92	
4	3.91	3.78	4.52	4.71	-3.61	-4.47	-5.27	-6.37	-6.08
3	5.36	5.78	6.81	5.48	4.31	-4.64	-4.90	-5.54	-5.43
2	4.81	7.64	8.58	8.19	4.91	4.01	-3.92	-4.49	-5.10
1	6.25	10.08	11.17	9.13	8.43	6.85	4.76	-4.61	-4.98
Root Mean Square, RMS									
	1	2	3	4	5	6	7	8	9
5		0.34	0.41	0.32	0.38	0.36	0.32	0.25	
4	0.36	0.48	0.41	0.48	0.37	0.33	0.31	0.30	0.33
3	0.42	0.48	0.41	0.46	0.42	0.32	0.33	0.28	0.41
2	0.45	0.38	0.43	0.37	0.46	0.28	0.32	0.35	0.40
1	0.46	0.27	0.25	0.34	0.34	0.39	0.36	0.33	0.41

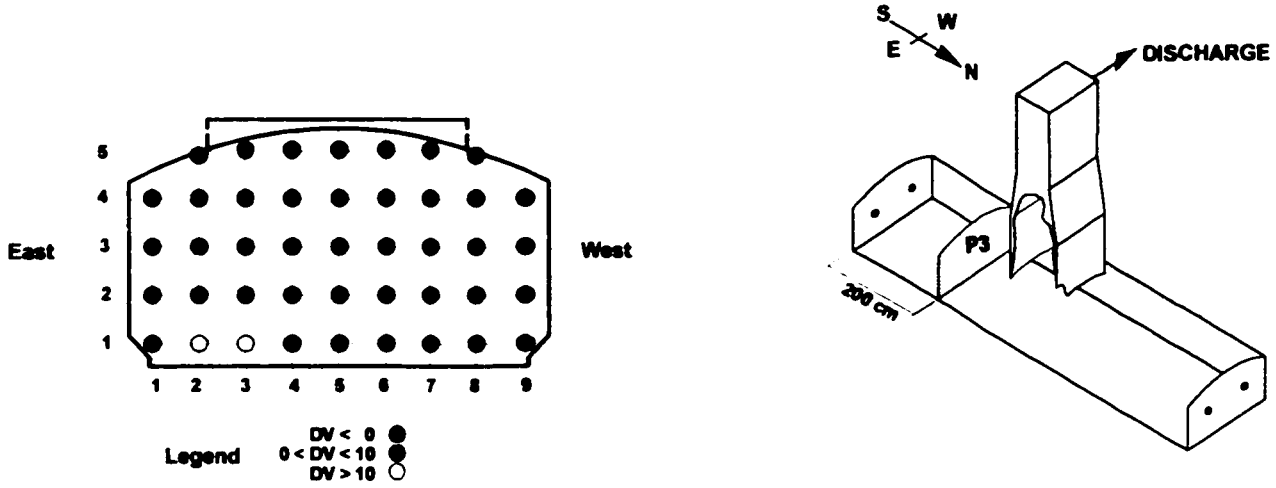

Figure B.1.20 Test V2A - Velocity Profile at Plane P3
(DV > 0 ≡ flow towards uptake)

Table B.1.19 Test V2A - Velocity Profile at Plane P4

Average Uptake Velocity	82.3 cm/s	(based on measured flows to the main burner jets)
	84.0 cm/s	(based on velocity profile)

Dimensionless Velocity, DV

	1	2	3	4	5	6
6	-1.21	1.53	1.56	1.31	1.85	-1.22
5	-1.06	1.47	1.67	1.44	1.23	-1.38
4	-1.27	1.49	1.37	1.59	1.50	-1.18
3	1.60	1.26	1.56	1.69	1.59	1.28
2	1.75	1.56	1.54	1.54	1.46	1.63
1	1.22	0.95	1.45	1.25	1.44	1.28

Root Mean Square, RMS

	1	2	3	4	5	6
6	0.41	0.36	0.40	0.41	0.33	0.40
5	0.37	0.30	0.32	0.42	0.38	0.53
4	0.38	0.36	0.31	0.28	0.42	0.48
3	0.42	0.43	0.30	0.33	0.33	0.48
2	0.46	0.41	0.44	0.32	0.34	0.44
1	0.53	0.55	0.41	0.41	0.50	0.56

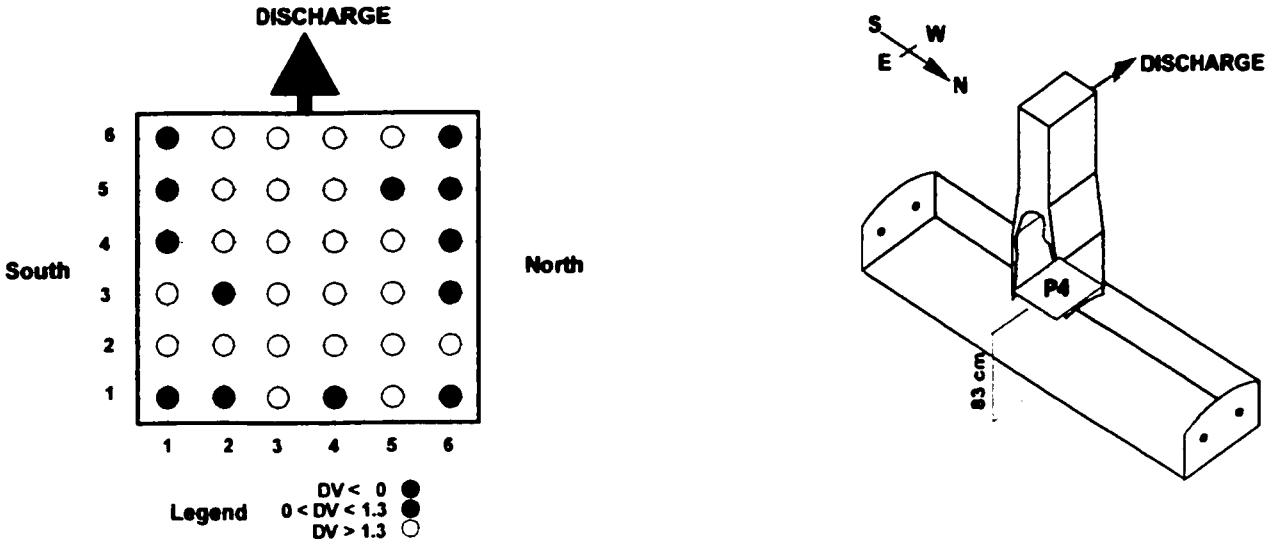

Figure B.1.21 Test V2A - Velocity Profile at Plane P4
(DV > 0 ≡ upward flow)

Table B.1.20 Test V2A - Velocity Profile at Plane P5

Average Uptake Velocity				82.3 cm/s	(based on measured flows to the main burner jets)	
				94.3 cm/s	(based on velocity profile)	
Dimensionless Velocity, DV						
	1	2	3	4	5	6
6	1.95	1.64	1.35	1.64	1.42	1.61
5	2.01	1.72	1.53	1.62	1.45	1.41
4	1.90	1.70	1.47	1.35	1.57	1.53
3	1.54	1.41	1.22	1.12	1.25	1.46
2	1.40	0.98	0.92	0.94	1.09	1.21
1	-1.31	-1.09	1.10	0.95	-0.77	-1.04
Root Mean Square, RMS						
	1	2	3	4	5	6
6	0.24	0.32	0.25	0.26	0.25	0.21
5	0.27	0.35	0.29	0.28	0.26	0.33
4	0.39	0.30	0.31	0.33	0.35	0.36
3	0.49	0.40	0.40	0.40	0.39	0.37
2	0.45	0.42	0.49	0.40	0.45	0.43
1	0.50	0.46	0.42	0.39	0.34	0.46

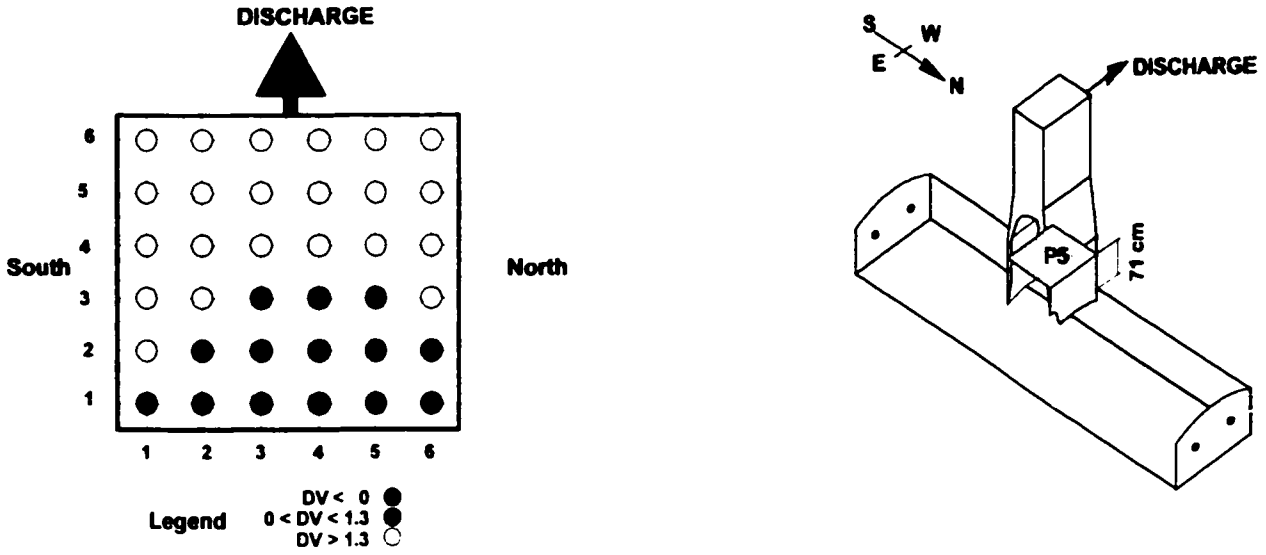

Figure B.1.22 Test V2A - Velocity Profile at Plane P5
(DV > 0 ≡ upward flow)

Table B.1.21 Test V2A - Velocity Profile at Plane P6

Average Uptake Velocity	119.1 cm/s	(based on measured flows to the main burner jets)
	145.9 cm/s	(based on velocity profile)

Dimensionless Velocity, DV

	1	2	3	4	5
6	1.49	1.31	1.35	1.25	1.37
5	1.50	1.42	1.36	1.28	1.34
4	1.41	1.27	1.25	1.18	1.19
3	1.22	1.21	1.11	1.13	1.11
2	1.20	1.11	1.12	1.15	1.07
1	0.97	1.10	1.08	1.16	1.05

Root Mean Square, RMS

	1	2	3	4	5
6	0.14	0.15	0.16	0.16	0.15
5	0.17	0.13	0.16	0.13	0.13
4	0.19	0.15	0.12	0.20	0.18
3	0.17	0.12	0.15	0.18	0.17
2	0.21	0.14	0.17	0.12	0.17
1	0.25	0.14	0.20	0.16	0.20

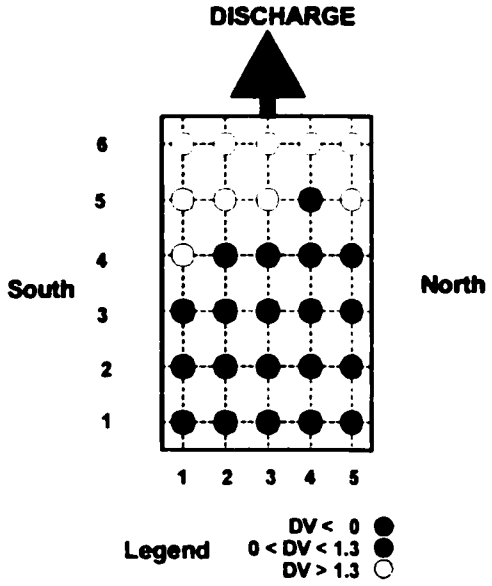

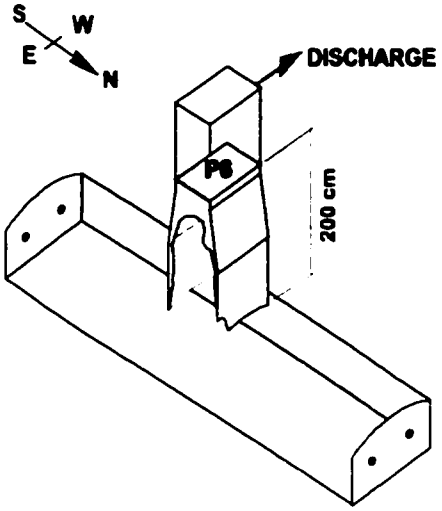

Figure B.1.23 Test V2A - Velocity Profile at Plane P6
(DV > 0 ≡ upward flow)

Table B.1.22 Test V2B - Velocity Profile at Plane P2

Average Furnace Velocity				27.4 cm/s	(based on measured flows to the main burner jets)				
				32.3 cm/s	(based on velocity profile)				
Dimensionless Velocity, DV									
	1	2	3	4	5	6	7	8	9
5		-5.05	-4.77	-4.69	-4.55	-4.49	-5.83	-5.18	
4	-4.97	-4.87	4.41	4.17	3.89	-4.81	-4.71	-4.64	-5.18
3	4.81	4.70	4.86	5.60	4.56	5.00	-3.93	-4.97	-4.93
2	5.02	6.46	7.52	8.03	5.60	5.40	3.76	-3.82	-4.18
1	6.84	8.35	9.09	9.71	7.41	6.16	4.29	-3.69	-3.95
Root Mean Square, RMS									
	1	2	3	4	5	6	7	8	9
5		0.44	0.41	0.34	0.40	0.30	0.29	0.32	
4	0.42	0.45	0.40	0.43	0.37	0.38	0.30	0.36	0.34
3	0.47	0.47	0.50	0.54	0.48	0.41	0.40	0.33	0.38
2	0.43	0.45	0.39	0.38	0.47	0.55	0.38	0.35	0.40
1	0.51	0.40	0.39	0.32	0.35	0.38	0.42	0.34	0.43

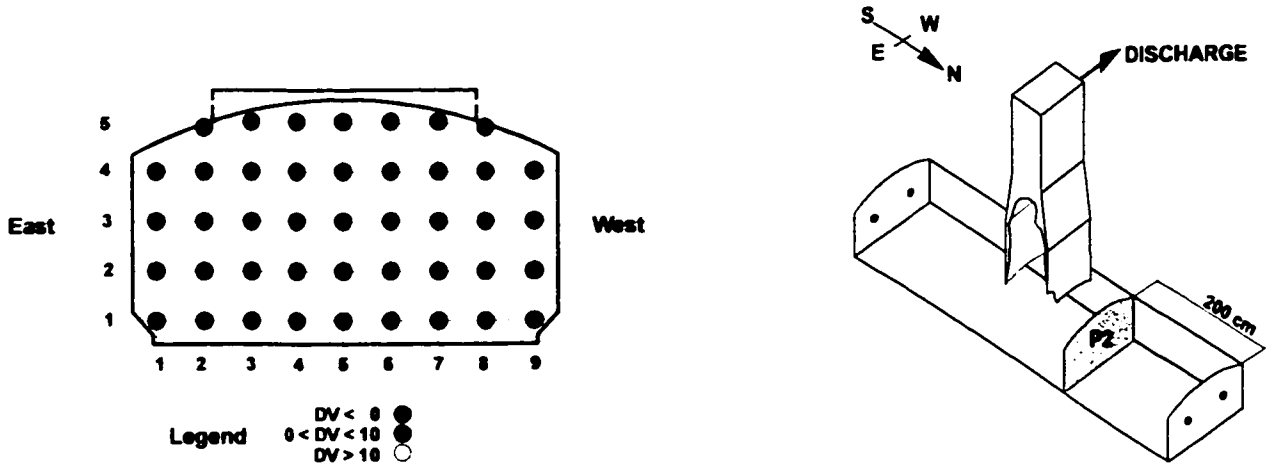

Figure B.1.24 Test V2B - Velocity Profile at Plane P2
(DV > 0 ≡ flow towards uptake)

Table B.1.23 Test V2B - Velocity Profile at Plane P3

Average Furnace Velocity				27.2 cm/s	(based on measured flows to the main burner jets)				
				27.8 cm/s	(based on velocity profile)				
Dimensionless Velocity, DV									
	1	2	3	4	5	6	7	8	9
5		-4.15	-3.38	-3.84	-4.18	-4.72	-5.40	-5.78	
4	-3.93	3.97	2.77	3.87	-3.30	-4.06	-5.03	-5.22	-6.10
3	4.65	4.57	4.29	4.73	4.20	3.90	-4.01	-4.65	-4.85
2	4.39	5.62	7.61	7.35	5.30	3.85	3.58	-4.00	-4.22
1	5.12	8.39	9.12	9.59	7.74	5.89	4.15	-3.80	-4.19
Root Mean Square, RMS									
	1	2	3	4	5	6	7	8	9
5		0.40	0.38	0.39	0.34	0.30	0.30	0.22	
4	0.44	0.46	0.44	0.39	0.40	0.33	0.26	0.30	0.27
3	0.43	0.43	0.50	0.52	0.43	0.45	0.35	0.34	0.40
2	0.52	0.45	0.40	0.43	0.43	0.44	0.41	0.35	0.41
1	0.52	0.36	0.35	0.30	0.35	0.40	0.43	0.39	0.50

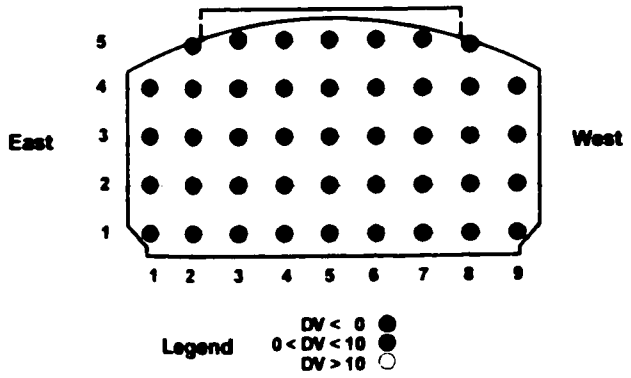

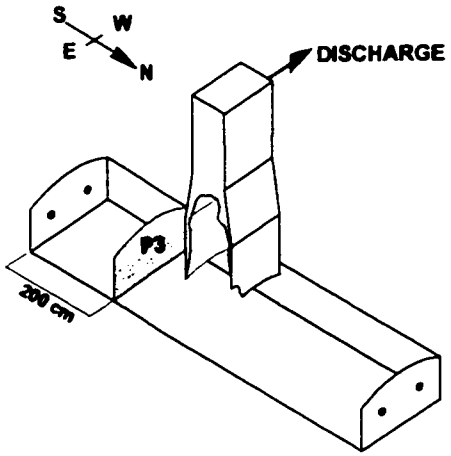

Figure B.1.25 Test V2B - Velocity Profile at Plane P3
(DV > 0 ≡ flow towards uptake)

Table B.1.24 Test V2B - Velocity Profile at Plane P5

Average Uptake Velocity	80.6 cm/s	(based on measured flows to the main burner jets)
	77.6 cm/s	(based on velocity profile)

Dimensionless Velocity, DV

	1	2	3	4	5	6
6	1.50	1.58	1.28	1.35	1.47	1.67
5	1.62	1.38	1.18	1.40	1.38	1.53
4	1.46	1.22	1.04	1.10	1.31	1.39
3	1.39	1.07	0.88	1.00	1.04	1.55
2	1.12	0.84	0.61	0.76	0.91	0.98
1	-1.06	-0.82	0.60	0.68	-0.76	-0.95

Root Mean Square, RMS

	1	2	3	4	5	6
6	0.32	0.28	0.37	0.31	0.27	0.36
5	0.34	0.32	0.29	0.33	0.34	0.29
4	0.37	0.37	0.36	0.39	0.36	0.37
3	0.39	0.40	0.43	0.46	0.39	0.44
2	0.44	0.44	0.50	0.45	0.46	0.49
1	0.49	0.44	0.50	0.48	0.44	0.49

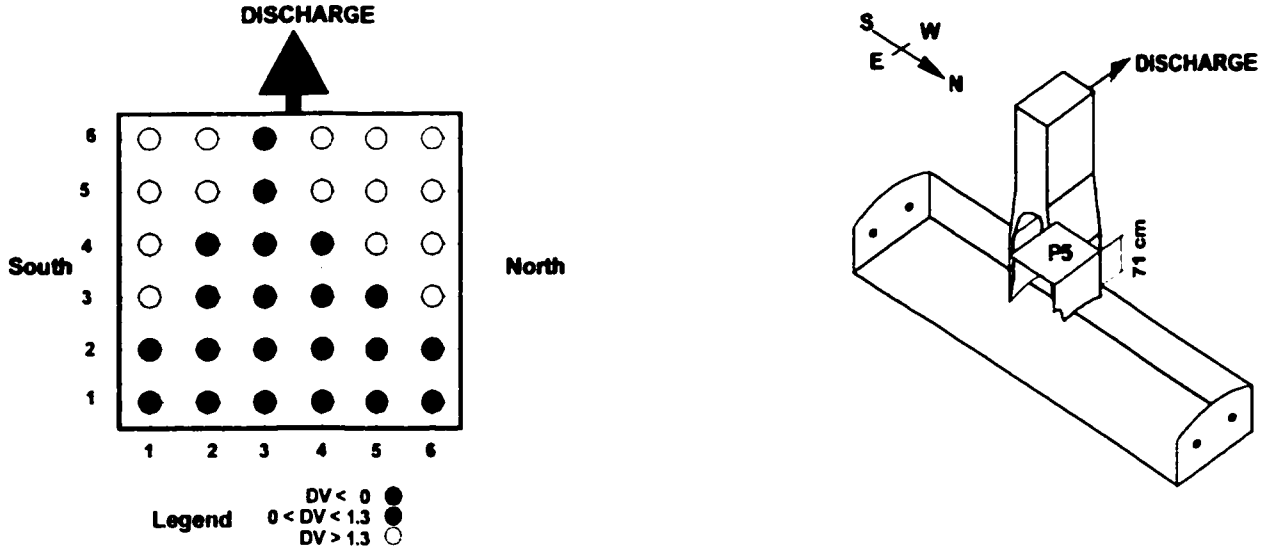

Figure B.1.26 Test V2B - Velocity Profile at Plane P5
(DV > 0 ≡ upward flow)

Table B.1.25 Test V2C - Velocity Profile at Plane P3

Average Furnace Velocity				27.4 cm/s	(based on measured flows to the main burner jets)				
				28.5 cm/s	(based on velocity profile)				
Dimensionless Velocity, DV									
	1	2	3	4	5	6	7	8	9
5		-3.61	-5.45	-5.53	-5.49	-5.82	-6.91	-4.49	
4	5.03	4.30	4.54	4.32	-4.62	-4.38	-4.90	-6.50	-6.58
3	5.27	5.80	6.53	9.21	4.78	-4.16	-4.51	-6.21	-5.91
2	5.56	6.86	8.77	9.21	5.47	3.75	-4.25	-4.16	-6.72
1	7.04	10.40	10.07	9.70	9.10	5.98	5.04	-4.73	-5.37
Root Mean Square, RMS									
	1	2	3	4	5	6	7	8	9
5		0.44	0.39	0.41	0.38	0.30	0.25	0.19	
4	0.38	0.38	0.43	0.36	0.40	0.30	0.37	0.31	0.32
3	0.39	0.42	0.49	0.36	0.50	0.37	0.35	0.29	0.38
2	0.46	0.41	0.40	0.36	0.53	0.34	0.41	0.42	0.44
1	0.65	0.33	0.30	0.32	0.34	0.40	0.44	0.33	0.45

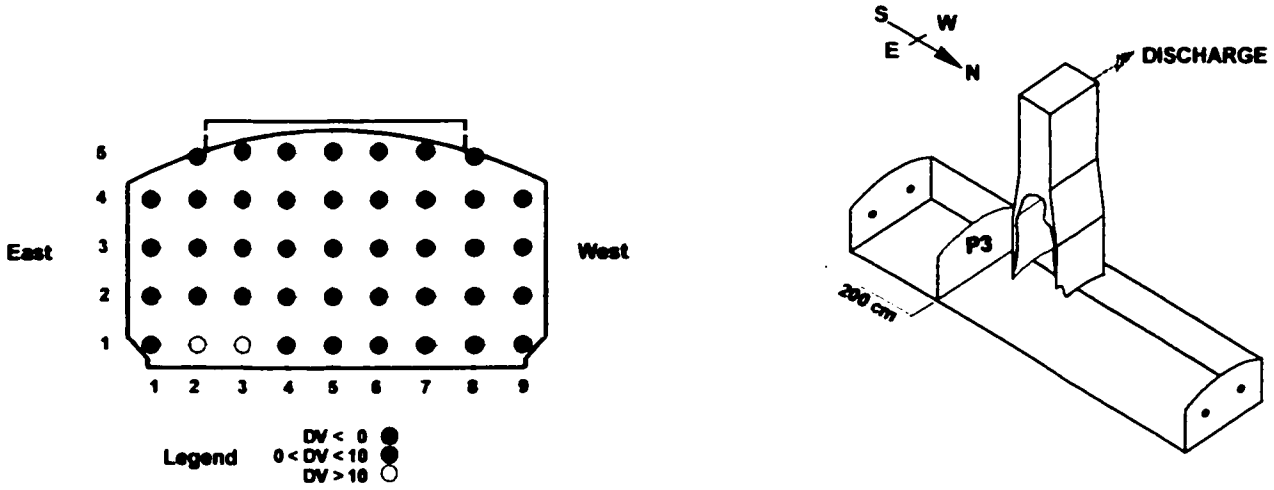

Figure B.1.27 Test V2C - Velocity Profile at Plane P3
(DV > 0 ≡ flow towards uptake)

Table B.1.26 Test V2C - Velocity Profile at Plane P4

Average Uptake Velocity			80.4 cm/s	(based on measured flows to the main burner jets)		
			90.1 cm/s	(based on velocity profile)		

Dimensionless Velocity, DV

	1	2	3	4	5	6
6	-1.28	1.59	1.77	1.49	1.68	-1.66
5	-1.67	1.57	1.71	1.65	1.59	-1.43
4	-1.43	1.70	1.70	1.62	1.39	-1.52
3	1.46	1.54	1.70	1.93	1.79	1.60
2	1.69	1.54	1.88	1.83	1.93	1.52
1	1.74	1.46	1.66	1.44	1.81	1.35

Root Mean Square, RMS

	1	2	3	4	5	6
6	0.33	0.39	0.31	0.34	0.36	0.40
5	0.43	0.38	0.29	0.30	0.36	0.36
4	0.42	0.33	0.28	0.34	0.40	0.43
3	0.40	0.36	0.28	0.30	0.33	0.35
2	0.43	0.36	0.30	0.33	0.38	0.46
1	0.47	0.47	0.47	0.44	0.42	0.45

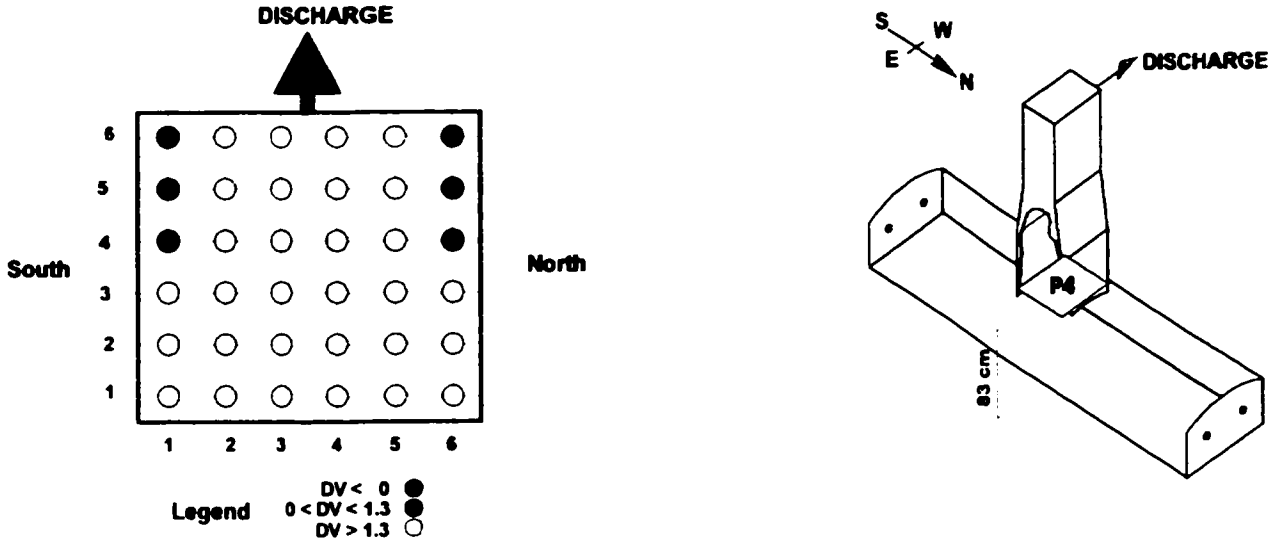

Figure B.1.28 Test V2C - Velocity Profile at Plane P4
(DV > 0 ≡ upward flow)

Table B.1.27 Test V2C - Velocity Profile at Plane P5

Average Uptake Velocity	94.7 cm/s	(based on measured flows to the main burner + afterburner + SO_2 jets)
	158.9 cm/s	(based on velocity profile)

Dimensionless Velocity, DV

	1	2	3	4	5	6
6	1.82	1.93	2.17	1.82	2.14	2.09
5	1.78	1.84	1.77	1.69	1.92	2.28
4	1.71	1.57	1.59	1.32	1.52	2.02
3	1.48	1.43	1.14	1.71	1.44	1.37
2	1.87	1.37	1.23	1.48	1.47	1.24
1	2.04	1.91	1.79	1.82	1.54	1.07

Root Mean Square, RMS

	1	2	3	4	5	6
6	0.27	0.28	0.28	0.27	0.19	0.26
5	0.32	0.36	0.35	0.33	0.34	0.25
4	0.32	0.34	0.40	0.30	0.30	0.31
3	0.41	0.30	0.32	0.31	0.32	0.44
2	0.31	0.34	0.35	0.40	0.35	0.36
1	0.29	0.30	0.25	0.26	0.31	0.37

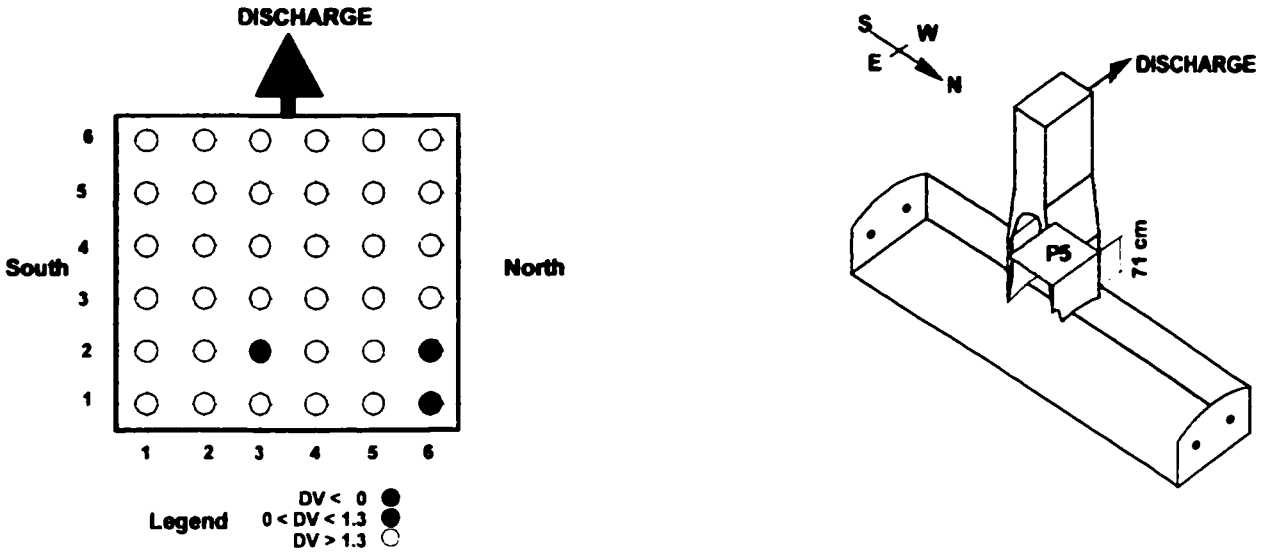

Figure B.1.29 Test V2C - Velocity Profile at Plane P5
(DV > 0 ≡ upward flow)

Table B.1.28 Test V2C - Velocity Profile at Plane P6

Average Uptake Velocity	137.1 cm/s	(based on measured flows to the main burner + afterburner + SO_2 jets)
	170.5 cm/s	(based on velocity profile)

Dimensionless Velocity, DV

	1	2	3	4	5
6	1.55	1.38	1.41	1.37	1.67
5	1.38	1.17	1.18	1.14	1.25
4	1.14	0.93	0.88	0.91	1.14
3	1.14	1.07	1.00	1.03	1.34
2	1.40	1.22	1.13	1.14	1.14
1	1.73	1.47	1.18	1.36	1.48

Root Mean Square, RMS

	1	2	3	4	5
6	0.14	0.16	0.16	0.18	0.12
5	0.15	0.18	0.18	0.20	0.17
4	0.13	0.18	0.24	0.18	0.19
3	0.15	0.22	0.16	0.14	0.16
2	0.21	0.16	0.18	0.22	0.15
1	0.13	0.16	0.18	0.17	0.16

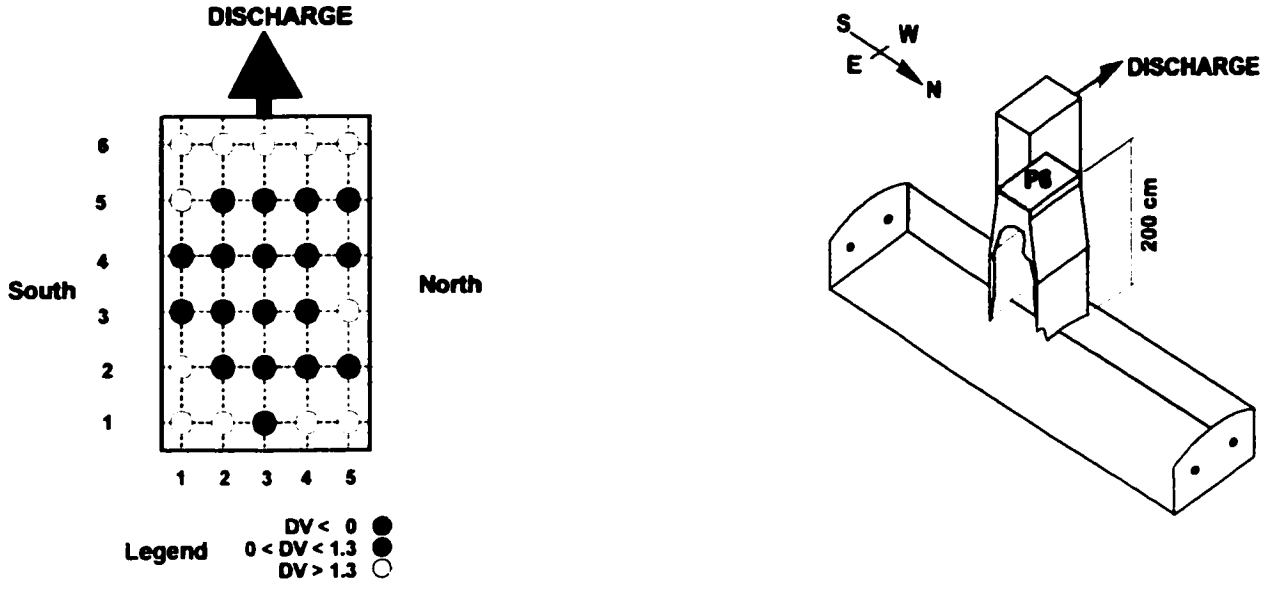

Figure B.1.30 Test V2C - Velocity Profile at Plane P6
(DV > 0 ≡ upward flow)

Table B.1.29 Test V2D - Velocity Profile at Plane P3

Average Furnace Velocity				27.5 cm/s	(based on measured flows to the main burner jets)				
				32.9 cm/s	(based on velocity profile)				
Dimensionless Velocity, DV									
	1	2	3	4	5	6	7	8	9
5		-3.22	-4.89	-4.92	-5.09	-6.41	-6.88	-6.15	
4	4.75	5.00	4.26	5.73	-5.18	-4.07	-6.13	-6.19	-6.02
3	5.29	6.32	8.08	6.48	5.18	-4.21	-5.40	-6.02	-6.38
2	5.45	8.22	8.91	7.14	6.51	5.13	-4.21	-5.28	-5.76
1	6.02	11.47	12.16	11.32	8.33	7.09	5.61	-4.52	-5.26
Root Mean Square, RMS									
	1	2	3	4	5	6	7	8	9
5		0.38	0.42	0.37	0.37	0.30	0.26	0.29	
4	0.44	0.37	0.37	0.40	0.50	0.35	0.27	0.24	0.44
3	0.39	0.42	0.44	0.52	0.50	0.30	0.30	0.32	0.36
2	0.49	0.36	0.36	0.40	0.47	0.51	0.37	0.38	0.36
1	0.50	0.39	0.25	0.25	0.36	0.40	0.35	0.29	0.33

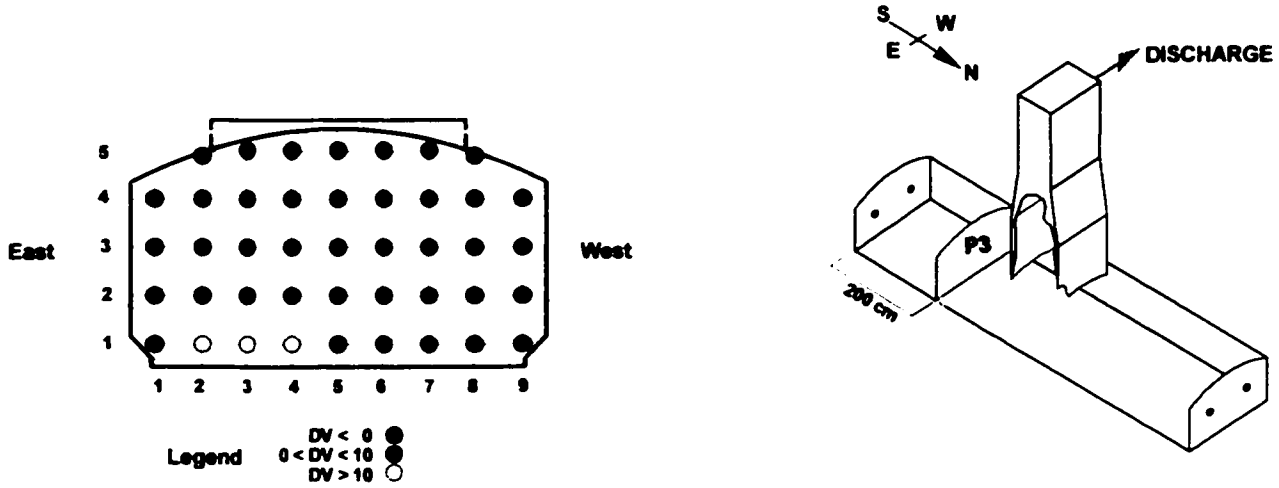

Figure B.1.31 Test V2D - Velocity Profile at Plane P3
(DV > 0 ≡ flow towards uptake)

Table B.1.30 Test V2D - Velocity Profile at Plane P4

Average Uptake Velocity	80.5 cm/s	(based on measured flows to the main burner jets)
	80.4 cm/s	(based on velocity profile)

Dimensionless Velocity, DV

	1	2	3	4	5	6
6	-1.24	1.34	1.44	1.38	1.37	-1.59
5	-1.34	1.43	1.44	1.53	1.30	-1.42
4	-1.48	1.55	1.44	1.55	1.76	-1.41
3	1.57	1.54	1.71	1.79	1.41	1.33
2	1.55	1.60	1.49	1.77	1.74	1.68
1	1.68	1.13	1.04	1.31	1.43	1.13

Root Mean Square, RMS

	1	2	3	4	5	6
6	0.50	0.35	0.36	0.32	0.35	0.37
5	0.37	0.37	0.37	0.32	0.38	0.48
4	0.45	0.41	0.40	0.33	0.38	0.39
3	0.42	0.38	0.33	0.37	0.36	0.41
2	0.38	0.37	0.32	0.31	0.32	0.42
1	0.48	0.47	0.51	0.47	0.55	0.56

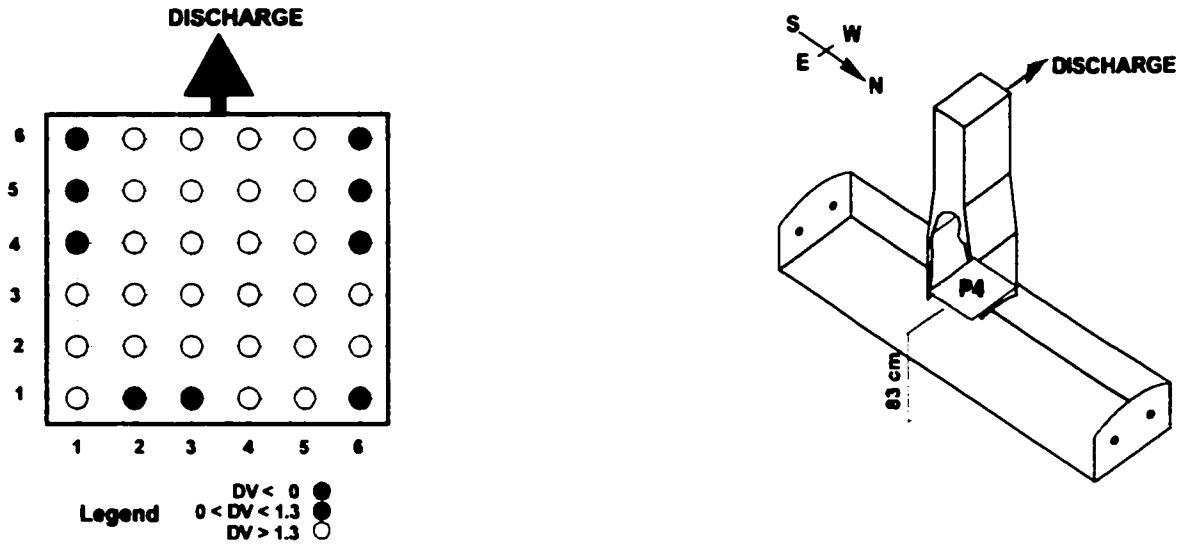

Figure B.1.32 Test V2D - Velocity Profile at Plane P4
(DV > 0 ≡ upward flow)

Table B.1.31 Test V2D - Velocity Profile at Plane P5

Average Uptake Velocity	90.6 cm/s	(based on measured flows to the main burner + afterburner jets)
	131.7 cm/s	(based on velocity profile)

Dimensionless Velocity, DV

	1	2	3	4	5	6
6	1.91	1.59	2.15	1.78	1.67	1.70
5	1.49	1.64	2.22	2.04	1.62	1.50
4	1.20	1.22	1.92	1.61	1.06	1.10
3	1.16	1.22	1.93	1.94	1.18	1.00
2	1.06	1.15	1.72	1.57	1.03	0.96
1	1.08	1.07	1.08	1.37	1.25	1.20

Root Mean Square, RMS

	1	2	3	4	5	6
6	0.27	0.20	0.22	0.22	0.22	0.18
5	0.26	0.27	0.27	0.28	0.28	0.21
4	0.31	0.40	0.33	0.36	0.30	0.36
3	0.42	0.43	0.32	0.28	0.45	0.48
2	0.48	0.44	0.37	0.36	0.33	0.46
1	0.57	0.39	0.34	0.41	0.33	0.49

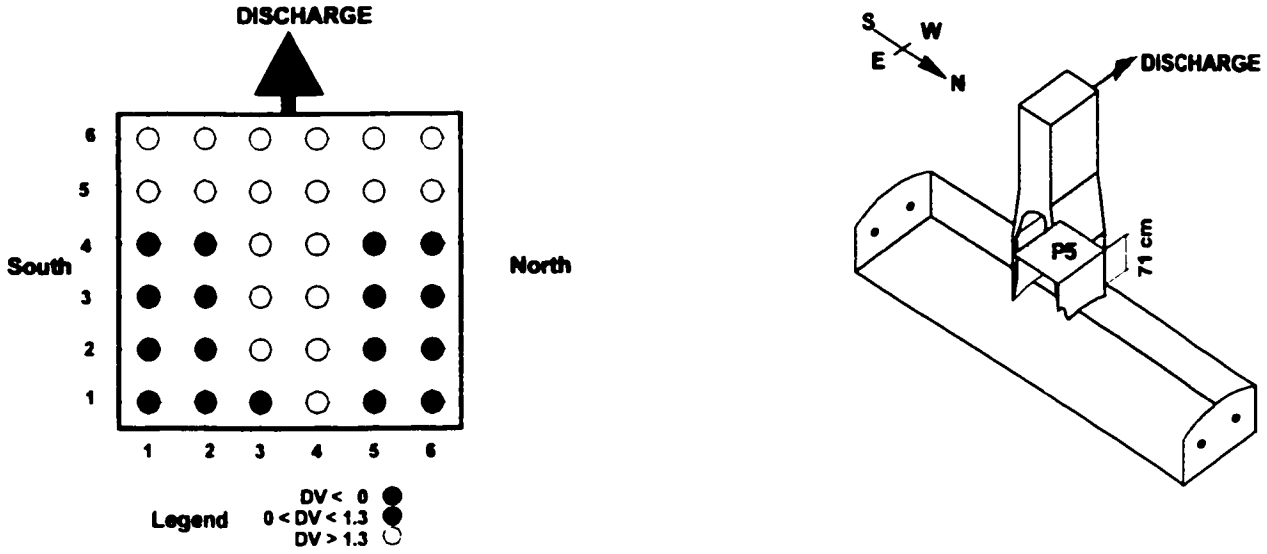

Figure B.1.33 Test V2D - Velocity Profile at Plane P5
(DV > 0 ≡ upward flow)

Table B.1.32 Test V2D - Velocity Profile at Plane P6

Average Uptake Velocity	131.1 cm/s	(based on measured flows to the main burner + afterburner jets)
	166.5 cm/s	(based on velocity profile)

Dimensionless Velocity, DV

	1	2	3	4	5
6	1.38	1.42	1.41	1.40	1.44
5	1.36	1.41	1.31	1.38	1.39
4	1.27	1.27	1.23	1.27	1.37
3	1.22	1.18	1.12	1.21	1.23
2	1.21	1.14	1.14	1.18	1.25
1	1.09	1.25	1.16	1.16	1.21

Root Mean Square, RMS

	1	2	3	4	5
6	0.12	0.09	0.11	0.13	0.11
5	0.13	0.10	0.12	0.12	0.10
4	0.14	0.12	0.13	0.11	0.09
3	0.14	0.12	0.16	0.11	0.16
2	0.13	0.13	0.12	0.12	0.13
1	0.15	0.13	0.11	0.11	0.17

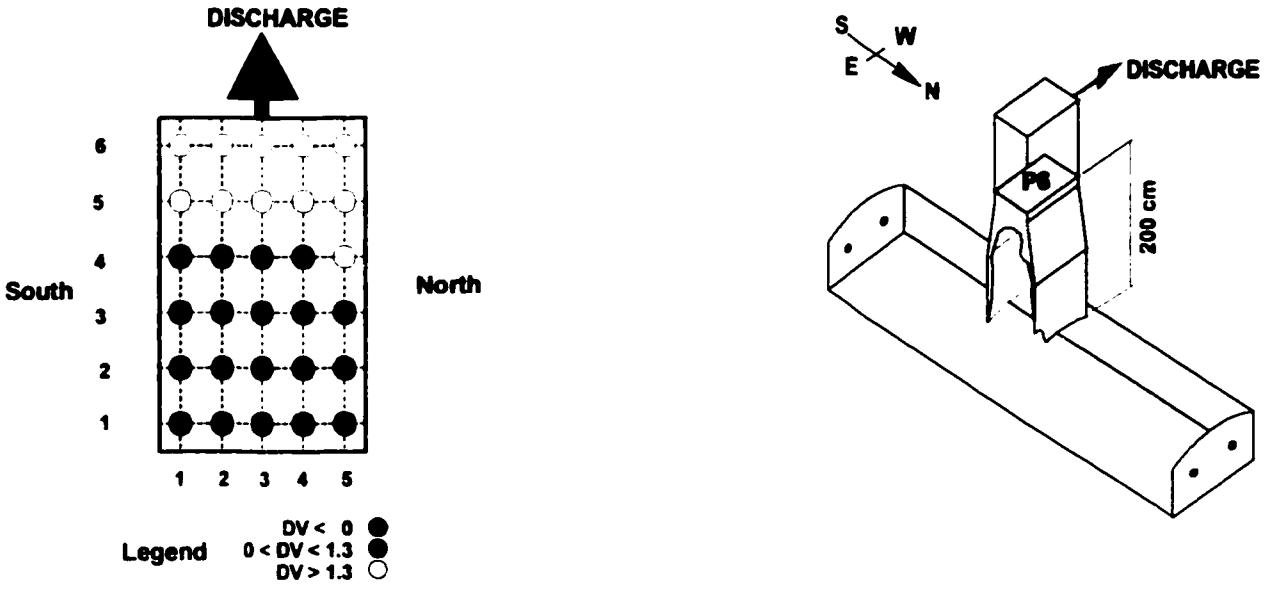

Figure B.1.34 Test V2D - Velocity Profile at Plane P6
(DV > 0 ≡ upward flow)

Table B.1.33 Test V3A - Velocity Profile at Plane P2

Average Furnace Velocity				27.4 cm/s	(based on measured flows to the main burner jets)				
				28.7 cm/s	(based on velocity profile)				
Dimensionless Velocity, DV									
	1	2	3	4	5	6	7	8	9
5		-12.78	-11.39	-11.41	-10.38	-10.02	-11.46	-11.46	
4	-9.37	-9.15	-9.37	8.81	10.22	-8.74	-9.87	-8.56	-10.28
3	-10.32	-8.73	9.61	11.74	14.73	12.48	9.00	-8.21	-8.66
2	-9.21	8.05	9.64	16.02	17.96	13.15	10.03	-8.47	-8.41
1	-9.04	11.06	13.36	18.96	17.94	15.80	10.53	8.90	-8.08
Root Mean Square, RMS									
	1	2	3	4	5	6	7	8	9
5		0.32	0.33	0.28	0.26	0.33	0.25	0.27	
4	0.46	0.34	0.33	0.30	0.43	0.37	0.25	0.37	0.34
3	0.42	0.29	0.39	0.52	0.37	0.49	0.39	0.33	0.44
2	0.38	0.36	0.43	0.41	0.36	0.46	0.43	0.39	0.37
1	0.41	0.36	0.47	0.33	0.38	0.38	0.47	0.36	0.35

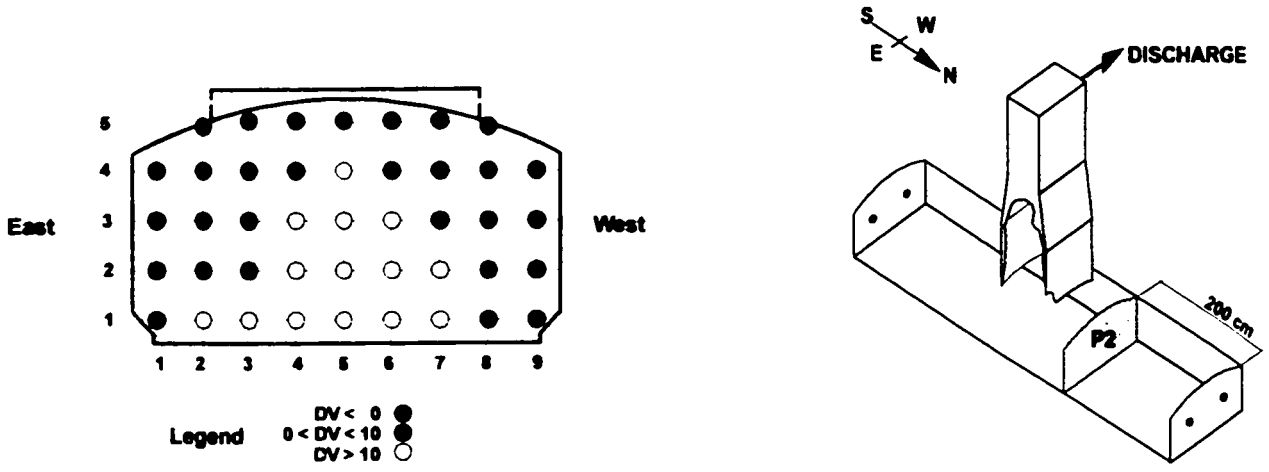

Figure B.1.35 Test V3A - Velocity Profile at Plane P2
(DV > 0 ≡ flow towards uptake)

Table B.1.34 Test V3A - Velocity Profile at Plane P3

Average Furnace Velocity 26.7 cm/s (based on measured flows to the main burner jets)
22.5 cm/s (based on velocity profile)

Dimensionless Velocity, DV

	1	2	3	4	5	6	7	8	9
5		-9.87	-10.71	-10.11	-9.54	-10.66	-11.48	-11.77	
4	-8.22	-8.54	-9.40	10.32	9.25	-8.88	-9.47	-9.91	-11.94
3	-7.21	-8.83	11.17	14.00	11.96	9.37	-9.04	-9.00	-10.00
2	-8.59	8.94	11.37	14.88	15.43	12.52	8.50	-8.29	-7.26
1	6.60	9.73	14.60	16.57	16.68	14.13	11.42	8.93	-7.12

Root Mean Square, RMS

	1	2	3	4	5	6	7	8	9
5		0.33	0.37	0.30	0.32	0.25	0.26	0.24	
4	0.47	0.34	0.34	0.41	0.37	0.28	0.30	0.34	0.25
3	0.41	0.37	0.43	0.42	0.42	0.36	0.34	0.34	0.34
2	0.47	0.45	0.41	0.39	0.33	0.41	0.46	0.32	0.31
1	0.43	0.43	0.37	0.40	0.36	0.38	0.41	0.38	0.33

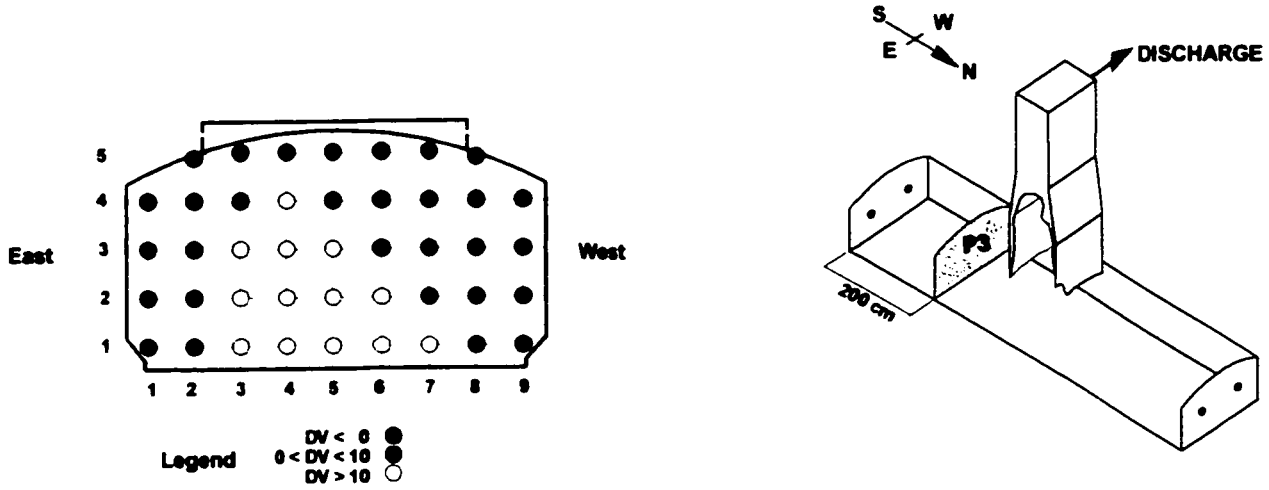

Figure B.1.36 Test V3A - Velocity Profile at Plane P3
(DV > 0 ≡ flow towards uptake)

Table B.1.35 Test V3A - Velocity Profile at Plane P5

Average Uptake Velocity	79.7 cm/s	(based on measured flows to the main burner jets)
	75.8 cm/s	(based on velocity profile)

Dimensionless Velocity, DV

	1	2	3	4	5	6
6	1.60	1.50	1.21	1.46	1.54	1.57
5	1.51	1.18	1.20	1.36	1.18	1.53
4	1.49	1.02	0.91	0.96	1.16	1.48
3	1.36	1.06	0.84	1.02	0.96	1.73
2	1.21	0.94	0.96	0.87	0.95	1.45
1	-1.20	-1.14	1.05	1.08	-1.19	-1.52

Root Mean Square, RMS

	1	2	3	4	5	6
6	0.43	0.48	0.47	0.53	0.46	0.50
5	0.42	0.40	0.46	0.47	0.53	0.52
4	0.46	0.41	0.55	0.50	0.51	0.47
3	0.54	0.45	0.44	0.58	0.45	0.39
2	0.62	0.50	0.46	0.47	0.49	0.51
1	0.45	0.42	0.42	0.46	0.51	0.43

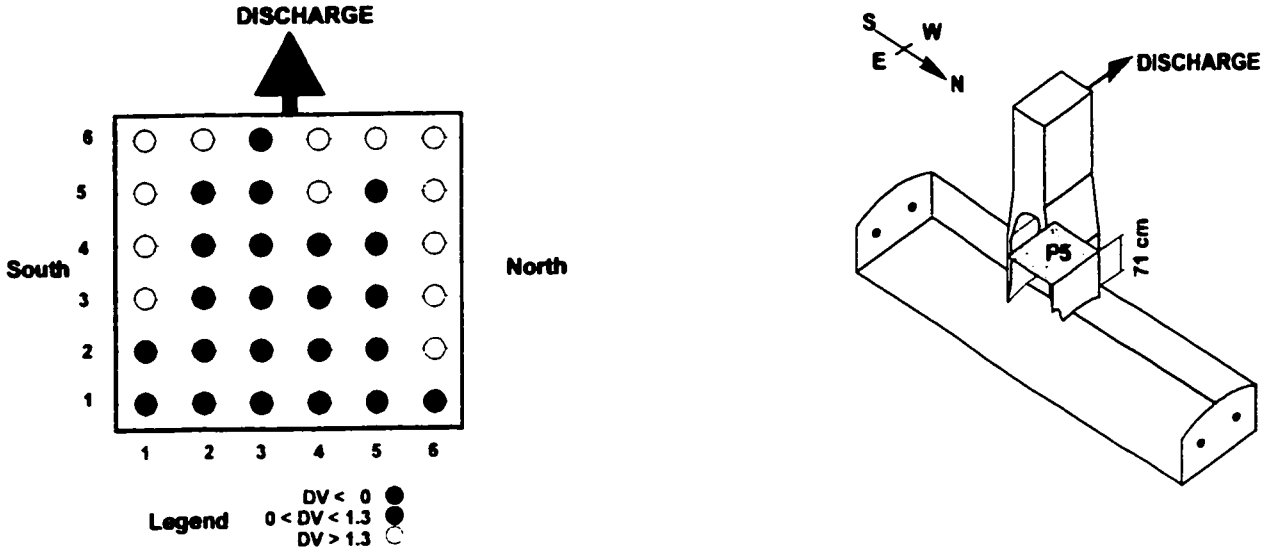

Figure B.1.37 Test V3A - Velocity Profile at Plane P5
(DV > 0 ≡ upward flow)

Table B.1.36 Test V4A - Velocity Profile at Plane P2

Average Furnace Velocity				23.9 cm/s	(based on measured flows to the main burner jets)				
				26.1 cm/s	(based on velocity profile)				
Dimensionless Velocity, DV									
	1	2	3	4	5	6	7	8	9
5		-9.05	-8.73	-6.56	-6.54	-7.61	-7.99	-7.94	
4	-7.24	-8.90	-5.83	5.56	6.79	6.73	-6.72	-8.01	-7.10
3	-6.14	-6.68	6.52	9.51	6.68	6.13	5.78	-7.60	-5.65
2	-7.68	7.37	6.95	10.67	10.93	5.93	6.49	-6.43	-5.53
1	7.44	9.66	11.35	14.36	11.92	9.21	9.53	6.78	-5.51
Root Mean Square, RMS									
	1	2	3	4	5	6	7	8	9
5		0.31	0.35	0.34	0.34	0.33	0.28	0.28	
4	0.42	0.36	0.32	0.39	0.42	0.31	0.32	0.27	0.34
3	0.40	0.35	0.45	0.39	0.54	0.48	0.33	0.38	0.45
2	0.40	0.36	0.43	0.40	0.39	0.41	0.42	0.38	0.41
1	0.56	0.45	0.40	0.27	0.33	0.47	0.46	0.38	0.47

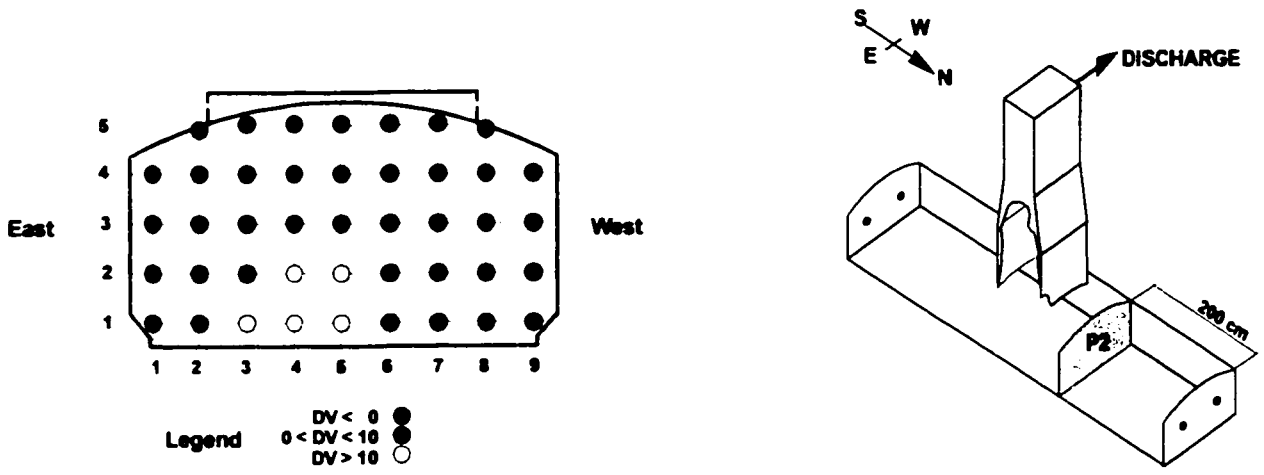

Figure B.1.38 Test V4A - Velocity Profile at Plane P2
(DV > 0 ≡ flow towards uptake)

Table B.1.37 Test V4A - Velocity Profile at Plane P3

Average Furnace Velocity				23.8 cm/s	(based on measured flows to the main burner jets)				
				25.0 cm/s	(based on velocity profile)				
Dimensionless Velocity, DV									
	9	8	7	6	5	4	3	2	1
5		-7.36	-6.24	-6.06	-7.17	-7.91	-8.56	-7.74	
4	-6.19	-6.08	6.16	5.76	4.91	-6.45	-7.05	-7.40	-7.28
3	-5.96	5.53	8.68	9.50	7.12	5.34	-6.25	-6.77	-6.55
2	-4.96	7.38	9.60	11.02	9.28	7.74	5.00	-5.99	-6.82
1	4.87	6.64	12.08	15.23	12.73	7.66	6.34	5.60	-6.17
Root Mean Square, RMS									
	9	8	7	6	5	4	3	2	1
5		0.38	0.40	0.30	0.31	0.28	0.32	0.25	
4	0.39	0.39	0.35	0.37	0.36	0.32	0.28	0.24	0.34
3	0.41	0.44	0.49	0.44	0.43	0.28	0.31	0.34	0.28
2	0.41	0.42	0.40	0.38	0.43	0.47	0.40	0.37	0.39
1	0.47	0.32	0.33	0.22	0.31	0.46	0.36	0.32	0.31

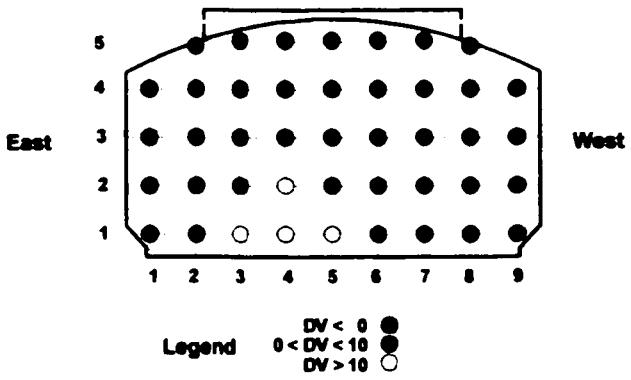

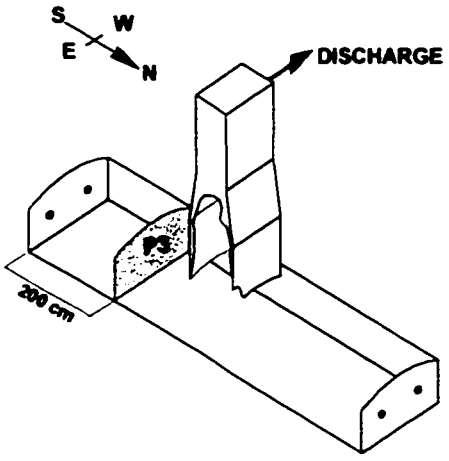

Figure B.1.39 Test V4A - Velocity Profile at Plane P3
(DV > 0 ≡ flow towards uptake)

Table B.1.38 Test V4A - Velocity Profile at Plane P5

Average Uptake Velocity	70.4 cm/s	(based on measured flows to the main burner jets)
	66.9 cm/s	(based on velocity profile)

Dimensionless Velocity, DV

	1	2	3	4	5	6
6	1.39	1.80	1.47	1.21	1.14	1.39
5	1.27	1.41	1.16	1.19	1.61	1.65
4	1.49	1.24	1.17	1.07	1.23	1.41
3	1.42	1.13	1.01	0.95	1.03	1.26
2	1.11	0.84	0.80	0.84	0.83	1.08
1	-1.09	-0.86	0.73	0.69	-0.75	-1.12

Root Mean Square, RMS

	1	2	3	4	5	6
6	0.38	0.27	0.32	0.35	0.38	0.47
5	0.34	0.46	0.39	0.29	0.37	0.38
4	0.27	0.37	0.40	0.39	0.34	0.35
3	0.47	0.35	0.45	0.42	0.44	0.40
2	0.51	0.48	0.39	0.44	0.41	0.45
1	0.46	0.59	0.44	0.44	0.59	0.46

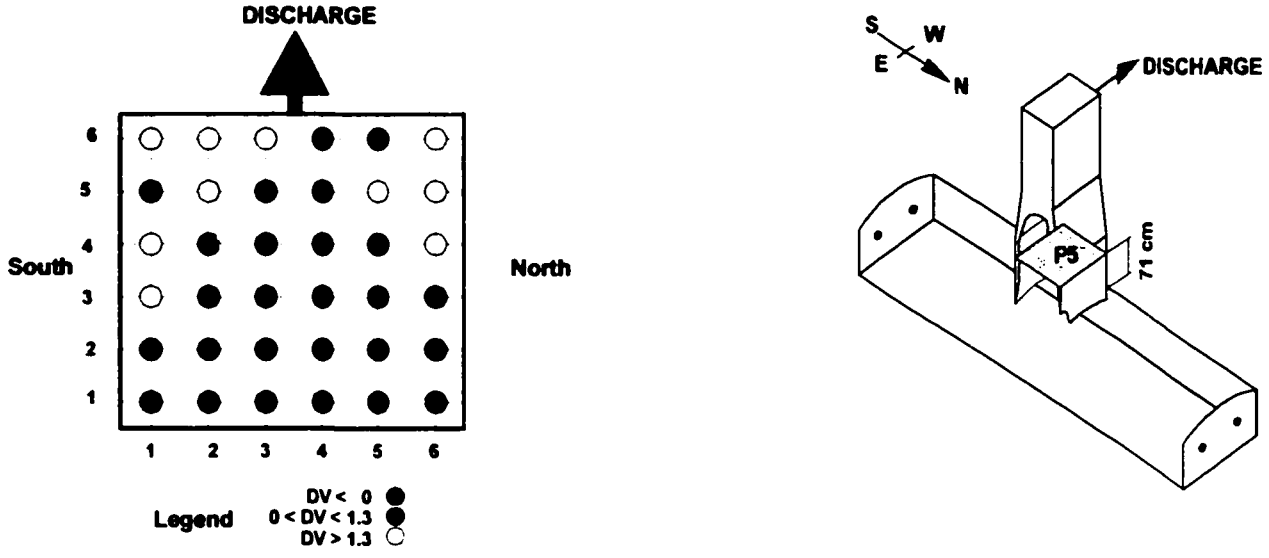

Figure B.1.40 Test V4A - Velocity Profile at Plane P5
(DV > 0 ≡ upward flow)

B.2 Thermal Mixing in Air Model (Uniformity of Mixing Experiments)

The experimental methodology used for the thermal mixing experiments simulated the uniformity of mixing experiments carried out in the water model with potassium chloride. The method of measuring the mixing uniformity was similar to the procedure proposed by Sroka and Forney (1989). In the air model, heated air was introduced through the afterburner jets and the steady state temperature rise was measured at three horizontal planes in the uptake (figure B.2.1). Each plane was subdivided in to cells of equal area, and the temperature was sampled at the center of each cell. The grid system orientation and spacing used in these experiments is illustrated in figure B.2.2 and B.2.3, respectively.

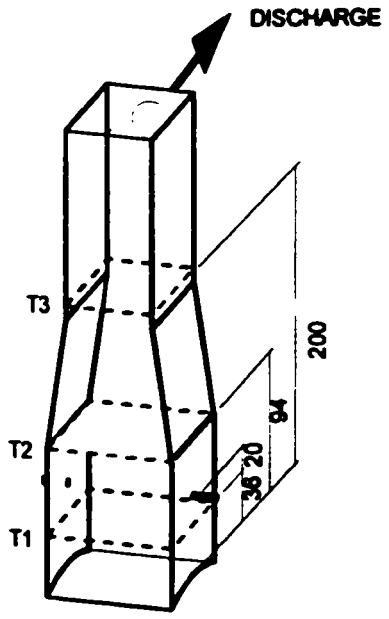

Figure B.2.1 Uniformity of Mixing Experiments in Air Model - Location of Sampling Planes (dimensions in cm, measured relative to top of roof arch)

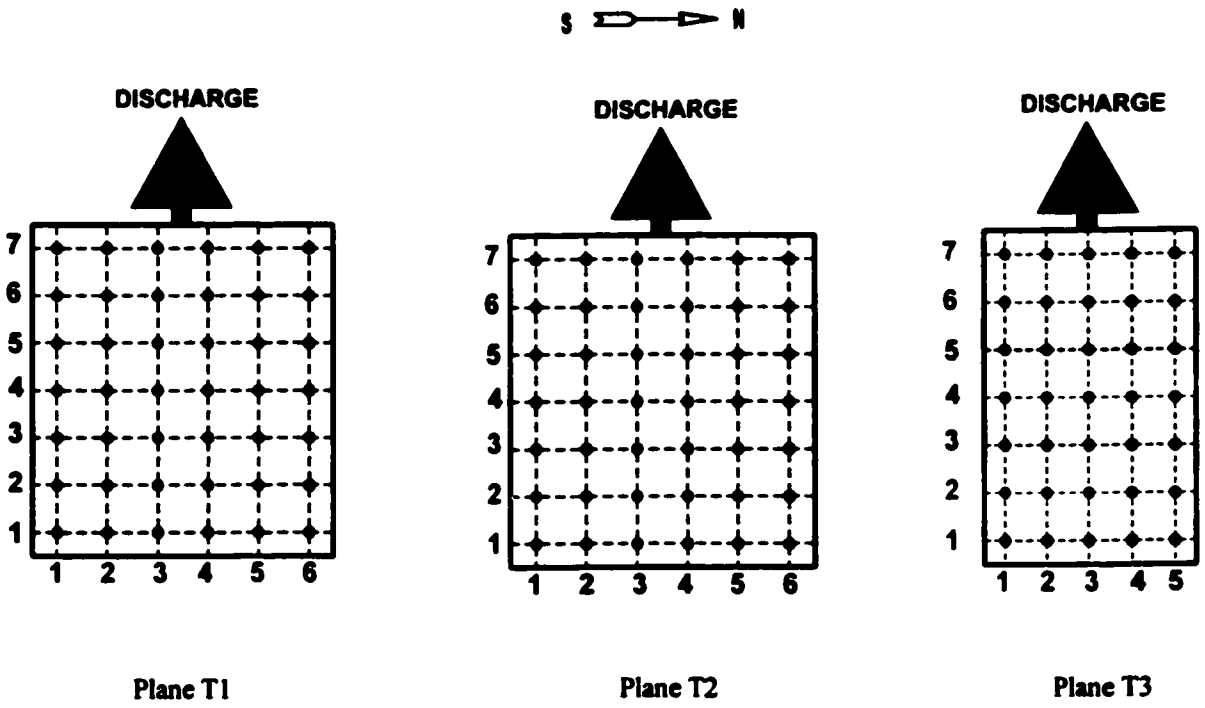

Figure B.2.2 Uniformity of Mixing Experiments in Air Model - Grid System Orientation

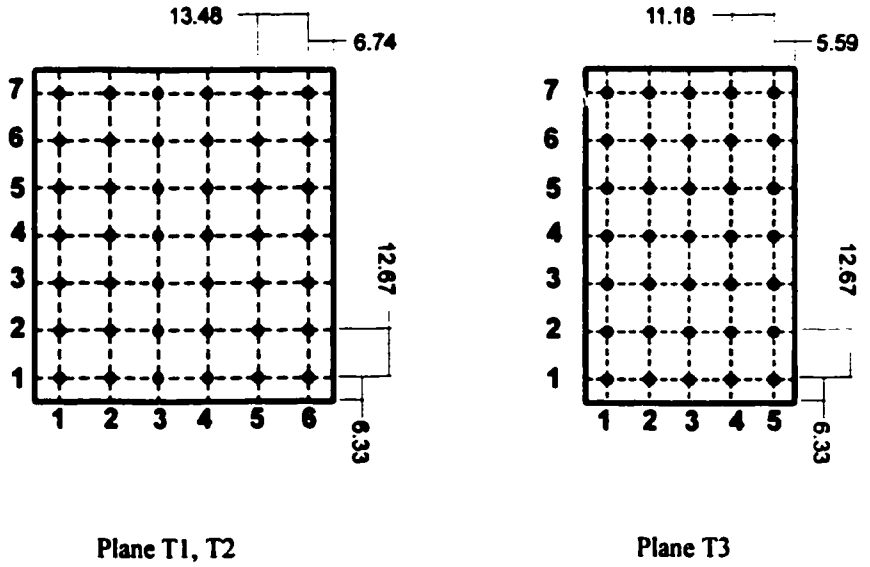

Figure B.2.3 Uniformity of Mixing Experiments in Air Model - Grid System Spacing (dimensions in cm)

In these experiments, two sets of temperature distributions were collected per sampling plane for each set of flow conditions. The initial temperature profile was obtained after the air flows to the main burner were stabilized. The final temperature profile was taken after introducing the hot afterburner jets and the model reached steady state. The average local initial and final temperatures were given by equation B.2.1, and the average local temperature rise was defined as the difference between the local final and initial temperatures (equation B.2.2).

$$\overline{T}_{i,j} = \frac{1}{n}\sum_{n=1}^{n} T_{i,j} \quad ; \text{where n = number of measurements} \tag{B.2.1}$$

$$\Delta\overline{T}_{i,j} = \overline{T}_{final_{i,j}} - \overline{T}_{initial_{i,j}} \tag{B.2.2}$$

The temperature rise data, $\Delta\overline{T}_{i,j}$, was made dimensionless with respect to the adiabatic temperature rise, as calculated from the heat balance (equation B.2.3). In this way, the results obtained for each set of experimental conditions could be compared directly. It was worth noting that the average temperature rise on sampling planes T2 and T3 (equation B.2.4) was in good agreement with the adiabatic temperature rise. Equation B.2.5 describes the dimensionless temperature rise for a given sampling point.

$$\Delta T_{ad} = \left(\frac{\Delta H_{jets_{fce}} + \Delta H_{jets_{uptake}}}{\rho\left(Q_{jets_{fce}} + Q_{jets_{uptake}}\right) c_p} \right) \quad ; \text{where } \Delta H_{jet} = \rho Q_{jet} c_p \Delta T_{jet} \tag{B.2.3}$$

$$\Delta T_{jet} = (T_{final} - T_{initial})_{jet}$$

$$\Delta\overline{T} = \frac{1}{A}\sum_{i=1}^{7}\sum_{j=1}^{5or6}\Delta\overline{T}_{i,j}\,\Delta A \tag{B.2.4}$$

$$\Delta\overline{T}_{i,j} = DT_{i,j} = \frac{\Delta\overline{T}_{i,j}}{\Delta T_{ad}} \tag{B.2.5}$$

In characterizing the uniformity of the mixture within the uptake, the second moment, M, of the dimensionless temperature rise measured on a given sampling plane was used (equation B.2.6)

$$M = \frac{1}{A}\sum_{i=1}^{7}\sum_{j=1}^{5or6}\left(\Delta\bar{T}_{i,j} - 1\right)^2 \Delta A \qquad \text{(B.2.6)}$$

The experimental conditions are given in table B.2.1 to B.2.7, and a summary of the data collected is provided in table B.2.8. The numbering sequence used for the main burner and afterburner jets was identical to the one used in the velocity distribution study (figure B.1.1). The afterburner configurations tested are illustrated in figure B.2.4. The temperature distributions measured in the air model are tabulated in table B2.9 to B2.23, and the dimensionless temperature profiles are illustrated in figures B.2.5 to B.2.10.

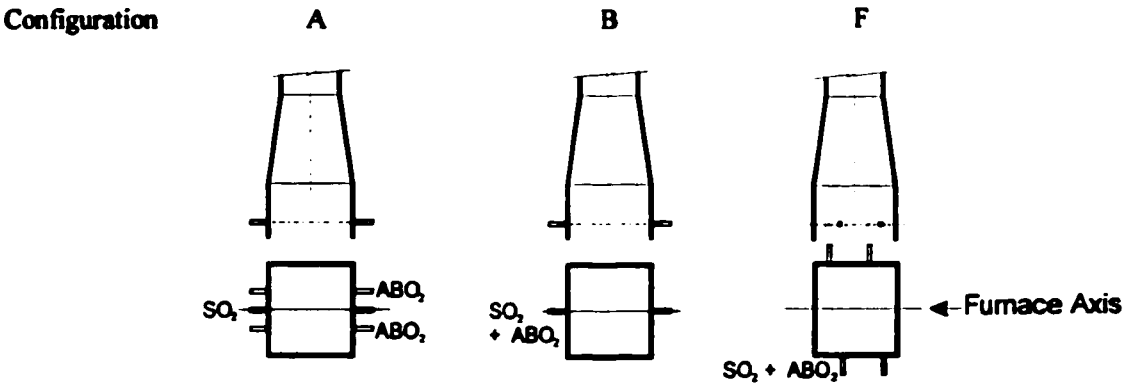

Figure B2.4 Uniformity of Mixing Experiments in Air Model - Afterburner Configurations

The temperature rise on plane T1, upstream of the afterburner jets, provided a measure of the amount of heat drawn downward due to backmixing (table B.2.8). The axial thermal dispersion coefficient, E_t, which is a measure of the amount of backmixing, was estimated from a 1-dimensional transport model in the axial direction. In this model, the temperature rise profile was assumed to be uniform upstream and downstream of the afterburner jets, and the velocity profile at the entrance of the uptake was also assumed to be uniform. Although this was an over-simplification of the problem, it provided a simple assessment of the degree of backmixing. Upstream of the jets, the net flux of heat was zero and was given by equation B.2.7.

$$u(T-T_o) - E_t \frac{d(T-T_o)}{dx} = 0; \quad \text{b.c. } x=0 \text{ cm}, \; T-T_o = \Delta T_{ad}$$

$$\text{Hence: } (T-T_o) = \Delta T_{ad} \exp\left(u x / E_t\right) \text{ for } x < 0 \tag{B.2.7}$$

The value of E_t was obtained by fitting data to equation B.2.7, and the axial thermal dispersion number was calculated using equation B.2.8. The axial thermal dispersion number was compared with the model developed by Levenspiel (1972), describing the dispersion of fluids flow in pipes (figure A.3.35).

$$N_d = \frac{E_t}{u\,\ell} \tag{B.2.8}$$

Table B.2.1 Uniformity of Mixing Experiments in Air Model - Test Conditions

Test		M1	M2	M3	M4	M5	M6
Afterburner Configuration		F	F	F	F	A	B
Burner	Reynolds # (x 10^3)	133.5	137.4	144.5	196.4	141.0	137.7
	Velocity (m/s)	21.4	22.0	23.1	31.4	21.7	21.2
Furnace	Reynolds # (x 10^3)	20.2	20.8	21.9	29.7	20.6	20.1
	Superficial Velocity (cm/s)	30.5	31.4	33.0	44.8	31.0	30.3
Uptake	Entrance Reynolds # (x 10^3)	48.5	49.9	52.5	71.3	49.4	48.2
	Superficial Entrance Velocity (cm/s)	89.8	92.5	97.2	132.1	91.4	89.3
Afterburner O_2 Jet	Reynolds # (x 10^3)					24.5	
	Velocity (cm/s)					27.8	
	Velocity Ratio					30.4	
	Momentum Ratio					0.25	
	Modified Froude # (x 10^3)					34.2	
SO_2 Recycle Jet	Reynolds # (x 10^3)					26.5	
	Velocity (cm/s)					8.3	
	Velocity Ratio					9.1	
	Momentum Ratio					0.37	
SO_2 Recycle+O_2 Jet	Ø (cm)	3.81	3.81	3.81	3.81		6.27
	Reynolds # (x 10^3)	45.7	43.3	57.7	59.9		44.5
	Velocity (cm/s)	23.7	22.7	30.2	31.4		14.0
	Velocity Ratio	26.4	24.4	31.1	23.8		15.7
	Momentum Ratio	0.97	0.83	1.34	0.78		0.94
	Modified Froude # (x 10^3)	10.3	9.5	16.8	18.1		2.2

Table B.2.2 Uniformity of Mixing Experiments in Air Model - Test M1 Flow Conditions

Sampling Plane		Main Burner Jets				SO_2 Recycle+O_2 Jet			
		1	2	3	4	1	2	3	4
T1	Flow (L/min)	10110	9690	9000	9770	1580	1720	1670	1540
	Velocity (m/s)	22.3	21.4	19.9	21.6	23.1	25.1	24.5	22.5
	Reynolds # (x 10^3)	139.7	133.9	124.4	135.0	44.1	48.0	46.7	42.8
	Modified Froude # (x 10^3)					9.8	11.6	11.0	9.3
	ΔT from Heat Supply (°C)	2.3	2.3	2.3	2.3	53.4	51.3	52.5	55.0
	ΔH (W)	460	440	410	440	1430	1500	1490	1430
T2	Flow (L/min)	9870	9550	9090	9950	1600	1660	1660	1450
	Velocity (m/s)	21.8	21.1	20.1	22.0	23.4	24.3	24.2	21.3
	Reynolds # (x 10^3)	136.4	132.0	125.6	137.6	44.7	46.4	46.3	40.5
	Modified Froude # (x 10^3)					10.1	10.9	10.8	8.3
	ΔT from Heat Supply (°C)	2.6	2.6	2.6	2.6	52.2	51.1	52.7	54.8
	ΔH (W)	510	490	470	510	1420	1450	1490	1340
T3	Flow (L/min)	10080	9780	9290	9720	1580	1800	1650	1530
	Velocity (m/s)	22.3	21.6	20.5	21.5	23.1	26.4	24.1	22.4
	Reynolds # (x 10^3)	139.3	135.1	128.4	134.3	44.0	50.3	45.9	42.8
	Modified Froude # (x 10^3)					9.8	12.7	10.6	9.2
	ΔT from Heat Supply (°C)	2.1	2.1	2.1	2.1	52.6	50.1	52.1	56.0
	ΔH (W)	410	400	380	390	1410	1550	1460	1440
Average	Flow (L/min)	10020	9670	9130	9810	1590	1730	1660	1510
	Velocity (m/s)	22.2	21.4	20.2	21.7	23.2	25.3	24.3	22.0
	Reynolds # (x 10^3)	138.5	133.6	126.1	135.6	44.3	48.2	46.3	42.1
	Modified Froude # (x 10^3)					9.9	11.7	10.8	8.9

Table B.2.3 Uniformity of Mixing Experiments in Air Model - Test M2 Flow Conditions

Sampling Plane		Main Burner Jets				SO_2 Recycle+O_2 Jet			
		1	2	3	4	1	2	3	4
T1	Flow (L/min)	10130	9280	9480	9940	1420	1520	1520	1310
	Velocity (m/s)	22.4	20.5	21.0	22.0	20.8	22.2	22.2	19.1
	Reynolds # (x 10^3)	140.0	128.3	131.1	137.4	39.6	42.4	42.3	36.4
	Modified Froude # (x 10^3)					7.9	9.0	9.0	6.7
	ΔT from Heat Supply (°C)	3.7	3.7	3.7	3.7	53.5	51.0	54.6	56.8
	ΔH (W)	740	680	690	730	1290	1330	1410	1250
T2	Flow (L/min)	10050	9760	9290	9990	1470	1510	1530	1440
	Velocity (m/s)	22.2	21.6	20.5	22.1	21.4	22.0	22.3	21.1
	Reynolds # (x 10^3)	138.9	134.9	128.4	138.0	40.9	42.0	42.6	40.2
	Modified Froude # (x 10^3)					8.4	8.9	9.2	8.2
	ΔT from Heat Supply (°C)	2.2	2.2	2.2	2.2	54.0	52.1	53.3	57.2
	ΔH (W)	440	430	410	440	1340	1340	1380	1380
T3	Flow (L/min)	10750	10230	9910	10460	1700	1850	1770	1600
	Velocity (m/s)	23.8	22.6	21.9	23.1	24.8	27.0	25.9	23.5
	Reynolds # (x 10^3)	148.6	141.4	137.0	144.6	47.3	51.6	49.3	44.7
	Modified Froude # (x 10^3)					11.3	13.4	12.3	10.1
	ΔT from Heat Supply (°C)	1.5	1.5	1.5	1.5	47.0	44.3	45.6	47.9
	ΔH (W)	320	310	300	310	1380	1430	1400	1320
Average	Flow (L/min)	10310	9760	9560	10130	1530	1630	1610	1450
	Velocity (m/s)	22.8	21.6	21.1	22.4	22.3	23.7	23.5	21.2
	Reynolds # (x 10^3)	142.5	134.9	132.1	140.0	42.6	45.3	44.8	40.5
	Modified Froude # (x 10^3)					9.2	10.4	10.2	8.3

Table B.2.4 Uniformity of Mixing Experiments in Air Model - Test M3 Flow Conditions

Sampling Plane		Main Burner Jets				SO_2 Recycle+O_2 Jet			
		1	2	3	4	1	2	3	4
T1	Flow (L/min)	10680	10140	9790	10380	1960	2130	2040	1950
	Velocity (m/s)	23.6	22.4	21.6	23.0	28.7	31.1	29.8	28.5
	Reynolds # (x 10^3)	147.6	140.1	135.3	143.5	54.8	59.3	56.9	54.3
	Modified Froude # (x 10^3)					15.1	17.8	16.3	14.9
	ΔT from Heat Supply (°C)	2.1	2.1	2.1	2.1	47.2	44.2	45.1	47.3
	ΔH (W)	440	420	410	430	1600	1640	1600	1590
T2	Flow (L/min)	11350	10480	9980	10600	2080	2310	2160	1940
	Velocity (m/s)	25.1	23.2	22.1	23.4	30.5	33.8	31.6	28.4
	Reynolds # (x 10^3)	156.9	144.8	137.9	146.5	58.1	64.6	60.3	54.1
	Modified Froude # (x 10^3)					17.0	21.0	18.3	14.8
	ΔT from Heat Supply (°C)	2.0	2.0	2.0	2.0	46.0	43.6	45.0	46.2
	ΔH (W)	440	410	390	410	1660	1760	1690	1550
T3	Flow (L/min)	10960	10560	9880	10700	2040	2160	2110	1910
	Velocity (m/s)	24.2	23.3	21.8	23.6	29.9	31.6	30.9	28.0
	Reynolds # (x 10^3)	151.5	145.9	136.5	147.8	57.0	60.3	58.9	53.4
	Modified Froude # (x 10^3)					16.4	18.4	17.5	14.4
	ΔT from Heat Supply (°C)	2.3	2.3	2.3	2.3	45.0	42.3	43.5	45.0
	ΔH (W)	480	470	440	470	1600	1600	1600	1490
Average	Flow (L/min)	11000	10390	9880	10560	2030	2200	2100	1930
	Velocity (m/s)	24.3	23.0	21.8	23.3	29.7	32.2	30.8	28.3
	Reynolds # (x 10^3)	152.0	143.6	136.6	145.9	56.6	61.4	58.7	53.9
	Modified Froude # (x 10^3)					16.2	19.0	17.4	14.7

Table B.2.5 Uniformity of Mixing in Air Model - Test M4 Flow Conditions

Sampling Plane		Main Burner Jets				SO_2 Recycle+O_2 Jet			
		1	2	3	4	1	2	3	4
T1	Flow (L/min)	14600	13710	13730	14430	2150	2240	2230	2060
	Velocity (m/s)	32.3	30.3	30.4	31.9	31.4	32.7	32.6	30.2
	Reynolds # (x 10^3)	201.8	189.5	189.8	199.4	59.8	62.5	62.2	57.6
	Modified Froude # (x 10^3)					18.1	19.7	19.5	16.7
	ΔT from Heat Supply (°C)	2.6	2.6	2.6	2.6	49.8	46.8	48.2	49.3
	ΔH (W)	750	710	710	740	1830	1810	1850	1740
T2	Flow (L/min)	14530	14220	14260	14380	2180	2330	2270	2020
	Velocity (m/s)	32.1	31.4	31.5	31.8	31.8	34.1	33.1	29.5
	Reynolds # (x 10^3)	200.8	196.5	197.1	198.7	60.7	65.0	63.2	56.3
	Modified Froude # (x 10^3)					18.6	21.3	20.2	16.0
	ΔT from Heat Supply (°C)	2.4	2.4	2.4	2.4	50.0	47.1	48.4	49.6
	ΔH (W)	670	660	660	670	1860	1890	1890	1710
T3	Flow (L/min)	14860	13430	13930	14480	2080	2160	2120	1950
	Velocity (m/s)	32.8	29.7	30.8	32.0	30.5	31.6	31.0	28.4
	Reynolds # (x 10^3)	205.3	185.6	192.6	200.1	58.1	60.3	59.1	54.3
	Modified Froude # (x 10^3)					17.0	18.4	17.6	14.8
	ΔT from Heat Supply (°C)	3.3	3.3	3.3	3.3	51.4	48.4	49.8	51.5
	ΔH (W)	950	860	900	930	1830	1800	1810	1710
Average	Flow (L/min)	14660	13790	13970	14430	2140	2240	2210	2010
	Velocity (m/s)	32.4	30.5	30.9	31.9	31.2	32.8	32.2	29.4
	Reynolds # (x 10^3)	202.7	190.5	193.1	199.4	59.6	62.6	61.5	56.0
	Modified Froude # (x 10^3)					17.9	19.8	19.1	15.8

Table B.2.6 Uniformity of Mixing Experiments in Air Model - Test M5 Flow Conditions

Sampling Plane		Main Burner Jets				Afterburner O_2 Jet				SO_2 Recycle Jet	
		1	2	3	4	1	2	3	4	1	2
T2	Flow (L/min)	9930	9980	9640	9800	340	330	330	310	1590	1590
	Velocity (m/s)	22.0	22.1	21.3	21.7	29.0	28.1	28.2	26.1	8.3	8.3
	Reynolds # (x 10^3)	142.3	143.0	138.1	140.5	25.5	24.7	24.8	23.0	26.5	26.5
	Modified Froude # (x 10^3)					37.1	34.7	35.0	30.0		
	ΔT from Heat Supply (°C)	1.5	1.5	1.5	1.5	28.1	19.4	20.1	19.3	1.5	1.5
	DH (W)	300	300	290	290	180	120	130	110	50	50

Table B.2.7 Uniformity of Mixing Experiments in Air Model - Test M6 Flow Conditions

Sampling Plane		Main Burner Jets				SO_2 Recycle+O_2 Jet	
		1	2	3	4	1	2
T2	Flow (L/min)	10080	9400	9130	9970	2670	2670
	Velocity (m/s)	22.3	20.8	20.2	22.0	14.1	14.0
	Reynolds # (x 10^3)	144.5	134.7	130.8	142.9	44.7	44.6
	Modified Froude # (x 10^3)					2.2	2.2
	ΔT from Heat Supply (°C)	1.5	1.5	1.5	1.5	48.4	51.6
	ΔH (W)	290	270	260	290	2220	2340
T3	Flow (L/min)	9940	9400	9020	9950	2660	2650
	Velocity (m/s)	22.0	20.8	19.9	22.0	14.0	13.9
	Reynolds # (x 10^3)	142.4	134.7	129.3	142.6	44.5	44.3
	Modified Froude # (x 10^3)					2.2	2.1
	ΔT from Heat Supply (°C)	2.8	2.8	2.8	2.8	51.4	53.8
	ΔH (W)	540	510	490	540	2330	2410
Average	Flow (L/min)	10010	9400	9080	9960	2670	2660
	Velocity (m/s)	22.1	20.8	20.1	22.0	14.0	14.0
	Reynolds # (x 10^3)	143.5	134.7	130.0	142.8	44.6	44.5
	Modified Froude # (x 10^3)					2.2	2.2

Table B.2.8 Uniformity of Mixing Experiments in Air Model - Summary of Findings

			M1	M2	M3	M4	M5	M6
Afterburner Configuration			F	F	F	F	A	B
Plane T1	Temperature Rise - Average (°C)		3.0	4.2	3.4	3.1		
	Adiabatic Temperature Rise from Heat Balance (°C)		8.5	9.2	8.4	7.9		
Plane T2	Temperature Rise - Average (°C)		8.6	8.1	8.1	7.5	2.1	6.3
	Adiabatic Temperature Rise from Heat Balance (°C)		8.7	8.1	8.3	7.7	2.1	6.5
Plane T3	Temperature Rise - Average (°C)		8.2	6.9	8.1	8.4		7.7
	Adiabatic Temperature Rise from Heat Balance (°C)		8.3	7.1	8.2	8.4		7.9
Degree of Unmixedness - Second Moment								
	Plane T1	L/D = -0.250	0.0093	0.0038	0.0195	0.0055		
	Plane T2	L/D = 0.475	0.0126	0.0126	0.0131	0.0115	0.0199	0.1195
	Plane T3	L/D = 1.800	0.0009	0.0030	0.0006	0.0008		0.0016
Thermal Dispersion Number, E_z/uL								
	Fully Developed Turbulent Flow in Pipe		0.06	0.06	0.06	0.05		
	1-D Transport Model		0.06	0.10	0.07	0.07		

Note: L based on distance from afterburners
D based on hydraulic diameter of uptake = 76.5 cm
Grid Size: Lower Uptake (Planes T1 & T2) = 7 x 6, Upper Uptake (Plane T3) = 7 x 5
Second Moment based on Forney's paper (1989)

Note: Thermal dispersion number calculated for fully developed turbulent flow in pipes was based on Levenspiel's dispersion model (Levenspiel, 1972).
L_{uptake} = 302.3 cm
d_t = hydraulic diameter of uptake = 76.5 cm

Table B.2.9 Test M1 - Temperature Distribution at Plane T1

Initial Temperatures

Average 24.7 °C

	1	2	3	4	5	6
7	22.2	24.2	24.4	25.7	25.7	25.7
6	22.8	24.1	25.1	25.8	26.0	25.8
5	23.3	24.1	25.4	25.9	26.0	24.5
4	23.7	24.1	25.5	25.9	25.8	24.8
3	23.8	23.9	25.7	24.4	25.7	25.1
2	23.6	23.7	25.7	24.6	25.5	25.0
1	23.4	21.3	23.9	24.4	25.2	25.0

Final Temperatures

Average 28.7 °C

	1	2	3	4	5	6
7	25.0	26.5	27.4	28.4	28.3	28.4
6	25.5	26.6	27.8	28.4	28.3	28.3
5	25.9	26.5	28.2	28.4	28.4	27.1
4	26.3	26.6	28.3	28.6	28.4	27.3
3	26.6	26.7	28.7	27.1	28.6	27.9
2	27.6	27.1	27.5	27.8	29.0	28.7
1	28.9	25.8	28.8	29.3	29.8	29.3

Delta Temperatures

Average 3.0 °C

	1	2	3	4	5	6
7	2.9	2.4	3.0	2.7	2.6	2.7
6	2.7	2.5	2.8	2.5	2.3	2.5
5	2.6	2.4	2.9	2.5	2.4	2.5
4	2.7	2.5	2.9	2.7	2.6	2.5
3	2.8	2.8	3.0	2.6	2.9	2.8
2	3.9	3.3	1.8	3.3	3.5	3.6
1	5.6	4.5	4.9	4.9	4.6	4.4

Table B.2.10 Test M1 - Temperature Distribution at Plane T2

Initial Temperatures

Average 24.3 °C

	1	2	3	4	5	6
7	21.9	23.4	24.5	25.4	25.3	25.4
6	22.6	23.4	24.9	25.5	25.5	25.3
5	22.9	23.4	25.1	25.6	25.5	24.4
4	23.2	23.4	25.5	25.6	25.3	24.5
3	23.4	23.3	25.6	23.7	25.2	24.7
2	23.4	23.3	23.4	24.0	25.3	24.8
1	23.4	21.4	23.3	24.4	25.2	24.9

Final Temperatures

Average 32.9 °C

	1	2	3	4	5	6
7	30.4	32.8	34.1	34.6	34.2	33.9
6	29.8	31.9	33.9	34.2	33.5	33.2
5	29.6	31.2	33.7	34.0	32.9	31.7
4	29.7	30.8	33.7	34.1	33.0	32.4
3	30.7	30.9	34.1	32.6	33.5	33.5
2	32.2	31.7	32.8	33.8	34.4	34.2
1	33.2	31.1	33.6	34.9	35.5	34.9

Delta Temperatures

Average 8.6 °C

	1	2	3	4	5	6
7	8.5	9.4	9.6	9.2	8.9	8.5
6	7.2	8.6	8.9	8.6	8.1	7.9
5	6.7	7.8	8.6	8.4	7.4	7.3
4	6.5	7.4	8.2	8.5	7.7	7.9
3	7.3	7.6	8.5	8.9	8.3	8.8
2	8.8	8.5	9.4	9.8	9.1	9.4
1	9.8	9.8	10.3	10.5	10.3	10.0

Table B.2.11 Test M1 - Temperature Distribution at Plane T3

Initial Temperatures

Average 24.1 °C

	1	2	3	4	5
7	21.7	23.4	24.4	25.5	25.0
6	22.4	23.4	24.8	25.5	25.3
5	22.8	23.4	25.0	25.6	25.4
4	23.2	23.4	25.2	25.5	25.4
3	23.3	23.4	25.5	23.6	25.4
2	23.4	23.3	23.4	23.9	25.3
1	23.4	21.2	23.4	24.3	25.3

Final Temperatures

Average 32.3 °C

	1	2	3	4	5
7	30.0	31.5	32.7	33.4	32.8
6	30.7	31.5	32.8	33.6	33.1
5	30.9	31.4	33.1	33.7	33.5
4	31.2	31.2	33.2	33.7	33.9
3	31.2	31.1	33.3	32.1	34.0
2	31.5	31.4	31.6	32.6	34.0
1	31.8	29.6	31.5	32.7	33.7

Delta Temperatures

Average 8.2 °C

	1	2	3	4	5
7	8.3	8.0	8.2	7.9	7.8
6	8.4	8.1	8.0	8.0	7.8
5	8.1	7.9	8.0	8.1	8.1
4	8.0	7.9	7.9	8.2	8.5
3	7.9	7.7	7.8	8.5	8.7
2	8.1	8.2	8.2	8.7	8.7
1	8.4	8.4	8.1	8.4	8.5

Table B.2.12 Test M2 - Temperature Distribution at Plane T1

Initial Temperatures

Average 23.0 °C

	1	2	3	4	5	6
7	20.6	22.2	23.6	24.1	23.8	23.9
6	21.2	22.3	23.8	24.1	24.1	24.1
5	21.6	22.3	24.0	24.2	24.2	22.8
4	22.1	22.2	24.1	24.2	24.1	23.2
3	22.2	22.2	24.1	23.0	24.0	23.4
2	22.1	22.1	22.2	23.0	23.8	23.5
1	22.0	19.8	21.9	22.9	23.6	23.3

Final Temperatures

Average 27.2 °C

	1	2	3	4	5	6
7	24.5	26.1	27.3	28.0	27.8	27.8
6	25.1	26.1	27.7	28.0	28.1	27.8
5	25.5	26.1	27.9	28.1	28.1	27.0
4	26.0	26.1	28.2	28.1	27.9	27.2
3	26.4	26.2	28.4	26.6	28.1	27.6
2	26.8	26.5	26.9	27.2	28.4	28.0
1	28.0	25.3	27.7	28.2	28.6	28.3

Delta Temperatures

Average 4.2 °C

	1	2	3	4	5	6
7	3.9	3.9	3.7	3.9	4.0	3.9
6	3.9	3.8	3.9	3.9	4.1	3.7
5	3.9	3.8	3.8	3.9	4.0	4.1
4	3.9	3.9	4.1	4.0	3.8	4.0
3	4.1	4.1	4.2	3.5	4.0	4.2
2	4.7	4.4	4.7	4.3	4.5	4.5
1	6.0	5.4	5.7	5.3	5.0	5.1

Table B.2.13 Test M2 - Temperature Distribution at Plane T2

Initial Temperatures

Average 23.7 °C

	1	2	3	4	5	6
7	21.5	23.2	23.9	25.0	24.3	24.7
6	22.1	23.1	24.2	25.0	24.6	24.8
5	22.6	23.1	24.5	25.1	24.9	23.5
4	22.8	23.0	24.6	24.9	24.9	23.7
3	22.9	23.0	25.0	23.2	24.8	23.9
2	23.0	23.0	23.1	23.3	24.7	24.0
1	23.1	20.7	22.9	23.8	24.7	24.3

Final Temperatures

Average 31.8 °C

	1	2	3	4	5	6
7	28.2	31.0	32.3	33.1	33.1	33.0
6	28.2	30.6	32.3	32.7	32.7	32.4
5	28.6	30.4	32.9	32.9	32.3	30.7
4	29.1	30.3	33.2	33.2	32.4	31.0
3	30.0	30.6	33.6	32.0	32.7	31.8
2	31.4	31.4	32.0	32.7	33.2	32.4
1	32.4	30.3	32.5	33.4	34.0	33.0

Delta Temperatures

Average 8.1 °C

	1	2	3	4	5	6
7	6.6	7.8	8.4	8.1	8.8	8.2
6	6.1	7.4	8.1	7.7	8.2	7.6
5	6.0	7.3	8.4	7.9	7.4	7.2
4	6.3	7.3	8.5	8.3	7.5	7.2
3	7.1	7.6	8.6	8.8	7.9	7.9
2	8.4	8.4	8.9	9.3	8.5	8.5
1	9.3	9.6	9.6	9.6	9.3	8.7

Table B.2.14 Test M2 - Temperature Distribution at Plane T3

Initial Temperatures

Average 24.5 °C

	1	2	3	4	5
7	22.5	24.0	24.6	25.2	25.4
6	23.2	24.0	25.0	25.4	25.6
5	23.4	23.9	25.2	25.5	25.6
4	23.9	23.9	25.4	25.6	25.2
3	23.9	23.9	25.6	25.6	25.3
2	23.9	23.8	24.0	24.0	25.3
1	23.9	21.8	24.0	24.3	25.2

Final Temperatures

Average 31.4 °C

	1	2	3	4	5
7	29.0	30.8	31.7	32.4	32.3
6	30.0	30.9	31.9	32.5	32.4
5	30.3	30.6	32.1	32.6	32.7
4	30.5	30.5	32.2	32.6	32.5
3	30.5	30.4	32.4	30.9	32.7
2	30.7	30.6	30.8	31.5	32.8
1	31.1	28.5	30.9	31.6	32.6

Delta Temperatures

Average 6.9 °C

	1	2	3	4	5
7	6.5	6.8	7.0	7.2	6.8
6	6.8	6.9	6.9	7.1	6.8
5	6.9	6.7	6.9	7.1	7.0
4	6.7	6.6	6.8	6.9	7.3
3	6.6	6.6	6.8	5.2	7.4
2	6.8	6.8	6.7	7.5	7.5
1	7.2	6.8	6.9	7.4	7.4

Table B.2.15 Test M3 - Temperature Distribution at Plane T1

Initial Temperatures

Average 24.9 °C

	1	2	3	4	5	6
7	23.0	24.4	25.0	25.7	25.8	25.7
6	23.7	24.5	25.4	25.9	26.0	25.8
5	24.0	24.6	25.6	26.0	26.1	24.9
4	24.3	24.4	25.8	25.9	25.6	25.0
3	24.2	24.3	25.8	24.3	25.7	25.1
2	24.1	24.1	24.4	24.5	25.4	25.1
1	23.9	22.1	23.9	24.5	25.0	25.0

Final Temperatures

Average 28.2 °C

	1	2	3	4	5	6
7	25.2	27.0	27.7	28.7	28.5	28.8
6	25.8	27.0	27.8	28.5	28.6	28.7
5	26.4	27.0	28.2	28.6	28.6	27.4
4	26.9	27.1	28.5	28.8	28.6	27.8
3	27.4	27.3	28.9	27.2	28.9	28.3
2	28.8	27.8	28.4	28.3	29.6	29.2
1	30.3	27.3	30.3	30.6	30.9	30.2

Delta Temperatures

Average 3.4 °C

	1	2	3	4	5	6
7	2.1	2.6	2.7	3.0	2.6	3.1
6	2.1	2.6	2.4	2.6	2.6	2.9
5	2.4	2.4	2.6	2.6	2.6	2.4
4	2.5	2.6	2.7	2.9	3.0	2.8
3	3.1	3.0	3.2	2.9	3.2	3.3
2	4.6	3.7	4.0	3.8	4.2	4.1
1	6.4	5.1	6.4	6.1	5.8	5.3

Table B.2.16 Test M3 - Temperature Distribution at Plane T2

Initial Temperatures

Average 24.5 °C

	1	2	3	4	5	6
7	22.3	23.8	24.7	25.5	25.5	25.5
6	23.0	23.9	25.0	25.5	25.6	25.5
5	23.3	23.8	25.3	25.5	25.5	24.5
4	23.7	23.8	25.5	25.5	25.4	24.8
3	23.7	23.7	25.5	23.5	25.4	24.9
2	23.7	23.6	23.8	23.9	25.4	25.0
1	23.8	21.7	23.7	24.4	25.3	25.2

Final Temperatures

Average 32.6 °C

	1	2	3	4	5	6
7	30.8	32.8	33.6	34.3	33.7	33.5
6	30.6	32.1	33.4	33.6	32.9	32.6
5	30.4	31.2	33.2	33.2	32.5	31.3
4	30.2	30.5	33.2	33.5	32.6	32.7
3	30.4	30.5	33.4	32.1	33.5	33.7
2	31.9	31.0	32.4	33.4	34.3	34.3
1	32.8	30.4	33.3	34.6	35.4	34.9

Delta Temperatures

Average 8.1 °C

	1	2	3	4	5	6
7	8.5	9.1	8.9	8.8	8.3	8.1
6	7.6	8.2	8.4	8.0	7.3	7.1
5	7.1	7.4	8.0	7.7	7.0	6.8
4	6.5	6.8	7.7	7.9	7.2	7.9
3	6.6	6.8	7.9	8.6	8.0	8.7
2	8.2	7.4	8.6	9.4	8.9	9.3
1	9.0	8.8	9.6	10.2	10.1	9.7

Table B.2.17 Test M3 - Temperature Distribution at Plane T3

Initial Temperatures

Average 24.1 °C

	1	2	3	4	5
7	21.9	23.4	24.4	25.4	25.1
6	22.5	23.4	24.6	25.4	25.3
5	22.8	23.4	24.9	25.5	25.4
4	23.3	23.4	25.2	25.5	25.4
3	23.4	23.4	25.5	23.8	25.4
2	23.4	23.4	23.4	23.9	25.3
1	23.5	21.3	23.3	24.3	25.2

Final Temperatures

Average 32.3 °C

	1	2	3	4	5
7	30.1	31.7	32.5	33.2	32.8
6	30.7	31.8	32.8	33.3	33.1
5	31.0	31.7	33.0	33.5	33.4
4	31.4	31.6	33.0	33.4	33.7
3	31.3	31.4	33.2	32.1	33.7
2	31.5	31.5	31.5	32.5	33.7
1	31.7	29.3	31.4	32.6	33.5

Delta Temperatures

Average 8.1 °C

	1	2	3	4	5
7	8.2	8.3	8.1	7.8	7.7
6	8.2	8.4	8.1	7.9	7.8
5	8.2	8.3	8.1	7.9	8.0
4	8.1	8.2	7.8	7.9	8.3
3	7.9	8.1	7.7	8.3	8.4
2	8.1	8.1	8.0	8.5	8.4
1	8.3	8.0	8.1	8.3	8.2

Table B.2.18 Test M4 - Temperature Distribution at Plane T1

Initial Temperatures

Average 25.6 °C

	1	2	3	4	5	6
7	23.4	25.1	25.7	26.5	26.6	26.6
6	24.4	25.1	26.1	26.6	26.7	26.6
5	24.6	25.1	26.3	26.6	26.8	25.4
4	25.0	25.0	26.5	26.6	26.4	25.6
3	25.0	25.0	26.6	24.8	26.4	26.0
2	25.0	24.8	25.0	25.0	26.1	26.0
1	24.8	22.7	24.8	25.0	26.0	26.1

Final Temperatures

Average 28.6 °C

	1	2	3	4	5	6
7	26.1	27.6	28.5	29.3	29.3	29.4
6	26.7	27.6	28.8	29.4	29.5	29.3
5	27.0	27.6	29.0	29.4	29.5	28.2
4	27.4	27.6	29.4	29.4	29.3	28.4
3	27.7	27.7	29.6	27.9	29.5	29.0
2	28.3	28.0	28.4	28.6	29.8	29.5
1	29.3	26.7	29.3	29.5	30.3	30.1

Delta Temperatures

Average 3.1 °C

	1	2	3	4	5	6
7	2.7	2.5	2.8	2.8	2.8	2.9
6	2.3	2.5	2.7	2.7	2.8	2.7
5	2.4	2.5	2.7	2.8	2.7	2.8
4	2.5	2.6	2.8	2.9	2.9	2.8
3	2.7	2.7	2.9	3.1	3.2	3.0
2	3.4	3.2	3.4	3.6	3.6	3.5
1	4.5	4.1	4.5	4.4	4.3	4.0

Table B.2.19 Test M4 - Temperature Distribution at Plane T2

Initial Temperatures

Average 25.7 °C

	1	2	3	4	5	6
7	23.7	25.1	25.9	26.7	26.5	26.6
6	24.4	25.1	26.2	26.7	26.7	26.5
5	24.7	25.1	26.4	26.7	26.7	25.4
4	25.0	25.1	26.6	26.7	26.5	25.6
3	25.2	25.0	26.6	25.2	26.6	25.9
2	25.1	25.0	25.1	25.5	26.5	26.1
1	24.9	23.1	24.9	25.7	26.6	26.1

Final Temperatures

Average 33.2 °C

	1	2	3	4	5	6
7	30.7	33.1	34.1	34.5	34.2	34.0
6	30.0	32.4	34.0	34.1	34.0	33.5
5	30.1	32.0	34.1	34.2	33.7	31.8
4	30.7	31.6	34.3	34.4	33.5	32.4
3	31.6	32.1	34.6	33.2	34.0	33.2
2	32.9	32.6	33.4	33.9	34.5	33.8
1	33.5	31.7	33.8	34.7	35.2	34.6

Delta Temperatures

Average 7.5 °C

	1	2	3	4	5	6
7	7.0	8.0	8.1	7.8	7.7	7.4
6	5.7	7.3	7.8	7.4	7.3	7.0
5	5.4	6.9	7.7	7.4	7.0	6.5
4	5.7	6.5	7.7	7.7	7.0	6.8
3	6.5	7.1	8.0	8.0	7.3	7.3
2	7.7	7.6	8.3	8.4	8.0	7.7
1	8.6	8.6	8.8	9.1	8.6	8.4

Table B.2.20 Test M4 - Temperature Distribution at Plane T3

Initial Temperatures

Average 24.2 °C

	1	2	3	4	5
7	22.2	23.7	24.4	25.4	25.2
6	22.7	23.7	24.7	25.4	25.4
5	23.1	23.6	25.0	25.5	25.4
4	23.3	23.6	25.4	25.5	25.3
3	23.6	23.6	25.4	23.6	25.3
2	23.6	23.5	23.7	23.8	25.2
1	23.5	21.8	23.5	24.2	25.2

Final Temperatures

Average 32.7 °C

	1	2	3	4	5
7	30.6	32.1	32.7	33.5	33.3
6	31.2	32.1	32.9	33.6	33.6
5	31.4	32.1	33.2	33.8	33.9
4	31.8	31.9	33.3	33.8	33.9
3	31.9	31.9	33.4	32.2	34.0
2	32.1	32.0	32.2	32.6	34.2
1	32.5	30.2	32.3	32.9	33.8

Delta Temperatures

Average 8.4 °C

	1	2	3	4	5
7	8.3	8.4	8.3	8.1	8.1
6	8.4	8.5	8.2	8.2	8.2
5	8.3	8.5	8.2	8.2	8.4
4	8.4	8.3	8.0	8.2	8.6
3	8.2	8.3	8.0	8.6	8.7
2	8.5	8.5	8.5	8.8	8.9
1	9.0	8.4	8.8	8.8	8.6

Table B.2.21 Test M5 - Temperature Distribution at Plane T2

Initial Temperatures

Average 22.7 °C

	1	2	3	4	5	6
7	20.5	21.7	22.9	23.9	23.6	23.7
6	21.0	21.7	23.6	24.0	23.9	23.8
5	21.3	21.8	23.9	24.2	23.9	22.5
4	21.7	21.8	24.2	24.3	24.0	22.6
3	21.9	21.7	24.3	22.3	24.0	22.7
2	22.7	21.7	21.7	22.4	23.8	22.8
1	21.7	19.5	21.6	22.7	23.7	22.8

Final Temperatures

Average 24.8 °C

	1	2	3	4	5	6
7	22.2	23.8	25.7	26.2	25.5	25.1
6	22.7	23.9	26.0	26.4	25.9	25.3
5	23.3	23.9	26.0	26.2	25.8	24.4
4	23.7	23.7	26.2	26.1	25.8	24.6
3	23.7	23.7	26.4	24.5	25.9	24.9
2	24.6	23.8	24.3	25.0	26.0	25.1
1	23.6	21.8	24.0	25.3	25.9	25.1

Delta Temperatures

Average 2.1 °C

	1	2	3	4	5	6
7	1.6	2.1	2.7	2.2	1.9	1.3
6	1.7	2.2	2.4	2.3	2.0	1.4
5	1.9	2.1	2.2	1.9	1.9	1.9
4	1.9	1.9	1.9	1.8	1.8	2.0
3	1.9	2.1	2.1	2.2	2.0	2.2
2	1.8	2.2	2.7	2.6	2.2	2.3
1	1.9	2.3	2.4	2.7	2.2	2.3

Table B.2.22 Test M6 - Temperature Distribution at Plane T2

Initial Temperatures

Average 24.6 °C

	1	2	3	4	5	6
7	22.4	23.9	25.4	26.0	25.6	25.7
6	22.9	23.9	25.6	25.9	25.6	25.7
5	23.2	23.8	25.6	25.8	25.6	24.4
4	23.4	23.7	25.9	25.6	25.8	24.5
3	23.7	23.4	25.9	24.2	25.7	24.7
2	23.9	23.4	23.5	24.6	25.7	24.8
1	23.8	21.7	23.4	24.8	25.6	24.9

Final Temperatures

Average 30.9 °C

	1	2	3	4	5	6
7	27.8	26.3	28.7	30.5	30.8	29.4
6	28.6	29.5	30.9	32.4	32.3	30.3
5	28.9	30.2	34.3	34.2	33.9	31.0
4	28.7	30.2	34.4	36.7	34.5	31.3
3	27.6	29.5	33.9	36.3	34.4	30.7
2	26.4	28.8	32.7	34.5	32.7	30.6
1	24.8	27.5	30.3	31.6	29.9	29.0

Delta Temperatures

Average 6.3 °C

	1	2	3	4	5	6
7	5.5	2.3	3.3	4.5	5.2	3.7
6	5.6	5.6	5.4	6.5	6.7	4.6
5	5.7	6.4	8.7	8.4	8.4	6.6
4	5.3	6.5	8.6	11.1	8.7	6.8
3	4.0	6.1	8.0	12.1	8.7	6.0
2	2.5	5.4	9.2	9.9	7.0	5.8
1	1.0	5.9	6.8	6.8	4.3	4.1

Table B.2.23 Test M6 - Temperature Distribution at Plane T3

Initial Temperatures

Average 22.8 °C

	1	2	3	4	5
7	20.6	22.0	23.0	24.2	23.5
6	21.1	22.2	23.4	24.3	23.8
5	21.3	22.2	23.7	24.4	23.9
4	21.7	22.1	23.9	24.2	24.1
3	21.9	22.0	24.0	22.3	23.9
2	22.1	21.9	22.2	22.6	23.9
1	22.0	20.3	21.9	22.8	23.9

Final Temperatures

Average 30.4 °C

	1	2	3	4	5
7	27.2	29.3	30.8	31.9	31.4
6	28.2	29.4	30.9	31.9	31.8
5	28.8	29.5	31.3	31.9	32.0
4	29.4	29.5	31.7	32.1	32.2
3	29.8	29.6	31.8	30.3	32.2
2	29.8	29.7	29.9	30.4	31.8
1	29.5	27.9	29.6	30.6	31.1

Delta Temperatures

Average 7.7 °C

	1	2	3	4	5
7	6.6	7.3	7.7	7.6	8.0
6	7.0	7.2	7.6	7.5	8.0
5	7.5	7.3	7.6	7.5	8.1
4	7.7	7.5	7.8	7.9	8.2
3	7.9	7.7	7.8	7.9	8.2
2	7.7	7.8	7.8	7.9	7.9
1	7.5	7.6	7.7	7.8	7.3

Plane T1 x/D = -0.261

	1	2	3	4	5	6
7	0.34	0.28	0.35	0.31	0.30	0.32
6	0.32	0.29	0.32	0.30	0.28	0.30
5	0.30	0.28	0.33	0.29	0.28	0.29
4	0.31	0.29	0.34	0.31	0.30	0.29
3	0.33	0.33	0.36	0.31	0.34	0.33
2	0.46	0.39	0.21	0.38	0.41	0.42
1	0.65	0.53	0.57	0.57	0.53	0.51

Plane T2 x/D = 0.497

	1	2	3	4	5	6
7	0.98	1.08	1.10	1.07	1.02	0.98
6	0.83	0.99	1.03	0.99	0.93	0.91
5	0.77	0.90	0.99	0.97	0.86	0.85
4	0.75	0.85	0.94	0.98	0.89	0.91
3	0.84	0.87	0.98	1.02	0.96	1.02
2	1.02	0.98	1.09	1.13	1.05	1.08
1	1.12	1.13	1.19	1.21	1.19	1.15

Plane T3 x/D = 1.882

	1	2	3	4	5
7	1.00	0.97	0.99	0.95	0.94
6	1.01	0.98	0.97	0.97	0.94
5	0.98	0.96	0.97	0.98	0.97
4	0.97	0.95	0.95	0.99	1.02
3	0.95	0.93	0.94	1.02	1.04
2	0.97	0.99	0.99	1.05	1.05
1	1.01	1.01	0.98	1.02	1.02

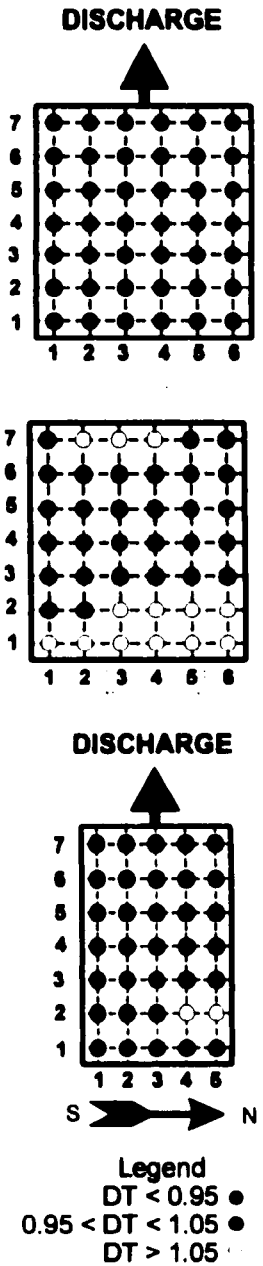

Figure B.2.5 Uniformity of Mixing Experiments in Air Model - Test M1 Dimensionless Temperature Rise

Plane T1 x/D = -0.261

	1	2	3	4	5	6
7	0.43	0.42	0.40	0.42	0.43	0.42
6	0.42	0.41	0.42	0.42	0.44	0.40
5	0.43	0.41	0.42	0.42	0.43	0.45
4	0.43	0.42	0.44	0.43	0.41	0.44
3	0.45	0.44	0.46	0.38	0.44	0.45
2	0.51	0.48	0.51	0.46	0.49	0.49
1	0.65	0.59	0.62	0.57	0.55	0.55

Plane T2 x/D = 0.497

	1	2	3	4	5	6
7	0.82	0.97	1.04	1.00	1.09	1.02
6	0.76	0.92	1.00	0.96	1.01	0.95
5	0.74	0.91	1.04	0.98	0.92	0.89
4	0.78	0.90	1.06	1.03	0.93	0.90
3	0.88	0.94	1.07	1.10	0.99	0.98
2	1.04	1.05	1.11	1.16	1.05	1.05
1	1.15	1.19	1.19	1.19	1.16	1.09

Plane T3 x/D = 1.882

	1	2	3	4	5
7	0.92	0.96	0.99	1.01	0.96
6	0.95	0.98	0.98	1.00	0.95
5	0.97	0.95	0.98	1.00	0.99
4	0.94	0.94	0.96	0.97	1.03
3	0.93	0.92	0.95	0.74	1.03
2	0.96	0.96	0.95	1.05	1.06
1	1.02	0.95	0.97	1.04	1.04

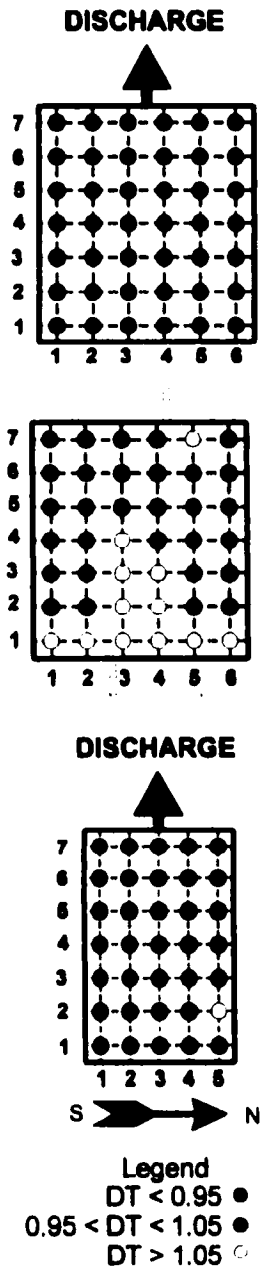

Figure B.2.6 Uniformity of Mixing Experiments in Air Model - Test M2 Dimensionless Temperature Rise

Plane T1 x/D = -0.261

	1	2	3	4	5	6
7	0.26	0.31	0.32	0.36	0.31	0.37
6	0.25	0.31	0.29	0.32	0.30	0.34
5	0.29	0.29	0.31	0.31	0.31	0.29
4	0.30	0.31	0.32	0.34	0.35	0.34
3	0.37	0.36	0.38	0.35	0.38	0.39
2	0.55	0.45	0.48	0.45	0.50	0.49
1	0.76	0.61	0.77	0.72	0.70	0.63

Plane T2 x/D = 0.497

	1	2	3	4	5	6
7	1.03	1.10	1.08	1.06	1.00	0.97
6	0.92	0.99	1.01	0.97	0.88	0.86
5	0.86	0.89	0.96	0.93	0.84	0.82
4	0.79	0.82	0.93	0.96	0.87	0.95
3	0.80	0.82	0.95	1.05	0.97	1.05
2	0.99	0.90	1.04	1.14	1.08	1.12
1	1.08	1.06	1.16	1.24	1.22	1.17

Plane T3 x/D = 1.882

	1	2	3	4	5
7	1.00	1.02	0.99	0.95	0.94
6	1.00	1.02	0.99	0.97	0.95
5	1.00	1.01	0.98	0.96	0.98
4	0.99	1.00	0.95	0.96	1.01
3	0.96	0.98	0.94	1.02	1.02
2	0.99	0.99	0.98	1.04	1.03
1	1.01	0.98	0.98	1.01	1.00

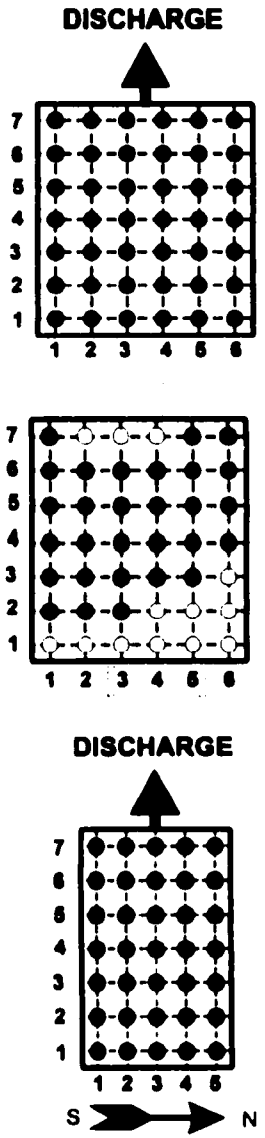

Figure B.2.7 Uniformity of Mixing Experiments in Air Model - Test M3 Dimensionless Temperature Rise

Plane T1 x/D = -0.261

	1	2	3	4	5	6
7	0.34	0.32	0.35	0.35	0.35	0.36
6	0.30	0.32	0.35	0.35	0.35	0.34
5	0.30	0.32	0.35	0.36	0.35	0.35
4	0.32	0.33	0.36	0.36	0.37	0.35
3	0.35	0.35	0.37	0.40	0.40	0.38
2	0.43	0.40	0.43	0.46	0.46	0.44
1	0.57	0.51	0.57	0.56	0.54	0.50

Plane T2 x/D = 0.497

	1	2	3	4	5	6
7	0.91	1.05	1.06	1.01	1.00	0.97
6	0.74	0.96	1.02	0.96	0.95	0.92
5	0.71	0.90	1.00	0.97	0.91	0.84
4	0.74	0.85	1.01	1.01	0.91	0.89
3	0.84	0.92	1.05	1.05	0.96	0.95
2	1.01	0.99	1.09	1.10	1.04	1.01
1	1.12	1.12	1.15	1.18	1.13	1.10

Plane T3 x/D = 1.882

	1	2	3	4	5
7	0.99	1.00	0.99	0.96	0.97
6	1.00	1.01	0.98	0.98	0.97
5	0.99	1.01	0.98	0.98	1.00
4	1.00	0.99	0.95	0.98	1.02
3	0.98	0.99	0.95	1.02	1.03
2	1.01	1.01	1.01	1.04	1.06
1	1.07	1.00	1.04	1.04	1.02

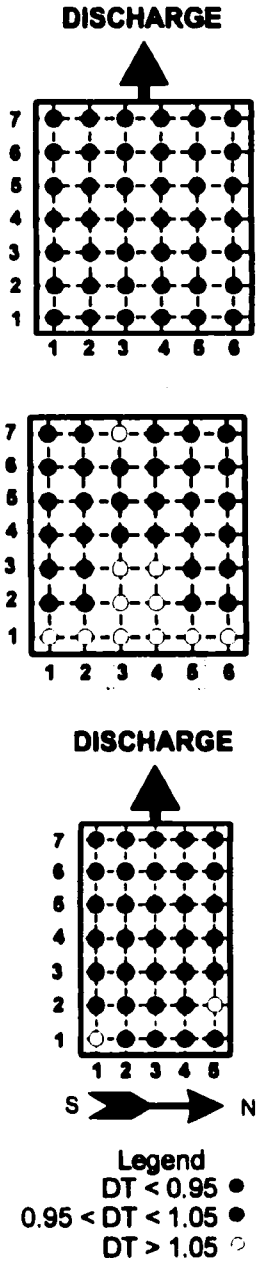

Figure B.2.8 Uniformity of Mixing Experiments in Air Model - Test M4 Dimensionless Temperature Rise

Plane T2 x/D = 0.497

	1	2	3	4	5	6
7	0.78	0.99	1.30	1.07	0.92	0.63
6	0.80	1.03	1.13	1.10	0.95	0.68
5	0.91	0.98	1.04	0.92	0.89	0.91
4	0.92	0.92	0.93	0.88	0.86	0.96
3	0.89	0.99	0.99	1.06	0.95	1.05
2	0.88	1.03	1.27	1.23	1.04	1.10
1	0.89	1.07	1.16	1.26	1.04	1.09

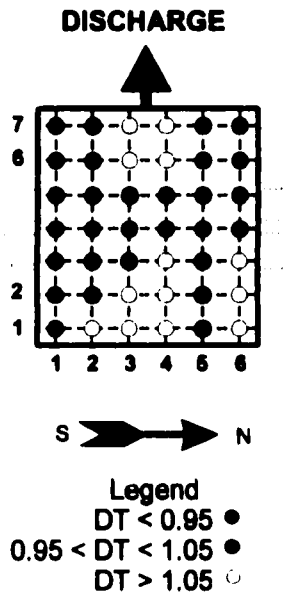

Figure B.2.9 Uniformity of Mixing Experiments in Air Model - Test M5 Dimensionless Temperature Rise

Plane T2 x/D = 0.497

	1	2	3	4	5	6
7	0.84	0.36	0.50	0.69	0.79	0.56
6	0.86	0.85	0.82	1.00	1.03	0.71
5	0.87	0.98	1.33	1.29	1.28	1.01
4	0.80	1.00	1.31	1.70	1.33	1.04
3	0.61	0.94	1.22	1.85	1.33	0.91
2	0.38	0.83	1.40	1.52	1.07	0.89
1	0.16	0.90	1.04	1.04	0.66	0.63

Plane T3 x/D = 1.882

	1	2	3	4	5
7	0.84	0.92	0.98	0.96	1.00
6	0.89	0.91	0.96	0.95	1.01
5	0.95	0.93	0.96	0.95	1.02
4	0.98	0.94	0.99	1.00	1.03
3	0.99	0.97	0.99	1.00	1.04
2	0.97	0.98	0.98	0.99	1.00
1	0.94	0.96	0.97	0.98	0.92

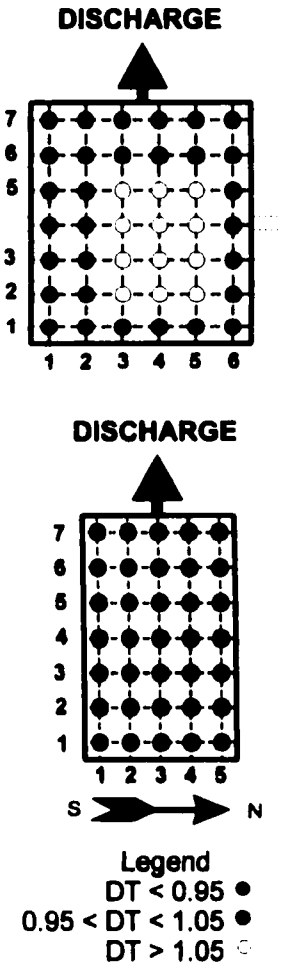

Figure B.2.10 Uniformity of Mixing Experiments in Air Model - Test M6 Dimensionless Temperature Rise

Appendix C

PLANT TRIALS - EXPERIMENTAL CONDITIONS AND RAW DATA

A series of experimental trials were carried out in the plant at the Inco Copper Cliff Smelter Complex. The experimental apparatus was constructed at the Inco Research Laboratory in Mississauga, Ontario and the experimental procedure was developed in the plant. The plant experiments attempted to collect data regarding the post combustion occurring in the flash furnace uptake.

C.1 Experimental Apparatus

In the experimental trials, a suction-type sampler was used to extract samples of gas and particulate from the uptake which was equipped with two sampling ports, SP1 and SP2 (figure C.1.1). The suction-type sampler comprised a sampling probe (12.7 mm Ø 316 SS Sched. 80 pipe) connected to a sample conditioning unit (figure C.1.2). With this apparatus, samples were collected by inserting the probe through a sampling port in the north wall of the uptake. In this way, the gas sample stream was aspirated at right angles to the axial direction of the gas. The probes were 182 cm (6 ft) in length and were inserted about 91 cm (3 ft) into the gas stream. Due to the harsh environment in the uptake, the probes were observed to bend downward making their removal from the port difficult, and there was evidence of chemical attack of the steel. As a result the probes could not be reused.

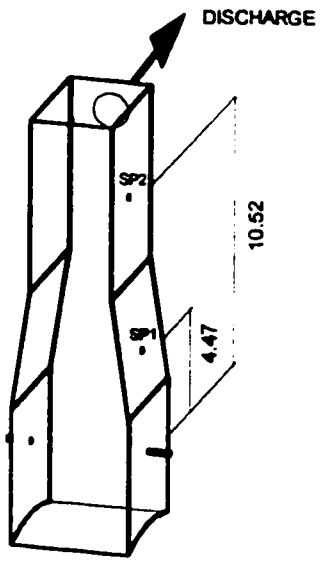

Figure C.1.1 Plant Trials - Schematic of Uptake Sampling Ports

(not to scale, dimensions in m)

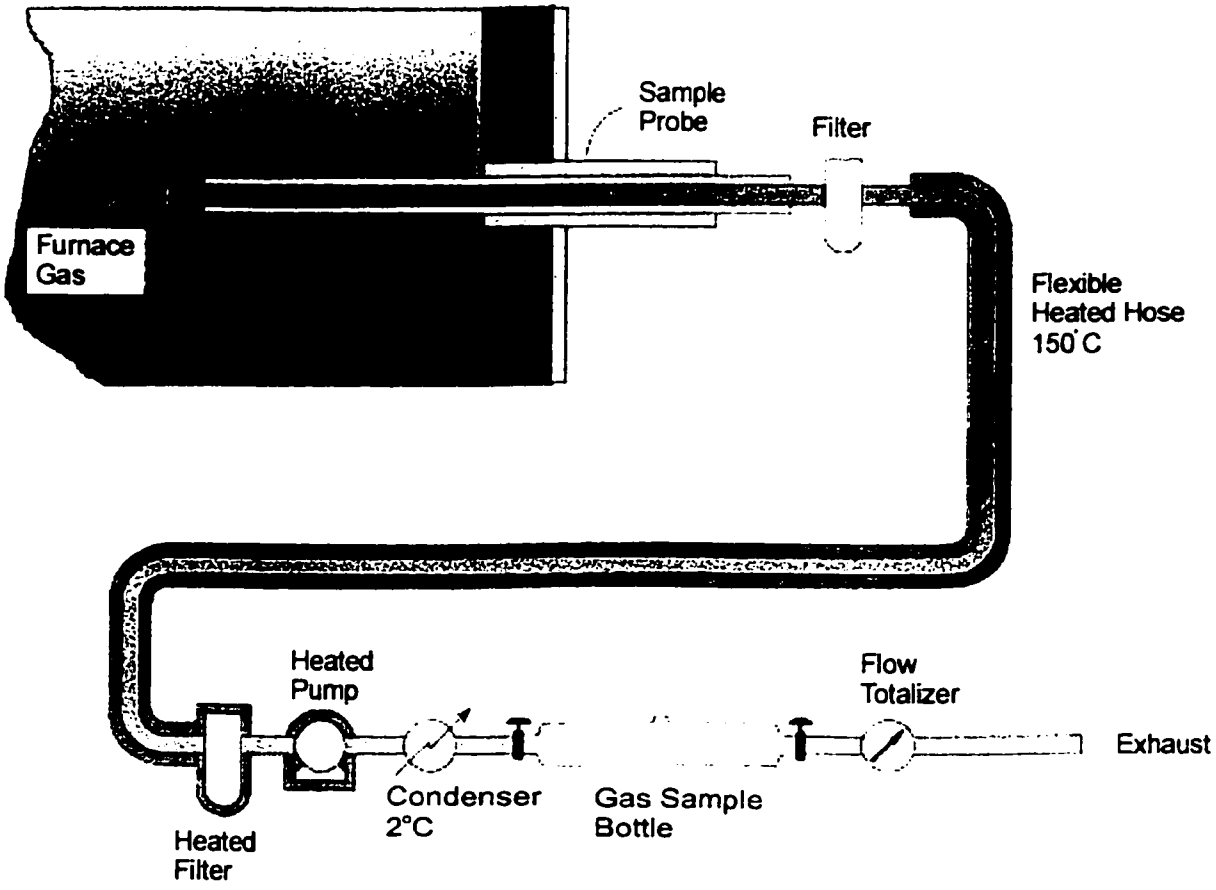

Figure C.1.2 Plant Trials - Schematic of Suction-Type Sampling Apparatus

The sample conditioning unit was designed to recover the condensable phases in the sample stream and to collect a sample of dry gas for analysis. The condensable phases of interest were the particulate, elemental sulfur and moisture. The unit comprised two solids traps in series, a heated pump, a moisture condenser and a dry gas flow totalizer. In an attempt to minimize further reaction between the particulate and gas, the primary solids trap was positioned at the end of the sampling probe and was air cooled. The gas sample drawn through the 182 cm probe was cooled from uptake temperatures of 1300-1400°C to 130°C in the solids trap. However, because the samples were not rapidly quenched, they cannot be considered to be representative of their chemical state in the uptake.

The primary solids trap consisted an 20.3 cm (8 in.) Balston microfiber filter tube encased in a stainless steel housing. The cylindrical filters were composed of borosilicate glass microfibers with an inorganic resin binder and were sealed into the housing by compression at both ends. The filters, resistant to temperatures of 480°C, had a reported efficiency of 99.99% for 0.1 micron particles. In sampling the uptake, the primary solids trap effectively collected 100% of the particulate and condensed sulfur in the gas stream drawn through the sampling unit. No particulate matter was carried over to the back-up solids trap which contained a 10.2 cm (4 in.) Balston microfiber filter tube.

The primary filter was connected to the back-up filter with a flexible heated hose maintained at 150°C to prevent moisture condensation. In addition, to prevent corrosion of the back-up filter and the sampling pump, their temperature was controlled to 150°C. The sampling pump was capable of drawing a sample at a rate of about 8 l/min (0.28 cfm), which was sufficient to prevent settling of suspended particulate in the sample probe. At this sampling rate, the conditioning unit was thoroughly flushed within 1.5 minutes.

Various attempts to sample at iso-kinetic rates proved futile due to the excessive solids loading and the inability to measure the gas velocity at the sampling point. This was unfortunate, as theory suggests that a suction-type collector sampling at a tip velocity greater than the process stream will sample the fine particles preferentially, with the heavier particles not following the

flow lines as well. Therefore, the solids samples collected were not representative of the dust in the process stream and the interpretation of solids sample analysis must take this effect into account.

Subsequent to filtering, the moisture in the sample gas stream was condensed in a U-shape moisture condenser and trapped in a flask. One sample of the dry gas exiting the condenser was collected per experimental trial in a 350 mL glass bottle. The gas bottle was pressurized to 0.5 kPa to prevent air infiltration.

C.2 Sample Analysis

The gas samples withdrawn from the uptake were analyzed with a Varian gas chromatograph for SO_2, CO_2, N_2 and O_2. The gas chromatograph was calibrated with standards injected before, during and after the injection of gas samples, thus ensuring reliable analysis. The gas standard comprised (analysis in volume %): 55% SO_2, 15% CO_2, 5% O_2, 25% N_2.

The preparation and analysis of the solids samples was performed at the Inco J.Roy Gordon Research Laboratory in Mississauga, Ontario. The samples were analyzed for copper, nickel, iron, sulfur, and silica. The analysis of the elements was performed using the inductively coupled plasma (ICP) technique. All calibration standards were prepared by the analytical group at the Inco research laboratory. Unfortunately, insufficient particulate sample was collected with the technique used to sample the gas in the uptake, to permit the analysis of elemental sulfur (S^o) and ferric iron (Fe^{3+}).

Many of the samples were qualitatively examined using scanning electron microscopy (SEM) and x-ray diffraction (XRD) techniques, to determine the species and phases present.

C.3 Operating Procedure

The experimental trials were carried out during periods of stable furnace operation. The operating conditions were varied in order to determine the effect of the afterburner oxygen-to-dry solid feed ratio on the extent of combustion in the uptake under two afterburner configurations. However due to the difficulties encountered with the sampling method and the constraints of time, it was not possible to investigate thoroughly the effects of operating conditions on the combustion carried out in the uptake.

In order to collect a sufficient quantity of solids for chemical analysis, at least 5 minutes of sampling were required. The procedure used to take gas and solid samples was as follows:

1. The probe was connected to the conditioning unit, and a leak check of the probe and condition unit was performed - measured leakage rate was 0.05 l/min.

2. The probe was inserted through the sampling port about 91 cm (3 ft) into the uptake gas space, and the port hole was sealed with a steel plug and ceramic wool to reduce air infiltration.

3. The sampling pump was started, and the sampling train was thoroughly flushed with sample stream for about 3 minutes prior to collecting a sample of the dry gas exiting the condenser. The glass sample bottle was removed, labelled identifying its location, and stored.

4. Sampling continued another 2-4 minutes to collect a sufficient quantity of solids.

5. The sample pump was shut off, the probe was removed from the uptake, and the port hole sealed. The probe and filter were disconnected from the conditioning unit and stored. The unit was flushed with air for several minutes.

6. Solids which had collected in the filter casing were weighed and put in labelled bags identifying their location. The sampling unit was prepared for another sample.

In an attempt to verify the fact that the gas sample bottle was thoroughly flushed with new sample and not contaminated with residual quanitities of air, samples were taken at different times. No difference in gas concentration was observed, indicating that the experimental technique employed was valid (table C.3.1).

C.3.1 Sample Gas Analysis as a Function of Purging

Duration of Purge (min)	Gas Analysis (% vol) SO_2	CO_2	N_2	O_2
1.5	58	9	25	2.9
3.0	58	8	25	2.8

The temperature of uptake gases was then measured with a R-type thermocouple inserted through the sample port about 91 cm (3 ft) into the uptake. The thermocouple was protected with an alumina sheath inside a 12.7 mm Ø inch 316 SS Sched. 80 pipe. These temperature measurements did not use any suction, and must therefore be regarded as only an estimate of the gas and solids temperature in the uptake.

C.4 Experimental Results

The objective of these experiments was to collect samples of solid particulate and gas from the uptake. The experiments was carried out, first, with the afterburner oxygen off to establish a baseline and, then, with it on to evaluate the effect of afterburner oxygen on the post combustion process at different elevation in the uptake. The combustion in the uptake was examined under two afterburner configurations, A and F (figure C.4.1).

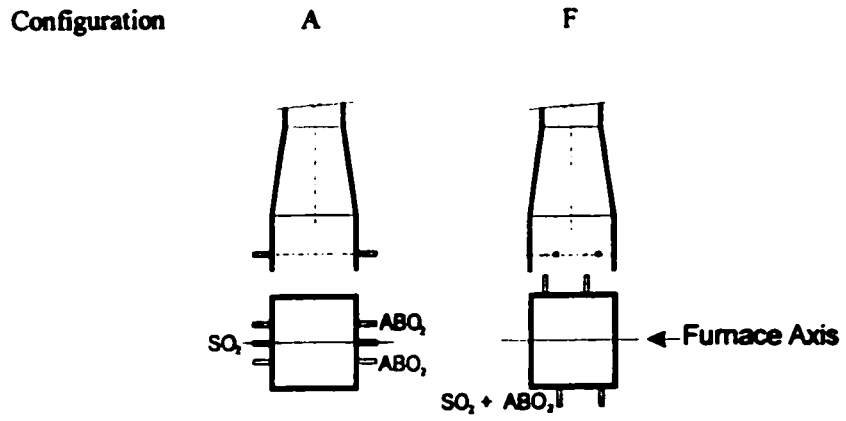

Figure C.4.1 Plant Trials - Afterburner Configurations Tested

A total of 12 experiments, extracting some 60 samples, were attempted but only 3 experiments were considered to be successful. The sampling of solids and gases in the uptake was by no means a trivial task. The presence of particulate, sulfur dioxide and elemental sulfur at high temperature caused considerable problems for the collection equipment. The major problems encountered with this sampling technique were:

- insufficient sample collected for chemical analysis due to premature blockage of the sampling probe.
- contaminated gas samples due to inadequate purging of the sampling unit.
- air contamination of gas sample due to improper assembly of the sampling unit.
- process upsets resulting in a change to the operating conditions of the flash furnace.

Rapid blockage of the probe and/or the filter was the main problem with this sampling method. The blockage would preclude the continuation of sampling and typically occurred during an unexpected process upset, especially converter slag return. During slag returns, it was observed that the furnace rapidly pressurized as indicated by puffing of furnace gas through the sampling port. In addition, a large amount of solids accumulated on the inner and outer surface of the probe suggesting that the dust loading in the furnace gas was greater than normal during slag returns.

The experimental conditions for which the 3 successful tests were carried out, are given in table C.4.1. Tables C.4.2, C.4.3 and C.4.4 provide the chemical analysis of the bulk concentrate and dry solid charge smelted and the gas cleaning slimes produced during the test period, respectively. The dry solid charge processed in the flash furnace is a blend consisting of bulk concentrate, siliceous flux and gas cleaning slimes. The chemical analysis of the bulk concentrate, dry solid charge and gas cleaning slimes represents the average composition of grab samples collected at 4 hour intervals over a period of a 24 hours.

The chemical analysis of the solid particulate sampled from the furnace gas is presented in tables C4.5, C.4.6 and C.4.7. for experimental trials test 1, 2, and 3, respectively. The solid particulate sample comprised two components:

1. loose material collected from the filter housing and the sampling probe, referred to as "loose" in the tables.
2. material entrapped in the fibers of the filter, referred to as "filter" in the tables.

The composite analysis of the solid particulate is a weighted average of the loose material and the material entrapped on the filter.

The composition of the furnace gas in the uptake is found in table C.4.8. Tables C.4.9 and C.4.10 give the results of the X-ray diffraction analysis and the size analysis, respectively, of the bulk concentrate, solid particulate and the gas cleaning slimes. The particle size analysis was determined on a Microtrac X100 particle analyzer. The XRD and size analysis were carried out on the loose material.

Table C.4.1 Plant Trials - Operating Conditions

	Afterburner Configuration	DSC [1] (tph)	Oxygen (Nm^3/hr)	Natural Gas (Nm^3/hr)	Coke (tph)	Furnace Gas [2] (Nm^3/hr)	ABO_2 [3] (Nm^3/hr)	SO_2 Recycle (Nm^3/hr)
Test 1	**A**	102	14300	340	1.1	17000	720	1200
Test 2	**F**	104	14600	0	1.3	15600	950	1280
Test 3	**F**	112	15700	400	1.3	17700	800	1480

Note 1: DSC ≡ Dry Solid Charge

Note 2: Estimated furnace off-gas flow (dry basis) from mass balance.

Note 3: ABO_2 ≡ Afterburner Oxygen

Table C.4.2 Bulk Concentrate Chemical Analysis (% w/w)

		% wt	Cu	Ni	Co	Fe	CaO	Al_2O_3	MgO	SiO_2	S	As	Pb	Zn	Total
Test 1	**Composite**		9.17	9.95	0.36	35.03	0.93	1.78	1.83	8.40	30.39	0.05	0.08	0.12	98.08
	+150 µm	3.48	17.80	6.73	0.25	31.40	0.98	1.85	0.71	7.13	32.20	0.03	0.03	0.10	99.21
	-150 - +75 µm	13.92	12.30	13.70	0.48	34.30	0.60	1.02	0.61	4.13	32.30	0.05	0.05	0.10	99.65
	-75 - +53 µm	14.21	10.00	13.00	0.48	35.20	0.60	1.12	1.13	5.22	32.90	0.05	0.07	0.12	99.89
	-53 - +38 µm	9.64	9.04	11.70	0.43	36.70	0.66	1.25	1.46	6.12	31.70	0.05	0.08	0.12	99.31
	-38 µm	58.75	7.74	8.23	0.30	35.10	1.12	2.21	2.42	10.62	29.00	0.05	0.09	0.13	97.01
Test 2	**Composite**		9.31	10.44	0.39	36.74	0.71	1.45	1.66	6.86	32.04	0.05	0.06	0.10	99.82
	+150 µm	3.95	15.90	6.95	0.28	34.40	0.97	1.93	0.78	7.22	31.00	0.03	0.05	0.09	99.59
	-150 - +75 µm	13.06	12.00	13.30	0.49	36.00	0.45	0.89	0.58	3.51	33.50	0.05	0.05	0.08	100.90
	-75 - +53 µm	12.36	10.70	14.00	0.53	35.40	0.49	0.89	0.85	3.90	33.90	0.05	0.05	0.09	100.84
	-53 - +38 µm	8.79	9.57	13.20	0.50	36.80	0.52	0.85	1.16	4.35	34.30	0.05	0.05	0.10	101.45
	-38 µm	61.84	8.01	8.96	0.34	37.30	0.83	1.74	2.17	8.50	31.10	0.05	0.07	0.11	99.18
Test 3	**Composite**		9.53	10.65	0.37	35.01	0.94	1.89	2.32	9.53	29.91	0.05	0.05	0.10	100.36
	+150 µm	3.03	15.40	7.93	0.28	30.90	1.36	2.57	1.11	10.13	30.30	0.05	0.05	0.11	100.19
	-150 - +75 µm	12.64	11.90	12.60	0.43	33.50	0.80	1.51	1.13	6.45	32.60	0.05	0.05	0.09	101.11
	-75 - +53 µm	8.55	10.30	13.80	0.47	33.70	0.73	1.27	1.41	6.15	32.40	0.05	0.05	0.09	100.41
	-53 - +38 µm	12.91	10.90	13.50	0.51	36.40	0.52	0.95	1.01	4.37	33.40	0.05	0.05	0.10	101.75
	-38 µm	62.87	8.39	9.38	0.32	35.40	1.06	2.21	3.02	11.65	28.30	0.05	0.05	0.10	99.93

Table C.4.3 Dry Solid Charge Chemical Analysis (% w/w)

	Cu	Ni	Co	Fe	CaO	Al_2O_3	MgO	SiO_2	S	As	Pb	Zn	Total
Test 1	7.76	8.08	0.29	28.29	1.37	3.38	2.07	22.48	24.25	0.05	0.07	0.10	98.19
Test 2	8.33	9.17	0.33	31.33	0.93	2.25	1.69	20.50	24.70	0.05	0.06	0.09	99.43
Test 3	8.27	9.6	0.29	30.46	1.02	2.76	1.31	20.08	25.38	0.05	0.07	0.07	99.37

Table C.4.4 Gas Cleaning Slimes Chemical Analysis (% w/w)

	Cu	Ni	Co	Fe	Fe^{3+}	CaO	Al_2O_3	MgO	SiO_2	S_{tot}	SO_4	As	Pb	Zn	Total
Test 1	11.50	9.12	0.29	36.50	19.8	1.26	3.08	2.27	13.88	5.36	1.45	0.19	0.77	0.31	84.53
Test 2	11.10	9.29	0.29	36.05	27.55	0.86	2.58	2.20	11.31	3.49	0.85	0.20	0.53	0.42	77.81
Test 3	11.10	8.44	0.25	31.35	19.30	0.85	3.10	1.34	13.28	8.84	2.99	0.09	0.98	0.24	79.85

Table C.4.5 Test 1 - Solid Particulate Chemical Analysis (% w/w)

	Sample Location	Sample Description	Total (g)	Cu	Ni	Co	Fe	CaO	Al_2O_3	MgO	SiO_2	S	As	Pb	Zn	Total
ABO_x/DSC = 0.00	SP2	loose	3.1	7.29	5.48	0.18	24.40	1.15	2.34	2.06	10.70	37.60	0.33	1.24	0.12	92.89
		filter	1.4	8.33	5.77	0.20	24.64	1.31	2.54	2.69		33.70	0.44	1.71	0.45	81.77
		composite	4.5	7.61	5.57	0.19	24.47	1.20	2.41	2.25		36.39	0.36	1.39	0.22	
ABO_x/DSC = 0.01	SP1	loose	2.0	8.11	6.03	0.20	27.20	1.39	2.74	2.21	11.31	28.80	0.29	0.74	0.32	89.33
		filter	3.0	7.59	5.28	0.17	25.22	1.30	2.38	1.97		32.30	0.40	0.99	0.43	78.02
		composite	5.0	7.80	5.58	0.18	26.01	1.33	2.52	2.06		30.90	0.35	0.89	0.38	
ABO_x/DSC = 0.01	SP2	loose	2.4	8.94	6.56	0.21	29.70	1.55	3.02	2.49	11.48	23.70	0.33	0.80	0.39	89.18
		filter	3.3	8.60	6.60	0.15	26.76	1.15	2.25	1.77		28.60	0.35	0.88	0.39	77.50
		composite	5.7	8.74	6.58	0.18	28.00	1.32	2.57	2.07		26.54	0.34	0.85	0.39	

Note: A silica analysis was not reported for the "filter" samples because the filter material was composed of borosilicate glass fibers, thus contained elevated background levels of silica.

Table C.4.6 Test 2 - Solid Particulate Chemical Analysis (% w/w)

	Sample Location	Sample Description	Total (g)	Cu	Ni	Co	Fe	CaO	Al_2O_3	MgO	SiO_2	S	As	Pb	Zn	Total
ABO_3/DSC = 0.00	SP2	loose	1.6	8.17	6.14	0.21	26.60	1.23	2.48	2.19	10.56	30.20	0.28	0.23	1.02	89.31
		filter	1.7	7.43	5.50	0.15	24.05	1.05	2.01	1.63		35.60	0.57	1.90	0.49	80.38
		composite	3.3	7.79	5.81	0.18	25.29	1.14	2.23	1.90		32.98	0.43	1.09	0.75	
ABO_3/DSC = 0.013	SP1	loose	1.8	8.34	7.20	0.22	26.60	1.16	2.33	2.32	10.02	30.10	0.25	0.61	0.45	89.60
		filter	3.1	8.75	6.11	0.18	27.69	1.20	2.01	1.87		27.90	0.22	0.57	0.41	76.90
		composite	4.9	8.60	6.51	0.19	27.29	1.19	2.12	2.04		28.71	0.23	0.58	0.42	
ABO_3/DSC = 0.013	SP1	loose	1.8	8.16	6.31	0.21	27.70	1.25	2.31	2.02	9.53	30.80	0.25	0.51	0.34	89.38
		filter	2.7	8.15	5.81	0.16	28.29	1.11	2.00	1.64		28.50	0.30	0.68	0.47	77.10
		composite	4.5	8.15	6.01	0.18	28.05	1.16	2.12	1.79		29.42	0.28	0.61	0.42	
ABO_3/DSC = 0.013	SP2	loose	0.7	8.35	6.70	0.21	26.30	1.12	2.27	2.19	9.68	29.90	0.22	0.55	0.40	87.89
		filter	3.0	8.78	6.50	0.20	29.33	1.37	2.34	2.15		23.90	0.25	0.68	0.49	76.01
		composite	3.7	8.70	6.54	0.21	28.76	1.32	2.33	2.16		25.04	0.24	0.66	0.48	
ABO_3/DSC = 0.013	SP2	loose	1.8	8.35	6.63	0.22	28.50	1.25	2.19	2.01	9.49	28.40	0.20	0.40	0.27	87.90
		filter	3.5	8.64	6.61	0.22	30.63	1.37	2.39	2.00		23.00	0.26	0.58	0.66	76.36
		composite	5.3	8.54	6.61	0.22	29.91	1.33	2.33	2.00		24.83	0.24	0.52	0.53	

Note: A silica analysis was not reported for the "filter" samples because the filter material was composed of borosilicate glass fibers, thus contained elevated background levels of silica.

Table C.4.7 Test 3 - Solid Particulate Chemical Analysis (% w/w)

	Sample Location	Sample Description	Total (g)	Cu	Ni	Co	Fe	CaO	Al_2O_3	MgO	SiO_2	S	As	Pb	Zn	Total
ABO_3/DSC = 0.00	SP2	loose	3.1	8.75	6.70	0.18	25.70	1.41	2.91	1.87	10.71	28.40	0.52	2.86	0.69	90.71
		filter	4.5	8.23	6.21	0.18	24.25	1.56	3.02	1.72		32.00	0.43	1.89	1.20	80.68
		composite	7.6	8.44	6.41	0.18	24.84	1.50	2.98	1.78		30.53	0.46	2.28	0.99	
ABO_3/DSC = 0.00	SP2	loose	2.5	7.66	6.52	0.17	25.30	1.19	2.55	1.63	9.87	34.90	0.40	1.22	0.25	91.66
		filter	4.5	8.60	6.34	0.18	26.75	1.27	3.01	1.71		28.90	0.43	2.79	0.40	80.38
		composite	7.0	8.26	6.40	0.18	26.23	1.24	2.84	1.68		31.04	0.42	2.23	0.35	
ABO_3/DSC = 0.01	SP1	loose	2.7	8.21	6.47	0.18	26.50	1.25	2.74	1.87	10.26	30.00	0.33	1.14	0.32	89.27
		filter	5.0	8.31	6.31	0.15	26.60	1.02	2.36	1.44		28.00	0.21	1.48	0.31	76.20
		composite	7.7	8.27	6.37	0.16	26.56	1.10	2.50	1.59		28.70	0.25	1.36	0.31	
ABO_3/DSC = 0.01	SP2	loose	9.6	9.67	7.28	0.21	27.20	1.53	3.18	1.99	10.86	23.40	0.25	1.21	0.47	87.24
		filter	0.7	8.80	6.23	0.18	25.45	1.67	3.20	1.76		28.20	0.23	1.13	0.87	77.71
		composite	10.3	9.61	7.21	0.21	27.08	1.54	3.18	1.97		23.73	0.25	1.20	0.50	

Note: A silica analysis was not reported for the "filter" samples because the filter material was composed of borosilicate glass fibers, thus contained elevated background levels of silica.

Table C.4.8 Plant Trials - Gas Composition (% v/v)

		Sample Location	Gas Temperature [1] (°C)	Dust Loading [2] (g/Nm³)	Dry Gas Analysis (% vol) SO_2	CO_2	O_2	N_2	Total	Log (P) [3] O_2	H_2O
Test 1	ABO_2/DSC = 0.00	SP2	1305	159	56	12	2.4	28	98.4	-1.66	-1.04
	ABO_2/DSC = 0.01	SP1	N/A	132	54	13	3.2	28	98.2	-1.54	-1.02
	ABO_2/DSC = 0.01	SP2	1360	146	55	12	2.6	30	99.6	-1.62	-1.06
Test 2	ABO_2/DSC = 0.00	SP2	N/A	239	59	14	2.3	22	97.3	-1.68	-1.08
	ABO_2/DSC = 0.013	SP1	1392	212	60	14	2.7	21	97.7	-1.61	-1.04
	ABO_2/DSC = 0.013	SP1	N/A	256	61	13	2.9	22	98.9	-1.58	-1.02
	ABO_2/DSC = 0.013	SP2	1405	238	59	15	2.4	21	97.4	-1.65	-1.12
	ABO_2/DSC = 0.013	SP2	N/A	203	61	13	2.3	22	98.3	-1.68	-1.06
Test 3	ABO_2/DSC = 0.00	SP2	N/A	173	56	15	2.3	26	99.3	-1.68	-1.05
	ABO_2/DSC = 0.00	SP2	1279	201	56	14	2.4	27	99.4	-1.66	-1.07
	ABO_2/DSC = 0.01	SP1	1357	186	57	15	2.7	24	98.7	-1.61	-1.02
	ABO_2/DSC = 0.01	SP2	N/A	237	57	14	2.4	26	99.4	-1.66	-1.10

Note 1: Gas temperature measured in the uptake with an R-type thermocouple.

Note 2: Dust loading was calculated based on the weight of solid particulate collected and the total volume of gas drawn through the conditioning unit.

Note 3: The partial pressure (kPa) of O_2 and H_2O was based on the wet gas composition, % by volume.

Table C.4.9 Plant Trials - XRD Analysis of Solid Particulate (Loose Material)

		Sample Location	Sample Description	Chalcopyrite $CuFeS_2$	Pentlandite $(Ni,Fe)_9S_8$	Pyrrhotite Fe_7S_8	Digenite Cu_9S_5	Ni Sulfide NiS	Ferrite Spinel $Ni,FeO\ Fe_2O_3$	Elemental Sulfur S^o	Silicates
Test 1			concentrate	M	m	m					vm
	ABO_x/DSC = 0.00	**SP2**	particulate	M				m	m	M	
	ABO_x/DSC = 0.01	**SP2**	particulate	M				p	M	m	
Test 2	**ABO_x/DSC = 0.000**	**SP2**	particulate	M				m	m	M	
	ABO_x/DSC = 0.013	**SP1**	particulate	M				vm	m	M	
	ABO_x/DSC = 0.013	**SP2**	particulate	M				p	M	m	
Test 3			concentrate	M	m	m					vm
	ABO_x/DSC = 0.00	**SP2**	particulate	M				m	m	M	
	ABO_x/DSC = 0.001	**SP2**	particulate	M				p	M	m	
			gas cleaning slimes				m		M		

Symbols: M = Major; m = minor; vm = very minor; p = possible

Comments: The uptake particulate samples produced very weak diffraction patterns with broadened peaks, indicating poor crystallinity or very small crystal size. The XRD pattern for NiS in the particulate samples was too weak to be conclusive. The copper sulfide phase present in the particulate samples was found to have an XRD pattern similar to that of chalcopyrite.

Table C.4.10 Plant Trials - Size Analysis of Solid Particulate (Loose Material)

		Sample Location	Sample Description	As Received				Effect of Ultrasonic Pulses [3] (8 x 5 second pulses)			
				mv [1]	d_{90} [2]	d_{50} [2]	d_{10} [2]	mv	d_{90}	d_{50}	d_{10}
Test 1			concentrate	35.5	79.2	25.1	3.2	34.3	78.1	24.1	2.9
	ABO_3/DSC = 0.00	**SP2**	particulate	27.4	58.1	20.9	6.1	12.2	24.9	7.9	2.8
	ABO_3/DSC = 0.01	**SP1**	particulate	28.2	63.4	17.4	4.4	13.3	25.3	7.2	2.2
	ABO_3/DSC = 0.01	**SP2**	particulate	16.0	31.6	11.9	4.8	8.4	16.2	6.2	2.8
			gas cleaning slimes					19.4	33.2	7.4	1.4
Test 3	**ABO_3/DSC = 0.01**	**SP2**	particulate					12.1	23.7	6.7	2.7

Note 1: mv ≡ mean diameter (microns) of the volume distribution

Note 2: d_{90} ≡ 90% of the volume weight (assuming uniform specific gravity of the particles) smaller than indicated sized (microns)
d_{50} ≡ 50% of the volume weight (assuming uniform specific gravity of the particles) smaller than indicated sized (microns)
d_{10}≡ 10% of the volume weight (assuming uniform specific gravity of the particles) smaller than indicated sized (microns)

Note 3: The samples were treated in an ultrasonic bath to break apart weakly bonded or agglomerated particles, held together by a webbing of elemental sulphur. Exposing the particle to 8 x 5 second ultrasonic pulses was found to be sufficient to breakdown the bond between the particles.